



HAL
open science

Etude de la combustion de mélanges pauvres sur la base de biocarburant. Application par auto-allumage contrôlé par injection de particules de biomasse

Mira Ibrahim

► To cite this version:

Mira Ibrahim. Etude de la combustion de mélanges pauvres sur la base de biocarburant. Application par auto-allumage contrôlé par injection de particules de biomasse. Milieux fluides et réactifs. Sorbonne Université, 2020. Français. NNT : 2020SORUS088 . tel-03892695

HAL Id: tel-03892695

<https://theses.hal.science/tel-03892695v1>

Submitted on 10 Dec 2022

HAL is a multi-disciplinary open access archive for the deposit and dissemination of scientific research documents, whether they are published or not. The documents may come from teaching and research institutions in France or abroad, or from public or private research centers.

L'archive ouverte pluridisciplinaire **HAL**, est destinée au dépôt et à la diffusion de documents scientifiques de niveau recherche, publiés ou non, émanant des établissements d'enseignement et de recherche français ou étrangers, des laboratoires publics ou privés.

THÈSE

Pour l'obtention du Grade de
Docteur de Sorbonne Université

Présentée par :

Mira IBRAHIM

Etude de la combustion de mélanges pauvres sur la base de biocarburant.
Application par auto-allumage contrôlé par injection de particules de
biomasse

Directeur de Thèse : M. Philippe GUIBERT

Co-encadrant: M. Khanh-Hung TRAN

Soutenue le 08 Décembre 2020

Membres de jury

| | | | |
|---------------------|----------------------------|--------------|---|
| M. Marc BELLENOUE | Professeur des Universités | Rapporteur | Institut Pprime, Poitiers |
| M. Patrick DA COSTA | Professeur des Universités | Examineur | Sorbonne Université |
| M. Philippe GUIBERT | Professeur des Universités | Directeur | Sorbonne Université |
| M. Pascal HIGELIN | Professeur des Universités | Rapporteur | Université d'Orléans |
| Mme Céline MORIN | Professeur des Universités | Examinatrice | Université Polytechnique Hauts-de-France |
| M. Khanh-Hung TRAN | Maitre de Conférences | Co-encadrant | Université Paris Nanterre |

Remerciements

Je voudrais tout d'abord adresser ma très profonde gratitude à mon directeur de thèse M. Philippe Guibert, pour sa patience, sa disponibilité et surtout ses conseils judicieux, qui ont contribué à alimenter ma réflexion. Il m'a accompagné dans la maîtrise de mes connaissances et a enrichi ce travail avec ces conseils précieux et avisés. Merci beaucoup pour tous les remarques et les encouragements depuis le master.

Je tiens à remercier également M. Khanh-Hung Tran, pour son soutien, sa disponibilité, ses connaissances et ses questions critiques qui m'ont aidé tout au long de la thèse et ont fait de moi une meilleure chercheuse.

Je remercie M. Marc Bellenoue et M. Pascal Higelin d'avoir accepté d'être les rapporteurs de ce mémoire de thèse, ainsi que Mme Céline Morin pour sa participation au jury. Je tiens à remercier également M. Patrick Da Costa, pour sa participation au jury, ses conseils et son support durant les trois années de thèse.

Un grand merci à tout l'équipe technique de l'Institut Jean Le Rond d'Alembert, en particulier M. Frédéric Segretain qui m'a toujours aidé surtout dans les problèmes liés à la machine à compression rapide.

Mes remerciements vont à mes collègues avec qui j'ai partagé de très bons moments, pauses café et de très belles soirées : Chao, Marcellin, Ye, Golshid, Paulina, Yutao, Bo, Renaud, Hailong, Akshay et tous les autres doctorants, stagiaires et post-doctorants. Je remercie également Jean-François Krawczynski, Alexis Matynias, Jérôme Bonnetty, Guillaume Legros et tous les autres membres du laboratoire ainsi que les secrétaires pour leur travail.

J'adresse ma reconnaissance et bien plus... à tous mes amis pour leur soutien. Sans eux je n'aurais pas eu la joie de continuer sur ce long chemin studieux. Ce succès est également un peu le leur. À eux tous, je souhaite beaucoup de bien. Je tiens à adresser un remerciement spécial à Salim Sayssouk pour sa disponibilité et ses conseils judicieux.

Ma reconnaissance va à ceux qui ont plus particulièrement assuré le soutien affectif de cette journée : ma famille. Mes parents, mon oncle Mahmoud et mes sœurs, Rim, Sara et Maria (ma compatriote libanaise qui est devenue ma sœur). Grâce à eux mon séjour en France et la poursuite de mes études jusqu'à ce stade ont été possibles. Je les remercie de tout mon cœur pour leur amour et leur soutien discret et essentiel. C'est avec leurs encouragements que j'ai pu accomplir ce travail de thèse. J'en profite pour glisser un clin d'œil aussi au reste de la famille sans qui je n'aurais pas eu le goût de me lancer dans cette aventure.

Enfin, je finirai par une tendre pensée pour mon très cher Moustafa toujours très optimiste, qui m'a soutenu, encouragé et rassuré tout au long de cette thèse, ce qui n'a certainement pas dû être simple tous les jours... Merci infiniment.

Résumé

La combinaison d'une technologie alternative comme l'allumage par compression de la charge (HCCI) avec une énergie renouvelable comme la biomasse est un bon compromis pour réduire les émissions polluantes à la source. L'un des problèmes majeurs de cette combustion est le contrôle du moment de l'allumage ; l'injection directe de particules solides en suspension dans le mélange réactif permet de contrôler le début de la combustion.

Dans la première partie de ce travail, la combustion de la biomasse gazeuse a été étudiée expérimentalement sur une machine à compression rapide dans des conditions HCCI. En raison de la complexité de ce mode de combustion, une approche simplifiée du processus a été simulée numériquement sur Chemkin-Pro pour étudier les effets des conditions initiales et de la composition du combustible sur les aspects physico-chimiques de la combustion ainsi que sur les émissions produites. Après avoir mis en évidence les avantages de la combustion pauvre, et d'un combustible type (biogaz/gaz de synthèse) dans la réduction des émissions polluantes, une base de données a été constituée pour sélectionner une gamme optimisée de conditions pour des émissions minimales et une réactivité spécifique.

La deuxième partie de ce travail a été consacrée au contrôle du moment de l'allumage. Un injecteur de particules a été conçu pour injecter directement la poudre de biomasse dans le mélange réactif. Ce système a été combiné avec la machine à compression rapide, permettant l'étude de la combustion de biomasse dans différentes conditions initiales avant son injection dans le gaz réactif. Les résultats de cette étude ont mis en lumière les effets prometteurs de l'injection de poudre sur le contrôle de la combustion homogène pauvre.

Mots clés : HCCI ; Biomasse ; Combustion diphasique gaz/solide ; Contrôle d'allumage ; système d'injection de particules ; Emissions polluantes ; Machine à compression rapide ; Chemkin-Pro

Abstract

Combining an alternative technology like charge compression ignition (HCCI) with renewable energy such as biomass is a good compromise to reduce pollutant emissions at the source. One major problem of this combustion is the control of ignition timing; the direct injection of solid particles in suspension into the reactive mixture may control the start of ignition.

Hence, the work was divided into two parts. In the first part, gaseous biomass combustion was studied experimentally on a rapid compression machine under HCCI conditions. Because of the complexity of this combustion mode, a simplified approach of the process was simulated numerically on Chemkin-Pro to study the effects of initial conditions and fuel composition on the physico-chemical aspects of the combustion as well as the produced pollutant emissions. After highlighting the advantages of lean combustion, and a fuel type biogas/syngas in reducing pollutant emissions, a database was built to select an optimized range of conditions for minimal emissions and a specific reactivity.

The second part of this work was dedicated to ignition control. A particle injector was conceived to inject biomass powder into the reactive mixture directly. This system was combined with the rapid compression machine, allowing the study of biomass combustion with different initial conditions prior to its injection into reactive gas. The results of this study shed light on the promising effects of powder injection in the control of lean homogeneous combustion.

Key words: HCCI; Biomass; Diphasic combustion gas/solid; Ignition control; particle injector system; pollutant emissions; Rapid compression machine; Chemkin-Pro;

Table of Contents

| | |
|---|----|
| Résumé | 3 |
| Abstract | 4 |
| Glossary..... | 10 |
| General introduction and objectives of this thesis | 12 |
| Chapter 1: | 15 |
| State of art: Alternative solutions of biomass and lean homogeneous combustion | 15 |
| I. Scientific context..... | 16 |
| II. Use of biomass as renewing fuel..... | 19 |
| 1. Origin and production of gaseous biomass | 19 |
| 1.1. Biomass methanisation | 20 |
| 1.2. Biomass gasification | 21 |
| 2. Applications in internal combustion engine..... | 24 |
| III. Homogeneous combustion | 26 |
| 1. Definition of homogeneous combustion | 26 |
| 2. Combustion process and heterogeneities | 28 |
| 3. Major problematic and challenges of homogeneous combustion | 30 |
| 4. Strategies into homogenization and control ignition timing | 32 |
| IV. Conclusions | 34 |
| Chapter 2: | 35 |
| An experimental study of the combustion of biogas/syngas mixtures under lean homogeneous conditions | 35 |
| I. Introduction | 36 |
| II. Characterization of the experimental setup: SU RCM..... | 37 |
| 1. SU RCM presentation | 37 |
| 1.1. SU RCM description..... | 37 |
| 1.2. Compression time | 38 |
| 1.3. Mixture preparation | 40 |
| 1.4. Experimental procedure | 40 |
| 2. Definition and identification of experimental auto-ignition delay time..... | 42 |
| 2.1. Definition of auto-ignition delay time | 42 |
| 2.2. Experimental identification on rapid compression machine..... | 43 |
| 3. End of compression calculations..... | 45 |

| | | |
|------|--|----|
| 3.1. | Adiabatic temperature | 45 |
| 3.2. | Polytropic and non-adiabatic temperature | 46 |
| 4. | Study of reliability of results: comparing SU RCM results to other RCM in the literature | 47 |
| 4.1. | Comparison tests | 47 |
| 4.2. | Comparison RCM designs | 48 |
| 4.3. | Reliability of results | 50 |
| 5. | Conclusions | 53 |
| III. | Experimental study of the combustion of biomass-derived fuel | 54 |
| 1. | The choice of the studied biomass-derived fuel mixture | 55 |
| 2. | Presentation of experimental conditions | 57 |
| 3. | Experimental results | 58 |
| 3.1. | Study of reproducibility of results pressure and heat release profile during compression, post-compression, and combustion phase | 58 |
| 3.2. | The auto-ignition of methane and hydrogen mixtures | 62 |
| 3.3. | The auto-ignition of CH ₄ /H ₂ /CO ₂ mixtures | 64 |
| 3.4. | The auto-ignition of CH ₄ /H ₂ /CO ₂ /CO mixtures | 66 |
| 4. | Conclusions on the experimental study of biofuel combustion | 67 |
| 5. | Conclusions | 69 |
| | Chapter 3: | 71 |
| | A numerical study of the combustion of biogas/syngas mixtures under lean homogeneous conditions | 71 |
| I. | Introduction | 72 |
| II. | Simplified approach and simulation conditions | 72 |
| III. | The selection of chemical mechanisms | 75 |
| 1. | Definition and use of chemical mechanisms | 75 |
| 2. | Closed homogeneous reactor | 80 |
| 3. | Comparison of calculated and measured ignition delay time for the selection of a chemical mechanism | 82 |
| IV. | Approach I: Closed homogeneous reactor | 87 |
| 1. | Simulated conditions and assumptions | 88 |
| 2. | Auto-ignition delay time and temperature | 90 |
| 2.1. | Influence of the pressure and temperature | 91 |
| 2.2. | Influence of the equivalence ratio | 94 |
| 2.3. | Influence of the fuel composition | 97 |

| | | |
|-------|---|-----|
| 3. | Pollutant emissions..... | 102 |
| 3.1. | Types of pollutant emissions and greenhouse gases at the end of the combustion ... | 102 |
| 3.2. | Methods of calculation..... | 104 |
| 3.3. | Influence of different parameters on the pollutant emissions..... | 106 |
| 4. | Conclusions and discussions on optimal mixtures and conditions in auto-ignition point of view | 115 |
| V. | Approach II: Adiabatic premixed flame..... | 118 |
| 1. | Simulated conditions and assumptions | 118 |
| 2. | Flame characteristics and properties | 119 |
| 5.1. | 2.1. Flame speed and thickness..... | 119 |
| 2.2. | Flame Stability and types of instabilities | 122 |
| 3. | Parametric study of flame speed | 125 |
| | Pressure and equivalence ratio influence | 125 |
| | Fuel composition influence | 127 |
| 4. | Parametric study of pollutant emissions..... | 130 |
| 5. | Parametric study of flame stability..... | 135 |
| 5.2. | Calculation of Lewis number and critical Lewis number | 135 |
| 5.3. | Parametric study..... | 137 |
| 6. | Conclusions on optimal mixtures and conditions in premixed flame point of view | 140 |
| VI. | Optimization on the simplified approach..... | 142 |
| VII. | Turbulent combustion | 144 |
| 1. | Non-dimensional numbers in turbulent combustion | 144 |
| 2. | Combustion diagram | 146 |
| 3. | Positioning of optimal mixtures on combustion diagram | 148 |
| 4. | Conclusions and proposed experimental study | 153 |
| VIII. | Conclusions | 155 |
| | Chapter 4: | 157 |
| | Biomass combustion | 157 |
| I. | Introduction | 158 |
| II. | Particle injection system..... | 160 |
| 1. | Description of the experimental setup..... | 160 |
| 2. | Determining the start and duration of the particle injection process..... | 163 |
| 3. | Determining the particle jet characteristics | 164 |

| | | |
|------|--|-----|
| 3.1. | Definition and calculations | 164 |
| 3.2. | Results..... | 165 |
| 4. | PIV measurements..... | 168 |
| 4.1. | Definition and calculation..... | 168 |
| 4.2. | Results..... | 169 |
| 5. | Conclusions on this section | 172 |
| III. | Biomass Composition | 174 |
| 1. | Cellulose..... | 175 |
| 2. | Hemicellulose..... | 177 |
| 3. | Lignin | 178 |
| 4. | Extractives, inorganic, and moisture contents..... | 179 |
| IV. | Biomass combustion | 180 |
| 1. | Introduction | 180 |
| 2. | Ignition mechanism | 182 |
| 3. | Biomass Pyrolysis | 182 |
| 3.1. | Factors Affecting Biomass Pyrolysis | 183 |
| 3.2. | Modeling the pyrolysis process..... | 185 |
| 3.3. | Conclusions of this section..... | 186 |
| 4. | Experimental study of biomass combustion..... | 187 |
| 4.1. | Experimental tests and conditions of the combustion of solid biomass | 187 |
| 4.2. | Ignition delay time and ignition temperature..... | 190 |
| 4.3. | Assumption calculations and experimental challenges..... | 191 |
| 4.4. | Effect of temperature, injection time, aerodynamics | 193 |
| V. | Conclusions | 201 |
| | Chapter 5: | 203 |
| | Diphasic combustion gas/solid..... | 203 |
| I. | Introduction | 204 |
| II. | The fundamentals of direct visualization | 205 |
| III. | Experimental Setup | 206 |
| IV. | Chronograms of direct visualization | 207 |
| V. | Biofuel combustion | 208 |
| 1. | Experimental mixtures and conditions of biofuel combustion..... | 208 |
| 2. | Law of heat release and chemiluminescence | 209 |

| | | |
|------|---|-----|
| 3. | Extracting of combustion properties | 210 |
| 3.1. | Auto-ignition sites | 210 |
| 3.2. | Apparent surface and combustion speed | 212 |
| 4. | Visualization of the combustion process by chemiluminescence | 214 |
| 5. | Conclusions | 233 |
| VI. | Gas/solid biomass combustion | 234 |
| 1. | Experimental mixtures and conditions of gas/solid biomass combustion..... | 234 |
| 2. | Results on the effect of solid biomass over biofuel combustion..... | 235 |
| 2.1. | Mixture 13..... | 236 |
| 2.2. | Mixture 14..... | 240 |
| 2.3. | Mixture 15..... | 244 |
| VII. | Conclusions of this chapter | 249 |
| | Conclusions and perspectives..... | 250 |
| | Figure List | 252 |
| | Table List..... | 257 |
| | Appendix Chapter 3 | 259 |
| | References | 278 |

Glossary

| | | |
|------------|---|--|
| C | Charge | (mol.m ⁻³) |
| C_p, C_v | Heat Capacity at constant pressure and volume | (J.K ⁻¹) |
| D_i | Mass diffusion coefficient of component i | (-) |
| d | jet penetration length | (m) |
| dP | Pressure increase compared to P_c | (Pa) |
| Da | Damköhler number | (-) |
| E_a | Activation energy | (J.mol ⁻¹) |
| EI | Emission Index | (g. kJ ⁻¹) |
| Ka | Karlovitz number | (-) |
| Le | Lewis number | (-) |
| Le_c | Critical Lewis number | (-) |
| LHV | Low Heating Value | (J.mol ⁻¹) |
| l_T | Integral length scale | (m) |
| M_u, M_b | Molecular weight of fresh and burnt gas | (g.mol ⁻¹) |
| P | Pressure | (Pa) |
| P_0 | Initial pressure | (Pa) |
| P_c | End of compression pressure | (Pa) |
| P_{max} | Peak pressure of combustion | (Pa) |
| R | Universal Perfect Gas Constant (8.314) | (J.mol ⁻¹ . K ⁻¹) |
| S_L^o | Laminar Flame Speed | (m.s ⁻¹) |
| T | Temperature | (K) |
| T_0 | Initial Temperature | (K) |
| T_c | End of compression temperature | (K) |
| T_{isen} | Isentropic temperature | (K) |
| T_{ac} | Adiabatic core temperature | (K) |
| T_{poly} | Polytropic temperature | (K) |
| T_u, T_b | Temperature of fresh and burnt gas | (K) |
| u' | Fluctuating turbulent velocity | (m.s ⁻¹) |
| x, y, z | Spatial coordinates | (m) |
| x_{O_2} | molar fraction of oxygen in the mixture | (-) |

Greek Symbols

| | | |
|----------------|---|-------------------------------------|
| θ | Jet cone angle | (°) |
| $\bar{\theta}$ | Average jet angles | (°) |
| δ_L | laminar flame thickness | (m) |
| ϕ | Equivalence ratio | (-) |
| λ | Thermal conductivity | J.m ⁻¹ . K ⁻¹ |
| γ | the temperature-dependent specific heat ratio | (-) |
| α | Thermal diffusion coefficient | (-) |
| β | Zeldovich number | (-) |

| | | |
|---------------|--|-------------------------------------|
| σ | Standard deviation of ignition delay times | (s) |
| ε | Volumetric compression ratio | (-) |
| τ | Ignition delay time | (s) |
| ρ | Density of a mixture | (g.m ⁻³) |
| ν | Kinematic Viscosity | (m ² . s ⁻¹) |

Acronyms

| | |
|--------|---|
| GHG | Greenhouse Gas Emissions |
| CAI | Controlled Auto Ignition |
| CFD | Computational Fluid Dynamics |
| CI | Compression Ignition |
| DNS | Direct Numerical Simulation |
| DP | degree of polymerization |
| EGR | Exhaust Gas Recirculation |
| EOC | End of Compression |
| HCCI | Homogeneous Charge Compression Ignition |
| HPC | Highly Premixed Combustion |
| IMEP | Indicated Mean Effective Pressure |
| LDI | Lean Direct Injection |
| LIF | Laser-Induced Fluorescence |
| LPP | Lean Premixed Pre-vaporized |
| LTR | Low Temperature Reaction |
| LULUCF | Land Use, land-Use Change, and Forestry |
| NTC | Negative Temperature Coefficient |
| NUIG | National University of Ireland, Galway |
| MIT | Massachusetts Institute of Technology |
| PIV | Particle Image Velocimetry |
| PLIF | Planar Laser Induced Fluorescence |
| PPC | Partially Premixed Combustion |
| PRF | Primary Reference Fuel |
| PS | Pollutant Specie |
| RCM | Rapid Compression Machine |
| RON | Research Octane Number |
| SACI | Spark Assisted Compression Ignition |
| SI | Spark Ignition |
| SU | Sorbonne University |
| TDC | Top Dead Center |
| TGA | Thermogravimetric Analysis |
| VCR | Variable Compression Timing |
| VVT | Variable Valve Timing |
| WOT | Wide-Open Throttle |

General introduction and objectives of this thesis

The sustained population growth will induce a sharp increase in global transport, and economic demand over the next few decades, impacting the environment and requiring an ever-increasing reduction in polluting emissions from vehicles. Due to the growth in environmental, climate, and health issues, legislators are making the standards for pollutant emissions from vehicles increasingly stringent over time.

The standards impose emission limit values for nitrogen oxides (NO_x), carbon monoxide (CO), hydrocarbons (HC), and particulate matter (PM). Environmental considerations are, therefore, the center of car manufacturers' concerns. As a result, manufacturers are looking for alternative solutions to meet the pollutant levels set by the standards. Among all the solutions proposed to address this issue is the equipment of the conventional types of engines with exhaust post-treatment systems. The use of three-way catalysts (CO, HC, NO_x) reduces pollutant emissions by treatment at the combustion chamber's exit. However, the use of these catalysts requires operation at near stoichiometric conditions. The major drawbacks of these engines are reduced efficiency at moderate loads caused by pumping losses and low thermodynamic efficiency—the latter results from the relatively low compression ratios used to avoid the knocking phenomenon.

Even though the compression-ignition engine has a higher manufacturing cost, it has higher thermodynamic efficiency. However, the emissions of nitrogen oxides (NO_x) and particulates are significant and require costly post-treatment systems. Future anti-pollution standards will impose contradictory constraints in terms of emissions and consumption. They will, therefore, be costly and challenging to meet with the conventional engines described above. Various technological solutions are possible in the long term to improve fuel consumption and reduce pollutant emissions. These can include the combustion of alternative fuels derived from biomass, downsizing, and the use of variable valve timing or compression ratio, hybridization, electric vehicles, and fuel cells. Hybridization technology makes it possible to reduce CO_2 emissions compared to gasoline vehicles significantly. The CO_2 emissions of this technology are close to those of diesel vehicles. However, the challenges related to this technology are numerous: improving battery performance, operating conditions, reducing costs, and the environmental impact of the combustion engine.

Innovative solutions can also be found in the way combustion may occur. One of the most promising alternatives in this regard is lean homogeneous combustion. Many acronyms are generally used in the literature to refer to this combustion mode in engine applications. In the following study, we will refer to it by the abbreviation HCCI.

Lean homogeneous combustion is a clean technology that reduces emissions by inhibiting NO_x and soot formation while maintaining appreciable efficiency due to its high combustion rate, therefore to mass combustion controlled by auto-ignition. Hence, this combustion process must face low reactivity at low combustion temperature or lean-burn conditions; it is necessary to adapt the fuel in this operating range. The use of this combustion process with a gaseous mixture based on biomass is, from a carbon balance point of view, a good compromise to have minimal polluting emissions. Therefore, we will only focus on the fuels emitted from biomass in the thesis work.

However, the complexity of the physico-chemical phenomena of biofuel combustion in HCCI mode is mainly linked to the heterogeneities created during combustion and the control of the ignition timing. Research domains of dust explosions shed the lights on diphasic combustion

gas/solid and on the effects that can have the powder in suspension in promoting the ignition of a reactive gas mixture.

Thus, the advances in combustion research methods by HCCI with the addition of the research domains of dust explosions and thermochemical biomass conversion constitute the core of this thesis. In other words, the innovative solution of ignition control will be based on the injection of dust and/or particles into the reactive gas.

The injected particles in suspension may not only control and stabilize the lean homogeneous combustion of gas but can also ignite the reactive mixture in different sites of the combustion chamber, which can offset the thermal heterogeneities. The understanding of two-phase combustion will remain a fundamental challenge of the thesis.

This thesis's first primary objective is to provide a database to characterize biofuel combustion in lean homogeneous mixtures. This includes studying the effects of the initial conditions (temperature, pressure, and equivalence ratio) and the fuel composition on the combustion's physical and chemical properties. Furthermore, their effects on the produced pollutant emissions are also studied throughout this manuscript. This database allows for choosing the range conditions and biofuels suitable for an engine application of lean combustion. Another primary objective is to study the effects of biomass particles in controlling the combustion process and stability of lean homogeneous gas mixtures.

The numerous objectives of this thesis can be classified into five chapters:

The purpose of chapter I is to present the context of the study. In addition to the brief description of future regulations, it highlights the need to develop new combustion mechanisms that reduce pollutants at the source of combustion with a limited post-treatment system. The first part will be devoted to the presentation of biofuels derived from biomass, in particular biogas and synthesis gas. The origin, the composition, and the process of gasification and anaerobic digestion will be presented briefly. Another part will be dedicated to the presentation of homogeneous combustion; after explaining the general principle of this type of combustion and comparing it to conventional diesel and gasoline combustion, a short review of the various challenges and proposed solutions will be presented.

This bibliographical work will then make it possible to identify the main work lines to be pursued within this study's framework.

Chapters II and III focus on studying the combustion of the gaseous mixture of biomass (CH_4 , CO_2 , H_2 , and CO). Experimental and numerical studies are conducted to determine the self-ignition and flame propagation properties of hydrogen-enriched biofuel gas mixtures. More specifically, the effect of different parameters (such as temperature, pressure, equivalence ratio, and the composition of the fuel mixture) on the combustion properties and the resulting pollutant emissions (including NO_x , CO_2 , CO) will be studied.

Experimental studies are carried out on the Sorbonne University rapid compression machine (SU RCM) and are presented in the second chapter. The rapid compression machine's main technical characteristics are also presented. The numerical simulations are carried out on Chemkin-Pro software through the Grimech3.0 reaction mechanism and are presented in Chapter III. The obtained results allow the optimization of fuel mixture both in terms of the auto-ignition process and flame propagation.

In chapter IV, a literature review on solid biomass is presented; this review is mainly devoted to presenting biomass chemical compositions, the physical and chemical properties, and existing combustion models of particles. A particle injection system has been designed and mounted on the rapid compression machine. A PIV study was first conducted to better characterize this injection system (start and end of injection, reproducibility of the injected volume, depth of field, and the injection speed). The combustion of the biomass powder was carried out on the rapid compression machine; the particles were injected at non-reactive Ar/O₂ mixtures and under different temperatures to identify their combustion properties.

Finally, chapter V will conduct rapid cinematography on the SU RCM to visualize biofuel mixtures' combustion process. This will help complete the database of their combustion characterization and better understand physico-chemical phenomena. In the second part of this chapter, solid biomass particles' effect on biofuel combustion is studied. Biomass particles are directly injected into the reactive gas mixtures; the effects of particles in controlling the combustion initiation will be highlighted.

Chapter 1:

State of art: Alternative solutions of biomass and lean homogeneous combustion

Chapter 1

I. Scientific context

During the last two decades, a strong interest in the development of renewable energy sources has grown. The reasons for this interest are mainly the increase of the pollutant emissions in the environment produced from hydrocarbon and nuclear energy sources and the increasing anxiety regarding the security and sustainability of fossil fuels.

According to the annual European Union greenhouse gas inventory 1990–2018[1], the total greenhouse gas (GHG) emissions (without LULUCF and international aviation and maritime transport) have decreased by 1425 million tons (25.2 %), reaching a lower level of 4234 Mt CO₂ equivalent in 2018. This significant reduction in greenhouse gas emissions over the 28 years was due to various factors, including the growing use of renewable energy, the multiple improvements in energy efficiency, and the structural changes in the economy and the economic recession. Another factor contributing to lower GHG emissions in Europe includes the use of less carbon-intensive fossil fuels, such as biomass for energy purposes. This emission reduction concerns major sources, except for Road transportation, which accounts for 26 % of CO₂ emissions in 2018, as shown in Figure 1 below.

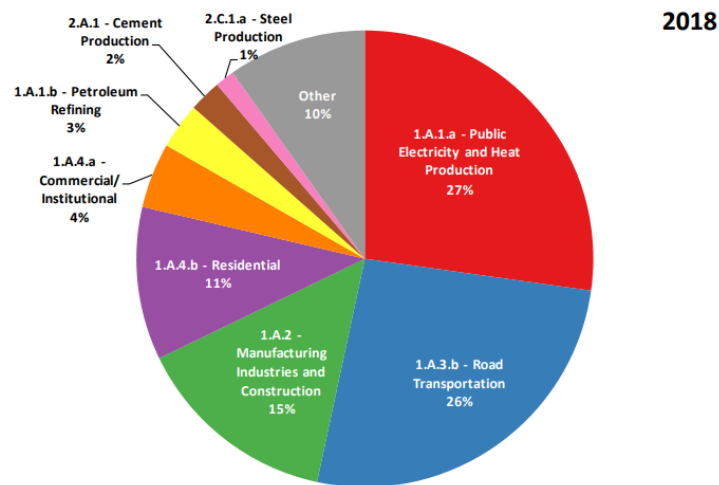


Figure 1: CO₂ emissions: Share of key source categories and all remaining categories in 2018 for EU-KP [1]

This image shows that road transportation along with public electricity and heat production have the higher share in CO₂ emission in Europe for the year 2018.

Furthermore, in 2018, international shipping and aviation accounted for 150 million tons and 167 million tons of CO₂ equivalent, respectively, majorly due to economic growth and demand; this is equivalent to an increase of emissions by nearly 141% and 35% respectively over the past two decades [1]. Thus, the transport sector is considered one of the biggest sources of CO₂ emissions in Europe, being responsible for the emission of over a quarter of all greenhouse gases.

However, France differs from the rest of the EU due to the low share of emissions from the energy industry because of its large nuclear electricity production capacity [2], as shown in Figure 2.

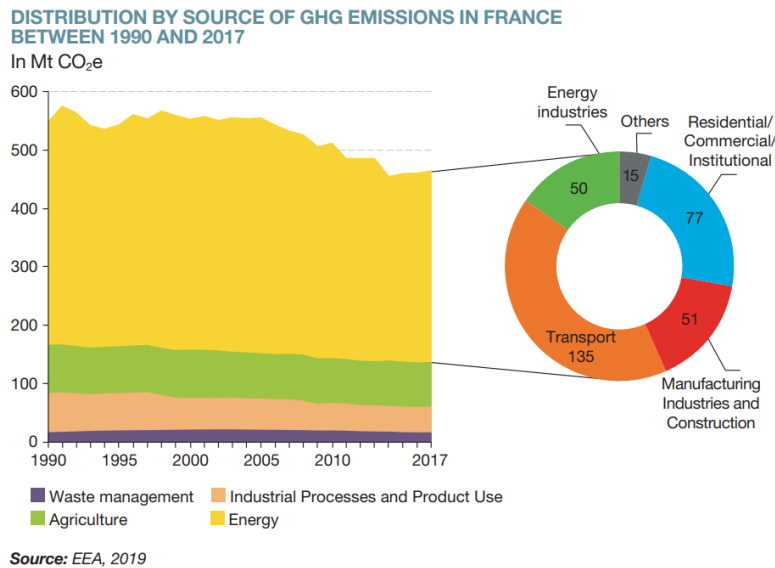


Figure 2: Distribution by the source of GHG emissions in France between 1990-2017 [2]
This statistical study illustrates the decrease of GHG emission in France between 1990-2017. This decrease is mainly related to the drop in the emissions from the energy industry, using nuclear electricity.

In 2017, total emissions (without LULUCF) increased by 0.9% since 2016. Over the longer term, 15% of emissions have been reduced since 1990, with decreases in all sectors except for transport. Other statistics made in 2015 have shown that the transport sector accounts for 33% of final energy consumption in France and is also the leading emitter of CO₂, with 39% of total greenhouse gas emissions [3]. Similarly, according to the inventory of pollutant and greenhouse gas emissions in France in 2014, among the percentage of emissions from the transport sector, cars running on conventional petrol and diesel represent 13% and 43%, respectively.

Furthermore, technical developments in the transport sector primarily respond to global environmental concerns about vehicle emissions of GHG, such as carbon dioxide CO₂ and pollutants such as NO_x and soot particles. Nevertheless, there will be a sharp increase in global transport and economic demand over the next few decades because of the sustained population growth. This growing demand will obviously impact the environment and require an over-increasing reduction in polluting emissions from vehicles. For example, this demand growth will increase the seaborne trade volumes, which will lead to a significant increase in associated GHG emissions. According to a study from the International Maritime Organization (IMO), global shipping emissions could grow between 50% and 250% by 2050 [4]. If no measurements are taken, the aviation and road transport emissions will also increase; this can risk undermining the Paris Agreement's goals in limiting the temperature increase and the efforts deployed by other sectors.

For this reason, the European Union (EU) is taking action to reduce transport emissions in Europe and work with the international community to develop measures with global reach; for road transportation, targets were set to reduce emissions from new vehicles to 95 g CO₂ /Km by 2021

compared to 127 g CO₂ /Km in 2018 [5]. The European standard emissions regulation consists of six stages of increasingly stringent emission control requirements, starting with Euro I in 1992 and progressing through Euro VI in 2015. The Euro VI limits for heavy-duty vehicles came after those for light-duty vehicles introduced along with Euro V limits in 2007. The standard emissions of both Euro V and Euro VI provided the automotive industry with a more extended period to develop strategies for meeting future emission limits [6].

The standard emission limits for both Euro V and Euro VI for these two types of vehicles are presented in Table 1 below.

Table 1: The Euro V and Euro VI heavy-duty vehicle emission standards for diesel engines[6]

| | Euro V Heavy-Duty | | Euro VI Heavy-Duty | |
|-------------------------------|------------------------|-----------------------|-------------------------|------------------------|
| | Euro V SS ^a | Euro V T ^b | Euro VI SS ^a | Euro VI T ^b |
| Emission limits (g/km) | | | | |
| CO | 1.5 | 4.0 | 1.5 | 4.0 |
| HC | 0.46 | 0.55 | 0.13 | 0.16 ^d |
| CH ₄ ^c | | 1.1 | | 0.5 |
| NO _x | 2.0 | 2.0 | 0.4 | 0.46 |
| PM | 0.02 | 0.03 | 0.01 | 0.01 |
| PN (#/km) | | | 8.0 × 10 ¹¹ | 6.0 × 10 ¹¹ |
| Smoke (1/m) | 0.5 | | | |
| Ammonia (ppm) ¹² | | | 0.01 | 0.01 |
| Fuel Sulfur Limit (ppm) | 10 | 10 | 10 | 10 |
| Test Cycle | ESC & ELR | ETC | WHSC | WHTC |

^a Steady-state testing; ^b Transient testing; ^c For Euro V for Natural Gas only, for Euro VI, NG and LPG; ^d Total HC for diesel engines, non-methane HC for others

There is a considerable reduction in the NO_x emission limit of about 80% in light-duty vehicles while passing from euro V to euro VI in steady-state testing and 70 % in transient testing. The particle mass limit was also significantly reduced; it was cut to half on steady-state testing and reduced about 66% in transient testing.

The Euro VI standards not only includes for the first time the particle number limit but also set emission limits for ammonia. In fact, due to the requirement of tighter NO_x emissions, an after-treatment Selective Catalytic Reduction in which the urea (CH₄N₂O) is injected into the exhaust stream will be used in the process. As a result, the catalytic reaction can produce ammonia as an unwanted by-product, which explains the limits imposed on ammonia emissions for heavy-duty diesel vehicles [6].

Thus, the Euro VI emission standards for light- and heavy-duty vehicles require the most significant emission reductions of any previous stage along the European regulatory pathway.

Lean homogeneous combustion is one of the most promising alternatives in reducing greenhouse gases and improve ambient air quality while meeting emissions standards. Many acronyms are generally used in the literature to refer to this combustion mode in engine applications. This includes LDI (Lean, Direct Injection), LPP (Lean Premixed Pre-vaporized) in applications dedicated to aeronautical propulsion and HCCI (Homogeneous Charge Compression Ignition), CAI (Controlled Auto Ignition), PPC (Partially Premixed Combustion), HPC (Highly Premixed

Combustion), and LTC (Low-Temperature Combustion). In the following study, we will refer to it by the acronym HCCI.

Lean homogeneous combustion consists of the compression ignition of a relatively homogeneous mixture. Based on the ignition of a generally lean mixture, it allows a drastic reduction in NO_x emissions. It also combines the advantages of both types of conventional engines: while it reduces fuel consumption compared to a spark-ignition engine, it also emits very few particles compared to a conventional diesel engine. Therefore, the use of this combustion mode will make it possible to dispense with a post-treatment system for NO_x and soot, which will lead to a significant cost saving. However, it is necessary to understand and characterize this combustion mode. The use of this combustion process with a gaseous mixture based on biomass is, from a carbon balance point of view, a good compromise to have minimal polluting emissions. Therefore, the study of the combustion of a mixture derived from biomass in lean homogeneous combustion constitutes the first major objective of this thesis. Gaseous biomass is generally presented as biogas and syngas derived, respectively, from the methanisation and gasification of biomass. The origin, composition, and usage of these fuels in the internal combustion engine will be developed in the following section.

II. Use of biomass as renewing fuel

1. Origin and production of gaseous biomass

From an ecological perspective, fossil fuels used massively emit large quantities of CO₂ and are exhaustible. However, using biofuels as alternative energy has become a key solution to solve fossil fuel shortage and reduce greenhouse gas emissions.

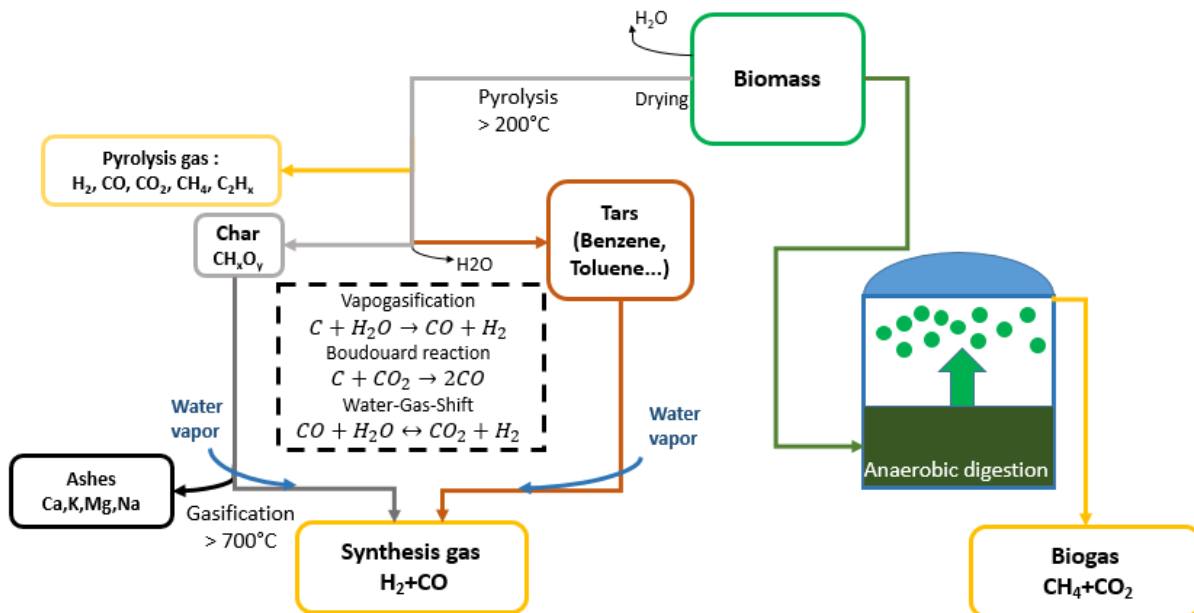


Figure 3: Simplified diagram of the reaction mechanism of biomass gasification (adapted from [7]). This image shows the two biofuel gas origins. They can be produced by anaerobic fermentation or gasification of solid biomass.

Biofuels, derived from biomass, are fuels produced from non-fossil plant or animal matter. With the development of biomass energy conversion, biofuels show significant improvement in product yield, fuel quality, and combustion characteristics, making them useful for engine applications. They can exist in the liquid and gas phases. In the framework of this thesis, we are only interested in studying the combustion of gaseous biofuel mixtures. These gases can be produced either by anaerobic fermentation or gasification of solid biomass, as shown in Figure 3. The methanisation (anaerobic fermentation) process of solid biomass produces biogas (CH_4/CO_2), and gasification technologies yield synthesis gas (H_2/CO). These processes, as well as the composition of the produced gases, are described briefly in the following section.

1.1. Biomass methanisation

Biogas is produced by anaerobic digestion of solid biomass, also known as methanisation. This process makes it possible to reduce the carbon load of waste and reduce the risk of pollution. It is particularly suitable for water-rich substrates containing easily degradable organic matter. Methanised waste can be of agricultural, agro-industrial, or municipal origin [8].

The produced biogas is essentially composed of methane CH_4 (45-70%), carbon dioxide CO_2 (15-45 %), hydrogen sulfide H_2S (0.005% - 2%), and other contaminants like halogenated compounds and siloxanes [8]. The methane bacteria responsible for the biogas formation are naturally present in the environment.

This process involves four major phases described below [9]:

- 1- Hydrolysis: It is the first phase of the biodegradation where the enzyme hydrolase cracks biopolymers of high-molecular-weight (carbohydrates, proteins, cellulose, and fats) into monomers (amino acids, fatty acids, monosaccharide) and water.
- 2- Acidogenesis: This phase consists of the degradation of the monomers resulting from the hydrolysis into short-chain organic acids (butyric acid, propionic acid, acetate, acetic alcohol), alcohol (methanol, ethanol, propanol, butanol, glycerin, and acetone), and gases (carbon dioxide, hydrogen sulfide, and ammonia).
- 3- Acetogenesis: during this phase, acetate is produced by the oxidation of a long chain of fatty acids.
- 4- Methanogenesis: This is the last step in which methane, carbon dioxide, and water are formed. About 27 to 30% of methane is produced by reducing $\text{CO}_2 + \text{H}_2$ and 70% through acetic acid oxidation.

The composition of biogas differs according to the sources, technology, and operational conditions of its production. Typically, biogas from anaerobic digestion consists of 30-75% methane, with the remainder being mainly carbon dioxide, hydrogen, and water vapor [11]. The contents vary even during daily production.

David [10] has grouped the biogas composition for three different production sources from landfill, wastewater digester, and farm plants (presented in Table 2):

Table 2 : Selected sources for anaerobic digestion and the relative biogas composition

| | Landfill | wastewater digester | Farm plant |
|---|----------|---------------------|------------|
| CH ₄ (%) vol | 47-67.9 | 57.8-65 | 55-70 |
| CO ₂ (%) vol | 37-41 | 33-39 | 37-38 |
| O ₂ (%) vol | <1 | <1 | <1 |
| N ₂ (%) vol | <17 | <3,7 | <1-2 |
| H ₂ S (ppmv) | <8000 | <8000 | 10-20000 |
| NH ₃ (mg. Nm ⁻³) | Traces | Traces | <2000 |
| Siloxanes (mg. Nm ⁻³) | 1-400 | - | - |
| Relative humidity | 100 | 100 | 100 |

Another gaseous fuel derived from biomass is the synthesis gas (syngas) obtained by biomass gasification. The gasification process and techniques, as well as their effects on the syngas composition, will be presented next.

1.2. Biomass gasification

Thermal biomass conversion is an alternative way to fossil fuels (oil, coal) to fabricate high energy value products (synthesis gas, liquid fuels). These can be used directly to produce heat or electricity or as renewable hydrocarbons in synthesis processes such as the Fischer-Tropsch process.[11].

Biomass gasification is a thermochemical process consisting of decomposing solid biomass in the presence of reactive gas to obtain the synthesis gas. It is an endothermic, high-temperature transformation of biomass that occurs through a succession of four complex thermochemical phenomena: drying, pyrolysis, oxidation, and reduction.

Drying is the first stage of the gasification process. It consists of the endothermic evaporation of biomass at a temperature between 100°C and 160°C; it allows the free and bound water present in the solid biomass to be removed.

The second stage is the pyrolysis of combustible and non-combustible gases obtained by the thermal decomposition of the dry biomass at temperatures between 200 and 400°C. The products of this degradation consist of non-condensable (H₂, CO, CO₂, CH₄, and C₂H_x) and condensable vapors (tars and water vapor), gaseous products as well as a solid carbonaceous residue called char.

Then, there is the partial combustion of char and volatile matter in the presence of O₂; this oxidation produced during the pyrolysis stage provides the necessary energy for the three phases of the gasification process.

Finally, there is char gasification known as the reduction phase; at temperatures above 700°C, the char reacts with steam and carbon dioxide to produce hydrogen and carbon monoxide, the main constituents of synthesis gas.

Nowadays, the technologies used for biomass gasification are of three types, fixed beds, fluidized beds, and entrained flow reactors (view Figure 4). The choice of the type of process depends on several factors, including the power of the installation, the characteristics and physico-chemical properties of the fuel, and the downstream application [7].

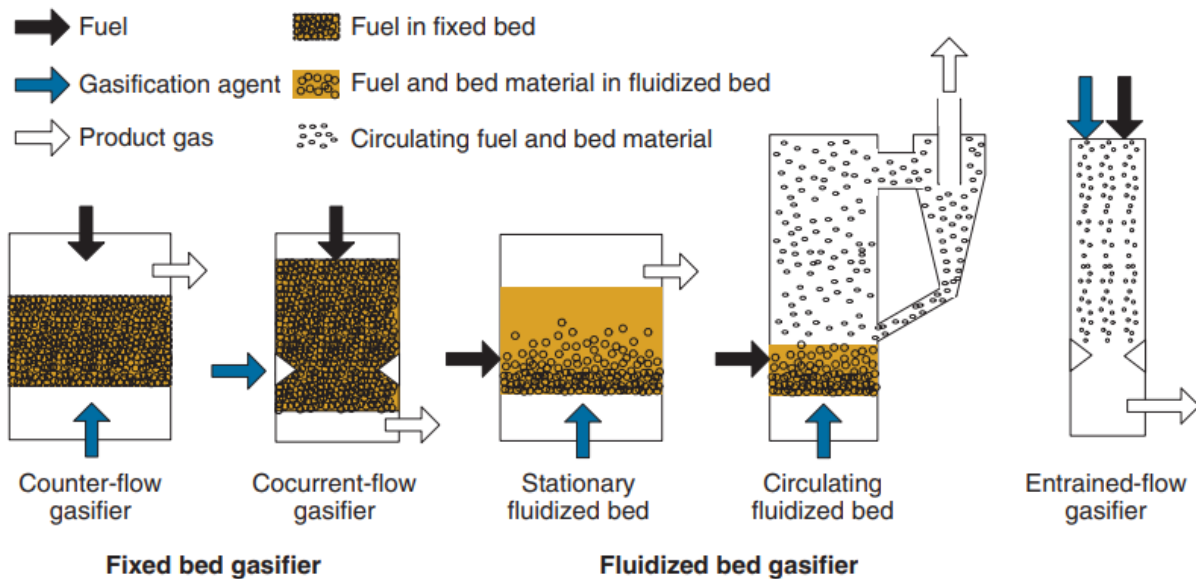


Figure 4: Different types of gasifiers [12]

Image showing the different technologies used for biomass gasification: fixed beds gasifier and fluidized beds gasifier

The main advantage of fixed bed processes is the simplicity of implementation, due to which they can be used in various applications and high thermal efficiency. The solid biomass is introduced from the top of the reactor and moves vertically downwards. These processes are classified into two technologies: co-current and counter-current processes. Generally, the former is used in power cogeneration installations of less than 1 MW electric, and the latter for thermal use installations [13].

In a fluidized bed gasifier, the bed consists of small-diameter particles of catalytic or non-catalytic particles such as sand or alumina to improve fluidization and transfer. Solid biomass is suspended with the bed particles and traversed by a gas whose flow rate is variable; according to the fluidization speed, two types of reactors can be presented: stationary fluidized beds and circulating fluidized beds.

For stationary fluidized beds, the fluidization speed is relatively low (1-2 m/sec); the particles are set in motion and mixed within the bed to ensure good heat and mass transfers. This process is not very flexible in operation, especially in terms of bed level control during load variations. Moreover, its operation is optimal if the particles are of a calibrated size.

For circulating fluidized beds, the fluidization speed is higher (4-6 m/sec), so that part of the particles in the bed is pulled out of the reactor. A cyclone separates the solid phase, which is then recirculated in the bed. The solid phase is thus continuously in motion in the reactor.

In terms of the incoming biomass's nature and conditioning, the fluidized bed gasifiers are more flexible than fixed beds. They also bring significant improvements in conversion efficiency and overall energy efficiency, as well as in the control of the reaction and the load in the reactor. Today, the situation is such that the small gasification plants are almost all oriented towards the co-current fixed bed and the large power units towards the fluidized bed.

On the other hand, in a gasifier with an entrained bed, the fluidization velocity is above 6 m/sec; the particle and gas velocities are very close. The fuel is introduced in a powder or mud form.

In a pressurized gasifier with an entrained bed, the temperature can go above 1700°C, which eventually affects the composition of the produced syngas and carbon conversion efficiency positively. However, the high temperatures require the cooling of the reactors and the gas, which imposes a very high level of process integration to recover them.

The presented gasifier reactors yield at the end of the process a syngas composed mainly of hydrogen, carbon monoxide, and methane. It can eventually present a small number of heavy hydrocarbons and other species, including CO₂, N₂, and O₂.

However, the syngas composition depends on several parameters such as the temperature and pressure of the gasification process, the type of gasifier and the gasifying agent, as well as the sources and properties of solid biomass. For example, a syngas derived by the use of steam or oxygen is typically composed of 25-30% H₂, 30-60 % CO, 0-5% CH₄, and 5-15 % CO₂[14].

We present in Table 3 some examples of syngas composition produced by three different existing gasification technologies.

Table 3: Selected Biomass Gasification Technologies

Table showing the syngas composition produced by three different gasification technologies: Cogebio, Xylowatt, and FastOx.

| Technologies | Biomass type | Gasifier type | CH ₄ (%) | CO ₂ (%) | CO (%) | H ₂ (%) | N ₂ (%) | O ₂ (%) | Ref. |
|--------------|---|--|---------------------|---------------------|--------|--------------------|--------------------|--------------------|------|
| Cogebio | wood | Fixed bed co-current gasifier (Gasclean) | 1.77 | 7.28 | 21.03 | 14.18 | 46.61 | 0.89 | [15] |
| Xylowatt | forest waste, wood, agricultural products, organic products | Co-current fixed bed reactor (Notar) | 2 | 10 | 8 | 22 | 45 | - | [16] |
| FastOx | Solid waste | Fixed bed countercurrent gasifier | 0.5-12 | 5-15 | 48-66 | 18-32 | 0.5-3 | - | [17] |

The produced syngas can be used in synthesis processes such as the methanation that transforms it into full methane. As renewable energy, it can also be used in internal combustion engine applications.

Biogas and syngas are two typical biofuels generated from solid biomass through biochemical and thermochemical processes, respectively. They are considered the future fuels for internal combustion engines due to their high self-ignition temperature, lower production cost, and growing technology.

2. Applications in internal combustion engine

Several studies have focused on the combustion of biogas and syngas separately, including the effect of initial conditions and gas composition.

Biogas can be considered a carbon-neutral fuel when it originates in the anaerobic digestion of organic matter by living organisms. As explained previously, the major components that form biogas are CH₄ and CO₂. It is considered a promising candidate to meet the regulation emission targets due to its flexibility as an energy source and its wide range of applications, including heating and electricity production. However, due to its considerable amount of CO₂, biogas has a low calorific value; therefore, its industrial applications are limited.

The use of biogas in engine applications is a good alternative, especially when enhanced by hydrogen. As seen earlier, the latter is present in syngas obtained from another renewable energy, biomass gasification.

The interest in using syngas is growing as renewable energy in internal combustion engines due to its richness of bio-resources and its shortage of fossil fuels. It is considered an intermediate step towards the transition from carbon-based to hydrogen-based fuels, promoted by emerging concerns about climate change and damage to the environment. It may lead to advantageous exhaust emissions by avoiding the formation of sulfur compounds, metals, halogens, and fly ashes thanks to the cleaning systems that can remove the contaminants before being burnt in an internal combustion engine. Syngas is also used to enhance hydrocarbon combustion; adding a volume of more than 50% of syngas to the mixture of isooctane/air reduces the ignition delay at low temperatures and increases it at high temperatures[18]. However, one disadvantage of the syngas mixture is the critical emissions NO_x and CO. While the amount of CO highly depends on syngas composition, NO_x is related to the engine geometry and its operating parameter ranges. In other words, NO_x emissions result from the high flame speed and combustion temperature, which may negatively affect the engine's performance. Exhaust gas recirculation (EGR) is one of the most promising strategies to reduce NO_x emissions near stoichiometric conditions [19]. The EGR technique involves the recirculation of a portion of exhaust gases (a mixture of water, carbon dioxide, and nitrogen) back into the engine cylinder chamber that consequently decreases the peak temperature. Several investigations were conducted to study the dilution and thermal effects of EGR on the syngas combustion. Results show that the EGR strategy not only reduces the NO_x emissions but it also has a stabilizing effect on the flame propagation, as it tends to increase the flame thickness and reduce its resistance to the hydro-dynamic perturbations related to the thermal expansion [20], [21]. The slower combustion arising from exhaust gas dilution significantly improved the indicated mean effective pressure (IMEP) (25 %) and reduced the engine wall temperature. EGR can also avoid irregular combustion and reduce the knock risk, although syngas has a high knock resistance, and it does not generally need anti-knock strategies for typical engine compression ratios[22].

To summarize, biogas is a renewable energy source neutral in CO_2 emission, whereas its low calorific value can be recovered by using syngas since it contains hydrogen. Syngas is also a renewable energy source that produces high NO_x emissions; the addition of CO_2 present in biogas leads to a decrease in these emissions (similar to the dilution effects of EGR).

Consequently, the use of mixtures of biogas and syngas seems to be the right way to reduce non-renewable fossil fuel dependency while decreasing emissions issues and conserving high efficiency. The main components of biogas/syngas mixtures are methane, hydrogen, carbon dioxide, and carbon monoxide. The percentage range of each component can be obtained by combining fuel composition from Table 2 and Table 3, as shown in Table 4.

Table 4: Percentages of components in biogas/syngas mixtures

| | CH ₄ (%) | H ₂ (%) | CO ₂ (%) | CO (%) |
|------------------------|---------------------|--------------------|---------------------|--------|
| Biogas | 30-70 | - | 30-40 | - |
| Syngas | 0-15 | 10-40 | 0-20 | 10-70 |
| Methanation of syngas | 99 | - | - | - |
| Mixtures Biogas/syngas | 0-99 | 0-40 | 0-40 | 0-70 |

In this study, the combustion of a blend of biogas/syngas, also known as CH₄/CO₂/CO/H₂ mixtures, will be studied in lean homogeneous conditions. Thus, the duality biofuels/ HCCI combustion engine combines the advantage of alternative fuels as well as alternative combustion strategies. In general, lean homogeneous combustion can be realized with fuels with a low LHV that contain several non-combustible components, and the enthalpy of the biofuel contributes to realizing the high-temperature pre-mixture conditions enabling auto-ignition.

In this study, the combustion of different compositions of CH₄/CO₂/CO/H₂ mixtures will be studied experimentally and numerically in HCCI conditions. The composition of the studied mixtures is chosen by varying each component's percentage in their limit range presented in Table 4. The method used and the selected mixtures are detailed in the experimental study of chapter 2.

In the following section, the fundamentals of HCCI combustion, its advantages in terms of efficiency and pollutant emissions, as well as its major challenges and problems, will be discussed.

III. Homogeneous combustion

1. Definition of homogeneous combustion

The lean homogeneous combustion is an alternative strategy for efficient combustion and replacement of conventional CI and SI engines. As mentioned earlier in this chapter, many acronyms in the literature are referred to this combustion mode; in particular, the acronym HCCI (Homogeneous Charge Compression Ignition) will be used in the following study.

The first study on the homogeneous combustion process was performed in 1979 on two-stroke engines by Onishi et al.[23]. Unlike conventional SI engines, there is no flame propagation; instead, the whole mixture burns slowly at the same time. The same combustion named Toyota-Soken (TS) combustion was demonstrated at the Toyota Motor Co. Ltd. by Noguchi et al. [24] in a two-stroke engine with an opposed-piston. Furthermore, Toyota Central Research had developed the PCCI (premixed charge compression ignition) engine [25]. This mode is considered by many authors to also refer to HCCI mode; It is very promising in achieving both higher efficiency and lowers nitrogen oxide (NO_x) emission. It operates stably in the air-fuel ratio range between 33 and 44, and

ignition occurs spontaneously at unspecified multi-points as it does in diesel engines [26]. The comparison of HCCI and conventional engines is presented in Figure 5 and Figure 6.

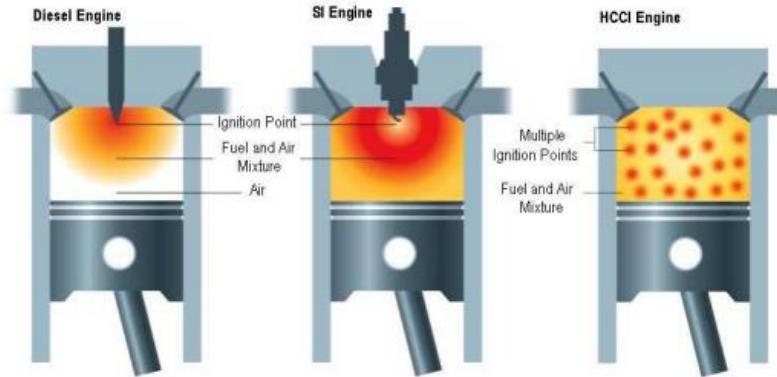


Figure 5 : Comparison of SI, DI and HCCI combustion modes [27]

| Parameters | SI | HCCI | CI |
|-------------------|--------------------------------------|--------------------------------------|------------------------------|
| Ignition method | Spark ignition | Auto-ignition | Compression ignition |
| Charge | Premixed homogeneous before ignition | Premixed homogeneous before ignition | In-Cylinder heterogeneous |
| Ignition point | Single | Multiple | Multiple |
| Throttle loss | Yes | No | - |
| Compression ratio | Low | High | - |
| Speed | High | Low | - |
| Combustion flame | Flame propagation | Multi-point auto-ignition | Diffusive flame |
| Major emissions | HC, CO, and NO _x | HC and CO | NO _x , PM, and HC |
| Injection type | Gasoline direct injection | Port and direct injection | Direct injection |
| Equivalence ratio | 1 | <1 | - |

Figure 6: Comparative parameters of spark ignition (SI), compression ignition (CI) and homogeneous charge compression ignition (HCCI) engines [28]

Theoretically, in the HCCI mode, the fuel can be introduced to the cylinder by direct or port injection, wide-open throttle (WOT) carburetion, manifold induction, or fumigation, etc. Unlike conventional CI combustion, fuel and air are well mixed (homogeneous) before the start of combustion. Due to the temperature increase after the compression stroke, the mixture is spontaneously self-ignited at several locations throughout the entire charge volume. The combustion process occurs under very lean and diluted conditions, resulting in lower overall and local combustion temperatures. Thus, the absence of fuel-rich regions in the combustion chamber results in a considerable reduction in particulate matter production [29]. Therefore, due to the low fuel mixture and the absence of high local temperatures, the simultaneous reduction of NO_x and fine particulate emissions is possible.

The HCCI mode study can be carried out on different experimental facilities, such as the static reactor, the flow reactor, the thoroughly stirred reactor, the shock tubes, and the rapid compression machine (RCM) [30]. In our study, the SU RCM will be devoted to study the combustion process under lean homogeneous conditions. A brief description of the combustion process is presented in the following paragraph.

2. Combustion process and heterogeneities

Theoretically, combustion in the HCCI mode is a mass self-ignition; when the homogeneous reactive mixture is heated to a temperature equal or greater than its self-ignition temperature, the explosion will occur throughout the volume a certain time after this temperature is reached. This time τ is called the self-ignition delay time or induction period.

This combustion process is widely studied in the literature, as many authors investigated the sensibility of the ignition delay time to several parameters and conditions of the combustion. It was found that the ignition delay time is highly dependent on the initial conditions (pressure, temperature, and load) as well as the fuel composition and the equivalence ratio, the induced aerodynamics in the combustion chamber, and the temperature distribution.

For example, for some fuels, and under a given temperature and pressure conditions, a first so-called cool flame stage appears and results in a small increase in pressure and temperature (first heat release); this induction period occurs over a period of time τ_1 . After a second period τ_2 , ignition occurs (second heat release) and results in a rapid increase in pressure and temperature (see Figure 7).

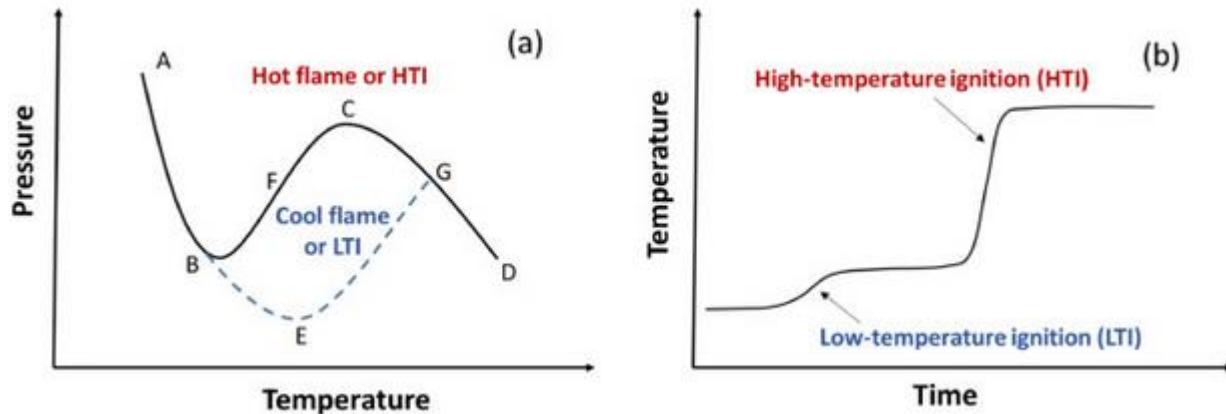


Figure 7: (a) Effects of pressure and temperature on spontaneous ignition of cool flames and hot flames. (b) Temperature versus time history of LTI and HTI in two-stage ignition [31].

The cold flame phenomenon occurs at relatively low temperatures (approximately 530 to 670 K). It manifests itself by a sudden and transient acceleration of the reaction speed, accompanied by a low spontaneous emission of chemiluminescence in the blue. The cold flame is usually followed by a region called the negative temperature coefficient (NTC) region, which results in a decrease in the reactivity of the system and thus an increase in the self-ignition time when the temperature of the medium increases at constant pressure. When the critical temperature is reached, this causes a thermal runaway of the chemical reactions, accompanied by a strong heat gradient called the main flame.

However, several authors have studied this combustion mode and have considered that it cannot be homogeneous. There are heterogeneities in the combustion chamber due to which combustion is initiated by a self-ignition nucleus, more reactive than the rest of the mixture, and develops in a non-uniform or deflagrating manner. These heterogeneities normally result from a combination of physico-chemical phenomena such as heat losses that induce temperature gradients, complex fluid dynamics, and turbulent fluctuations.

In this study, Sorbonne University rapid compression machine (SU RCM) is used to study the lean homogeneous combustion. Heat losses are particularly noticeable in RCMs since compression duration (τ_{comp}) and self-ignition delays (τ) can be long (e.g., $\tau_{comp} = 15\text{-}80$ msec, $\tau = 10\text{-}100$ msec); heat transfers are generated in the chamber since the walls of the reaction chamber are significantly cooler than the reactive gases. Clarkson et al. [32] used the PLIF (Planar Laser-Induced Fluorescence) method to measure the temperature and concentration fields throughout the combustion chamber of the RCM. They found temperature gradients between the core and the chamber walls that can reach 50 K during 1ms post-compression. This thermal stratification results from the forward movement of the piston, which produces a vortex promoting the interaction between the hot gas compressed in the core of the chamber and the cold gas on its walls.

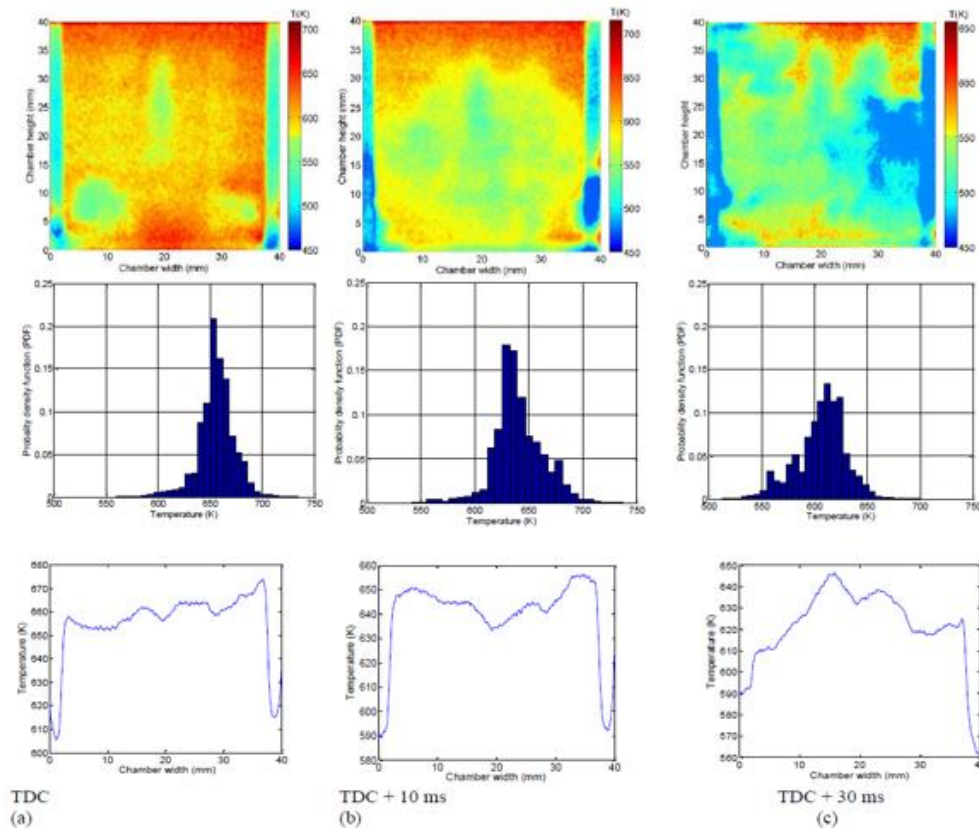


Figure 8: The temperature fields and their distributions along the combustion chamber of an inert mixture of $n\text{-C}_7\text{H}_{16}$ (load 180 mol/m^3 and equivalence ratio 0.8) measured at TDC, then after 10 msec and 40 msec of this instant [33].

These thermal heterogeneities were also presented by Tran et al.[33]. They measured the temperature distribution in a rapid compression machine by laser-induced fluorescence (LIF). The temperature fields of an inert mixture of $n\text{-C}_7\text{H}_{16}$ (charge 180 mol/m^3 and equivalence ratio 0.8) were measured at the instant when the piston was at TDC top dead center, then after 10 msec and 40 msec from this instant. These temperature fields and their distributions along the combustion chamber are shown in Figure 8.

Upon analyzing the temperature fields presented in the figure above, Tran et al. [33] noted significant temperature gradients between the hottest and coldest zones and the vortices circulating

in the combustion chamber and promoting interactions between these two zones. Thus, the temperature field is non-uniform; there are also convective heat transfers between the wall and the reactive gas during the compression phase and after the top dead center. The evolution of the vortex structures and residual turbulence level causes a combustion phenomenology that is highly dependent on local turbulence and temperature gradient.

Turbulence can be introduced into the RCM through boundary layer instabilities, the development of wedge vortices during the compression phase, the latent turbulence of the filling process as well as the turbulence generated by boundary layer instabilities [34]. These turbulent fluctuations can generate heterogeneities in the combustion chamber during the compression phase. They can also interact with the processes of chemical kinetics and heat release during the auto-ignition delay.

Hence, the lean homogeneous combustion is a complex phenomenon; characterizing the physico-chemical phenomena of the biogas/syngas combustion under HCCI conditions will be addressed in this manuscript both experimentally and numerically. Due to its complexity, it will be studied in a simplified approach presented in chapter 3.

However, the complexity of the combustion process is not the only challenge, as numerous researchers studied extensively the major HCCI challenges that need to be addressed before any engine application.

3. Major problematic and challenges of homogeneous combustion

Several reasons make the use of homogeneous combustion so beneficial and advantageous. First of all, it allows higher efficiencies than the SI engine because it operates at the fuel-lean condition with high compression ratios (>15) comparable to diesel engines. Besides, it can operate with a wide range of fuels and produce lower particulate matter and NO_x emissions.

Nevertheless, HCCI combustion also presents several disadvantages as it has to overcome some challenges:

1. combustion and auto-ignition phase control,
2. operation range,
3. weak cold-start capability [27]
4. homogeneous charge preparation [35]
5. higher emissions of unburned hydrocarbons and CO [36] ;

However, among all the presented challenges, the control of HCCI combustion timing constitutes a crucial problem in homogeneous combustion. Along with the homogeneous mixture preparation difficulty, it plays an essential role in determining the efficiency and emissions. Thus, the principal HCCI benefits and challenges are directly linked to HCCI ignition timing, as shown in Figure 9.

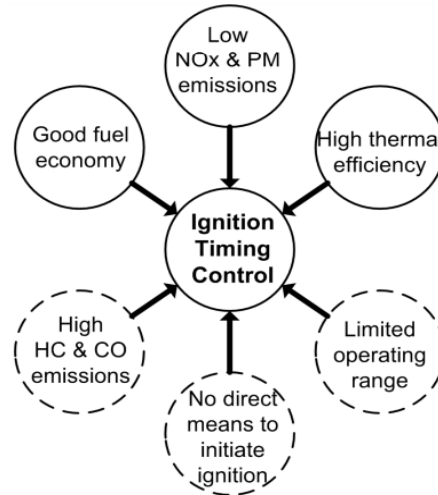


Figure 9 : Major HCCI benefits (solid circles) and drawbacks (dashed circles) pertinent to HCCI ignition timing[27]
Controlling the HCCI combustion timing is very crucial in homogeneous combustion; it has numerous challenges but also benefits.

The combustion and thermal efficiency depend on ignition timing; the completeness of combustion deteriorates by shifting the ignitions later in the expansion stroke, which increases the potential of partial burn and misfired cycles[27]. The operating range of the HCCI engine is also influenced by ignition timing. The late ignitions lead to high cyclic variation, which determines the instability limit, while early ignitions lead to high peak pressure and high-pressure rise rate, which determine the knock limit [37];[38]. Moreover, HC and CO emissions are highly dependent on the ignition timing. HC and CO emissions of the HCCI engine are relatively higher than those of diesel engines [27 ; 39]. They are mainly due to low in-cylinder temperature caused by lean-burn or high-dilution combustion. In lean mixtures, the production of HC and CO is dominated by incomplete bulk-gas reactions. With a sufficiently high exhaust gas temperature for the oxidation process in the catalyst to occur, high HC and CO emissions in HCCI can be significantly reduced.

In most cases, the controlling of unburned HC and CO emissions produced from HCCI engines will require exhaust emission control devices with further development of oxidation catalysts for low-temperature exhaust steams. However, these control devices are more straightforward, more durable, and less dependent on expensive precious metals than those of NO_x and PM emission [40]. NO_x and PM emissions are also affected by ignition timing by the mean of peak combustion temperature [41]. Besides, the weak cold start capability is dependent on the ignition timing; the compressed gas in the cylinder receives no preheating from the intake manifold, which will reduce the charge temperature in the HCCI engine. The compressed charge is further rapidly cooled by heat transfer to the cold combustion chamber walls. Consequently, this could prevent the combustion in HCCI engine. Thus, due to its effects on controlling HCCI challenges, the homogeneous combustion operation depends on the system's capacity to control the ignition timing.

Moreover, the homogeneous combustion is highly sensitive to the variations in charge properties and is characterized by the absence of a specific event to initiate the combustion[42]. Consequently, the control of ignition timing is considered the most challenging problem in HCCI engines. Therefore, precise control of the combustion conditions: temperature, pressure, and composition of the air-fuel mixture is needed to prevent misfire, excessive peak pressure, or excessive pressure

gradient, which could damage the engine and increase NO_x generation. Dealing with the ignition timing control constitutes the second primary objective of this thesis.

Several strategies with various success levels have been investigated in the literature to control HCCI combustion timing and extend the load range. Some of these strategies will be presented in the following paragraph.

4. Strategies into homogenization and control ignition timing

In order to control HCCI combustion ignition, various strategies were studied in the literature. Most of these strategies can be grouped into two main aspects: active and passive control. (these strategies are summarized in Figure 10).

The passive control strategies do not require any energy input. Generally, it corresponds to a modification of the system, such as geometry change or fuel composition. This can include the changing of fuel properties, dual-fuel technology, exhaust gas recirculation, variable compression ratio (VCR), or variable valve timing (VVT) to increase the compression ratio.

Changing the fuel properties of the cylinder mixture is a method that can be used for HCCI control. The required time and conditions needed for auto-ignition vary between fuels, so varying the fuel properties in an HCCI engine effectively controls combustion timing [43]. Dual fuel technology is another method that consists of creating a fuel mixture with an intermediate octane number by mixing fuels with a high/low octane number simultaneously. However, some high-octane fuel does not participate in oxidation reactions due to its poor self-ignition tendency, which increases the hydrocarbon emissions increase.

The use of the Spark Assisted Compression Ignition (SACI) is another practical approach to bridge the gap between HCCI and SI engines[44]. Direct fuel injection into the cylinder at different stages of the engine cycle can help control HCCI combustion. It allows the combustion timing to be advanced by improving mixture ignitability or retarded by increasing fuel stratification while expanding the low and high load operating limits [43].

Although these proposed solutions can control the ignition timing of the lean homogeneous combustion, each of them has some drawbacks. For example, variable intake temperature and pressure and variable coolant temperature have a slow response time, while VCR and VVT are somehow challenging to implement. Practicality and cost-effectiveness are the main concerns with most proposed options, such as water injection and modulating two or more fuels. The dual-fuel engine concept cannot be seen as a practical solution due to the indispensability of supplying and storing two fuels. Moreover, direct injection depends highly on the type of fuel and direct injection [27].

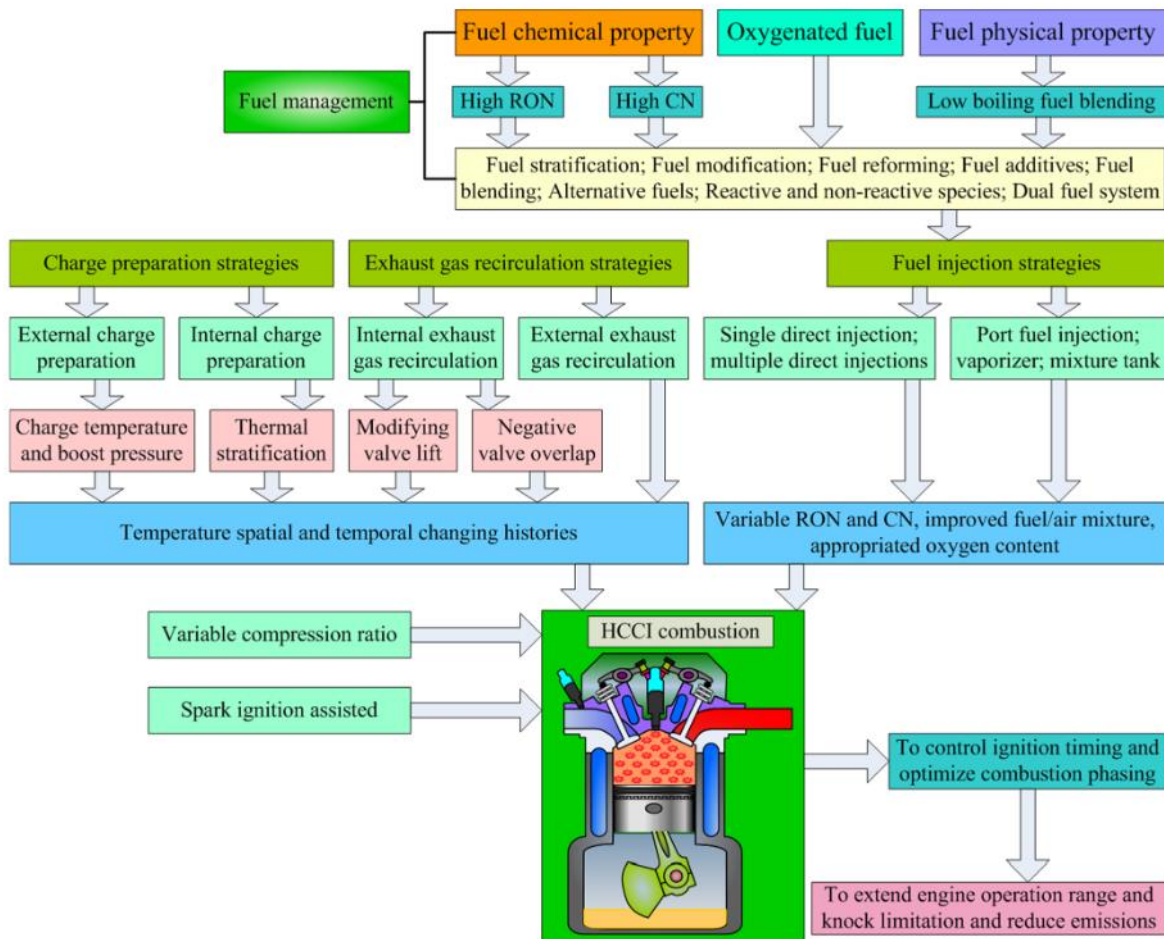


Figure 10 : Strategies for controlling the ignition timing and combustion phase of the HCCI engine [45]

Hence, the solution proposed in this manuscript is an active/passive strategy that consists of injecting biomass powder into the reactive mixtures. It combines the benefits of direct injection and dual fuel strategies. The control of the ignition timing can be assured by the injection timing and the ignition properties of the injected particles.

In diphasic, also known as heterogeneous combustion, solid particles such as coal behave as fuels. In the case of solid particles, the reaction occurs through the interaction of the carbon atoms with oxygen molecules. The diffusive processes, which occur in the gaseous film adjacent to the surface of the solid, influence the combustion kinetics. In other words, when a solid particle is exposed to a hot gas mixture containing oxygen, it undergoes a process in which the following three stages can be identified: loss of water by drying, loss of mass by the release of volatile gases, and finally the combustion. In literature, the study of the combustion of solid particles is primarily focused on coal and wood. However, the same analysis can be conducted with any other combustible material. Furthermore, most studies are limited to the combustion of the solid particle in a hot gaseous mixture, and very few consider the interaction of particles with the reactive gas mixture [46]. The diphasic combustion solid/gas will be presented in detail in chapters 4 and 5.

IV. Conclusions

The present bibliographical research has made it possible to establish the framework of the study to be followed.

The use of biogas in engine applications is a good alternative, especially when enhanced by hydrogen. As seen earlier, the latter is present in syngas obtained from another renewable energy, biomass gasification. It is not easy to ensure biogas production with a fixed composition under its biological origin; therefore, a mixture of biogas/syngas mixtures will be considered.

Lean homogeneous combustion is nowadays considered as an alternative combustion mode to diesel with high potential. Combining the advantages of this technology with those of renewable energy can lead to high thermal efficiency with minimum emissions. Rapid compression machines are a tool that allows this type of research to be carried out without the constraints of a conventional internal combustion engine. We have mentioned in this chapter that various parameters can influence the combustion process. Thus, we will study the self-ignition of various biogas/syngas mixtures on the rapid compression machine to determine the sensitivity of self-ignition to these different parameters for different fuel compositions.

Different authors have demonstrated the influence of turbulence and thermal heterogeneities on the combustion process by self-ignition, which generates different combustion modes within the chamber. Therefore, it is essential to precisely understand the phenomenology of homogeneous combustion and the parameters that can influence it.

Thus, a simplified approach will be proposed on a numerical basis to study the lean homogeneous combustion of biogas/syngas mixtures in two different configurations relative to the different combustion regimes.

In the continuation of this work, another simplified approach will be proposed for analyzing the turbulence. It allows predicting the type of combustion in the SU rapid compression machine from the knowledge of the characteristic properties of the flow and the studied fuels.

In order to validate this numerical approach, a study of the combustion process of fuels used in rapid cinematography will be proposed. It will make it possible to distinguish the observed modes of combustion and evaluate the influence that turbulence can have on self-ignition phenomenology.

Furthermore, in this chapter, we have seen that the control of the self-ignition process is problematic compared to other conventional combustion modes. Many strategies were proposed in the literature to solve these issues. The innovative solution of ignition control will be based on the injection of dust and/or particles into the reactive mixture.

A particle injector will be conceived and characterize to directly inject biomass powder into the biogas/syngas reactive mixture in the SU RCM. The combustion of solid biomass and its ignition factors will be first studied before studying the effects of biomass particles in controlling the combustion process and stability of lean homogeneous gas mixtures.

Chapter 2:

**An experimental study of the combustion of
biogas/syngas mixtures under lean
homogeneous conditions**

Chapter 2

I. Introduction

As explained in the previous chapter, homogeneous combustion is one solution that reduces pollutant emissions at the source while maintaining high fuel capacity. It reduces pollutant emissions by inhibiting the NO_x and soot formation while maintaining appreciable efficiency due to its high combustion rate.

The use of gaseous biofuel mixtures could be a good compromise to achieve a very low environmental impact from a carbon balance point of view. The gas obtained contains mainly the following compounds: H_2 , CO , CH_4 , CO_2 in variable proportions depending on the method of producing the biogas and syngas. Thus, this chapter provides the first results of the physico-chemical characterization of biofuel combustion in HCCI conditions. This study is carried on experimentally on the SU rapid compression machine, mainly used to determine self-ignition times of different fuels to validate kinetic mechanisms. Thus, it mainly focuses on investigating the effects of biofuel components and the end of compression temperature on the auto-ignition delay time.

Therefore, this chapter is composed of three parts. First, we will start with a brief presentation of the experimental setup while describing the main features of the SU RCM. The various existing methods for determining the induction time and the end of compression temperature are also described. Comparison tests are then carried on with two other rapid compression machines on hydrogen and methane mixtures. The aim of these tests is to determine the ignition delay time and end of compression calculations that will be considered in the following study. It also allows the validation of the SU RCM reliability compared to other RCMs in the literature to determine whether or not the study of self-ignition on the latter presents the same phenomenology observed by other authors.

Lastly, biogas/syngas blends will be selected to carry on the experimental combustion under lean and homogeneous conditions on the SU RCM. This study allows estimating homogeneous combustion sensitivity to the end of compression temperature and the fuel composition.

Hence, this chapter will provide initial elements of answers to understand the phenomenology of lean homogeneous combustion fueled with biogas/syngas mixtures. Based on the obtained results, the numerical parametric study will be addressed in the next chapter to complete this study by investing parameters difficult to achieve experimentally. Both studies will subsequently conduct to better characterize the lean homogeneous combustion mode (mass combustion and front flame propagation) of biofuel, allowing biofuel components and conditions optimization.

II. Characterization of the experimental setup: SU RCM

1. SU RCM presentation

RCMs are single-shot, piston-based machines that produce relatively fast compression of a gas mixture in a chamber, creating high pressure and temperature with nearly adiabatic conditions. These machines are usually used to study auto-ignition phenomena at conditions controlled by the design of the device. The relative simplicity, range of accessible pressure, and temperature conditions, as well as the ability to prepare and control the gas mixture composition, allow the RCMs acquired data to reliably quantify the reactivity and reaction pathways of a large range of fuels. They also provide valuable data for developing and validating chemical kinetic mechanisms.

Moreover, auto-ignition processes in RCMs represent those that occur within combustion engines, where these evolve through multiple thermo-chemical regimes. Thus, the biofuel combustion under HCCI conditions will be studied and characterized by the SU RCM in the following sections. But first, important features of the SU RCM will be presented.

1.1. SU RCM description

As a definition, rapid compression machines are combustion facilities assimilated into a simple piston-cylinder apparatus. They are typically used to determine the self-ignition times of different fuels to validate chemical kinetic mechanisms. In this study, experimental biogas/syngas combustion tests were carried on the SU rapid compression facility (SU RCM).

A schematic diagram of the SU RCM in a horizontal view is presented in the figure below (Figure 11).

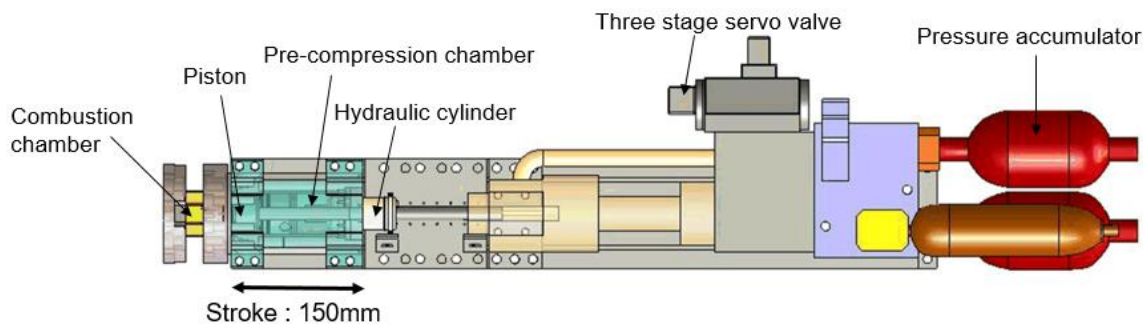


Figure 11: Schematic diagram of the SU rapid compression machine (Horizontal view)

Image showing the four main components of the SU rapid compression machine: the hydraulic system, the moving piston in the pre-compression chamber, the combustion chamber, and the control and acquisition system.

The machine consists of four main components: the hydraulic system, the moving piston in the pre-compression chamber, the combustion chamber, and the control and acquisition system.

A full description of each component can be found in Kéromnès's thesis [47]; only the principal elements and the experimental procedure are described in this manuscript.

As presented in Figure 11, the hydraulic system consists of a hydraulic power unit, five oil pressure accumulators, a three-stage servo valve, and a hydraulic cylinder. This system controls the movement of the piston and allows it to compress the gas in the pre-compression chamber. In its final position, the piston is locked at the top dead center (TDC), keeping the compressed gases in the combustion chamber to maintain high pressure and temperature for a longer time.

The converging section between the combustion chamber and the pre-compression chamber provides adequate volume for the turbulence grids set.

An ASM micrometer-scale, equipped with a sensor, examines and measures both the position and the speed of the piston. This type of control makes it easy to change the stroke, thus the compression ratio and the compression profile of the piston motion.

The control and acquisition system consists of three main cards: TA2000, ESPCI, and NI-PCI 6071E.

The TA2000 axis card manages the servo-control of the piston position. It allows controlling the pressure delivered by the hydraulic power unit. It also receives information on the position of the piston via an incremental rule (20 steps / mm, maximum speed 10 m/s) coupled to the fuse and controls the position. The ESPCI card manages the inputs and outputs of the system; it allows the control of the different solenoid valves, the starting of the machine, and the control of the emergency stop. The quantities measured by the acquisition card are of two types: fast (pressure, piston position, and temperature in the combustion chamber) or slow (temperatures of the different elements, intake pressure, and airflow). The different thermocouples used are of type K. The thermocouples used for temperature measurement in the chamber are unsheathed to improve their response time. The acquisition board also carries out the control of the air and fuel flows thanks to the Bronkhorst LM51 box. Moreover, the NI-PCI 6071E acquisition board acquires various quantities at a frequency of 200 kHz in 12 bits.

In order to absorb the vibrations due to the movement of the piston, the whole machine is mounted on a welded frame, which allows it to be fixed on the ground. The choice of vertical positioning has been made to reduce the stress on the floor mountings and facilitate the various interventions necessary for the maintenance of the machine. For safety reasons, the assembly is located in a dedicated test bench controlled from the outside.

The combustion chamber is a metallic cylinder (Stainless steel) with a 40 mm diameter and 40 mm height. However, it can be replaced by a transparent quartz cylinder for the direct visualization of the combustion process inside the chamber, detailed in chapter 5. Two cameras are arranged on the rails on both chamber sides to visualize a wide-angle of the combustion phenomenon and especially the ignition phase.

The compression time is an important parameter that influences the combustion process; the control and choice of this parameter are explained in the following paragraph.

1.2. Compression time

An important parameter that influences the combustion in a rapid compression machine is the compression time. Mittal et al. [48] conducted CFD investigations to determine the effect of the geometric parameters (the piston stroke length and the clearance volume), as well as the effect of the end of compression (EOC) temperature and pressure, on the post-compression temperature field. They noticed that a combination of shorter stroke, larger clearance, and higher EOC pressure resulted in higher temperature field uniformity.

Also, the piston velocity during compression is an essential parameter in controlling the homogeneity of the mixture. In general, shorter compression times are more desired, so heat loss and chemical reactions during the compression stroke are reduced. These conditions are promoted by higher piston velocities.

In SU RCM, the speed of the piston during acceleration and deceleration phases follows the characteristic profile of a control trapezoid. This profile controls the piston compression in three steps:

- the speed control or piston velocity in m/sec;
- the position control of the piston at the end of compression at the top dead center (TDC), also known as objective and is given in mm;
- the position control beyond the TDC for holding the position during combustion. It is controlled in the compression profile via deceleration m/s^2 .

The characteristic shape of the trapezoid control has a significant influence on the compression time. Thus, several compression profiles were tested to find the most suitable one, which will be adapted when carrying the experimental tests:

- Piston velocity 5 m/sec, objective of 3.5 mm, deceleration $1000 m/s^2$
- Piston velocity 7 m/sec, objective of 3.5 mm, deceleration $1000 m/s^2$
- Piston velocity 8.5 m/sec, objective of 3.5 mm, deceleration $1000 m/s^2$
- Piston velocity 8.5 m/sec, objective of 2.5 mm, deceleration $1000 m/s^2$
- Piston velocity 8.5 m/sec, objective of 5 mm, deceleration $1000 m/s^2$

The piston velocity and the pressure curve for each of these profiles, tested on inert nitrogen mixtures, are presented in Figure 12 A and B.

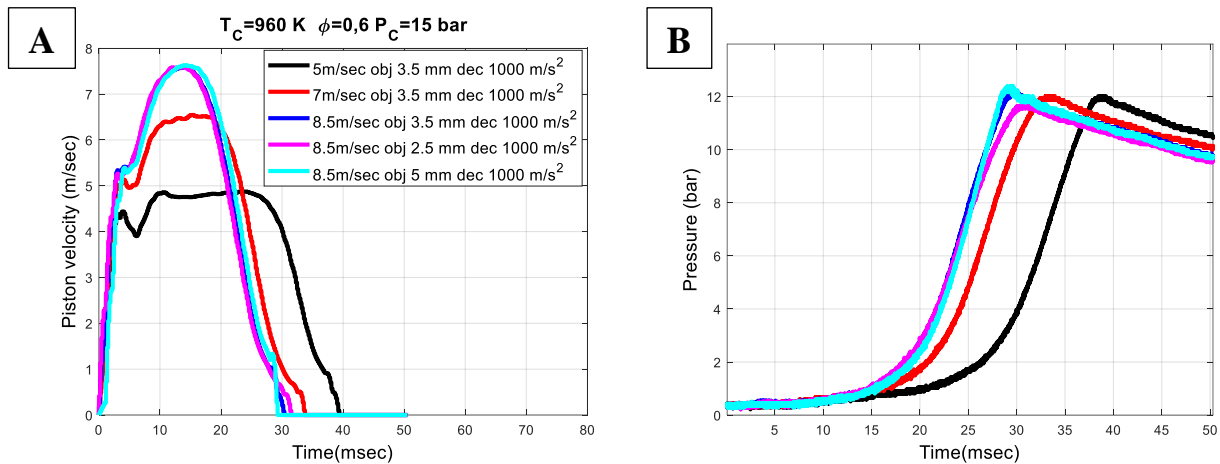


Figure 12: Comparison of different compression profiles; A. piston velocity versus time; B. Pressure curve in compression phase versus time

It can be observed that piston speed during the acceleration and deceleration phases respects the characteristic shape of the trapezoid control. The real maximum piston velocity is slightly lower than the theoretical one. The compression time is shown to be majorly dependent on the piston velocity as it is the longest for 5m/sec and the shortest for 8.5 m/s. However, the EOC pressure is more affected by the objective value. The compression profile of 8.5 m/s, obj. 3.5 mm and deceleration $1000 m/s^2$ (dark blue curve on Figure 12) shows a compression time relatively low (30 msec) and without pressure rebound at the (EOC) compared to other compression profiles. As explained earlier, shorter compression times are advantageous in reducing heat transfer and

inhibiting the occurrence of chemical reactions during the compression phase. Thus, this profile will be used to carry on the experimental combustion of biofuel mixtures in this chapter. The procedure of mixture preparation is described in the following paragraph.

1.3. Mixture preparation

The desired mixture is prepared in a 30 L capacity tank by a hot-wire mass flow regulator. The mixing tank is fitted with a stirrer to ensure the homogeneity of the fuel mixture, a heating system to promote fuel evaporation (in case of liquid fuel), and a safety valve to prevent overpressure in case of abnormal combustion.

The use of a large tank makes it possible to carry out several tests with the same mixture. Thus, a tank pressure of 1.5 bar allows us to carry out approximately 40 shots per tank; conducting several tests with the same tank makes it possible to make sure that the pressure profile and ignition delay are the same for each test of the same mixture.

In this manuscript, the dilution rate is described as the percentage of an inert gas such as nitrogen, carbon dioxide, and argon in the gas mixture. For the same fuel mixture, the compressed load temperature can be varied by changing the proportions of diluted gases. This method is favorable because it does not involve a change in the geometry of the chamber and avoids multiplying the waiting time required to stabilize the initial temperature, in case varying it was decided.

Argon is a monoatomic inert gas that reduces the heat capacity and allows higher compressed gas temperatures than pure nitrogen. Carbon dioxide, however, is a triatomic inert gas that has the opposite effect. Besides, an investigation of the effects of diluent gas on the ignition delay time was conducted in RCMs and shock tubes by Wurmel et al. [49]. They noted that using monatomic diluents leads to longer ignition delays relative to diatomic diluents due to the higher thermal diffusivity of the monatomic diluents.

Once the gaseous mixture is prepared, it is fed into the RCM pre-compression chamber via a heat-insulated Teflon tube and kept at a temperature of 55°C (328 K) using heating fibers. The piston is then fired to compress the mixture into the combustion chamber and to start the combustion process. The experimental procedure is kept the same for all studied tests to ensure the reproducibility of the process.

1.4. Experimental procedure

The intake circuit consists of a hot-wire pressure controller (Bronkhorst EL-FLOW), a piezoresistive pressure sensor (Bronkhorst EL-PRESS), an air heater (Vulcanic), a mixing tank, a Tyco heated line, and an injection circuit. The exhaust circuit consists of exhaust lines connecting the mixing tank and the combustion chamber to the vacuum pump. A general schematic diagram of the intake and exhaust circuits of SU RCM is shown below (Figure 13).

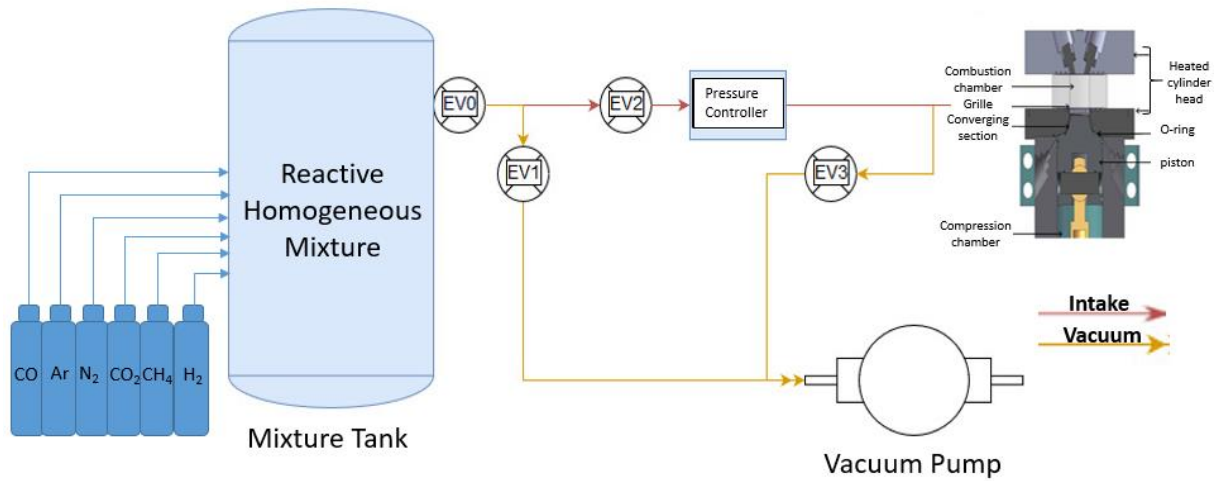


Figure 13: Diagram representing the filling and vacuum circuits of SU RCM

The image shows the intake circuit consisting of a hot-wire pressure controller, the mixing tank, and an injection circuit. The exhaust circuit consists of exhaust lines connecting the mixing tank and the combustion chamber to the vacuum pump

The heating of the compression and combustion chambers is ensured by three heating resistors located at the bottom of the chamber. The heating time is required to ensure that the tests are well performed at initial iso-conditions.

Numerous trials have been conducted by Kéromnès [47] to characterize and validate the SU rapid compression machine on different levels. One of them includes the verification of heating and temperature stabilization time of various elements of the rapid compression machine. According to this study, the entire combustion system is always heated for 3 to 4 hours before performing tests at a certain temperature (55°C in our study).

The vacuum is obtained in the entire intake system (tank mixing and RCM) using a vacuum pump. The desired mixture is then prepared and well stirred in the mixing tank. The vacuum is carried out again in the RCM, which is then filled in for the first time to the desired inlet pressure. The vacuum is again achieved in the RCM then refilled to the desired pressure a second time. The RCM is isolated from the rest of the circuit, and the shot can be fired.

This procedure (two cycles of vacuum and filling) is repeated between each firing to ensure that the previous combustion's residual gases have been evacuated. On the other hand, the filling is carried out according to a time-based procedure, allowing the thermal control set points to be reached.

A chronogram of the complete firing procedure is shown in Figure 14.

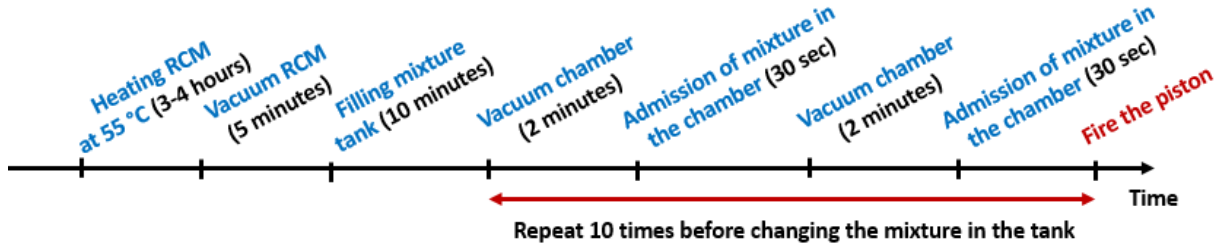


Figure 14: The chronogram of the complete firing procedure

The chronogram shows the heating, vacuum, and filling steps timing, as well as the repetition required before each firing.

In conclusion, the main technical characteristics of the rapid compression machine are presented in Table 5.

Table 5: Technical characteristics of SU RCM

| | |
|----------------------------------|---|
| Stroke length (mm) | 150 |
| Compression ratio | 15 |
| Compression time (msec) | 30 |
| Pressure measurement | Piezoelectric pressure transducer Kistler 601 A range |
| Maximum allowed pressure (bar) | 200 40 (for direct visualization experiments) |
| Heating system | Cylinder head and cylinder liner. Piston is also heated indirectly from the liner |
| Chamber diameter and height (mm) | 40 x 40 |
| Chamber material | Stainless steel Quartz (for direct visualization experiments) |
| Number of experiments | 10 per hour |

Although the main elements of the SU rapid compression facility were presented briefly in this section, the experiments of the biofuel combustion were carried on the SU RCM and are presented next.

2. Definition and identification of experimental auto-ignition delay time

2.1. Definition of auto-ignition delay time

Theoretically, homogeneous combustion occurs by auto-ignition: the reactive mixture in the combustion chamber explodes altogether when it reaches its auto-ignition temperature.

In reality, the conservation of temperature and pressure parameters in a closed system is the seat of exothermic chemical reactions. The conditions of concentration, pressure, temperature as well as the conditions of conservation, can lead to the runaway of these reactions after a more or less

long time. The time duration required to achieve the runaway of chemical reactions is the auto-ignition delay time or induction time. This delay corresponds to the time required for the radical species necessary for the chemical propagation of the reaction to be formed in sufficient concentration. Numerous radical species govern the self-ignition mechanism throughout the combustion process. Thus, its chemical modeling is complex because of the various species; therefore, the different reactions are numerous.

The auto-ignition delay τ is a key parameter characterizing combustion in HCCI mode. It is highly dependent on chemical kinetics and is influenced by temperature, pressure, equivalence ratio, and concentration of the component species in the fuel. Due to its importance as a fundamental physico-chemical characteristic of auto-ignition, determining the auto-ignition delay time for a given fuel-air mixture at a certain pressure and temperature is essential.

According to Bradley et al.[50], since the temperature (T) and pressure (P) are continuously changing in an engine, a practical approximation is that auto-ignition occurs when the integral of the reciprocal of $\tau(P, T)$ with respect to the time t attains a value of unity:

$$\int_0^t \frac{dt}{\tau(P, T)} = 1 \quad (II.1)$$

Besides, many authors in the literature have established an empirical correlation for determining the auto-ignition delay time for a specific fuel type in certain conditions. Experimental measurements were conducted mostly on rapid compression machines or shock tubes and numerical simulations in chemical kinetic models. For example, measurements of the ignition delay of hydrogen and methane carried out by Gersen et al. [51] on the rapid compression machine led them to establish an empirical correlation based on a global Arrhenius law:

$$\tau = A \left(\frac{P_c}{T_c} \right)^n \exp \left(\frac{E_a}{RT_c} \right) \quad (II.2)$$

where:

- A is the Arrhenius factor
- E_a is the activation energy
- P_c and T_c are respectively the pressure and the temperature at the end of the compression
- n is the factor of the mixture's density
- and R is the universal ideal gas constant equal to $8.3145 \text{ J} \cdot \text{mol}^{-1} \cdot \text{K}^{-1}$

For a chemical reaction to occur, the activation energy of the reactions that form the mechanism of chemical kinetics must be overcome. This energy differs according to the type of fuel studied. Therefore, as a result of this correlation, the ignition delay depends on the fuel chosen, the density of the mixture, the temperature, and the pressure at the end of compression.

The influences of these different parameters on the ignition delay will be discussed later.

2.2. Experimental identification on rapid compression machine

Given the importance of the ignition delay time in the combustion process, it will be measured and calculated for experimental and numerical studies, which will be conducted on the combustion of different biofuel mixtures. As mentioned before, the rapid compression machine is the

experimental device used in our research to study the chemistry of self-ignition and the fundamental processes of combustion under conditions relevant to internal combustion engines and gas turbines (high pressure and relatively low temperature).

The ignition time is defined based on the pressure measurement. However, the use of pressure signals is reliable in most cases, when ignition produces a noticeable increase in pressure. Several criteria were used to determine the ignition delay time from the pressure profile through time, whether on shock tubes or rapid compression machines. In our study, the ignition delay time was calculated by four methods in the literature applied to the pressure curve, as presented in Figure 15.

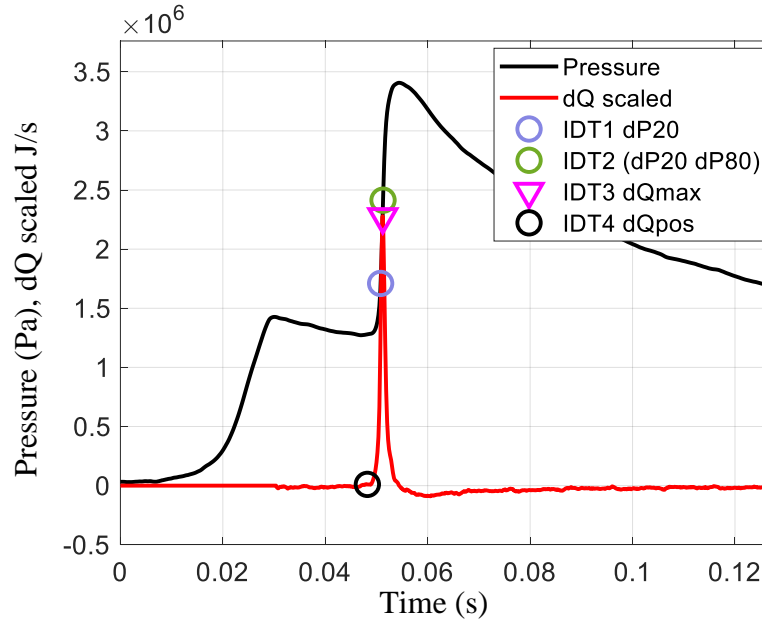


Figure 15: Several ignition delay times definitions (the curve of dQ (heat release rate) is scaled by $[2 * P_{max} / (3 * dQ_{max})]$). The pressure curve is used to estimate the ignition delay time, calculated by four methods IDT1, IDT2, IDT3 and IDT4

In this paragraph, dP represents the pressure increase compared to the end of the compression pressure P_c .

The first ignition delay time is calculated based on the definition of Tanaka et al. [52]. According to these authors, the ignition delay time of the air/fuel mixtures is defined as the time between the end of compression and the time at which dP reaches 20% of the maximum pressure (P_{max}) increase: $dP_{20} = 20\% (P_{max} - P_c)$. This corresponds to IDT1 in Figure 15.

The burn rate for the explosive phase of combustion is defined as the average rate of pressure increase during which dP rises from 20% to 80% of dPmax. Thus, IDT2 can be defined by the intersection between the straight line connecting dP20 to dP80 with the horizontal line $P = P_c$.

IDT3 corresponds to the moment when the heat release from the principal flame reaches its peak. This definition is the most widely used in the literature and is adopted in this study. Finally, IDT4 corresponds to when the heat release starts to increase.

For the different definitions, the ignition delay time starts at the end of compression; when the piston is at the TDC.

The amount of apparent heat that integrates heat transfers is calculated through the acquired pressure profile. Although to determine the maximum heat release as accurately as possible, it is advisable to locally approach the heat released by a polynomial of degree 2 around its maximum. This allows a more accurate determination of the moment when the heat release is at its peak. The same procedure is used to determine the maximum heat release of the cold flame.

Pounkin [53] compared the values of ignition delay times calculated by each of these methods for the combustion of hydrogen mixture on the SU RCM. He showed that the definition used to calculate the delay might impact the value of the delay. The maximum difference in the delay values was found to be 11%. Therefore, it is imperative to clarify how delays are determined before any comparison with other rapid compression machines is made.

Since the delays are usually represented as a function of the temperature at the end of compression, it will be necessary to determine how the latter is calculated and if the adiabatic core assumption is possible. The following paragraph will describe the different methods used to determine the end of compression temperature.

3. End of compression calculations

The temperature of the compressed gas mixture can only be measured using techniques that are difficult to implement (micro thermocouple, Rayleigh scattering [54]) and is therefore calculated. Initially, the gas mixture occupies a volume V_0 at a pressure P_0 . At the end of compression, it is brought to a pressure P_c and occupies a volume V .

The evolution of the self-ignition time is normally studied as a function of the end of compression temperature T_c . There are several different methods for calculating this temperature, either in a real environment, taking into account thermal losses, or in an environment where the core is adiabatic. The core of the mixture is the part that does not interact with the combustion chamber walls and, therefore, is not influenced by heat transfers [53].

3.1. Adiabatic temperature

The adiabatic temperature T_{isen} is calculated by assuming adiabatic compression and, therefore, the absence of heat losses for the whole gas. The calculation of T_{isen} is carried out by successive iterations using the Newton-Raphson method. The equation used is as follows:

$$T_{isen} = T_0(\varepsilon)^{\frac{\gamma-1}{\gamma}} \quad (II.3)$$

Where γ is the temperature-dependent specific heat ratio, ε is the volumetric compression ratio, and T_0 the initial temperature. This calculation is therefore based on the hypothesis of isentropic transformation:

$$S(T_0, P_0) = S(T_{isen}, P_c) \quad (II.4)$$

However, due to the heat transfer from hot gases to the wall, compression is not truly adiabatic. Although the actual pressure and temperature are lower than those achieved for adiabatic compression, various studies [54],[55] have shown that it is reasonable to assume an isentropically-compressed core region of the gas mixture, with the effective compression ratio being modified by heat transfer to the wall. While this assumption may fail for a flat piston head due to the effect of the roll-up vortex [56], it is expected to be valid for a properly designed creviced piston. The use

of a creviced piston design to promote the formation of a homogeneous core region is also studied by Mittal [48].

The adiabatic core temperature is the most used in the literature. It is given by the following equation:

$$T_{ac} = T_0 \left(\frac{P_c}{P_0} \right)^{\frac{\gamma-1}{\gamma}} \quad (II.5)$$

The calculation of this temperature assumes the existence of a zone less affected by heat losses than the boundary layer gas in contact with the walls; this zone is the core gas.

Having undergone quasi-adiabatic compression, the temperature of the core gas is higher than that of the boundary layer. On the other hand, the same pressure is assumed throughout the chamber. The pressure of the core gas at the end of compression is thus assimilated to the pressure P_c measured experimentally. The temperature T_{ac} of this core is calculated by an iterative process considering the temperature dependence of γ .

3.2. Polytropic and non-adiabatic temperature

The adiabatic core temperature described in the previous paragraph is the most used in the literature. However, several parameters are shown to influence the adiabatic core hypothesis. It was studied by Di et al. [57] that the validity of the adiabatic core hypothesis might not be dependent on the chemical and dilution effects. Nevertheless, the thermal effect may affect its validity by determining the extent of the boundary layer growth during and after the compression. Monatomic diluents may especially affect the adiabatic core assumption due to their higher thermal diffusivity, which leads to a larger boundary layer thickness, that may not be fully captured by a creviced piston optimized for a different diluent or different conditions.

Also, high piston velocities may lead to increased turbulence and the breakdown of the adiabatic core hypothesis [48]. As mentioned earlier, the piston velocity is an essential parameter in controlling the homogeneity of the mixture. In general, higher piston velocities are required for shorter compression times such that the heat loss and chemical reaction effects are reduced during the compression phase.

As a result of the uncertainty of the adiabatic core temperature calculation, the polytropic model was introduced. The polytropic temperature was used by several authors [58], [59], [60], [61], [62], [63]. It is defined as:

$$T_{poly} = T_0 (\varepsilon)^{\frac{n_p-1}{n_p}} \quad (II.6)$$

Where n_p is the temperature-dependent polytropic coefficient. The heat transfer model used in this comparison is a real model that considers heat exchanges and mass losses.

The ring creates a seal, preventing combustion gases from leaking out of the chamber. Nevertheless, a small mass fraction is leaked during the compression process. Therefore, the polytropic temperature is adjusted by applying the mass conservation between the start and the end of compression.

The differential temperature is a non-adiabatic temperature that accounts for heat loss. It is calculated based on a differential equation used to treat the data of the pressure curves relative to the RCM combustion tests.

Before proceeding with the experimental study of the biofuel combustion on the SU RCM, comparison tests were carried on to set the SU RCM with the other RCMs and ensure that it gives similar delay values. The adiabatic core, polytropic, and non-adiabatic (differential) temperature will be used in the following comparison to choose the calculation method that will be considered in this study.

4. Study of reliability of results: comparing SU RCM results to other RCM in the literature

As discussed earlier, rapid compression machines (RCM) have been designed and fabricated for chemical kinetics studies at elevated pressures and temperatures (600-1100 K). They are mainly used to study the combustion of a mixture under conditions where the reaction is very slow to be studied in shock tubes. The first machines used to determine auto-ignition conditions were built in the first decade of the last century. Many investigators improved on the original designs to allow the piston to be locked off in its final position, as well as to reduce the compression time and achieve suitable compression ratios. Thus, several RCM with different designs and characteristics exist nowadays in a few laboratories around the world.

These RCMs differ primarily by the nature of the system controlling the movement of the piston and the way to stop it. Usually, this system consists of compressed inert gases or liquids under pressure. Another difference is the compression time, as the major problem is maintaining the high pressure and temperature for a relatively long time. The third important characteristic is the control of the aerodynamics of the compressed gases.

In this section, the combustion of some mixtures studied previously on other RCMs will be first studied with the same conditions on the SU RCM. The measured induction time will then be compared with the auto-ignition time measured in the other RCMs.

Note that even if the same experimental study is repeated with exactly the same fuel composition, temperature, and pressure, some discrepancies may appear in the results when comparing one RCM to another. These differences are the results of various factors, including:

- the difference in the geometric conception (such as single or double pistons, the shape of the piston, the surface to area ratio, etc.);
- The difference of the internal aerodynamic fields and turbulence level
- The compression duration and the dynamic of the compression
- The isolation of the system and the heat loss at the wall of the chamber; heat transfer must inevitably occur since the reaction chamber walls are much cooler than the reacting gas, and heat loss occurs during the test period, decreasing the temperature and pressure in the test chamber and stratifying the mixture.

4.1. Comparison tests

As two of the main components of biofuel mixtures, hydrogen and methane mixtures will be the core of the comparison tests.

Thus, three mixtures were chosen from the literature and presented with their conditions in Table 6.

Table 6: Hydrogen and methane/hydrogen mixtures from the literature

| Mixtures | Composition | Φ | H ₂ (-) | CH ₄ (-) | O ₂ (-) | N ₂ /Ar (-) | P _c (bar) | T _c (K) | Ref |
|-----------|---|--------|-----------------------|------------------------|-----------------------|---------------------------|-------------------------|-----------------------|------|
| Mixture 1 | 100% H ₂ | 0.5 | 0.167 | 0 | 0.167 | 0.667 | 50 | [941-1050] | [64] |
| Mixture 2 | 100% H ₂ | 1 | 0.286 | 0 | 0.143 | 0.571 | 40 | [936-1006] | [64] |
| Mixture 3 | 40/60% CH ₄ /H ₂ | 0.5 | 0.01875 | 0.0125 | 0.06875 | 0.9 | 10 | [1015-1064] | [2] |

Lean and stoichiometric hydrogen mixtures were taken from the work of Gersen et al. [64] who studied the self-ignition of pure H₂ on the Netherland RCM. The end-of-compression pressure was 50 and 40 bar respectively, and the temperature between 930 and 1010 K; for these two mixtures, Argon and nitrogen were chosen as diluents.

On the other hand, the lean 40/60 % CH₄/H₂ mixture was taken from the study of Donohoe et al. [2] on the NUIG RCM. The end-of-compression pressure was 10 bar, and the diluents were also N₂ and Ar with a dilution ratio of 90 %.

In what follows, these three mixtures were exactly reproduced on the SU RCM with the same concentrations of components, diluents, and dilution rates. The high end of compression pressures of mixtures 1 and 2 requires a higher compression ratio than the one actually used. However, instead of changing the compression ratio, we choose to perform mixtures 1 and 2 with an end of compression pressure of 15 bar instead of 50 and 40 bars, respectively.

In order to correct the effects of different pressures, the self-ignition delays measured on the RCM were correlated to the oxygen concentration in the constant volume phase [O₂] (mol/cm³)[65]:

$$[O_2] = \frac{x_{O_2} P_c}{T_c R} \quad (II.7)$$

Where:

- x_{O_2} is the molar fraction of oxygen in the mixture
- P_c is the end-of-compression pressure,
- T_c is the end of the compression temperature,
- R is the universal perfect gas constant (8.314 J/mol/K)

4.2. Comparison RCM designs

Before proceeding with the comparison of the induction time values, it is particularly important to mention the significant differences in the design and conception of the studied RCMs. A comparison of SU, Netherland, and NUIG RCMs is presented in Table 7.

Table 7: Comparison of three different RCMs

Table showing the difference between the NUIG, Netherland, and SU RCMs in regards to the technical strategies, the compression ratios and duration, the higher compression pressure as well as the temperature and the auto-ignition delay time.

| | Technical Strategy | Compression ratio (-) | compression duration (msec) | Higher compression pressure (bar) | Temperature Calculation method (for the studied mixtures) | Auto-ignition delay time measurement (for the studied mixtures) |
|----------------|--|-----------------------|-----------------------------|-----------------------------------|---|--|
| NUIG RCM | Two opposing pistons with pneumatic drive and shut-off | 13,4 | <22 msec | 17 | Adiabatic core | The time interval between the end time of compression and the moment of maximum heat release |
| Netherland RCM | single piston pneumatically driven and hydraulically stopped | 19 | 10-30 msec | 70 | Adiabatic core | The time interval between the end time of compression and the moment of maximum heat release |
| SU RCM | single piston hydraulically driven and stopped | 15 | 30 msec | 40 | Non adiabatic temperature Polytropic temperature Adiabatic core temperature | The time interval between the end time of compression and the moment of maximum heat release |

The Netherland RCM is made with the same design, construction, and specification as MIT RCM [66]. The piston is driven downwards by compressed air and is stopped hydraulically by released oil through a variable area orifice to adjust the deceleration characteristics of the piston's motion. The gas mixtures were compressed with a maximum compression ratio of 19 in 10–20 msec to peak pressures, while the majority of the pressure rise takes place in less than 3 msec [67]. The schematic diagram of the MIT RCM is presented in Figure 16 A. The NUIG RCM, on the other hand, has a horizontally opposed, twin-piston design. The piston is driven and stopped pneumatically and thus, compression times below 16 msec can be achieved [68]. A photo of the NUIG RCM is presented in Figure 16 B.

It is important to highlight that the compression ratio, duration and peak pressure presented in Table 7 are the general operating conditions of these RCMs; the value of these parameters used for the studied mixtures are not known.

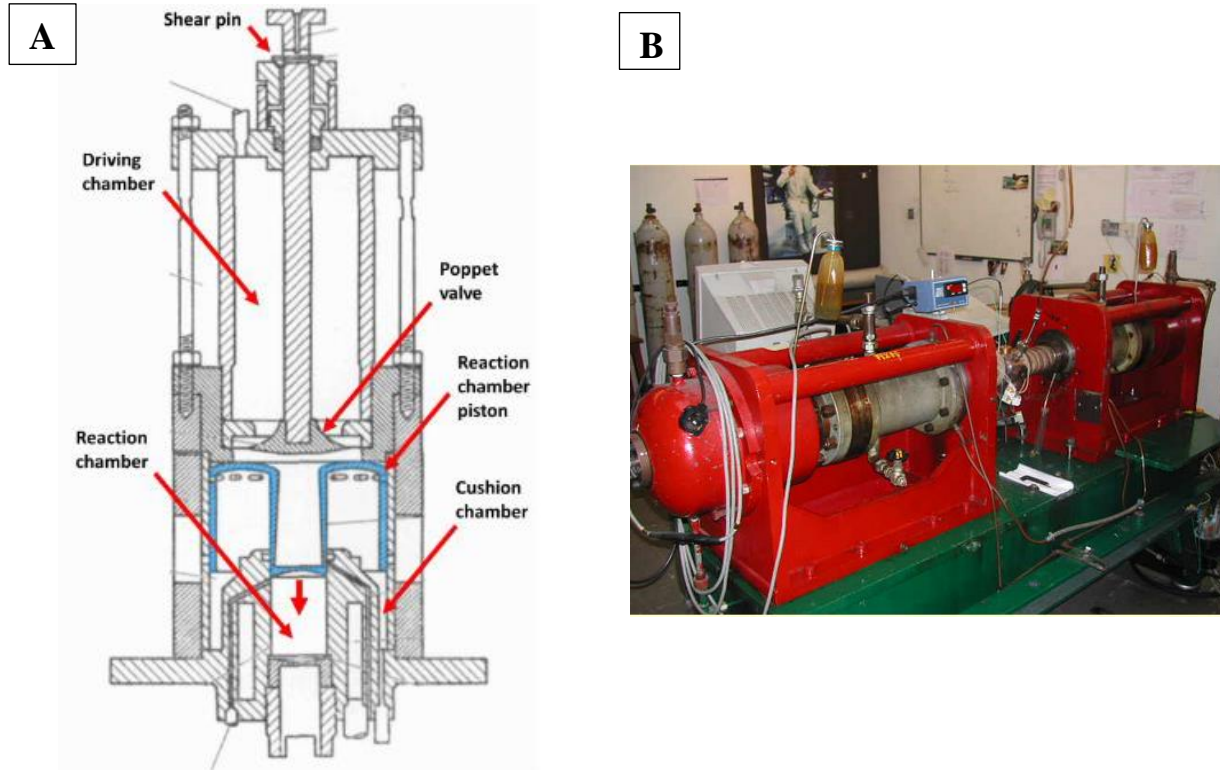


Figure 16: Representation of the other RCMs A. schematic diagram of the MIT RCM and B. photo of the NUIG RCM

For both RCMs, the crevice piston head designed was used to preserve a homogeneous reacting core gas. Therefore, the end of the compression temperature is calculated based on the adiabatic core hypothesis. The ignition delay time is defined as the time from the end of compression, taken as the time of peak compressed pressure, to the maximum rate of pressure rise at ignition.

The SU has thus adopted this fully hydraulic servo control with a compression ratio of 15 and a conventional compression time of the order of 30 msec as described in a previous section. These characteristics allow offering time ranges characteristic of turbulence and chemistry broad enough to study the interactions between combustion and aerodynamics internal.

4.3. Reliability of results

Mixtures 1 and 2

The measured delays of mixtures 1 and 2 corrected by the O_2 concentration were compared to those measured by Gersen et al. [64] on the Netherland RCM and presented in Figure 17 and Figure 18.

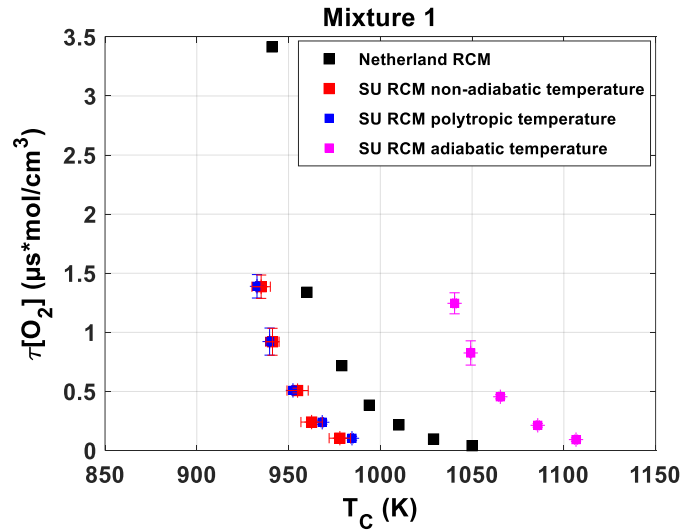


Figure 17: Comparison of the corrected self-ignition times of mixture 1 performed on SU RCM and Netherland RCM obtained from the literature [64]

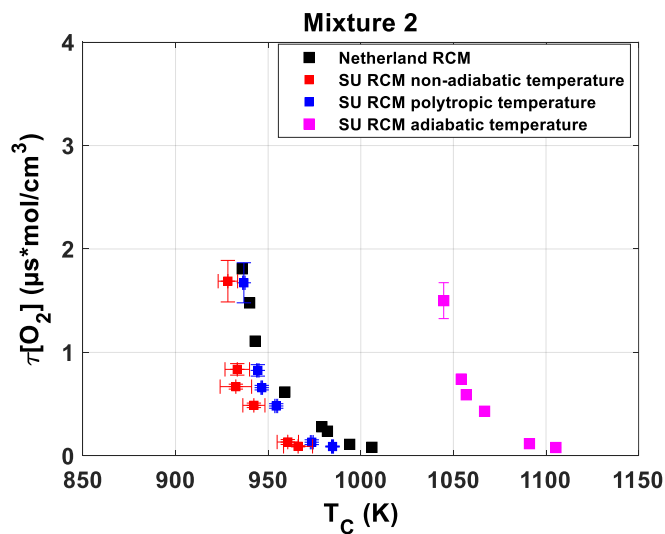


Figure 18: Comparison of the corrected self-ignition times of mixture 2 performed on SU RCM and Netherland RCM obtained from the literature [64]

It appears that in terms of trends, the corrected delays represent the same exponential evolution with temperature in both RCMs. For instance, it is shown the absence of cold flames as well as a reduction of the delay times with the increase in temperature. Moreover, the evolution of measured delays is the same, along with the three methods of temperature calculation.

As expected, the adiabatic temperature is the highest among the temperature calculations because it parts from the assumption of the absence of heat losses. It is followed by the polytropic temperature, where the real heat and mass losses are considered.

The polytropic and non-adiabatic calculations show closer values, especially in the lean hydrogen mixture, where the maximum difference of temperature is 5 K. It becomes 10 K in the case of the

stoichiometric hydrogen mixture. Although this temperature offset is dependent on the properties of the mixture, it is also dependent on the temperature and, therefore, on the diluents Ar/N₂ proportions.

It is perceived, however, that the polytropic temperature based on the heat transfer model of the SU RCM is the most consistent with the core temperature used by Gersen et al.[64].

Nevertheless, the adiabatic core temperature in the Netherland RCM is, on average higher than the polytropic temperature by 50 K for mixture 1 and 10 K for mixture 2.

Several reasons can be offered to explain such discrepancies, mostly connected to the lack of uniformity in the state of the reacting mixture. Another reason can be related to the slight differences in the RCMs designs and therefore heat losses as well as the difference in the calculation mode of the end of compression temperature.

Considering the assumption of the validity of the scaling method and that heat loss can vary significantly between the physically different machines, the agreement of the results obtained here and the data in the literature is considered good.

Mixture 3

Ignition delay times of mixture 3, scaled with oxygen concentrations are compared with those measured by Donohoe et al. [2], and are presented in Figure 19.

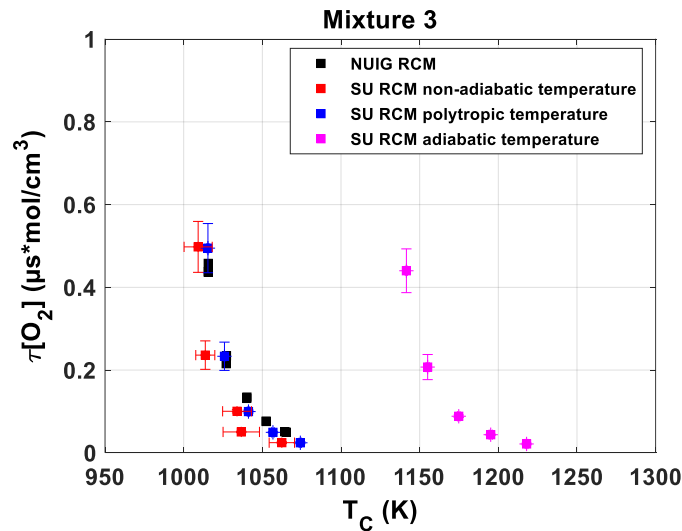


Figure 19 : Comparison of the corrected self-ignition times of mixture 3 performed on SU RCM and NUIG RCM [2]

Similar to previous mixtures, the scaled ignition delay time in the methane/hydrogen mixture measured on SU RCM represents the same exponential trend function of the reciprocal temperature as the NUIG RCM. The same remarks concerning the temperature calculations can be made. Nevertheless, there is a better agreement between the polytropic temperature in SU RCM and the core adiabatic temperature in NUIG RCM with a maximum difference of 5 K. As explained before, this difference is due to the difference in the conception, design, and heat losses in each RCM.

Moreover, in terms of ignition delay times, the experimental results in SU RCM are within an interval of 10% of those of NUIG RCM; thus, the obtained results are in good agreement with the literature.

5. Conclusions

The SU rapid compression machine is the experimental device used in this work to study the lean homogeneous combustion of biofuel mixtures.

Thus, the technical characteristics of the machine optimized to allow a good study of the auto-ignition process were described. A compression profile that allows a reduced compression time without pressure rebound at the end of compression was chosen to carry on the experimental study.

In order to assess the quality of the experimental data, the ignition delay times obtained in SU RCM were compared with the results of previous RCM studies of the auto-ignition of fuel mixtures. The purpose of this comparison is to place the SU RCM with other RCMs by ensuring reliability and accuracy in the measure of ignition delay times.

As two of the main components of biofuel mixtures, hydrogen and methane mixtures were chosen to be the core of the comparison tests. Thus, three mixtures were chosen from the literature: lean and stoichiometric pure hydrogen mixtures from the study of Gersen et al. on the Netherland RCM and H_2/CH_4 mixtures from the work of Donohoe et al. on the NUIG RCM.

Comparisons of self-ignition times measured by different authors have shown that the trends observed were following those of literature (thermal diffusivity of reactive mixtures can accentuate the effects of heat release). Nevertheless, disparities exist and can be due to the difference in designs and conception of each rapid compression machine. Although, each machine has a particular aerodynamic and, therefore, a different level of turbulence, heat transfer, and combustion process. Several studies in the literature focused on the sensitivity of the auto-ignition phenomena on temperature heterogeneities, heat transfer, aerodynamics, and the turbulence level in the chamber.

Furthermore, another reason for the disparity can be related to the method used to calculate the end of compression temperature. Three different methods to calculate the end of compression temperature were also presented. It seems that the polytropic assumption of temperature calculations on the SU RCM provides less disparity in the results compared to the literature. Therefore, this assumption will be considered in the study of biofuel combustion presented in the following section. The choice of the studied mixtures, as well as the conditions of the study, will be defined first. The performance and reproducibility of the machine during the compression and combustion phase will also be highlighted. As a result of the auto-ignition study, the effect of the leading biofuel components (CH_4 , H_2 , CO_2 , CO) on the induction time and thus on the combustion reactivity will be discussed.

Key parameters and conclusions

- The SU rapid compression machine is a single-shot, piston-based machine; its application is comparable to engine application
- The ignition delay time is the time between the end of compression and the maximum heat release
- The ignition delay values measured on SU RCM were validated by comparing its performance with two other rapid compression machines (MIT RCM and NUIG RCM);
- For all the studied mixtures, the results obtained on the SU RCM were in good agreement with the results of the other RCMs
- Disparities in the delay values exist but are due to the difference in the design of the machines, and the method of calculating the end of compression temperature
- The ignition delay times depend on the RCM designs especially the compression time, compression ratio and the system isolation
- Three different methods of calculating temperature were presented
- The polytropic temperature calculation is shown to be the closest to the adiabatic core calculations of other RCM; thus, this temperature will be used in the experimental study

III. Experimental study of the combustion of biomass-derived fuel

As explained previously, gaseous biofuel mixtures are renewable energy sources. Their use in many applications can be advantageous due to their neutral CO₂ emissions. The low calorific value of biogas is improved by hydrogen present in syngas; on the other hand, the high NO_x emitted from the combustion of syngas can be reduced by adding CO₂ present in biogas. Consequently, the use of mixtures of biogas and syngas seems to be the right way to reduce non-renewable fossil fuel dependency while decreasing emissions issues and conserving high efficiency. The main components of biogas/syngas mixtures are methane, hydrogen, carbon dioxide, and carbon monoxide.

Many researchers have investigated their applications separately in conventional internal combustion engines, and more recently, in the lean homogeneous combustion.

The use of syngas and biogas on the HCCI combustion engine combines the advantage of alternative fuels as well as alternative combustion strategies. Yamasaki and Kaneko [69] investigated the impact of a syngas, composed of H₂, CO, CO₂, N₂, and a small methane fraction, on auto-ignition and combustion characteristics of the HCCI engine. Their results reveal that regardless of the fuel composition, the ignition timing is determined by the in-cylinder gas temperature and the auto-ignition temperature of 1100 K, similar to that of hydrocarbon fuels.

Moreover, Przybyla et al. [70] experimentally investigated the performance of SI and HCCI engines fueled with low calorific syngas. Results indicate that the HCCI engine has higher CO emissions and lower thermal efficiency as compared to the SI engine. However, the HCCI engine's combustion duration is four times shorter than the SI engine.

In this study, the combustion of blended biofuel of biogas and syngas, also known as $\text{CH}_4/\text{CO}_2/\text{CO}/\text{H}_2$ mixtures, will be studied in lean homogeneous conditions. In general, lean homogeneous combustion can be realized with fuels with a low LHV that contain several non-combustible components, and the enthalpy of the blended mixture contributes to realizing the high-temperature pre-mixture conditions enabling auto-ignition.

Thus, the duality biofuels/ HCCI combustion engine combines the advantage of alternative fuels as well as alternative combustion strategies.

1. The choice of the studied biomass-derived fuel mixture

This study aims to characterize the physico-chemical properties of the lean homogeneous combustion of biogas/syngas mixtures. For this purpose, the experimental investigation of the auto-ignition of biofuel will be studied on the SU RCM. As described earlier in this chapter, the rapid compression machine is used specially to measure the induction time of the combustion to validate chemical kinetic mechanisms. As an indicator of the reactivity of the mixture, this parameter will be used to study the effect of biofuel composition on the reactivity during the auto-ignition process. Therefore, to study the influence of each component on the combustion process, the experimental mixtures and conditions will be chosen first.

As discussed in chapter 1, biogas majorly contains CH_4 and CO_2 , while syngas is mainly composed of H_2 and CO . consequently, the main components of biofuel mixtures are methane, hydrogen, carbon dioxide, and carbon monoxide. The percentage range of each component obtained by combining fuel composition from the methanisation and gasification is presented in Table 8. (see Table 4)

Table 8: percentages of components in biogas/syngas mixtures

| Components | CH_4 | H_2 | CO_2 | CO |
|---------------------|---------------|--------------|---------------|-------------|
| Volume fraction (%) | 0-99 | 0-40 | 0-40 | 0-70 |

In this study, the combustion of different compositions of $\text{CH}_4/\text{CO}_2/\text{CO}/\text{H}_2$ mixtures will be studied experimentally and numerically in HCCI conditions.

A volume fraction range between 30-75% of methane can be present in biogas issued from biomass methanisation, 0-40% in synthesis gas issued from biomass gasification, and higher than 99% in biomethane (from methanation). Thus, the percentage of CH_4 in a biofuel mixture can vary between 0 and 99%.

Similar to methane, carbon dioxide can be present in synthesis gas, but it is much more significantly present in biogas with a percentage range of up to 40%.

On the other hand, hydrogen and carbon monoxide are mostly present in synthesis gas with a percentage range of 0-40% and 0-70%, respectively.

In order to study the influence of a component on the auto-ignition, several mixtures were introduced by varying the percentage of the studied component and keeping the proportions of other components intact.

For instance, the combustion of pure methane mixture will be carried on first on the SU RCM. The effects of hydrogen on the auto-ignition of methane will be studied by varying the proportions of hydrogen and methane concerning their percentage range defined in Table 8. Although not in the biofuel range, it can be interesting to study a mixture with 100 % H₂ to investigate the effects of hydrogen on the ignition delay times. The different proportions of the CH₄/H₂ studied mixtures are presented in Table 9.

Table 9: different configurations of H₂/CH₄ mixtures

| | H₂/CH₄ | |
|-----------------|-------------------------------------|------------------------|
| mixtures | CH₄ % | H₂ % |
| 1 | 0 | 100 |
| 2 | 100 | 0 |
| 3 | 90 | 10 |
| 4 | 80 | 20 |
| 5 | 70 | 30 |
| 6 | 60 | 40 |

Following the experimental characterization of the combustion properties of these blends, a CH₄/H₂ mixture will be chosen to determine the effects of carbon dioxide on the auto-ignition process.

Numerous CH₄/H₂/CO₂ mixtures will then be studied by adding amounts of carbon dioxide such as that present in the biogas to the selected CH₄/H₂ mixture. The different blends of the CH₄/H₂/CO₂ studied mixtures are presented in Table 10.

Table 10: different configurations of CH₄/H₂/CO₂

| | CH₄/H₂/CO₂ | | |
|-------------------------------------|--|-------------------------|------------------------|
| mixtures | CO₂ % | CH₄ % | H₂ % |
| CH₄/H₂ | 0% | X % | Y% |
| 7 | 10 | 90 X | 90 Y |
| 8 | 20 | 80 X | 80 Y |
| 9 | 30 | 70 X | 70 Y |
| 10 | 40 | 60 X | 60 Y |

Finally, the same procedure is repeated to study the effects of carbon monoxide on the combustion process. Thus, the different blends of the CH₄/H₂/CO₂/CO studied mixtures are presented in Table

11 (with X', Y', and Z' the percentage of methane, hydrogen, and carbon dioxide respectively in the selected H₂/CH₄/CO₂ mixture).

Table 11: different configurations of CH₄/H₂/CO₂/CO

| Mixtures | CH ₄ /H ₂ /CO ₂ /CO | | | |
|--|--|-------------------|------------------|-------------------|
| | CO % | CH ₄ % | H ₂ % | CO ₂ % |
| CH ₄ /H ₂ /CO ₂ | 0 | X' | Y' | Z' |
| 11 | 15 | 85 X' | 85 Y' | 85 Z' |
| 12 | 30 | 70 X' | 70 Y' | 70 Z' |
| 13 | 45 | 55 X' | 55 Y' | 55 Z' |
| 14 | 60 | 40 X' | 40 Y' | 40 Z' |

We aim in this section to study the lean homogeneous combustion of biofuel mixtures. Thus, the conditions should be used wisely to cover a wider operating range experimentally. These conditions are presented in the following paragraph.

2. Presentation of experimental conditions

In order to achieve lean homogeneous combustion, a significant amount of charge dilution must be present[35]. As stated earlier in this chapter, the dilution rate is described as the percentage of an inert gas such as nitrogen, carbon dioxide, and argon in the gas mixture. It allows controlling the temperature of the compressed load by changing the proportions of diluted gases. Di et al. [57] investigated the effect of diluent composition on the ignition delay. They considered several competing effects of the diluent gas: the chemical effect, the dilution effect, and the thermal effect, whereas Wurmel et al. [49] only considered the thermal effect. The chemical effect influences the reaction rates through the third-body collision efficiency of the diluent gas, while the dilution effect influences the ignition delay by changing the oxygen concentration; the thermal effect is due to the varying specific heat of each of the diluents.

Nevertheless, because carbon dioxide is one of the main components of biofuel mixtures, it will not be used as a diluent. The diluent gases used in this study are the inert gases argon and nitrogen. Thus, the temperature range will be obtained by varying the proportions of the monoatomic (Ar) and diatomic (N₂) diluent gases due to the heat capacity ratio $\gamma=C_p/C_v$. The variation of their compositions is carried out without, however, changing the dilution ratio.

According to an investigation conducted by Mittal et al. [48], higher EOC pressure and temperature resulted in higher temperature field uniformity. Thus, an end of compression pressure of 15 bar was chosen, with a low to an intermediate temperature range of 900 to 1100 K, mainly chosen to reduce NO_x emissions.

The same experimental conditions were adapted to all tests; the combustion chamber was preheated at a temperature of 55°C, and the studied mixtures were compressed at the end of compression pressure of 15 bar and a temperature range from 900 to 1100 K.

Ten reproducibility tests are carried out for each end-of-compression temperature, using the same vessel filled to 1.5 bar. The procedures for filling and emptying the compression and combustion chambers of the RCM, as well as the time required to carry them out (4 minutes between each shot), are the same for each of these ten tests. This time is of great importance; it allows the exact reproduction of the vacuum and filling procedures and allows the walls of the combustion and compression chambers to cool down after each combustion shot to reach the regulation temperature.

3. Experimental results

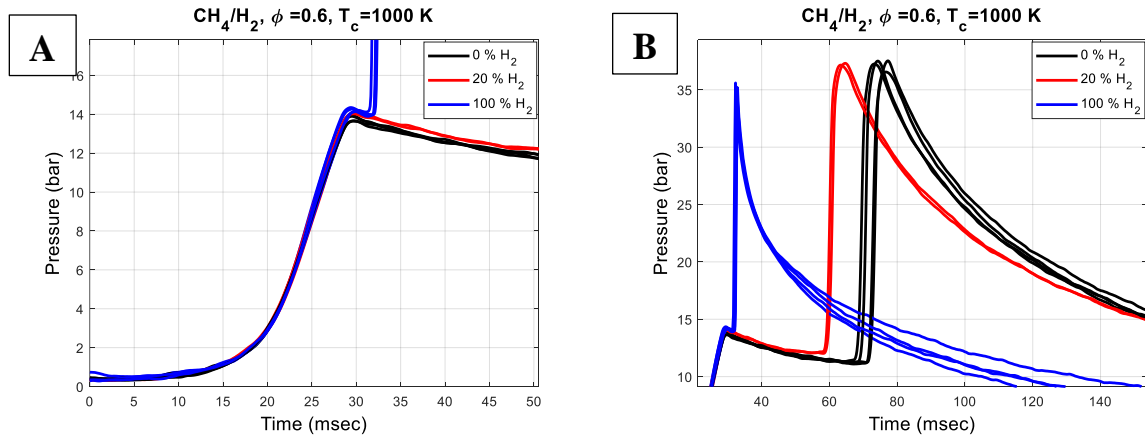
3.1. Study of reproducibility of results pressure and heat release profile during compression, post-compression, and combustion phase

Compression and post-compression phase

The acquisition pressure sensor is used for obtaining pressure values at any time during combustion. Together with the conditions of the reactive mixture studied (composition, initial pressure, tank pressure, piston speed profile, etc.), these pressure data will be processed from a MATLAB calculation code.

In particular, the pressure profile as a function of time is processed by eliminating any undesirable knocking phenomena in order to locate the start of ignition better. We then obtain the filtered pressure that will be presented in this study.

The evolution of the pressure through the various tests of combustion of CH_4/H_2 mixtures, for different percentages of hydrogen and under a compression end temperature of 1000 K (with the reproducibility tests carried out), is presented in Figure 20 A, B, and C.



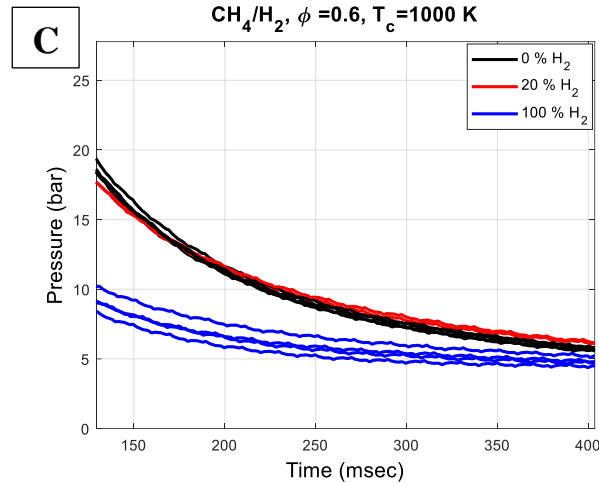


Figure 20 : Pressure as a function of time for the different percentages of H_2 A. compression phase B. heat exchange phase and C. end of combustion phase

Since the compression ratio (15) and profile (piston speed 8.5 m/s, target 3.5 and deceleration 1000 m/s^2) are the same for all these tests, the pressure profile in the compression phase is perfectly reproducible for the different percentages of hydrogen.

A slight pressure drop accompanies the post-compression phase. This drop is due to heat transfer phenomena between the reactive mixture at the heart of the combustion chamber, its walls, and the ambient air.

The drop in pressure is more remarkable for a pure methane mixture than for a CH_4/H_2 mixture. The induction period between the end of compression and maximum heat release decreases with the increase in hydrogen percentage. Consequently, heat transfer phenomena will have more time to occur with pure methane mixtures than with mixtures with a certain percentage of hydrogen.

The heat release Q calculation is carried out during the constant volume phase (piston at TDC). It is therefore assimilated to the pressure derivative. This amount of heat Q corresponds to the apparent heat, which integrates heat transfers. It is presented in Figure 21 for the different percentages of hydrogen at the end of compression temperature of 1000 K.

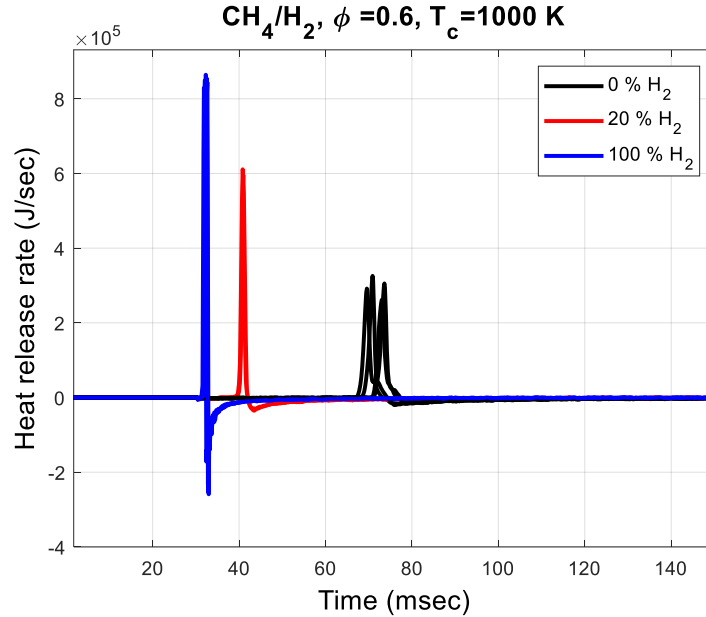


Figure 21: Heat release profile as a function of time for different percentages of H₂

As for the reproducibility of the tests, it is noted that the pressure curves overlap quite well, both in the compression and combustion phase and at the moment of self-ignition and end of combustion. The same is true for the heat release curves.

The curves shown in Figure 21 indicate a very high heat release rate at the time of self-ignition, which causes a rapid increase in pressure in the combustion chamber. From this point on, combustion is characterized by the significant rise in the cylinder pressure curve and the peak heat release. When the entire flammable mixture is burned, the rate of heat release decreases until the end of combustion.

As expected, the amount of heat released resulting from the combustion of the pure hydrogen mixture is greater than that of a 20% H₂ mixture. A 100% methane mixture has the lowest value.

Thus, the energy input resulting from the combustion of pure methane will be doubled following the addition of 20% hydrogen and then increased by 25% for 80% additional hydrogen.

The evolutions of the pressure and heat release profiles are shown in Figure 22 A and B, respectively, this time for the same reactive mixture of CH₄/H₂ with different end-of-compression temperatures.

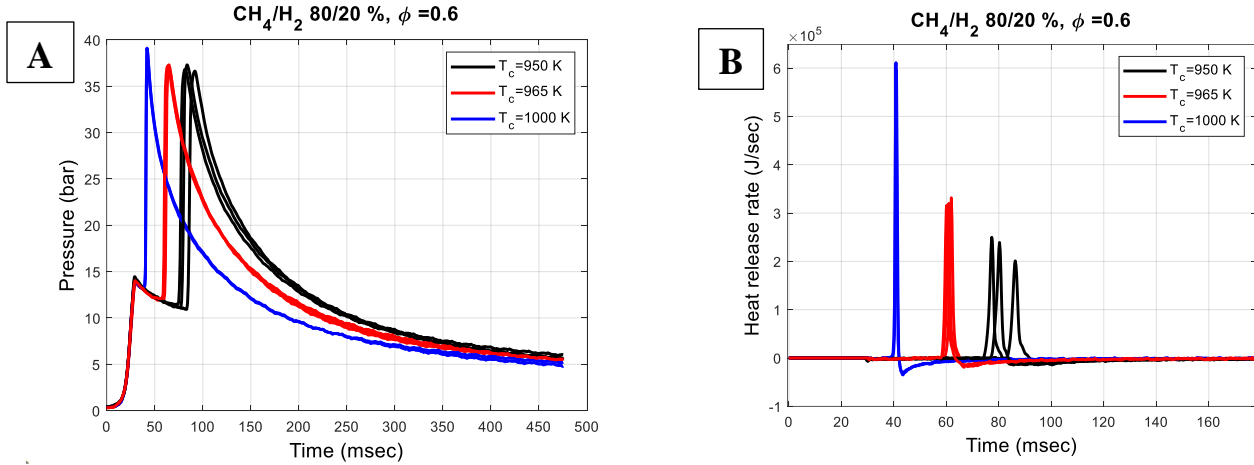


Figure 22 : Pressure and heat release profile as a function of time for different temperature values for H_2 - CH_4 mixture 20-80 %

Having the same hydrogen proportion, the different behaviors observed are largely a function of the temperature at the end of compression.

Combustion phase

In our study on the rapid compression machine, the auto-ignition delay is defined as the time between the end of compression and the maximum heat release.

For each of the studied mixtures, the standard deviation σ of ignition delay data was calculated. The definition of this calculated quantity is recalled in the following equation:

$$\sigma = \sqrt{\frac{1}{N} \sum_{i=1}^N (\tau_i - \bar{\tau})^2} \quad (III.1)$$

Where N represents the number of reproducibility tests from the same mixing vessel.

Figure 23 shows the evolution of the standard deviation of the ignition delay's data as a function of the end of compression temperatures for different $\text{CH}_4/\text{H}_2/\text{CO}_2/\text{CO}$ mixtures

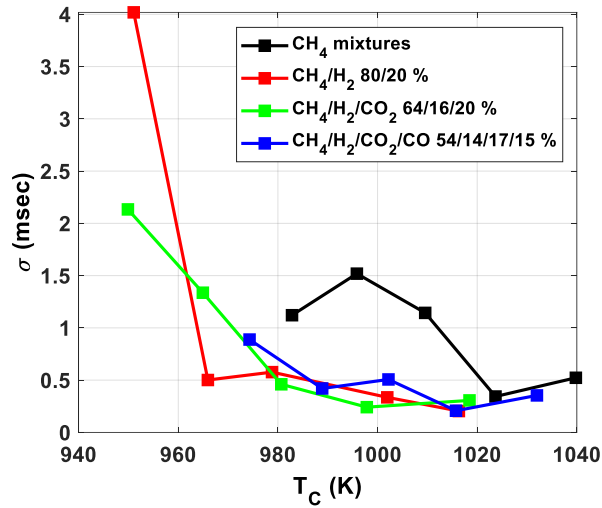


Figure 23 : Standard deviation of auto-ignition delay time for CH₄/H₂/CO₂/CO mixtures

As can be seen, the setting up of an experimental firing protocol ensured reproducibility during the combustion phase.

Moreover, the largest standard deviations are recorded at the lower end of compression temperatures. This logically corresponds to longer ignition delay times and therefore greater heat transfers, which leads to a greater dispersion of data. In fact, for longer delays, heat transfer in the combustion chamber has a longer time to establish themselves and can more strongly influence the delay from one piston firing to the other. At higher temperatures ($T_c > 960$ K), the standard deviation does not exceed 1.5 msec for all CH₄/H₂/CO₂/CO mixtures.

3.2. The auto-ignition of methane and hydrogen mixtures

The effects of methane and hydrogen on the lean homogeneous combustion will be studied for different CH₄/H₂ proportions. The experimental conditions of the studied mixtures are presented in Table 12.

Table 12: Experimental conditions corresponding to mixtures CH₄/H₂

| mixtures | CH ₄ (volume fraction %) | H ₂ (volume fraction %) | ϕ (-) | T _c (K) | P _c (bar) |
|----------|-------------------------------------|------------------------------------|------------|--------------------|----------------------|
| 1 | 0 | 100 | 0.6 | [940:1020] | 15 |
| 2 | 100 | 0 | 0.6 | [940:1020] | 15 |
| 3 | 90 | 10 | 0.6 | [940:1020] | 15 |
| 4 | 80 | 20 | 0.6 | [940:1020] | 15 |
| 5 | 70 | 30 | 0.6 | [940:1020] | 15 |
| 6 | 60 | 40 | 0.6 | [940:1020] | 15 |

The evolution of the self-ignition times of CH₄/H₂ mixtures and their standard deviations are shown in Figure 24 A and B as a function of the polytropic temperature and different percentages of hydrogen.

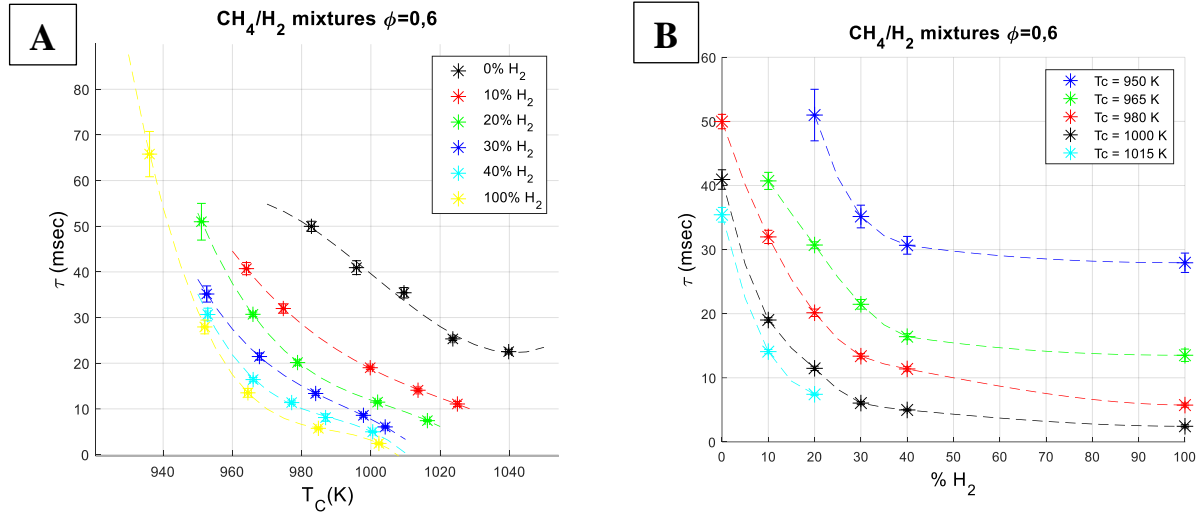


Figure 24 : Ignition delay times of CH₄/H₂ mixture as a function A. of temperature for different percentages of H₂ B. of H₂ percentages at different temperatures

As shown in these figures, the auto-ignition delay times decrease logarithmically with the addition of hydrogen; this decrease is more pronounced for the first 20% of hydrogen added to the methane mixture and becomes almost zero for percentages of hydrogen ranging from 40 to 100%. Thus, for a temperature of 1000 K, the addition of 10% H₂ is sufficient to reduce the ignition delay time by 57% and by 41% for a temperature of 980 K. Moreover, the addition of 20% H₂ is capable of reducing the ignition delay time of methane by 75% for a temperature of 1000 K and by 53% for a temperature of 980 K.

This means that the hydrogen effect becomes more important as the temperature rises and that a percentage of 10-20% of hydrogen is sufficient to predominate the self-ignition of methane. Consequently, in the following, the effect of carbon dioxide study will be carried on a CH₄/H₂ mixture that contains 20 % of hydrogen.

This promoting effect of hydrogen addition on methane combustion has been studied experimentally and numerically by several authors [71] [72] [73] [74]. It was explained by Gersen et al. [51] by the fact that the activation energy of hydrogen is two times higher than methane. ($E_a(\text{H}_2) = 2 \cdot E_a(\text{CH}_4)$).

It appears that the promoting effect of hydrogen on self-ignition is mainly due to its chemical kinetics. However, its kinetic effect is difficult to determine since its oxidation results from the formation of radicals, H, O, OH, and HO₂, and its behavior varies, whether at low or high temperatures.

For high temperatures, Huang et al. [75] studied the auto-ignition times of stoichiometric $\text{CH}_4/\text{H}_2/\text{air}$ mixtures in shock tubes for end pressures and temperatures of 16 to 40 bar and 1000 to 1300K, respectively. They explained the hydrogen promoting effect by two main causes:

- The decomposition of hydrogen into H radicals at high temperatures and their participation in the $\text{H} + \text{O}_2 \rightarrow \text{O} + \text{OH}$ reaction
- The rapid oxidation of hydrogen following the reaction $\text{OH} + \text{H}_2 \rightarrow \text{O} + \text{H}_2\text{O}$

Huang et al. [75] also explained that the slow $\text{CH}_3\text{O}_2 + \text{H}_2$ reaction is the reason why the effect of hydrogen is less important at low than at high temperatures. More recently, Liu et al. [76] conducted experiments on Tsinghua's MCR to determine the effects of hydrogen and carbon monoxide on the self-ignition delay and flame spread of methane for stoichiometric and rich mixtures at temperatures of 860-1080 K and a pressure of 20 bar. They found that the addition of H_2 has a small influence on the self-ignition delay for temperatures lower than 950 K and a large influence for temperatures above this value.

3.3. The auto-ignition of $\text{CH}_4/\text{H}_2/\text{CO}_2$ mixtures

It was found from the study of the effect of hydrogen on pure methane mixtures that a percentage of 10-20% of hydrogen is sufficient to predominate the self-ignition of methane. As a result, the 80/20 % CH_4/H_2 mixture was selected to carry on the effect of carbon dioxide study. The studied mixtures are presented in Table 13.

Table 13: Experimental conditions corresponding to mixtures $\text{CH}_4/\text{H}_2/\text{CO}_2$

| mixtures | CH_4 (volume fraction %) | H_2 (volume fraction %) | CO_2 (volume fraction %) | ϕ (-) | Tc (K) | Pc (bar) |
|----------|---|-------------------------------------|---|------------|------------|----------|
| 4 | 80 | 20 | 0 | 0.6 | [940:1020] | 15 |
| 7 | 72 | 18 | 10 | 0.6 | [940:1020] | 15 |
| 8 | 67.2 | 16.8 | 16 | 0.6 | [940:1020] | 15 |
| 9 | 64 | 16 | 20 | 0.6 | [940:1020] | 15 |
| 10 | 61.6 | 15.4 | 23 | 0.6 | [940:1020] | 15 |
| 11 | 56 | 14 | 30 | 0.6 | [940:1020] | 15 |
| 12 | 48 | 12 | 40 | 0.6 | [940:1020] | 15 |

The evolution of the self-ignition times of $\text{CH}_4/\text{H}_2/\text{CO}_2$ mixtures and their standard deviations are shown in Figure 25 as a function of the polytropic temperature and different percentages of carbon dioxide.

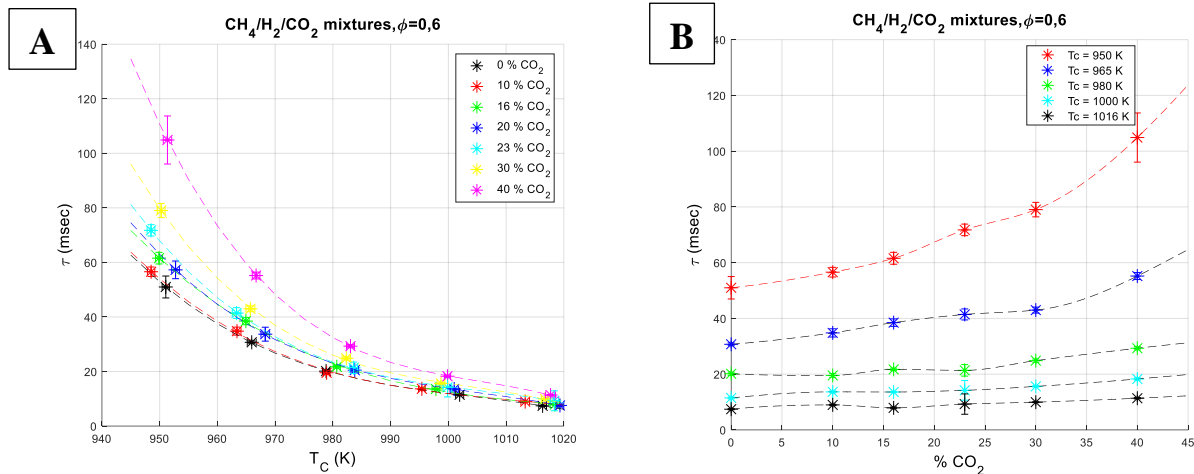


Figure 25 : Self-ignition time of the $\text{CH}_4/\text{H}_2/\text{CO}_2$ mixture A. for different percentages of CO_2 B. at different temperatures

As indicated in these figures, the self-ignition delay increases with the addition of carbon dioxide; this increase is almost negligible for CO_2 percentages below 20% and becomes increasingly important for higher percentages. Contrary to hydrogen, the effect of CO_2 is more important for low temperatures: Therefore, for a temperature of 1016 K, the addition of 40% CO_2 increases the values of the delays by a percentage of 53%, while this percentage becomes almost 100% for a temperature of 950 K.

Carbon dioxide is normally treated as a diluent due to its thermodynamic properties. Thereby, adding CO_2 reduces, on the one hand, the concentrations of reactive mixtures of methane and hydrogen and also the reactivity of the combustion. On the other hand, due to its high heat capacity, the combustion temperature will be reduced, which will consequently apply to the self-ignition time.

The greater effect of CO_2 on low rather than high temperatures may be due to the stronger effect of the chemical kinetics of hydrogen at high temperatures. However, this hypothesis is to be verified later in the numerical chapter by studying the effect of the addition of carbon dioxide on methane alone.

Similar to the hydrogen, several types of research were also carried out to study the effects of carbon dioxide on combustion [77]; [78]; [79]; [80]. However, the existing knowledge base of combustion kinetics in excess CO_2 covers only low pressures and low CO_2 .

Most literature studies for methane and hydrogen ignitions are with low CO_2 concentrations ($< 20\%$) [81]. Recently, Koroglu et al. [82] conducted measurements for mixtures of CH_4 , CO_2 , and O_2 in Argon bath gas at temperatures of 1577–2144 K, pressures of 0.53–4.4 atm, equivalence ratios of 0.5, 1, and 2, and CO_2 mole fractions of 0, 30, and 60%. Three different influences in regard to chemistry, collision efficiencies, and heat capacities were examined as a result of CO_2 addition into the gas mixtures. The chemistry and global collision efficiency effects were found to be negligibly small to alter the ignition delay time of methane for the experimental conditions of interest.

More important CO_2 addition was studied by Pryor et al. [83]; these authors conducted ignition delay time experiments behind reflected shock waves at pressures between 0.6 and 1.2 atm,

temperatures between 1650 and 2040 K, and an equivalence ratio equal to 1 for methane with CO₂ mole fraction varied between 0.0% to 89.5%. It was shown that for mixtures with large amounts of CO₂ dilution, the combustion process is no longer homogeneous, and the bifurcation of the shock wave is extreme, leading to increased uncertainty in the measurement.

3.4. The auto-ignition of CH₄/H₂/CO₂/CO mixtures

According to the study of the effect of carbon dioxide on CH₄/H₂ mixtures, it was found that for a percentage below 20%, the effect of carbon dioxide is negligible. Therefore, the 64/16/20 % CH₄/H₂/CO₂ mixture was selected to carry on the effect of the carbon monoxide study. The studied mixtures are presented in Table 14.

Table 14: Experimental conditions corresponding to mixtures CH₄/H₂/CO₂/CO

| mixtures | CH ₄ (volume fraction %) | H ₂ (volume fraction %) | CO ₂ (volume fraction %) | CO (volume fraction %) | T _c (K) | P _c (bar) |
|----------|-------------------------------------|------------------------------------|-------------------------------------|------------------------|--------------------|----------------------|
| 9 | 64 | 16 | 20 | 0 | [940:1020] | 15 |
| 13 | 54.4 | 13.6 | 17 | 15 | [940:1020] | 15 |
| 14 | 44.8 | 11.2 | 14 | 30 | [940:1020] | 15 |
| 15 | 35.2 | 8.8 | 11 | 45 | [940:1020] | 15 |
| 16 | 25.6 | 6.4 | 8 | 60 | [940:1020] | 15 |

The evolution of auto-ignition delay times of CH₄/H₂/CO₂/CO mixtures along with their standard deviations is presented in Figure 26 A and B, as a function of the end of compression temperature and carbon monoxide percentages.

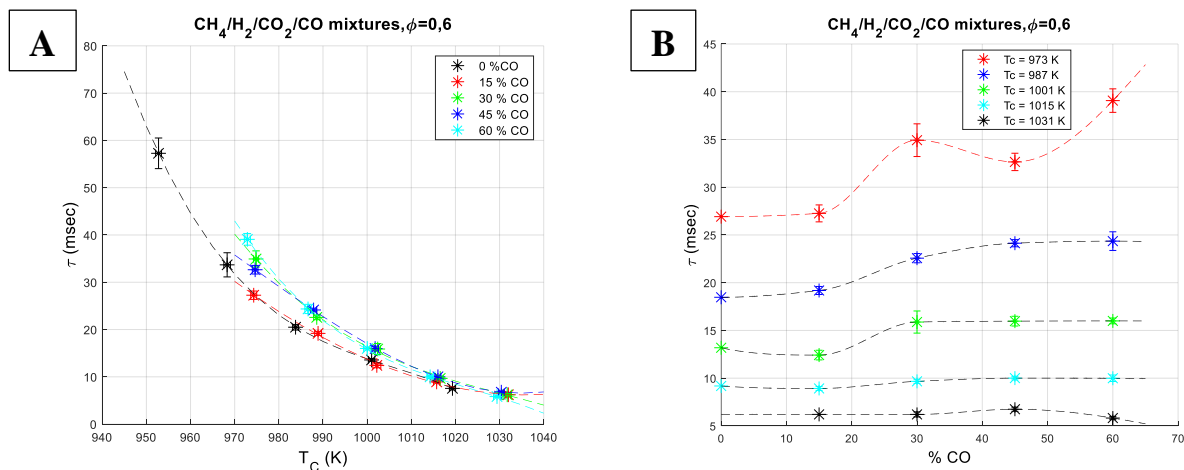


Figure 26: Auto-ignition delay times of CH₄/H₂/CO₂/CO mixtures A. for different percentages of CO; B. at different temperatures

As shown in these figures, CO has almost no effect on the auto-ignition times for high end-of-compression temperatures above 1015 K. However, for lower temperatures, its addition causes a

slight increase in the delays: for a temperature of 973 K, this increase is of the order of 45 % for an addition of 60 % CO and 31 % for a temperature of 987 K.

Several authors have studied the influence of carbon monoxide on synthesis gas combustion or methane mixtures. Although pure carbon monoxide is difficult to burn in air or oxygen, the presence of impurities containing hydrogen can significantly enhance the rate of CO oxidation reactions [84]. Kumar et al.[85] studied the effect of CO addition on ignition times for a range of hydrogen concentration. They found out that this effect of CO is dependent on the air to fuel ratio. For lean mixtures, there is an excess in oxygen quantity for CO oxidation, resulting in a significant increase in the concentration of chain carriers and energy release to the gas. As a result, the ignition time decreases with CO addition. These effects cause the induction time to decrease. Gersen et al. [64] studied the effects of carbon monoxide addition on the auto-ignition of CH₄ and CH₄/H₂ fuels at high pressure in an RCM and found that CO had little effect on ignition delay times of CH₄ and CH₄/H₂ fuels at pressures ranging from 20 to 80 atm and in the temperature range 900–1100 K.

Yu et al. [86] also found CO had no discernible effect on the ignition delay times of natural gas when CO proportions ranged from 10% to 30% in the reactant mixture and the equivalence ratio was held constant at $\phi = 1.0$. Liu et al. [76] studied the ignition of stoichiometric CH₄/air, CH₄/H₂/air, and CH₄/CO/air mixtures to investigate the effects of H₂ and CO addition on CH₄ ignition. The experimental results show that carbon monoxide (when included at 20% mole fraction of fuel) did not significantly affect the methane ignition delay time at any of the temperatures studied.

4. Conclusions on the experimental study of biofuel combustion

In this section, the combustion of biogas/syngas mixtures was studied on the SU RCM under HCCI conditions (low to intermediate temperatures 960-1040 K, lean mixtures $\phi=0.6$, high pressure (15 bar), and a dilution rate of 70 %).

Biogas/syngas mixtures are composed of methane, hydrogen, carbon dioxide, and carbon monoxide in order to detect the effects of parameters on the combustion process, fuel. At each time, only one percent was changed by fixing all the others. First of all, the effects of hydrogen were studied on methane mixtures. Then the effects of carbon dioxide on CH₄/H₂ mixtures were highlighted, followed by CO on CH₄/H₂/CO₂ mixtures.

The reproducibility tests study shows that the pressure curves overlap quite well, both in the compression and combustion phase and at the moment of self-ignition and end of combustion. The same is valid for the heat release curves. The slight pressure drop that accompanies the post-compression phase is majorly due to heat transfer phenomena between the reactive mixture at the core of the combustion chamber, its walls, and the ambient air. This drop is more remarkable for a pure methane mixture than for a CH₄/H₂ mixture. The induction period between the end of compression and maximum heat release decreases with increased hydrogen percentage. Consequently, heat transfer phenomena will have more time to occur with pure methane mixtures than with mixtures with a certain percentage of hydrogen.

Also, the largest standard deviations of ignition delays are recorded at the lower end of compression temperatures. This logically corresponds to longer ignition delay times and, therefore, greater heat transfers, which leads to a greater dispersion of data. In fact, for longer delays, heat transfer in the combustion chamber has a longer time to establish themselves and can more strongly influence the

delay from one piston firing to the other. At higher temperatures ($T_c > 960$ K), the standard deviation does not exceed 1.5 msec for all $\text{CH}_4/\text{H}_2/\text{CO}_2/\text{CO}$ mixtures.

For the study of CH_4/H_2 mixtures, results show that the auto-ignition delay times decrease with hydrogen's percentages in the fuel; the major reduction was observed for the first added hydrogen percentages. This percentage is dependent on the EOC temperature; 10% H_2 is sufficient to reduce the ignition delay time by 57% for a temperature of 1000 K, and 20% H_2 by 53% for a temperature of 980 K. Hence, 10-20% of hydrogen is sufficient to predominate methane's self-ignition and this effect is more important as the temperature rises. On the other hand, carbon dioxide is usually treated as a diluent due to its thermodynamic properties. Its impact was studied on a CH_4/H_2 mixture that contains 20 % of hydrogen. Due to the addition of carbon dioxide, the auto-ignition delay times increase; this can be majorly due to the reduction of the reactive mixture's concentrations and the combustion temperature because of the high heat capacity of CO_2 .

Furthermore, the increase in ignition delays becomes more critical for a CO_2 percentage above 20%. Moreover, its effects become more important for lower temperatures: for example, for a temperature of 1016 K, 40% CO_2 increases delay values by a percentage of 53%, while this percentage becomes almost 100% at 950 K. The more significant effect of CO_2 on low rather than high temperatures may be due to the more substantial impact of hydrogen's chemical kinetics at high temperatures. However, this hypothesis is to be verified later in the numerical chapter by studying the effect of carbon dioxide on methane alone.

Finally, the effects of CO on biogas/syngas mixtures were discussed. Results show that for temperatures above 1015 K, CO has almost no impact on the auto-ignition times. However, for lower temperatures below 1015 K, its addition induces a slight increase in the delays. For example, for a temperature of 973 K, this increase is of the order of 45 % for an addition of 60 % CO and 31% for a temperature of 987 K.

Key conclusions

- The reproducibility of the presented results is validated: pressure and the heat release curves overlap quite well, both in the compression and combustion phase and at the moment of self-ignition and end of combustion.
- The reproducibility was also validated for measured ignition delay times; deviations of ignition delays are recorded at the lower end of compression temperatures. This logically corresponds to longer ignition delay times and, therefore, greater heat transfers, which leads to a greater dispersion of data. In fact, for longer delays, heat transfer in the combustion chamber has a longer time to establish themselves and can more strongly influence the delay from one piston firing to the other.
- At higher temperatures ($T_c > 960$ K), the standard deviation does not exceed 1.5 msec for all $\text{CH}_4/\text{H}_2/\text{CO}_2/\text{CO}$ mixtures
- A slight pressure drop accompanies the post-compression phase. This drop is due to heat transfer phenomena between the reactive mixture at the heart of the combustion chamber, its walls, and the ambient air.
- 10-20% of hydrogen is sufficient to predominate methane's self-ignition
- the hydrogen effect becomes more important as the temperature rises

- Carbon dioxide increases the ignition delay times; this effect is almost negligible for CO₂ percentages below 20% and becomes increasingly important for higher percentages.
- The effect of CO₂ becomes more important at lower temperatures
- The carbon monoxide has no significant effect on the induction time of biofuel mixtures, especially at $T_c > 1015$ K. For lower temperatures, CO increases the ignition delay time slightly

5. Conclusions

The main objective of this chapter is to present the first results of the study of biogas/syngas mixtures using SU RCM. This study of the auto-ignition of these fuels also established the good reproducibility of the machine. As a result, biomass components (H₂, CO₂, CH₄, CO) on the auto-ignition delay times and thus on the combustion reactivity were discussed. The reproducibility of the presented results is validated: pressure and heat release curves. In the first part of this chapter, the SU rapid compression machine (SU RCM) was described briefly. The performance and reproducibility of the experimental setup were highlighted. Comparisons of self-ignition times measured by different authors have shown that the trends we observed were in accordance with those of literature. Nevertheless, disparities exist and can be due to the difference in designs and conception of each rapid compression machine. Thus, this can create different turbulence levels and heat transfers and can vary from one machine to another. Therefore, it will be interesting to characterize the impact that the geometry, varying from one RCM to another, will characterize for the following work. Thus, the geometry specific to each RCM leads to an evolution of the aerodynamic characteristics both during and after the compression. This means that the combustion occurs under completely different aerodynamic conditions, and therefore the heat loss at the wall of the chamber is different for each geometry. Another reason for these disparities is the difference in the methods used for calculating the end of compression temperature. It is shown that the polytropic assumption in terms of trends to the adiabatic core temperature of the other two RCMs, which highlights the difference in heat transfer from one RCM to another again.

The presented study mostly focused on the effects of the gas components on the combustion of biofuel mixtures. Results highlight the reactivity of hydrogen that was shown to predominate the methane auto-ignition for percentages of less than 20 %. This effect is highly dependent on the temperature as it was reduced at lower temperatures. The opposite effect is shown for carbon dioxide that reduces the reactivity of the mixture. Its effect is more important at low temperatures and higher CO₂ percentages (>20%). It seems that carbon dioxide does not contribute to the combustion reactions; it affects the combustion process through its thermal and dilution aspects. Carbon monoxide, on the other hand, has almost no effect on the auto-ignition times for EOC temperatures above 1015 K. However, for lower temperatures, its addition causes a slight increase in the delays. This study highlights the importance of mixing biogas/syngas regarding the degrading effects of carbon dioxide on the reactivity and the promoting effect of hydrogen.

This classic experimental study was based on the analysis of the evolution of pressure to better understand the combustion process. However, the pressure history does not highlight the possible predominance of a precise combustion mode, making the analysis insufficient to fundamentally characterize homogeneous combustion phenomenology.

Consequently, following this experimental approach, a more developed study will be carried out numerically on Chemkin-Pro and presented in chapter 3. The numerical study will better understand the physico-chemical phenomena by treating conditions difficult to achieve using the experimental setup. It will explain the chemical processes behind the observed component effects and study the effects of composition on other mixtures, as well as the effects of initial pressure, temperature, and equivalence ratio. The combination of the numerical and experimental results will create a database characterizing the physico-chemical aspects of the lean homogeneous combustion of biofuel mixtures.

Chapter 3:

A numerical study of the combustion of biogas/syngas mixtures under lean homogeneous conditions

Chapter 3

I. Introduction

In the previous chapter, the experimental study of biogas/syngas mixtures was performed using the rapid compression machine (SU RCM). As a result, the effects of biomass components (H_2 , CO_2 , CH_4 , CO) on the auto-ignition delay times and the combustion reactivity were discussed.

In this chapter, we will perform numerical analysis on Chemkin-Pro in order to understand the experimental results previously presented. The numerical study will better comprehend the physico-chemical phenomena by treating conditions challenging to achieve using the experimental setup. It will explain the chemical processes behind the observed component effects and extend the parametrical study to cover more parameters.

Due to the complexity of lean homogeneous combustion, several authors depicted the occurrence of multi- combustion regimes. As a result, the numerical study will be established on a simplified approach based on which the simulations will be modeled in two configurations: closed homogeneous reactor and laminar flame. The philosophy behind this simplified approach will be first presented.

Before proceeding with the numerical study, it is essential to select a suitable reaction mechanism based on which this part will be carried out. Several calculations of the auto-ignition times were performed with different chemical mechanisms and then compared with the measured experimental values. The mechanism allowing the closest delay possible to the experimental results (in terms of values as well as trends) will be used in the parametric analysis of both auto-ignition and propagating flame processes of biogas/syngas mixtures.

To better understand the duality between the physical and the chemical properties, non-dimensional numbers were studied in detail. Calculating them will allow the placing in the combustion diagram.

Following this study, we will have a complete and developed investigation on the effect of each variable (pressure, temperature, fuel concentrations, and equivalence ratio) on the parameters of combustion. The results will allow us to choose the most optimized fuel mixtures for both the auto-ignition and flame processes. Combining the numerical and experimental results will create a database characterizing the physico-chemical aspects of the lean homogeneous combustion of biofuel mixtures.

II. Simplified approach and simulation conditions

The explosive phenomenon studied previously cannot co-occur at each point in the considered volume unless the composition, the temperature, and the pressure have the same values, which can never really happen. This is related to several parameters, such as the temperature heterogeneities, heat loss, aerodynamics, and turbulence level induced in the combustion chamber.

As a result, the explosion arises at the central point, then invade the entire closed system where the fuel and the oxidizer are already mixed. The conditions of composition, temperature, and pressure around this central point must quickly lend themselves to the explosive phenomenon. In contrast,

the flame combustion occurs in a limited space, not the total volume of the system, after which, most often, it spreads.

Several authors have studied the effects of heterogeneities on the auto-ignition process. Chen et al.[87] studied the influence of temperature heterogeneities on the self-ignition and the development of constant volume combustion of a hydrogen/air mixture with an equivalence ratio of 0.1 using the two-dimensional Direct Numerical Simulation (DNS). Their attention focused on the transition from a regular deflagration regime to a subsonic propagation regime by spontaneous ignition. Combustion begins with self-ignition in the hottest part in the center of the zone and develops towards the coldest areas. As the combustion spreads, the fresh gases are compressed, increasing their reactivity, and consumed by the front flame. The propagation speed is always higher than the laminar deflagration speed. Thus, two modes of propagation can be highlighted: the propagation of a flame front and spontaneous self-ignition phenomena depending on the degree of heterogeneity in the combustion chamber.

Guibert et al.[88] also studied the effects of turbulence and thermal stratification on the auto-ignition of lean isooctane and propane mixtures on the SU RCM. They found that due to the temperature and concentration heterogeneities, or turbulence, kinetic interactions become essential during the combustion stages. Once initiated, the auto-ignition is likely to increase the level of inhomogeneity; the interaction of physics and kinetics phenomenon can introduce some intermediate combustion regimes (volumetric and front-like combustion modes).

This duality of the combustion regimes due to heterogeneities can be schematized in Figure 27.

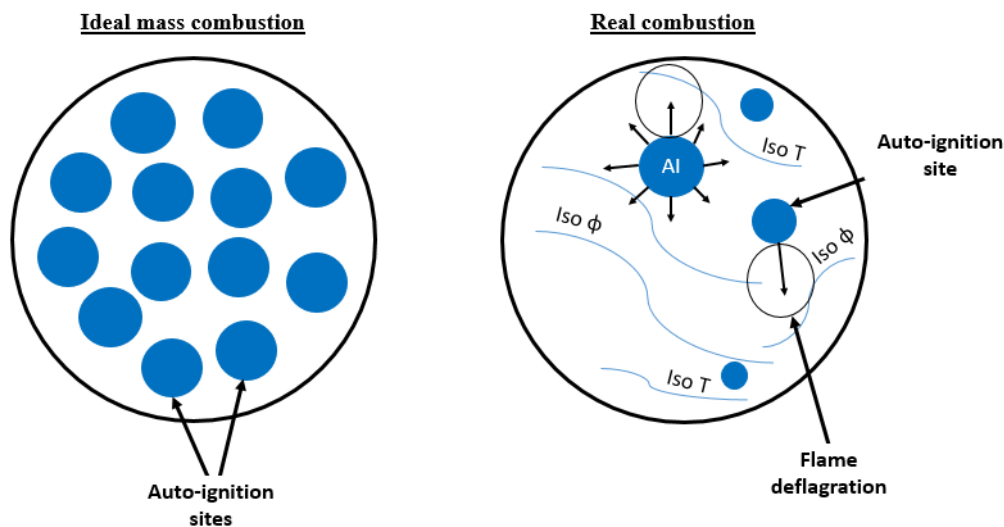


Figure 27 : Schema of the ideal and actual lean homogeneous combustion

This study aims to qualitatively analyze the combustion of biogas/syngas mixtures in lean homogeneous conditions. The results will give further initial information on the effect of each parameter of the initial conditions or the fuel composition on the combustion process. However, due to the coexistence of different combustion modes, it is clear that the study of the combustion in a homogeneous reactor is not representative of the actual process. A more globalizing approach should be considered.

Thus, the simplified approach that will be adapted in the following study consists of characterizing the combustion first in an adiabatic homogeneous reactor and second on a flame deflagration configuration.

This approach will provide a good understanding of the chemical aspects of the combustion, including the chemical reactions and the mixture reactivity, as well as the physical properties of the combustion characterized mostly by the flame speed, thickness, and stability. The pollutant emissions from each configuration will be calculated in order to highlight the suitable conditions that minimize these emissions.

Another simplified approach will be considered at the end of this chapter to account for the turbulence level in order to predict the effect of each parameter on the combustion mode. The turbulence characteristics were taken from a previous study on the characteristic properties of the flow on the SU rapid compression machine. The qualitative method for the prediction of the combustion phenomenology consists of the construction of the combustion diagram.

Therefore, by the end of this study, a database on the qualitative effects of the initial conditions (pressure and temperature), the percentage of dilution, the equivalence ratio, and the fuel composition on the combustion will be provided in auto-ignition and flame propagating configurations. Based on it, we will propose an optimized range of conditions that allow the minimization of the pollutant emissions in both configurations.

The studied conditions were mainly based on the experimental conditions but extended to allow the study of more parameters and understand the global effect of each of them (view Figure 28). This includes studying the chemical phenomenon and the contribution of these parameters on the combustion reaction, the flame speed, the pollutant emissions. The equivalence ratio is extended to cover lean, stoichiometric, and rich conditions majorly to highlight, in the end, the importance of lean mixtures in reducing pollutant emissions. The temperature range was chosen between 920 to 1040 K, and the pressure 10, 15, and 30 bar. The fuel composition extended to cover different possible mixtures. The simulation of these parameters on each configuration is studied in detail in this chapter.

However, it is crucial first to choose the chemical mechanism on which will be based all the numerical study.

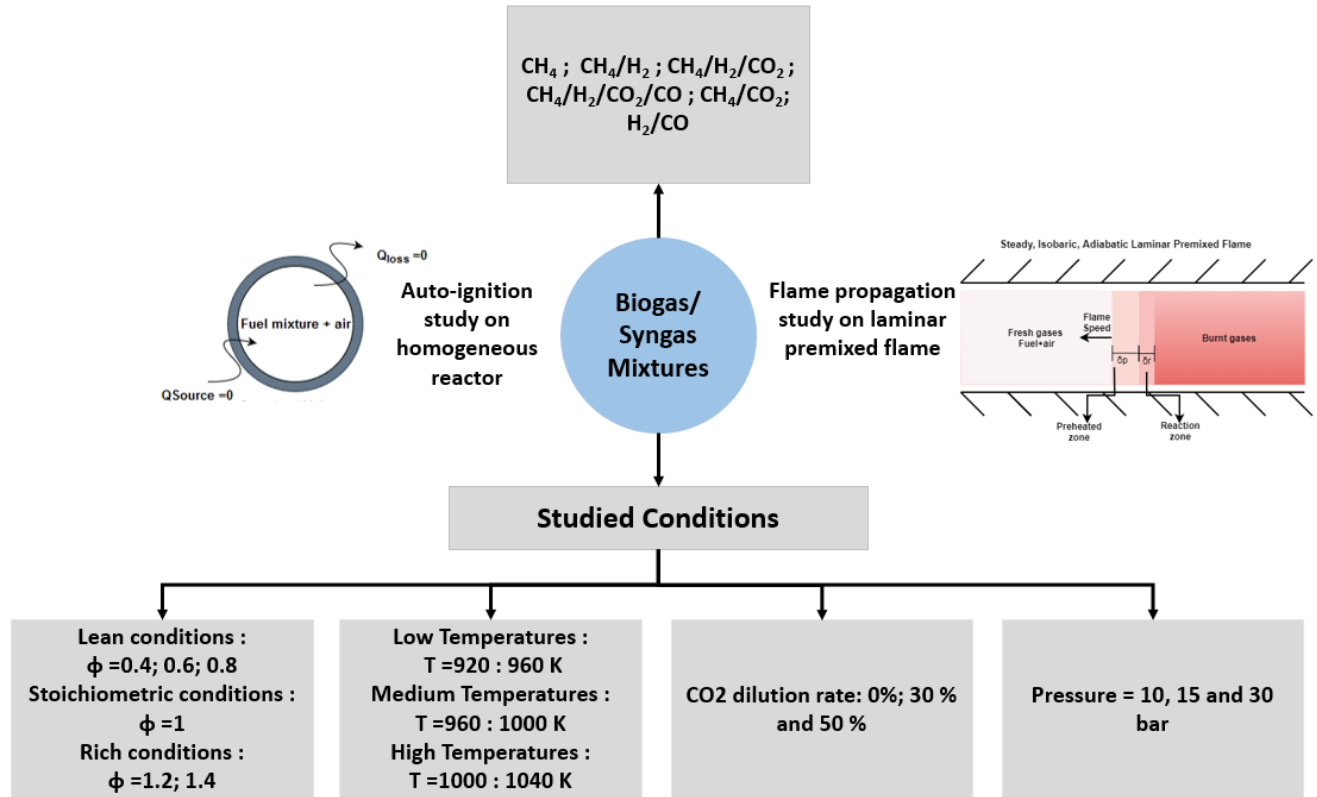


Figure 28: Simulation conditions of auto-ignition and propagating flame processes conducted on Chemkin-Pro

III. The selection of chemical mechanisms

Modeling the complex physical and chemical processes that occur during fuel combustion in industrial systems is one way to address the difficulties in understanding the uncertain behavior of combustion.

It greatly increases the reliability of predictions while significantly reducing experimental costs, highlighting the importance of such a strategy and, thus, computational fluid dynamics (CFD) simulations of real industrial systems. For combustion reactions in practical flames and closed homogeneous reactor, a single-step chemical reaction is not sufficient to describe the complex reactive process [89]. For example, a simple methane/air flame requires a minimum of tens of species and hundreds of reactions to describe the chemistry in the flame computationally. Therefore, chemical kinetic mechanisms are used to determine the reactions, transport, and thermodynamics of combustion. Their development became a considerably large area of research in the combustion community.

1. Definition and use of chemical mechanisms

The chemical mechanism describes the sequence of elementary steps that occurs while going from reactants to products. During this process, intermediate reactions are formed in one step and then consumed later in the reaction mechanism. On the other hand, the slowest step in the mechanism is called the rate-determining or rate-limiting step. The overall reaction rate is determined by the rates of the steps up to (and including) the rate-determining step.

In this section, the reaction mechanism that will be used in the following study in predicting the combustion process of biogas/syngas will be selected.

Numerous reaction mechanisms (global or reduced) were developed for studying the detailed combustion chemistry of mixtures containing CH₄, H₂, CO, and CO₂.

One of the most used chemical mechanisms in the literature is the Gas Research Institute mechanism "Grimech." It is a detailed chemical reaction mechanism essentially composed of a list of elementary chemical reactions and associated expressions of rate constants. Most of these reactions, as well as these constant rate parameters, are studied and measured in the laboratory [89, 90]. It is optimized to model natural gas flames and self-ignition. According to M. Fischer and X. Jiang [92], it is a widely used natural gas combustion model. Its performance concerning the combustion of carbon monoxide CO and hydrogen H₂ is similarly satisfying.

Improvements in this mechanism were made by updating the combustion kinetics according to the recent literature results. Some new and improved target experiments to the optimization, expanding the mechanism and target selection, and examining the sensitivity to the thermodynamics were included.

There are several versions of this mechanism, and each has a different number of reactions and species:

- Grimech 1.2 contains 177 reactions and 38 species.
- Grimech 2.11 contains 277 elementary chemical reactions of 49 species.
- Grimech 3.0 (1999) contains 325 elemental reactions with 53 species

The performance of this mechanism in predicting the ignition delay time and the flame speed of CH₄/H₂/CO₂/CO mixtures was validated by several authors in the literature, as shown in the table below.

Table 15: Validation of Grimech3.0 mechanism by some authors in the literature

| | Experimental setup | Mixtures | Pressure range (bar) | Temperature range (K) | ϕ (-) | Comments | Ref |
|-------------|----------------------|---|----------------------|-----------------------|------------|---|------|
| Grimech 3.0 | Shock tubes | CH ₄ H ₂ /air mixtures | 16 -40 | 1000-1300 | 1 | Good agreement with the measured results | [75] |
| | Shock tubes | CH ₄ /air mixtures | 1-10 | T 1000-2500 K | 0,1-5 | Good agreement with the measured results | [93] |
| | Laminar flame | CH ₄ /O ₂ mixtures | 1 | 298 K | 0.6-1.5 | Good agreement with the measured results | [19] |
| | Shock tubes | CH ₄ /O ₂ mixtures | 1-10 | 1420-1800 K | | Good agreement with the measured results | [19] |
| | Shock tubes | H ₂ -CO ₂ CH ₄ -CO ₂ | 1 -10 | 1500-2000 K | 0.5-2 | Good agreement with the measured results | [92] |
| | Laminar flame | CH ₄ /H ₂ /CO | 1 | 295 | 0.75-1.3 | Perform well lean mixtures, when ϕ higher than 1.1, numerical results deviate from the experimental measurements | [94] |
| | Shock tubes | CH ₄ /H ₂ | 5, 10, 20 | 1050-1820 | 0.5 | Discrepancies between measured and calculated delays increase with hydrogen content higher than 50% | [94] |
| | Bunsen burner method | CH ₄ /H ₂ | 1 | 298 | 0.5-1.3 | Discrepancies between measured and calculated delays increase with hydrogen content higher than 50% | [94] |
| | Bunsen burner method | H ₂ /CO | 1 | 295 K | 0.5-2 | Good agreement with the measurements except for lean CO ₂ diluted mixtures(under-prediction). Discrepancies +-12% for CO 75%. It decreases to 3% for 3% CO | [95] |

AramcoMech is another chemical mechanism widely used in the literature. It is a developed detailed chemical kinetic mechanism that characterizes the kinetic and thermochemical properties of various C1-C4 based hydrocarbon and oxygenated fuels over a wide range of experimental conditions. It was developed by the combustion chemistry center in NUI Galway and fully funded by Saudi Aramco.

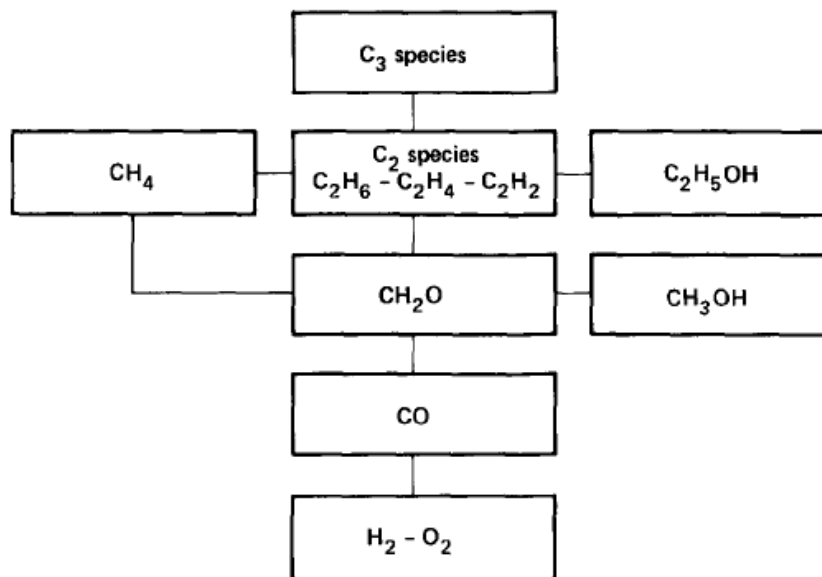


Figure 29: Hierarchical structure and overall interrelationships between oxidation mechanisms for simple hydrocarbon fuels [96]

AramcoMech-1.3 (2013) contains 766 reactions and 124 species [97]. It has been developed in a hierarchical way, starting with a sub mechanism H_2/O_2 , followed by a sub mechanism C1 and expanded by the inclusion of larger carbon species such as ethane, ethylene, acetylene, C3-C4, and oxygenated species [96] (view Figure 29).

AramcoMech3.0(2018) is an improved version based on the AramcoMech-1.3 mechanism. It contains 2716 reactions et 502 species [98].

Similar to Grimech3.0, these mechanisms have been validated against various experimental measurements, including data from shock tubes, rapid compression machines, flames, jet-stirred and plug-flow reactors (view Table 16).

Table 16 : Validation of AramcoMech mechanism by some authors in the literature

| | Experimental setup | Mixtures | Pressure range (bar) | Temperature range (K) | ϕ | Comments | Ref |
|-------------|----------------------|---|----------------------|-----------------------|---------|--|------|
| Aramco Mech | Bunsen burner method | H ₂ /CO/CO ₂ | 1 | 295 | 0.5-2 | Discrepancies 10% | [95] |
| | RCM MIT | CH ₄ /H ₂ /CO | 20-80 | 900-1100 | 0.5 - 1 | Good agreement with the measured results | [64] |
| | NUIG RCM | CH ₄ /H ₂ /O ₂ /diluted in air | 10-30 | 900-1500 | 0.5-1 | Good agreement with the measured results | [68] |
| | Shock tubes NUIG | CH ₄ /H ₂ /O ₂ /diluted in air | 10-30 | 900-1500 | 0.5-1 | Good agreement with the measured results | [68] |

Under lean and stoichiometric mixtures, it appears that the Aramco mechanism is the best predictor of biogas combustion. However, discrepancies still exist between the measured and calculated delays[99].

Furthermore, the Aramco mechanism involves too many species and unneeded reactions in the biogas/syngas combustion. To this end, a sensitivity analysis was conducted by Lee [99] to identify the cause of the observed discrepancies between the predicted results and the experimental data. He used the genetic algorithm (GA) to extract the relevant reactions of H₂/CO/CH₄/CO₂ mixtures. Based on this analysis, two new rate constants for the reactions $H + O_2 + (CO_2) \rightleftharpoons HO_2 + (CO_2)$ and $CH_4 + OH \rightleftharpoons CH_3 + H_2O$ were proposed; this change in rate constants reduced the observed discrepancies between the measured and calculated delay values. As a result of this study, 1777 unnecessary reactions in the NUIG mechanism were eliminated. The final reaction mechanism used to predict the chemical kinetics of biogas and syngas included 290 reactions and 72 species. This model was validated against a large number of experimental data, and excellent agreement was found between the predicted and experimental data. Therefore, this mechanism is currently the most appropriate chemical kinetic mechanism to predict the combustion properties of biogas accurately [99].

Many other reduced mechanisms were developed through the years for predicting the biogas/syngas combustion. However, the accuracy and reliability of a reduced model are always lower than that of the detailed parent mechanism [92].

Thus, among all the reaction mechanisms that predict relatively well, the combustion of mixtures containing CH₄/H₂/CO₂ /CO, Grimech3.0 (the most used mechanism), and AramcoMech (the best predictor of biogas composition) were selected to study their performances on the SU RCM experimental results. Two versions of Aramco will be used (Aramco1.2 and Aramco3.0) to check if the excessive numbers of reactions and species in AramcoMech3.0 are necessary or not for the combustion of biogas/syngas in lean conditions.

As a result, the performances of the three mechanisms: Grimech3.0, Aramco1.3, and Aramco 3.0 in the prediction of the auto-ignition delay times of biogas/syngas mixtures will be studied and

compared with the measured values. This comparison will decide which mechanism will be used for the computational study. Nevertheless, it is essential to choose first a suitable model for simulating the SU RCM experiments on Chemkin-Pro.

2. Closed homogeneous reactor

The modeling of the SU RCM experiments of biofuel mixtures was performed on Chemkin-Pro using a closed batch reactor.

In this type of reactor, there are no inlets or outlets flow during the period of interest. However, there may or may not be heat flow to the external environment. First, it is essential to choose a suitable model for simulating the auto-ignition phenomena. Numerous iterations were proposed to the adiabatic core HRM for simulating RCM experiments. These systems are inherently transient, where the chemical state changes as the production and destruction of species progress through a chemical reaction [100].

For example, Minetti et al. [101] used a frozen chemistry approximation. This assumption implies no appreciable composition or exothermicity changes, while the delay period is modeled under isochoric conditions. Hence, Curran et al. [102] demonstrated that under some conditions, chemical reactivity during piston compression can significantly alter the auto-ignition process and thus induction times, which motivates the account for gas reactivity during compression within the simulations. As a result, Mittal [68] proposed considering heat loss during and after the compression phase. This can be done by using the volume profile generated from the non-reactive pressure trace issued from the RCM in Chemkin simulations.

Based on these guidelines, three modeling approaches of the RCM experiments are investigated in this study.

Model 1 represents a simplified model where the effects of the reaction during compression are not included. Constant-volume and an adiabatic process are considered; the initial conditions are the effective temperature and pressure (at the end of compression) and the initial test gas composition [103].

In the second model (Model 2), the compression process of the core gases is simulated. This model assumes an adiabatic process with constant internal energy and a volume time-history that includes both the compression and post-compression processes. By involving the volume history during the compression phase in Chemkin calculation, the model simulates the actual compression and ignition processes of the core gas mixture.

In the third model (Model3), the compression process of the core gases is simulated as in Model 2. Unlike the first two models, the post-compression and the combustion processes are not adiabatic; convective heat transfer was simulated between the core gas and the chamber and the external air. The convective heat transfer coefficient was considered $20 \text{ W/m}^2/\text{K}$ (according to our experimental conditions), and the surface temperature is 328 K.

A comparison of the pressure curve of these three models is presented in Figure 30.

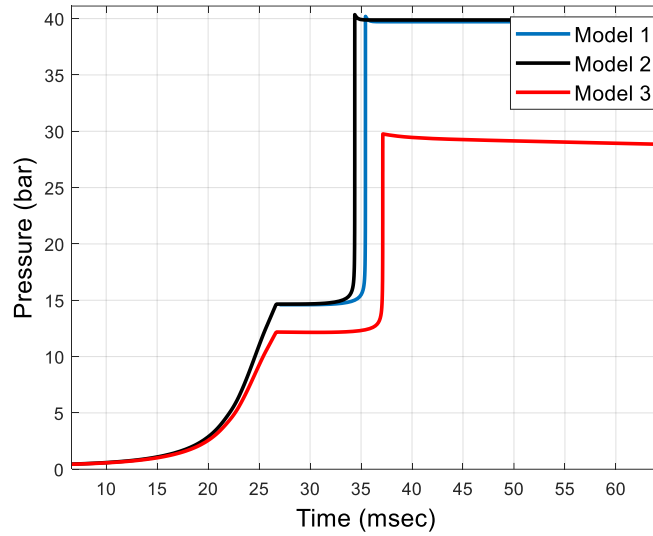


Figure 30 : Pressure curves of models 1, 2, and 3

It is observed that the pressure curves of models 1 and 2 are relatively similar; the results of the auto-ignition times are expected to be the same. However, the pressure curve of model 3 is considerably different; the simulation in this model seems to be highly dependent on the convective heat transfer coefficient. Also, the heat transfer is more applied to the compression phase than the post-compression phase because of the highest volume at the start of compression. Thus, model 3 will be excluded from this comparison.

Hence, Model 1 and 2 were simulated on Chemkin by the mean of the GriMech3.0, Aramco1.3, and Aramco 3.0 mechanism, for different mixtures: CH₄, CH₄/H₂, CH₄/H₂/CO₂, and CH₄/H₂/CO₂/CO. The simulation conditions as presented in Table 17.

Table 17: The simulation conditions of model 1 and 2 on different biogas/syngas mixtures

| | | CH ₄ Mixtures (%) | CH ₄ /H ₂ Mixtures (%) | CH ₄ /H ₂ /CO ₂ Mixtures (%) | CH ₄ /H ₂ /CO ₂ /CO Mixtures (%) | Conditions for all mixtures |
|--|---------|------------------------------------|--|---|---|--|
| GriMech3.0; AramcoMech1.3 and AramcoMech3.0 | Model 1 | 100 | 80/20 | 64/16/20 | 51/13/16/20 | Constant adiabatic volume, $P_0=P_c$ and $T_0=T_c$ |
| | Model 2 | 100 | 80/20 | 64/16/20 | 51/13/16/20 | compression phase (using SU RCM compression profile) + constant volume phase |

The comparison of the calculated ignition delay in models 1 and 2 for these mixtures and for the three chemical mechanisms is presented in Figure 31.

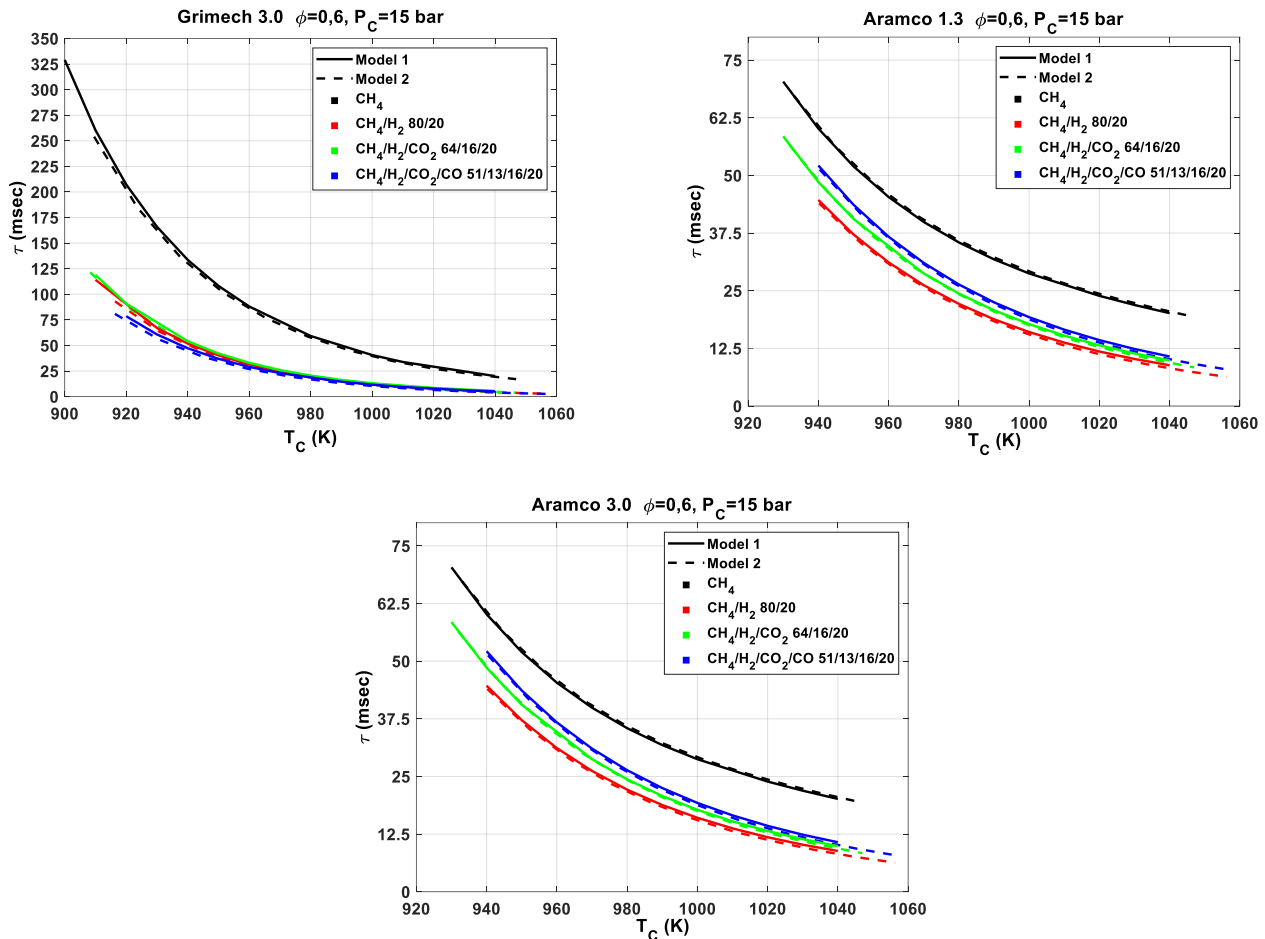


Figure 31: Auto-ignition delay times comparison for different biomass-derived fuel mixtures simulated by model 1, model 2, and model 3

The two models (Model 1 and Model 2) show similar results for the ignition delay times with a difference of less than 5%, and that for the three chemical mechanisms. The same difference is found in the study of He et al. [103].

Based on this good agreement between the two modeling approaches, the simplified Model 1 approach was considered sufficient for the evaluation of modeling trends. Thus, this model will be used in the following sections for the selection of the chemical mechanism, and then the study of the auto-ignition of biogas/syngas mixtures.

3. Comparison of calculated and measured ignition delay time for the selection of a chemical mechanism

As discussed previously, the performance of Grimech3.0, Aramco Mech 1.3, and Aramco Mech 3.0 in predicting the ignition delay times of biogas/syngas blends studied experimentally on the SU RCM will be carried out in this section.

We should clarify first that this study does not aim to validate the global performance of a chemical mechanism but to select the one that gives the closest trends to our studied mixtures. Thus, the comparison is highly dependent on:

- The temperature calculation in the experimental study
- The characteristics of the RCM
- The heat transfer conditions

The auto-ignition process of four types of biofuel mixtures performed on the SU RCM was simulated on a closed homogeneous reactor using model 1 and this for each mechanism. The selected mixtures are CH₄, CH₄/H₂ 80/20%, CH₄/H₂/CO₂ 64/16/20%, and CH₄/H₂/CO₂/CO 45/11/14/30 % (view Table 18).

Table 18: Biogas/syngas mixtures and their initial conditions used in the comparison of the three reaction mechanisms

| | CH ₄ Mixtures (% Vol.) | CH ₄ /H ₂ Mixtures (% Vol.) | CH ₄ /H ₂ /CO ₂ Mixtures (% Vol.) | CH ₄ /H ₂ /CO ₂ /CO Mixtures (% Vol.) | Conditions for all mixtures |
|-------------------|---|---|--|--|---|
| Grimech 3.0 | 100 | 80/20 | 64/16/20 | 45/11/14/30 | P _c =15 bar ϕ=0.6 T _c = [920 :1040] K |
| Aramco Mech1.3 | 100 | 80/20 | 64/16/20 | 45/11/14/30 | P _c =15 bar ϕ=0.6 T _c = [920 :1040] K |
| Aramco Mech3.0 | 100 | 80/20 | 64/16/20 | 45/11/14/30 | P _c =15 bar ϕ=0.6 T _c = [920:1040] K |

The results of this comparison are shown in Figure 32.

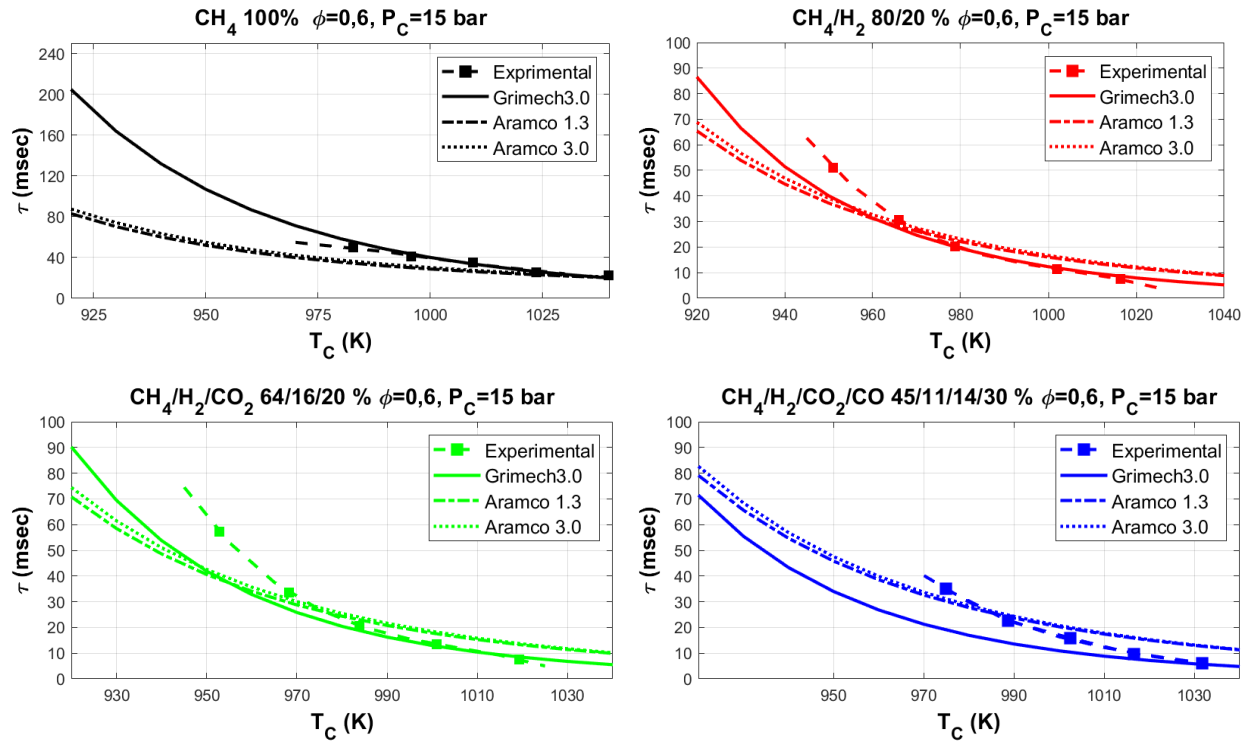


Figure 32: Comparison of measured and calculated auto-ignition delay times using different chemical mechanism and for different biomass derived -fuel mixtures

As can be seen, the numerical calculation of self-ignition delay values for the different mechanisms ranges from underestimation for low-temperature (~ 970 K) values to overestimation for intermediate to high temperatures (~ 970 K). This can be explained by the adiabatic assumption in the simulated model versus the heat transfer in the experimental setup. The Grimech3.0 mechanism best predicts self-ignition times for mixtures that do not contain carbon monoxide, in particular, methane mixtures in terms of trends.

A relative error of each mechanism should be calculated. This error represents the absolute deviation of the calculated ignition delay time in comparison to the measured values. It is defined as the ratio of the difference between the experimental and numerical delays to the experimentally measured auto-ignition delays:

$$\text{absolute deviation} = \frac{(\tau_{\text{measured}} - \tau_{\text{calculated}})}{\tau_{\text{measured}}} * 100 \quad (\text{III.1})$$

The evolution of the absolute deviations of the three reaction mechanisms as a function of temperature is presented in Figure 33.

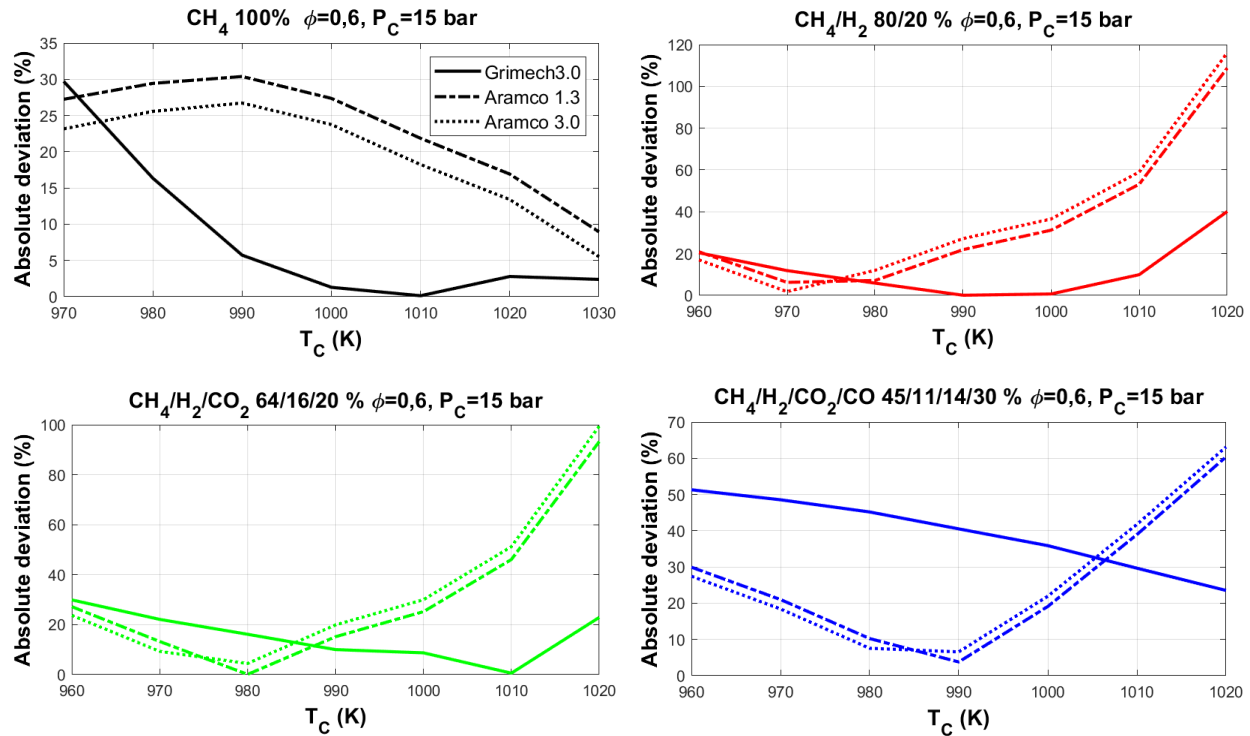


Figure 33: Standard deviation of auto-ignition delay times

Being designed to predict the self-ignition times of the natural gas mixture (consisting mainly of methane), grimech3.0 best predicts methane combustion with a maximum deviation of 30% for temperatures below 990 K and less than 5% for higher temperatures.

For other biofuel mixtures containing methane, hydrogen, and carbon dioxide, similar deviation values were shown at low temperatures below 960 K. In contrast, the performance of the two Aramco mechanisms deteriorates as the temperature increases. The grimech3.0, however, shows deviations lower than 40 %.

For mixtures containing carbon monoxide, the Grimech3.0 predicts the combustion process with a deviation between 20-50 %. On the other hand, the deviation is less than 30% for temperatures lower than 1050 K and > 30 % for higher temperatures. It is important to mention that Aramco mechanisms exhibit similar trends for all the studied mixtures, with small discrepancies in the calculated data.

The performance of the three chemical mechanisms in the prediction of the auto-ignition process of biofuel mixtures studied on the SU RCM is summarized and presented in Table 19.

Table 19: Absolute deviation of each chemical mechanism

| | CH ₄ mixtures | | CH ₄ /H ₂ mixtures | | CH ₄ /H ₂ /CO ₂ mixtures | | CH ₄ /H ₂ /CO ₂ /CO mixtures | |
|----------------|--------------------------|--------|--|------------|---|------------|---|-----------|
| | T<990 K | T>990K | T<980K | T>980 K | T<990K | T>990 K | T<1005 K | T>1005 K |
| GriMech3.0 | [5-30] % | <5% | < 20% | <40% | <30% | <20% | [40-50] % | [20-40] % |
| AramcoMech 1.3 | [25-30] % | <30% | < 20% | [20-100] % | <30% | [20-100] % | <30% | [10-60] % |
| AramcoMech 3.0 | [23-27] % | <30% | < 20% | [20-100] % | <30% | [20-100] % | <30% | [10-60] % |

Aramco Mechanisms show a better estimation of the combustion process of biofuel containing carbon monoxide for temperatures lower than 1050 K. However, for all the other conditions, the percentage of the deviation is less important in Grimech3.0 than in Aramco mechanisms.

As the size of the fuel molecule or the number of species making up the fuel increases, so does the size and the complexity of the chemical kinetics mechanism. Therefore, in terms of computational time and size and the trends of the time versus temperature, the GriMech3.0 reaction mechanism will be used in the following chapter to study the combustion of biogas/syngas mixtures under lean homogeneous conditions.

Nevertheless, it was shown that Grimech3.0 over-predicts the auto-ignition of the effect of carbon monoxide on biogas/syngas mixtures. According to the experimental results, the carbon monoxide has no significant effects on the combustion of biofuel mixtures under lean conditions; it can contribute to a slight increase in the auto-ignition delay time at lower temperatures. These effects were also validated by several authors in the literature and by other chemical mechanisms. On the other hand, according to Grimech3.0, carbon monoxide promotes the reactivity of the combustion by decreasing the ignition delay times. The reduction of ignition delay times was estimated to nearly 17% for an increase of 80% of carbon monoxide. Even though this reduction is quite small regarding the high percentage of carbon monoxide, it cannot be disregarded. Therefore, only for the study of the effect of carbon monoxide on the reactivity of biofuel combustion, AramcoMech (version 1.3 for less computation time) will be used to explain the chemical reactions induced by the addition of carbon monoxide.

The key ideas in this paragraph

- Three modeling approaches of the RCM experiments were investigated:
 - In Model 1: A constant-volume and an adiabatic combustion process are assumed where the initial conditions are the effective temperature and pressure, and the initial test gas composition
 - In Model 2: the adiabatic compression and combustion processes of the core gases are simulated.
 - In Model 3: the compression and combustion processes of the core gases are simulated with heat transfer assumption.
- Model 3 overestimates the ignition-delay times in comparison to the other two models. Since this model is strongly dependent on the convective heat transfer coefficient, it will not be used in the following study.
- Model 1 and Model 2 show similar results for the ignition delay times with a difference of less than 5%.
- The simplified Model 1 will be used in this chapter for the simulation of the auto-ignition process
- A comparison of the performances of the Aramco mechanisms and GriMech3.0 was carried out in this section to choose the most suitable mechanism to carry on the numerical study
- The comparison is highly dependent on the experimental temperature calculation at the end of compression, the geometry and aerodynamics of the RCM, and the heat loss; therefore, this study is not a validation of the performance of a certain mechanism
- According to this study, Grimech3.0 was shown to predict better (in term of trends and values) the combustion of pure CH₄ mixtures, CH₄/H₂ mixtures for temperature higher than 975 K, CH₄/H₂/CO₂ mixtures for temperature higher than 985 K, and CH₄/H₂/CO₂/CO mixtures for temperatures higher than 1010 K.
- AramcoMech 1.3 and AramcoMech 3.0 share the same trends for all the studied mixtures; there are small discrepancies in the calculated ignition times for each mechanism.
- GriMech3.0 over predicts the effect of CO on the biofuel combustion; the addition of carbon monoxide to the reactive mixtures decreases the ignition delay time. This is the opposite of the experimental trends.
- GriMech3.0 will be used in this chapter to study the effects of initial conditions and fuel composition on the combustion process.
- Only the effects of carbon monoxide on the auto-ignition of biofuel will be studied using AramcoMech 1.3.

IV. Approach I: Closed homogeneous reactor

Theoretically, combustion in the HCCI mode is a mass self-ignition; when the homogeneous reactive mixture is heated to a temperature greater than or equal to its self-ignition temperature AIT, the explosion will occur throughout the volume sometime after this temperature is reached.

However, heterogeneities in the combustion chamber cause the combustion to be initiated by a self-ignition core that is more reactive than the rest of the mixture and develops in a non-uniform or deflagrating manner. These heterogeneities typically result from a combination of physico-chemical phenomena such as heat losses that induce temperature gradients [33], complex fluid dynamics, and turbulent fluctuations [34].

Based on the simplified approach introduced at the beginning of this chapter, the first step in the lean homogeneous combustion characterization is to study the auto-ignition process.

Hence, a numerical study will be carried out on Chemkin Pro to study the auto-ignition phenomenon using the closed homogeneous reactor. Thus, a parametrical study on the effect of the initial conditions on the combustion properties will be studied in the following section. Different compositions of biofuel mixtures mainly consistent with methane, hydrogen, carbon dioxide, and carbon monoxide will be tested. The reactivity of these mixtures for different initial conditions will be examined by analyzing the chemical reactions that occur during the auto-ignition process. After that, the produced pollutant emissions of the combustion will be calculated for different initial configurations.

At the end of this study, we will propose an optimized range of conditions that minimize pollutant emissions while maintaining a specific reactivity.

1. Simulated conditions and assumptions

The numerical simulation on Chemkin-Pro of the auto-ignition times of the biomass-derived fuel mixtures is performed under the assumption of an adiabatic homogeneous reactor, as shown in Figure 34.

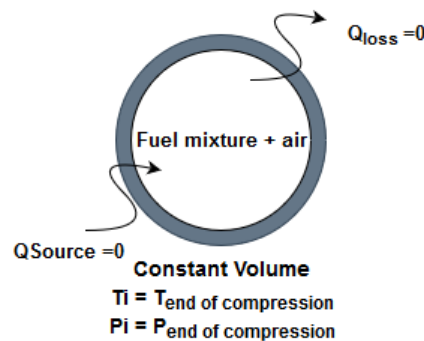
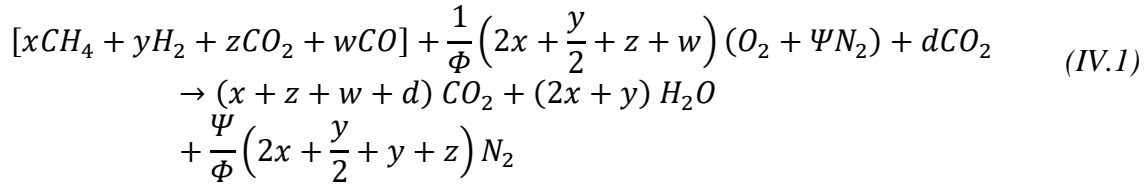


Figure 34: Closed homogeneous reactor

As found in the previous section, modeling the auto-ignition with or without the compression phase does not influence the ignition delay times by more than 5%. Thus, in the following, the adiabatic process of auto-ignition will occur in a constant-volume where the initial conditions are the effective temperature and pressure and the initial test gas composition.

It is essential to mention that these assumptions do not represent real-life equipment. Therefore, this section aims to understand the chemical behavior of the auto-ignition of biogas/syngas mixtures, explain the experimental results obtained on the SU RCM, and extend the parametric study on the auto-ignition process.

The complete combustion of biofuel and air (21 % oxygen O₂ and 79% nitrogen N₂) mixtures produce mainly water vapor H₂O and Carbon dioxide CO₂, through the balanced equation (IV.1):



Ψ represents the ratio between nitrogen and oxygen composition in the ambient air. It's equal to 3.76 in normal conditions.

Φ represents the equivalence ratio is defined as:

$$\Phi = \frac{(n_{fuel}/n_{oxygen})_{real\ conditions}}{(n_{fuel}/n_{oxygen})_{stoichiometric}} \quad (IV.2)$$

$\Phi > 1$ is referred to as rich mixtures whereas $\Phi < 1$ is referred to as lean mixtures.

The process of self-ignition combustion gives rise to many radical species. Therefore, chemical kinetics modeling is complicated by a large number of species and the many chemical reactions associated with them.

Indeed, the main compounds that govern self-ignition in HCCI mode are normally: H, OH, H₂O₂, and HO₂ (hydrogen, hydroxyl, hydrogen peroxide, and hydro-peroxide, respectively): During the compression phase, H₂O₂ and HO₂ concentrations increase progressively with increasing pressure and temperature. These two radicals also control the reactions at low temperatures (cold flame reactions)[104].

The evolution of the molar fractions of the major present species is presented in Figure 35 as a function of post-compression time for biofuel mixture subjected to a temperature and a pressure of 960 K and 15 bar, respectively.

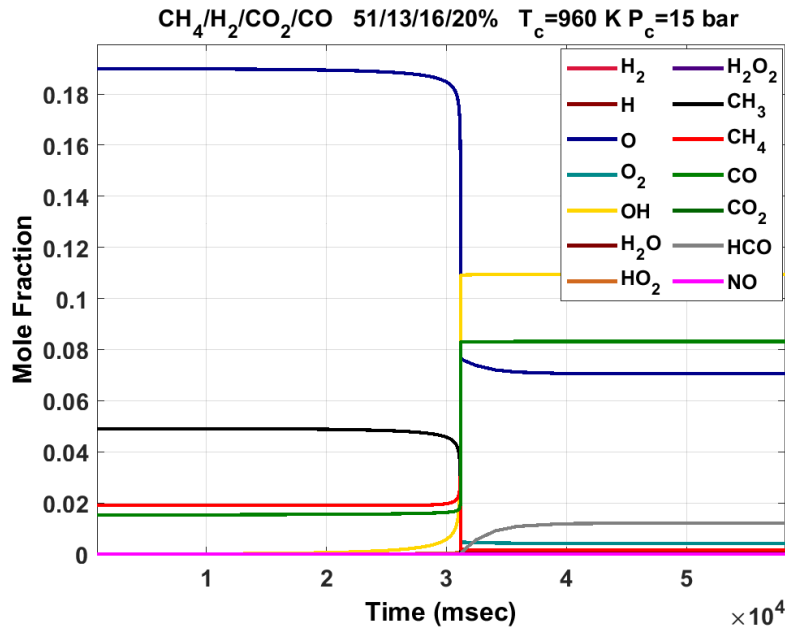


Figure 35: The molar fraction of created and consumed species due to the combustion of $\text{CH}_4/\text{H}_2/\text{CO}_2/\text{CO}$ mixtures

The activation energies of the chemical reactions associated with these species are high, and the amount of radicals created is low. The radicals can then react with the fuel or other intermediate molecules to multiply. This step is called branching. The activation energies of the reactions corresponding to branching are lower than those of the initiation. The next phase is propagation; it is associated with the release of heat during oxidation. These reactions are very exothermic. Finally, the termination reactions, which have zero activation energy, are responsible for the disappearance of the radicals. During this phase, the radicals react with each other, and final reaction products are formed.

It is the initiation and the succession of these chemical reactions that will define the ignition process, and therefore the auto-ignition delay time.

2. Auto-ignition delay time and temperature

Typically, the auto-ignition of a gas mixture occurs when the mixture ignites spontaneously in the absence of an external ignition source and after reaching its self-ignition temperature [105]. The self-ignition temperature (AIT) of a reactive gas mixture is, by definition, the lowest temperature at which the entire amount of a premixed gas self-ignites spontaneously.

The auto-ignition temperature is an important parameter that indicates the reactivity of the gas mixture. It is primarily influenced by various parameters such as pressure, vessel shape, volume, and the concentration of reactants and diluents, and others. It was also calculated on the closed homogeneous model described previously with an adiabatic assumption, the case of an ideal auto-ignition without heat exchange with the outside.

In order to determine this parameter, the simulations were initially carried out over a wide range of the end of compression temperatures to find approximately the minimum temperature needed to induce the auto-ignition of the mixture. We note that the ignition criterion used in our numerical study is the appearance of a temperature peak (as a result of pressure) within a maximum delay of

1 second. A second simulation is then carried out on a more refined range around the auto-ignition temperature found in the first simulation (with an error range $[-1.5;1.5]$ K).

In the experimental study of the biofuel mixtures combustion conducted on the SU RCM in the previous chapter, only the fuel composition effects on the auto-ignition delay time were determined in limited conditions. The following paragraph will determine the influence of the initial conditions and fuel composition on the auto-ignition delay and/or temperature. This can be a good indicator of their impact on the reactivity of the combustion.

Prior to the parametric study, we note that when studying the effects of pressure, temperature or equivalence ratios, four biogas/syngas mixtures are normally considered: CH_4 ; CH_4/H_2 80/20 %; $\text{CH}_4/\text{H}_2/\text{CO}_2$ 64/16/20 %; and $\text{CH}_4/\text{H}_2/\text{CO}_2/\text{CO}$ 51/13/16/20 %. These mixtures correspond to the experimental study conducted in chapter 2, and using them will allow the homogenization of the studied data. In other words, we could eventually select other mixtures, but our purpose is to give a qualitative database on the effect of each parameter.

2.1. Influence of the pressure and temperature

In order to study the influence of pressure and temperature at the end of compression on the auto-ignition of a reactive gas mixture, several simulations were carried out on Chemkin with different values of pressures: 10, 15, and 30 bars, and temperatures: 900-1100 K respectively.

The evolution of the auto-ignition delay times of the different biofuel lean mixtures ($\phi=0.6$) at $T_c=960$ K with the end-of-compression pressure is presented in Figure 36.

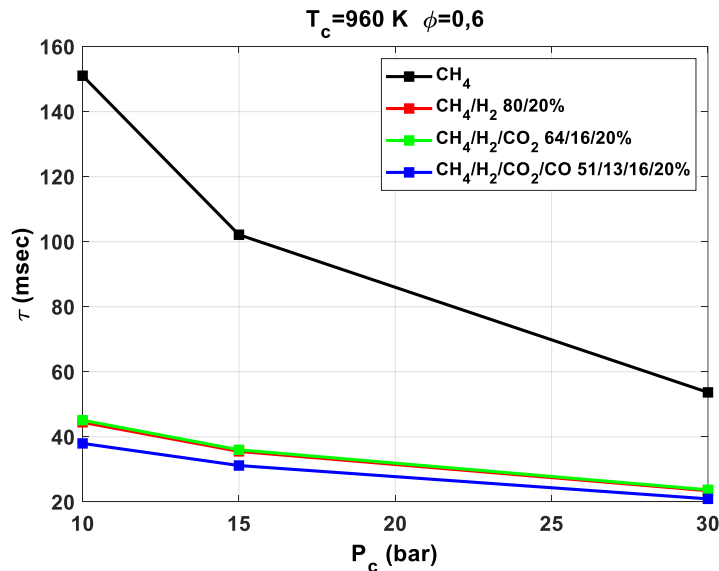


Figure 36: Auto-ignition delay time as a function of the end-of-compression pressure for different biomass-derived fuel mixtures

It is important to point out that increasing the end-of-compression pressure reduces the self-ignition time. The step of this reduction decreases with increasing pressure: it is more important when going from 10 to 15 bars than from 15 to 30 bars. It is also more important for pure methane mixture than other biofuel mixtures.

This effect of pressure on the reactivity can be explained by the proportionality between pressure and temperature at a constant volume. In fact, the self-ignition temperature of a reactive gas mixture is, by definition, the lowest temperature needed for its spontaneous auto-ignition. This temperature depends on the initial conditions of pressure, temperature, fuel composition, and air to fuel ratio.

Since reaction rates change with pressure, the auto-ignition temperature is also a function of the system pressure [106]; as the pressure increases at a constant volume, the reaction rate increases. Moreover, the molecules become closer one to another, which results in a more reactive mixture that requires lower auto-ignition temperature, as shown in Figure 37.

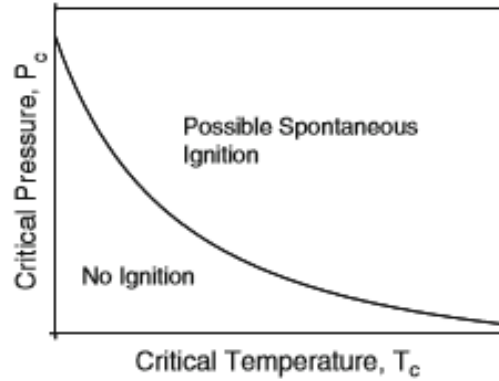


Figure 37: Critical pressure versus temperature. Ignition is possible in the region above the curve for combustion chemistry when the global order is greater than 1 [106]

As for the effects of temperature, the evolutions of the auto-ignition delay times of the different biofuel lean mixtures ($\phi=0.6$) with the end-of-compression temperature are shown in Figure 38.

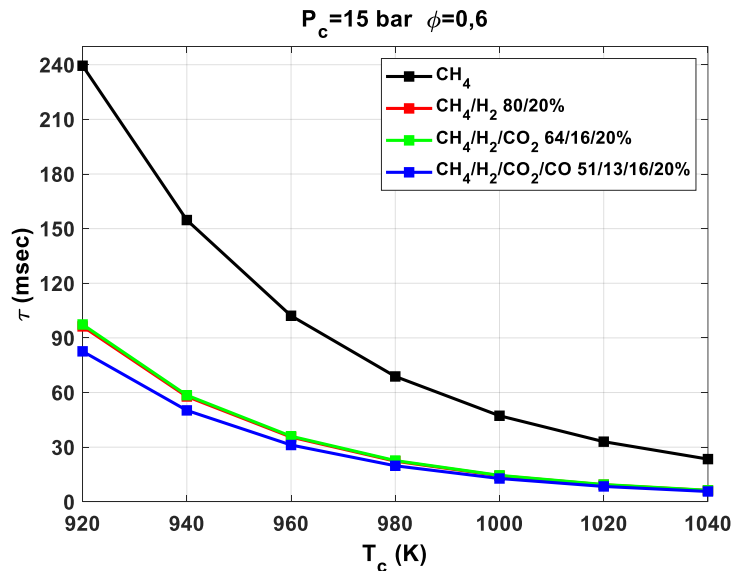


Figure 38: Auto-ignition delay time as a function of the end of compression temperature for different biomass-derived fuel mixtures

Similar to the effects of pressure, the increase at the end of compression temperature reduces self-ignition times. This exponential reduction can be explained by the sensitivity analysis of reactive radicals.

Sensitivity analysis of a solution allows a quantitative understanding of how the solution depends on the various parameters contained in a model. The computationally efficient sensitivity analysis methods exploit the fact that the differential equations describing the sensitivity coefficients are linear, regardless of any non-linearities in the model problem itself. The calculations and definitions of sensitivity analysis in general and in Chemkin particularly are presented in detail in Appendix Chapter 3.

The main radical species that govern the auto-ignition in HCCI mode are normally: H, OH, H₂O₂, and HO₂ (hydrogen, hydroxyl, hydrogen peroxide and hydro-peroxide respectively). So that in shock tube calculations, the auto-ignition delay time is determined by the necessary time to have a peak production of radical OH.

From this assumption, OH sensitivity for a biofuel mixture (H₂/CH₄/CO₂/CO) was represented as a function of the combustion time process for different end of compression temperature in Figure 39.

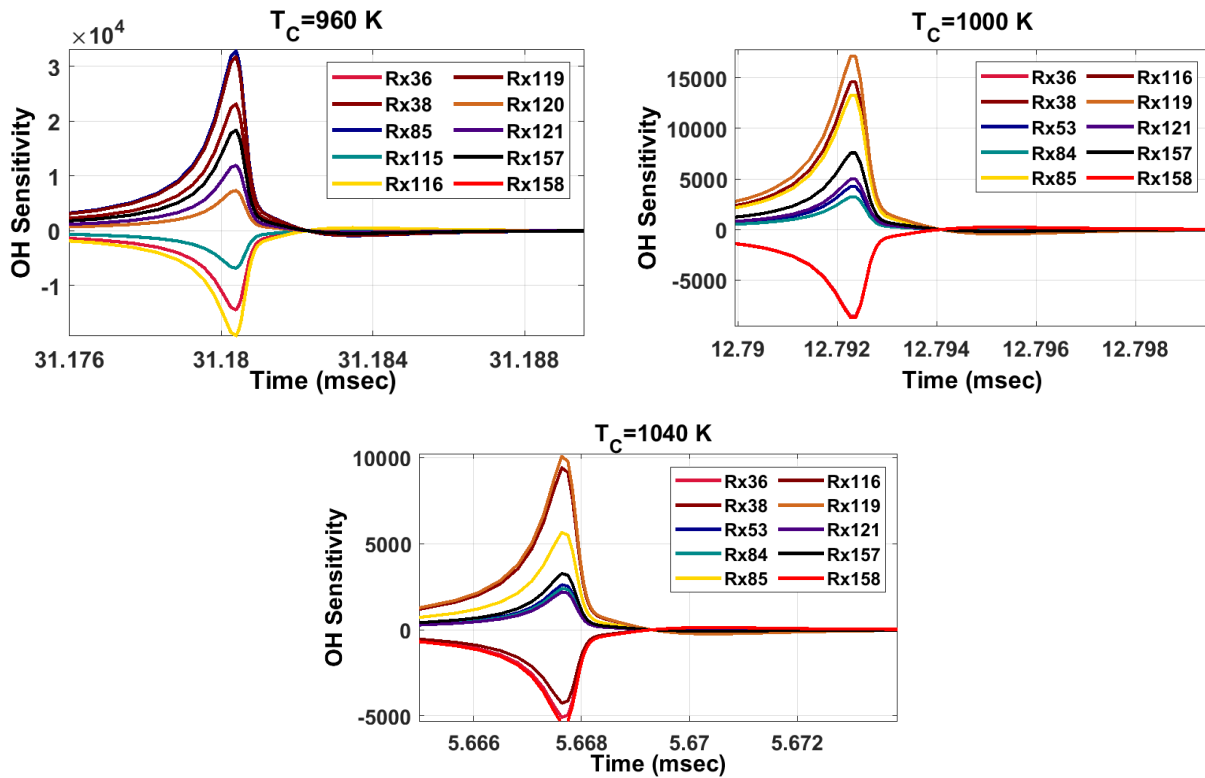


Figure 39: OH sensitivity as a function of time and temperature

Reactions that promote inflammation are those that lead to the accumulation of radical concentrations sufficient to initiate and maintain a rapid response. Inhibitory reactions are those

that lead to radical termination. Reactions of secondary importance are those that convert relatively non-reactive radicals, such as methyl CH_3 and hydroperoxyl HO_2 , into reactive species, such as hydrogen atoms[107].

For all the presented temperatures, three reactions are the most promoting of OH production:



And the three most inhibiting reaction are:



(R38) is a chain branching reaction, (R85) is an initiation reaction, (R119) and (R36) are both chain propagating reactions and finally (R116) and (R158) are chain-terminating reactions.

These reactions are common for all temperatures, but their sensitivity values are different.

The highest the temperature of the end of compression is, the less are these sensitivity values for all the reactions; in particular inhibiting reactions such as the reaction of recombination of two methyl radicals to produce inert ethane will have less effect on OH consumption and therefore on the reactivity of the mixture.

These effect of pressure and temperature at the end of compression on the reactivity of reactive gas mixtures has been verified by several experimental works carried out on a rapid compression machine by Healy et al. [108], Burke et al. [109], and Pounkin[53].

2.2. Influence of the equivalence ratio

The equivalence ratio ϕ represents the actual fuel/oxidant ratio on stoichiometric conditions (IV.2).

The influence of ϕ on the self-ignition of different biofuel mixtures is studied and presented in Figure 40.

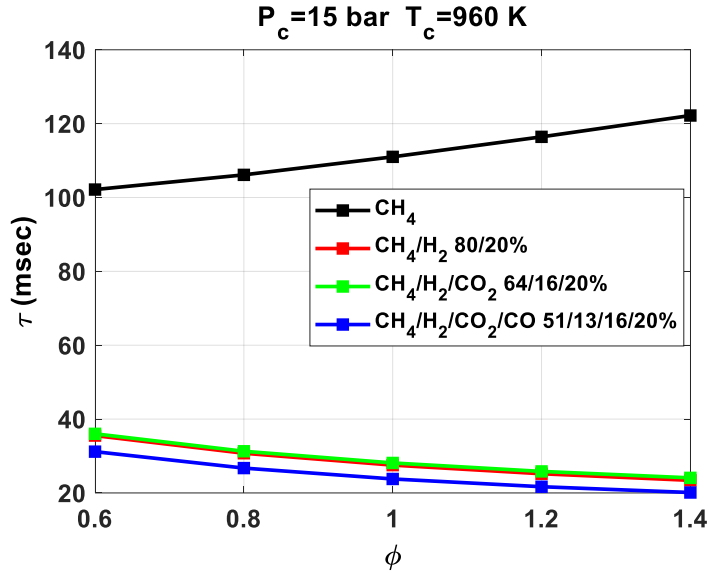


Figure 40: Auto-ignition delay time as a function of the equivalence ratio of different biomass-derived fuel mixtures

According to this study, the evolutions of the self-ignition times with ϕ are almost linear. On the other hand, two effects of the equivalence ratio are encountered:

- For a pure mixture of methane, the increase in the equivalence ratio leads to the increase of self-ignition times and therefore a decrease in the mixture's reactivity
- For other biofuel mixtures: the increase in the equivalence ratio leads to the decrease of self-ignition times and therefore an increase in the mixture's reactivity

This bipolar effect of the equivalence ratio was also studied by He et al. [110] and Kong et al [111]. Furthermore, Burke et al. [109] studied methane self-ignition and found that for high temperatures ($>1350 \text{ K}$), the equivalence ratio effect is reversed; as ϕ increases, the self-ignition time decreases.

For a better understanding of this effect, a chemical kinetic study is addressed. The normalized brute force sensitivity of methane/air mixtures for different equivalence ratios is firstly presented in Figure 41.

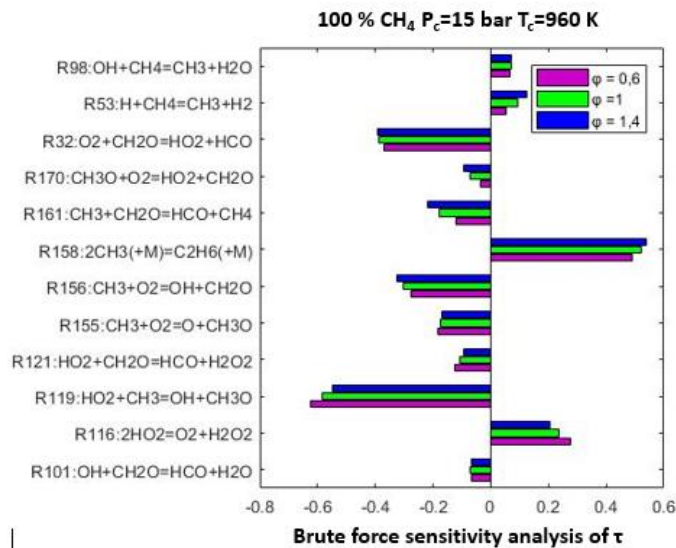


Figure 41: normalized brute force sensitivity of auto-ignition delay times for methane/air mixtures for different equivalence ratio

Based on the diagram in Figure 41, the chemistry of radicals CH₃, HO₂, CH₃O and H₂O₂, controls most of the self-ignition of methane. The reactions (R119), (R158), (R32), (R156), (R116), and (R161) are the most influential reactions of auto-ignition delay time. However, it's important to note, that the most effective promoter of the self-ignition is the reaction (R119). Its coefficient is greater for poor mixtures than for rich mixtures; this means that as the equivalence ratio increases, the sensitivity coefficient of this reaction will be reduced and the promoting effect of self-ignition weakens.

In addition, the most important self-ignition inhibition reactions are the chain termination reactions (R158) and (R116) and the methane consumption reactions (R53) and (R98).

As the equivalence ratio increases, the concentrations of methane in the mixture increase, so does the rate of methane consumption reactions (R53) and (R98) leading to the increase of the concentrations of methyl radicals. As a result, the rate of the inhibiting reaction (R158) in which two methyl radicals are combined to produce single ethane molecule increases.

In contrast, when dealing with another biofuel (not methane), increasing the equivalence ratio leads to the increase of biofuel concentrations as well as the concentrations of hydrogen radicals H. The sensitivity analysis of the replacement of 10% of CH₄ with H₂ is performed for different equivalence ratios (0.6; 1; and 1.4) and presented in Figure 42.

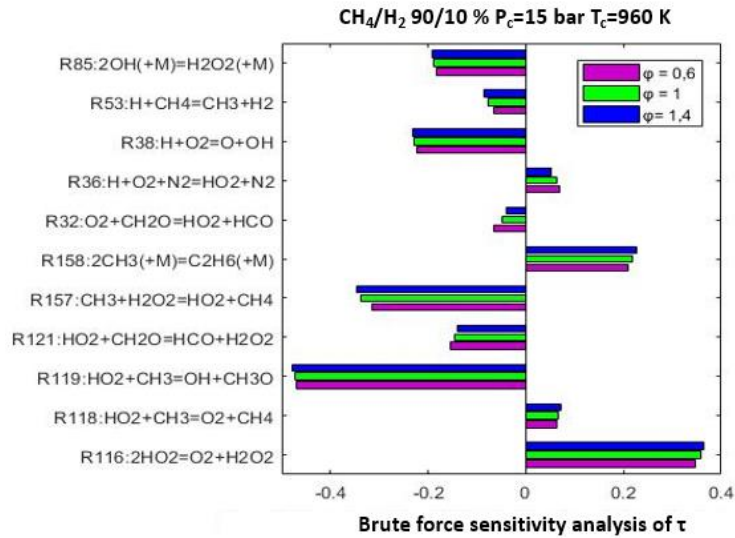


Figure 42: Brute force sensitivity analysis of auto-ignition delay time

The reactions that most promote self-ignition of CH_4/H_2 mixtures are mainly (R119), (R157), (R38), (R85), (R121), (R53) and (R32).

Similar to pure methane mixture, reaction (R119) is the most promising for self-ignition. However, its coefficient is greater for rich mixtures than for poor mixtures. It is the same for (R157) and (R38). This means that when the equivalence ratio increases, the methane and hydrogen concentrations increase; The sensitivity of (R38) (consumption of hydrogen radicals) will be increased and the promoting effect of self-ignition will be strengthened. In contrast to the pure methane mixture, the combination reaction of two HO_2 radicals to H_2O_2 (R116) has a more important inhibitory effect than the chain termination reaction (R158). This is due to the competition in methyl radical consumption between (R158) and the promoter reactions (R157) and (R119).

2.3. Influence of the fuel composition

In this section, the influence of fuel composition on the combustion process will be studied in particular on lean conditions.

As mentioned previously, the auto-ignition temperature is an indicative parameter of the reactivity of the gas mixture. It is largely influenced by the various parameters such as pressure, geometry, and volume, as well as the concentration of reactants and diluents and others.

The influence of fuel composition on the auto-ignition temperature is presented in Figure 43 for a compression pressure of 15 bar and an equivalence ratio of 0.6.

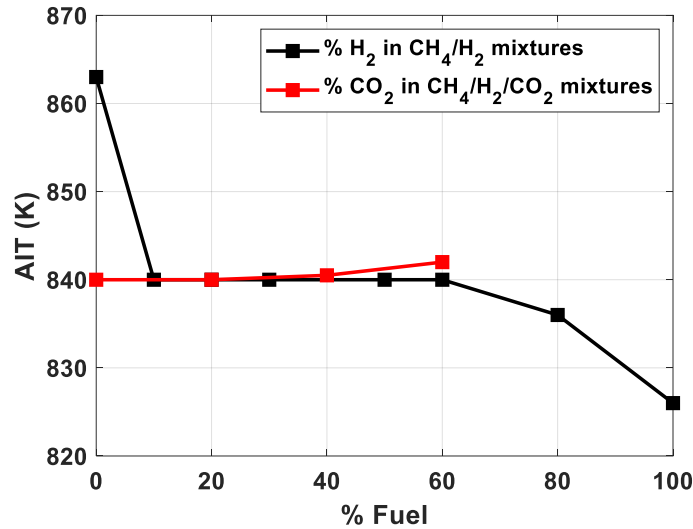


Figure 43: Auto-ignition temperature of different fuel composition $P_c=15$ bar, $\phi=0.6$

As can be observed, pure methane has a higher auto-ignition temperature than hydrogen thus a lower reactivity. The replacement of 10% CH₄ by hydrogen, increases the reactivity by decreasing the auto-ignition temperature to 840 K instead of 863 K. This value is quite the same for a percentage of hydrogen lower than 50 %. For a higher hydrogen percentage, the auto-ignition temperature decreases, it becomes 827 K for pure hydrogen. Meanwhile, adding carbon dioxide to CH₄/H₂ mixtures increases the auto-ignition temperature slightly.

The effect of each biofuel component on the reactivity of the mixture is better explained and analyzed in the following section.

Influence of hydrogen and methane

The effect of hydrogen addition on the auto-ignition delay time of biofuel mixtures is presented in Figure 44.

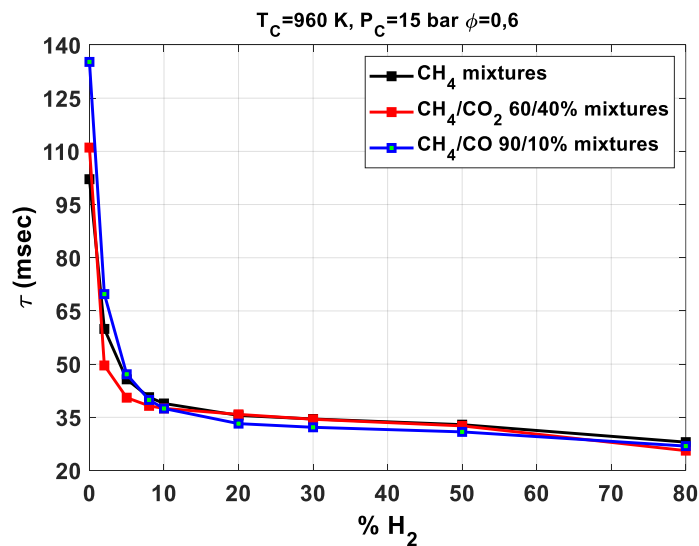


Figure 44: The effect of hydrogen addition on the ignition delay time of biomass-derived fuel mixtures

The auto-ignition delay time decreases when the hydrogen percentage in CH_4 , CH_4/CO_2 and CH_4/CO mixtures increases. The influence is the highest for a hydrogen percentage lower than 10%; then, the auto-ignition delay time decreases slightly. In other words, the addition of a small amount of hydrogen is sufficient to take control of the reactivity of pure methane mixture. This is in agreement with the experimental study on the effect of hydrogen on methane mixtures.

Generally, hydrocarbon fuels exhibit two-stage self-ignition processes:

- A low-temperature region (LTR) initiates the ignition process and leads to the formation of a group of radicals in the first stage. This stage is characterized by a negative temperature coefficient (NTC). NTC is used to designate the temperature regime in which the rate of fuel consumption decreases with increasing temperature, unlike all other regimes where it increases.
- A high-temperature region (HTR), in which most of the heat is released, forms the second stage.

Achieving stable HCCI combustion requires proper control of each temperature region.

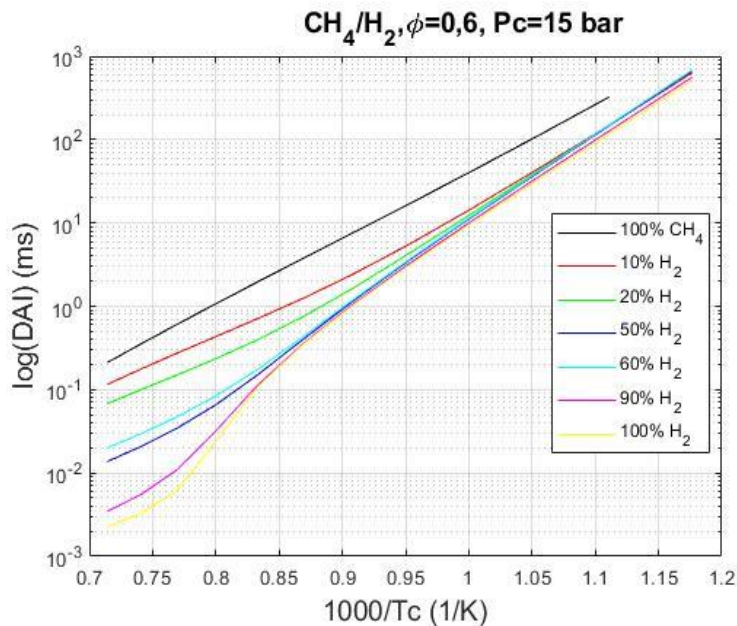


Figure 45: auto-ignition delay times of methane/hydrogen mixtures

The evolutions of the auto-ignition times of the different CH_4/H_2 mixtures with the end of compression temperatures are presented in logarithmic scale Figure 45. As can be seen, pure methane does not exhibit the low-temperature reaction (LTR) behavior, indicating that methane is very resistant to self-ignition since it has a very high octane rating (120) [112].

The effect of hydrogen on the combustion process is largely studied in the literature. Checkel et al. [113], [114] found that the impact of hydrogen on the combustion phase is depended on the octane rating of the base fuel. For low octane fuels, the addition of hydrogen delays the combustion, whereas for higher octane fuels, the combustion time varied with the initial temperature. Having a high-octane number, the addition of hydrogen to the methane mixture increases its reactivity.

Influence of carbon dioxide and dilution rate

The effect of CO₂ on the auto-ignition delay time of different biofuels is represented in Figure 46.

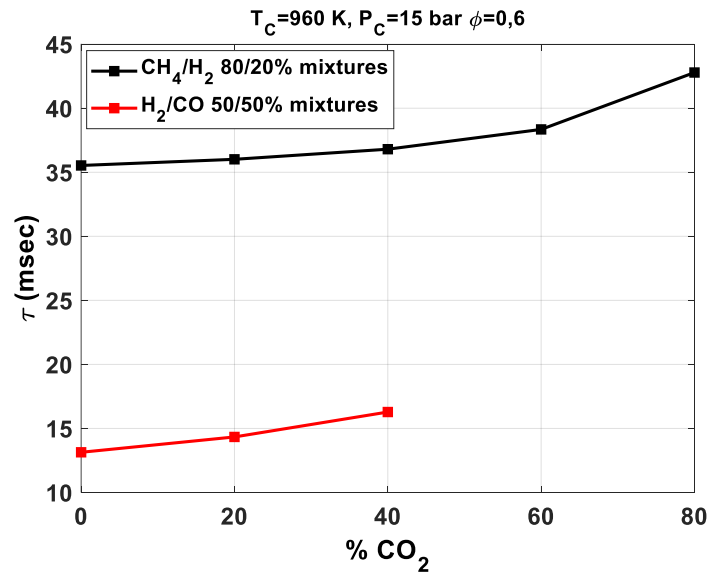


Figure 46: The effect of carbon dioxide addition on the ignition delay time of biomass-derived fuel mixtures

As shown in this figure, the increase in the percentage of CO₂ leads to an increase in the auto-ignition delay time. As the concentrations of CO₂ in the reactive mixtures go higher, the biofuel concentrations decrease while the slope of ignition delay times increases.

In fact, unlike other biofuel components (CH₄, H₂, and CO), carbon dioxide is a non-reactive component that does not participate in the ignition process. It is mostly considered as a dilution specie that reduces the combustion temperature of biofuel. As mentioned in a previous section, as the temperature decrease, the rate of branching chain reaction decreases whereas that of termination reactions are nearly the same.

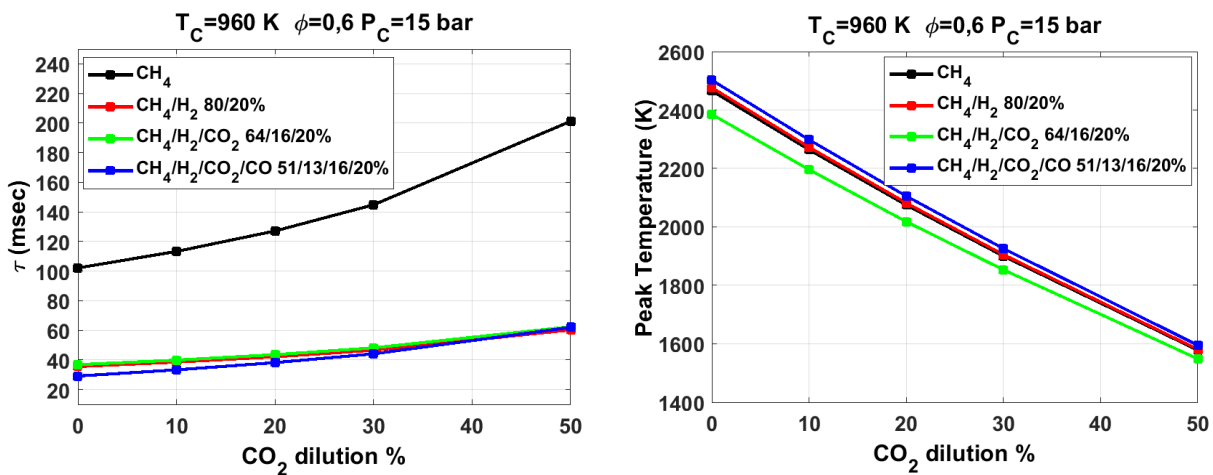


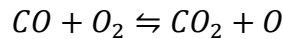
Figure 47: The effect CO₂ dilution rate on the ignition delay time of biomass-derived fuel mixtures

As a result, the reactivity of the mixtures decreases when the percentage of CO₂ in the mixture increases. This effect is more accentuated with higher CO₂ concentrations as shown in Figure 47.

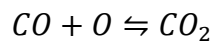
Influence of carbon monoxide

As mentioned earlier in this chapter, only the effects of carbon monoxide on the auto-ignition process will be studied on Aramco 1.3 mechanism. Since biofuel mixtures contain hydrogen, CO is expected to participate in the chemical reactions when added to biofuel-air mixtures.

According to the reactions of Aramco 1.3, the combustion of pure carbon monoxide in air initiates and ignites through two main reactions:



Followed by:



Although pure carbon monoxide is difficult to burn in air or oxygen, the presence of impurities containing hydrogen can significantly enhance the rate of CO oxidation reactions [84]. The auto-ignition temperatures of pure CO and CO/H₂ mixtures are presented in Table 20.

Table 20: Auto-ignition temperatures of CO with different percentage of hydrogen

| | CO | CO/H ₂ 90/10% | CO/H ₂ 80/20% | CO/H ₂ 50/50% |
|---------|------|--------------------------|--------------------------|--------------------------|
| AIT (K) | 1116 | 848 | 838 | 823 |

It is shown that the addition of a small percentage of hydrogen reduces the ignition temperature significantly, as the highly reactive hydrogen promotes the formation of radical H, OH, and O that will facilitate the decomposition of carbon monoxide. Hence, This effect of carbon monoxide on the auto-ignition temperature was validated by Mansfield et al. [115], and Olchewsky et al. [116]. They found that hydrogen is more reactive than methane, which in turn is more reactive than carbon monoxide.

Furthermore, the effect of the carbon monoxide observed experimentally in slightly decreasing the reactivity of the biofuel (CH₄/H₂/CO₂/CO) reactivity under lean homogeneous conditions ($\phi=0.6$, and Pc=15 bar) can be explained by the competitiveness of methane and carbon monoxide on the radical O. In other words, among the biofuel components, hydrogen is the first to decompose in radicals; its decomposition provides the mixture by radical O, H and OH. The co-occurrence of the reaction $CO + O \rightleftharpoons CO_2$ with the reaction $CH_4 + O \rightleftharpoons CH_3 + OH$ decreases the reactivity of the mixture slightly and increase the ignition delay times.

The results obtained in this section only allows the characterization of the biofuel reactivity under lean homogeneous conditions and thus are not sufficient to conclude a range of optimized fuel and conditions. Thus, the effects of each parameter will be evaluated on the pollutant emissions in order to allow the determination of optimized conditions.

Key ideas of this section

- Hydrogen is more reactive than methane that is more reactive than carbon monoxide
- Less than 10% of hydrogen is sufficient to control the auto-ignition of biogas/syngas ($\text{CH}_4/\text{CO}_2/\text{H}_2$ and CO/H_2) under lean homogeneous conditions
- The methane does not exhibit the low-temperature reaction (LTR) behavior due to its high-octane number
- The pure carbon monoxide is difficult to burn with air or oxygen, the addition of 10% of hydrogen decreases its auto-ignition temperature significantly
- Carbon monoxide does not have a significant effect on the combustion reactivity; it increases slightly the ignition delay times of biogas/syngas mixtures due to the competitively with methane on radical O
- Carbon dioxide is a diluent specie than does not contributes to the chemical reactions
- The high percentage of carbon monoxide decreases the temperature of the combustion and therefore reduces the reactivity
- All mixtures have a decreased reactivity at lean conditions except for the methane
- The pressure and temperature also increase the reactivity of the mixture

3. Pollutant emissions

Homogeneous combustion consists of creating spontaneous self-ignition of a homogeneous mixture. At very low loads, where homogeneous combustion is the most promising, self-ignition will take place at any point in areas of low fuel to air ratios [117]. Grimech3.0 accounts for hydrocarbon chemistry and its elaborated radical chemistry enables it to predict NO especially in low calorific value fuels even at high pressures[118].

3.1.Types of pollutant emissions and greenhouse gases at the end of the combustion

In general, with the application of homogeneous combustion strategies, the same pollutant emissions issued from spark as well as a compression-ignition engine will be produced. In this work, we will focus in particular on nitrogen oxides emissions, carbon monoxide as well as greenhouse gas emissions.

Nitrogen oxides (NO_x) emissions

Nitric oxide NO, nitrogen dioxide NO₂ and nitrous oxide N₂O are traditionally grouped under the term NO_x. In an engine, however, NO is mostly formed at the temperatures encountered during the combustion phase. Its formation is controlled by three different mechanisms largely written in the literature [119].

- Thermal NO corresponds to oxidation of atmospheric nitrogen described by the Zeldovitch mechanism. This mechanism represents the predominant pathway for NO formation during combustion.
- Prompt-NO includes all other reaction mechanisms within the flame (rich mixture) that are involved in the formation of NO.
- Fuel-NO is linked to the decomposition of the fuel which can release NO_x compounds. The nitrogen content of fuels today is so small that this NO formation pathway can be neglected.

In diesel engines, the NO formed in the gases burned at high temperatures can oxidize to NO₂ during the expansion phase, up to a [NO₂]/[NO] ratio of 10 to 20%. Chemical equilibrium calculations show that NO can be oxidized to NO₂ in the flame from reactions of the type:



The NO₂ is then reconverted into NO by the reaction:



However, this reaction can be stopped if the flame is mixed with a cooler fluid. In this case, the NO₂ reversion is only partial, which explains the presence of NO₂ at the opening of the exhaust valves. It should be noted that the actual European standards consider by default that all NO_x at the engine outlet has the molar mass of NO₂. The legislator is, therefore, deliberately overestimating the NO_x mass flow rate at the engine outlet.

Emissions of carbon monoxide (CO)

Carbon monoxide is a very toxic air pollutant. It is produced in the incomplete combustion of carbon-containing fuels, such as gasoline, natural gas, oil, coal, and wood. It is formed at the heart of the flame with other intermediate combustion products.

Most of these products are then converted to CO₂, so the presence of CO at the opening of the exhaust valves demonstrates the existence of an incomplete oxidation process. The emissions of CO thus increase as it approaches stoichiometry due to an oxygen depletion, which explains why CO emissions are often important for petrol engines that operate close to stoichiometry for the needs of three-way catalysts. However, for Diesel engines operating in a lean mixture, the final level is significantly lower than the maximum level existing in the cylinder. As for soot, a competition between the mechanisms of formation and oxidation.

Greenhouse gas GHG

The greenhouse gas can be defined as the gas in the atmosphere, which absorbs and re-emits heat, causing the planet's atmosphere to be warmer than it would be. It mainly consists of water vapor, carbon dioxide (CO₂), methane (CH₄), nitrous oxide (N₂O), and ozone. Although these gases occur naturally in the Earth's atmosphere, human activities, including the burning of fossil fuels, are increasing their level in the atmosphere, causing global warming and climate change [120].

Carbon dioxide equivalent is a term describing different greenhouse gases in a common unit. It implies the amount of CO₂, which would have an equivalent global warming impact. The global warming potentials of the most common greenhouse gases in our study are given in Table 21.

Table 21: Global warming potential of three greenhouse gases

| Greenhouse Gas | Global warming potential |
|-----------------------------------|--------------------------|
| Carbon dioxide (CO ₂) | 1 |
| Methane (CH ₄) | 25 |
| Nitrous oxide (N ₂ O) | 298 |

3.2. Methods of calculation

There exist several ways to evaluate pollutants emission. Emission index calculation is one of the most used methods in the literature. These indexes can be represented as the mass of the produced pollutant species by 1 kg of consumed fuel:

$$EI (PS) = \frac{\text{mass } PS \text{ produced}}{\text{mass fuel consumed}} * 1000 \text{ g/kg fuel} \quad (IV.5)$$

The mass is conserved before and after the combustion; therefore, the emission index of the pollutant species produced by the consumption of 1 Kg of the fuel is given by:

$$EI (PS) = \frac{X_{PS \text{ prod}} * M_{PS \text{ prod}} * (M_t)_u}{X_{fuel \text{ cons}} * M_{fuel \text{ cons}} * (M_t)_b} * 1000 \text{ g/kg fuel} \quad (IV.6)$$

Where: $X_{PS \text{ prod}}$ is the molar fraction of the produced pollutant specie and $X_{fuel \text{ cons}}$ is that of the consumed fuel.

$M_{PS \text{ prod}}$ is the molar weight of the pollutant specie and $M_{fuel \text{ cons}}$ is that of the consumed fuel in g/mol.

$(M_t)_b$ and $(M_t)_u$ are the molar weight of the burned and unburned mixture respectively.

This method of calculation is strongly dependent on the molar weight of the reactive fuel. It is convenient to use this method in case of similar values of molar weight. Therefore, in this study, the reactive fuel is the biofuel whose component's molar weight are quite different: methane ($M_{CH_4} = 16 \text{ g/mol}$), hydrogen ($M_{H_2} = 2 \text{ g/mol}$), carbon dioxide ($M_{CO_2} = 44 \text{ g/mol}$) and carbon monoxide ($M_{CO} = 28 \text{ g/mol}$).

Another way of calculating the emission index would be the mass of the produced pollutant species by 1 Kg of the total mixture.

$$EI (PS) = \frac{X_{PS \text{ prod}} * M_{PS \text{ prod}}}{(M_t)_b} * 1000 \text{ g/kg mixture} \quad (IV.7)$$

This method doesn't depend on the molar weight of the reactive fuel. Thus, according to this method, the more the mixture is diluted the lesser will be the emission index. In other words, it doesn't count the contribution of each reactive fuel in the released heat of the combustion.

Last but not least, the final method we will be presenting in this study is the emission indexes of the pollutant species by 1 kJ of produced energy.

$$EI (PS) = \frac{X_{PS \text{ prod}} * M_{PS \text{ prod}} * (M_t)_u}{X_{fuel \text{ cons}} * M_{fuel \text{ cons}} * (M_t)_b * LHV_{fuel}} * 1000 \text{ g/kJ} \quad (IV.8)$$

LHV is the low heating value of the reactive fuel. It depends on the fuel composition, temperature, and pressure. For a more simplified calculation, the lower heating value in the normal condition of temperature and pressure was used in this study. The values of LHV for different biofuel components are given in Table 22:

Table 22: Low heating value of biofuel components [121]

| | LHV MJ/m3 | Volumetric weight kg/m3 | LHV kJ/kg |
|----------|-----------|-------------------------|-------------|
| Methane | 35,8 | 0,656 | 54573,17073 |
| Hydrogen | 10,8 | 0,08988 | 120160,2136 |
| CO | 12,6 | 1,184 | 10641,89189 |

The emission indexes of pollutant species were determined by these three methods of calculation for biofuel mixtures and were presented in Figure 48.

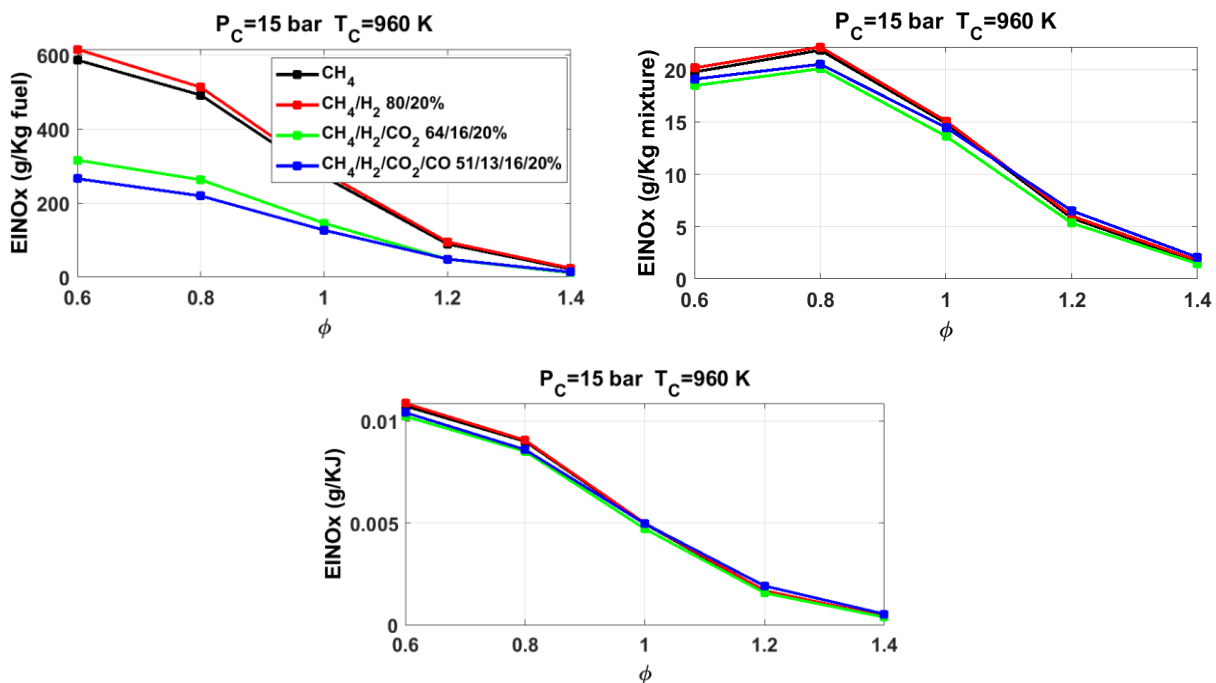


Figure 48: The emission indexes of pollutant species calculated by three methods

According to this comparison, the evolution emission indexes by kg of fuel represents different values and trends than the other emission indexes (by kg mixture and kJ). The values are also widely different according to the calculating method used. The first method (g/kg fuel) is strongly dependent on the molar weight of the reactive fuel. So, the pollutant emissions will always be overestimated for methane and hydrogen mixtures, which does not apply to mixtures containing carbon dioxide. As for the second method (g/kg mixtures), it has no significant physical meanings since it counts the mass of fuel, oxidizer and dilution specie regardless of the contribution of each reactive fuel in the released heat of the combustion.

The advantages of the last method (g/kJ) are that it counts for the energy contribution in the production of pollutant emissions. This seems to be the most coherent method as it energizes the

concept of emissions and combines two important aspects of the combustion (produced energy and pollutant emissions).

Hence in this chapter, the pollutant emissions will be presented as the mass of produced pollutant species by released energy unit (kJ). A parametrical study will be carried out to determine the effect of temperature, pressure and equivalence ratio as well as the fuel composition on the pollutant emissions.

3.3. Influence of different parameters on the pollutant emissions

The parametrical study in this section aims to highlight the importance of lean homogeneous combustion in reducing pollutant emissions. The results of the contribution of each parameter on the pollution will complete the earlier study concerning their effects on the reactivity of the combustion.

Influence of temperature and pressure

The mechanism of the formation of NO from atmospheric nitrogen is written in the form of the extended mechanism of Zeldovich:



$$k_1^+ = 7.6 * 10^{13} e^{-\frac{38000}{T}} \text{ and } k_1^- = 1.6 * 10^{13}$$



$$k_2^+ = T * 6.4 * 10^9 e^{-\frac{3150}{T}} \text{ and } k_2^- = T * 1.5 * 10^9 e^{-\frac{19500}{T}}$$



$$k_3^+ = 4.1 * 10^{13} \text{ and } k_3^- = 2 * 10^{14} e^{-\frac{23650}{T}}$$

Where k_i^+ and k_i^- represent the forward and reverse reaction constants, respectively, and T the temperature at chemical equilibrium.

The first two reactions constitute the initial Zeldovitch mechanism. It is valid for the high-temperature zones near the stoichiometry. The last reaction added by Lavoie et al. [122] concerns, especially the rich areas in the flame characterized by the presence of the OH radical.

The very high activation temperatures of these reactions show a great dependency on the formation of NO with the temperature. By introducing additional hypotheses on the concentrations of the species in chemical equilibrium as written in [119], it is possible to write the initial formation rate of thermal NO with the following equation:

$$\frac{d[NO]}{dt} = \frac{6 \cdot 10^6}{T^{0.5}} e^{-\frac{69090}{T}} [O_2]^{0.5} [N_2] \quad (IV.12)$$

The main interest of this expression is to show that NO formation depends directly on the temperature and oxygen concentration. A careful study of these two parameters seems, therefore, essential to explain the evolution of NO concentrations as a function of certain engine parameters.

The emission indexes of the pollutant species: NO_x , equivalent CO_2 , and CO were calculated for four lean biofuel mixtures ($\phi=0.6$). Their evolution with the end of compression pressure (at $T_c=960\text{ K}$) and temperature (at $P_c=15\text{ bar}$) are represented respectively in Figure 49 and Figure 50.

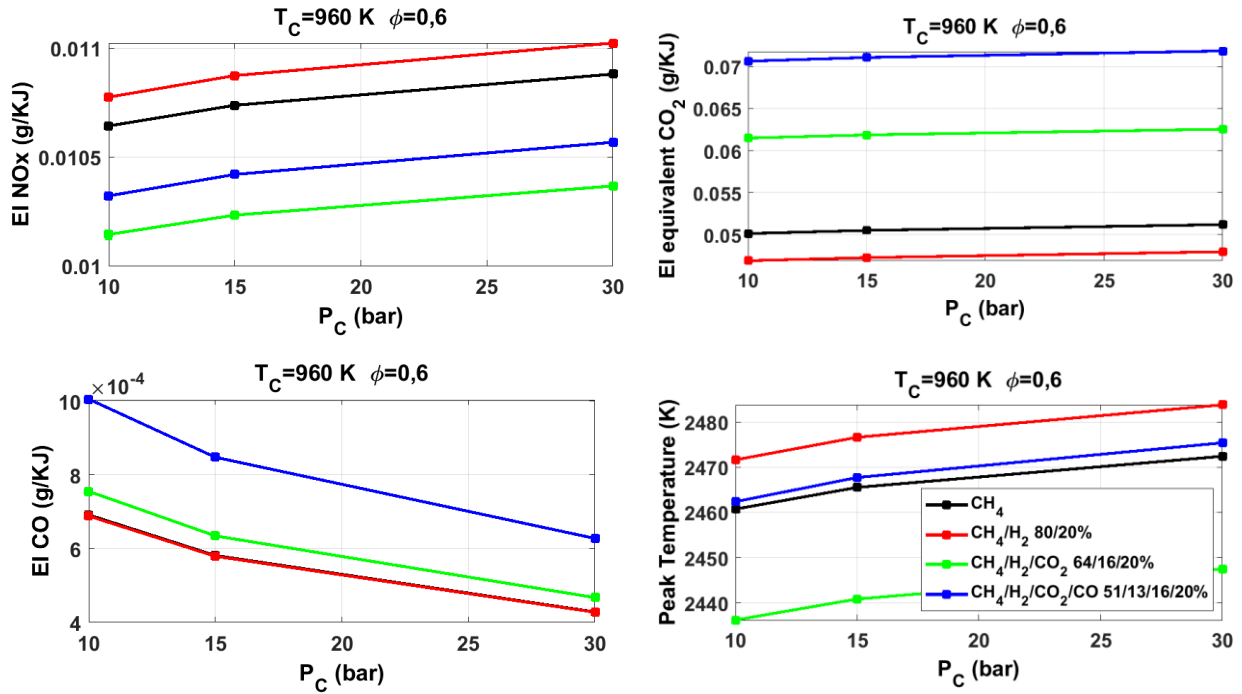


Figure 49: Influence of the pressure on pollutant emissions indexes

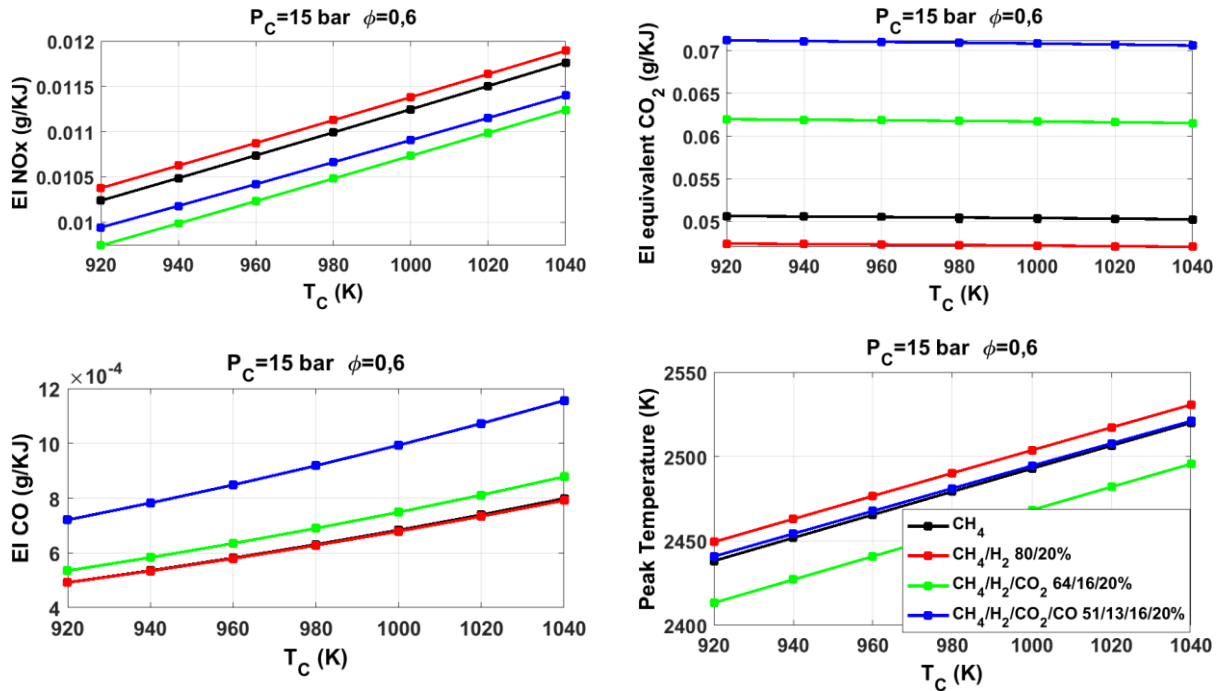


Figure 50: Influence of temperature on pollutant emissions indexes

As explained in the previous section, the increase in the initial pressure and temperature causes an increase in the temperature during the combustion process, and therefore in NO_x emission indexes.

However, mixtures containing carbon monoxide show higher temperatures than pure methane and H₂/CH₄ mixtures. And despite this, they represent lower NO_x indexes. This can be explained by the fact that NO_x formation depends on the temperature as well as the oxygen concentration. In fact, according to the equation (IV.1), for the same air to fuel ratio, the quantity of oxygen required for the combustion is proportional to the carbon monoxide quantity, half of the hydrogen quantity and to two times of the methane quantity.

As a result, for the same equivalence ratio, the oxygen quantity is lower in a biofuel mixture of CH₄/H₂/CO₂/CO, compared to that of H₂/CH₄, which explains the NO_x emissions evolution of these two mixtures.

As explained earlier, the emission index of equivalent carbon dioxide represents the emission indexes of methane, carbon dioxide and nitrous oxide with respect to their global warming potential.

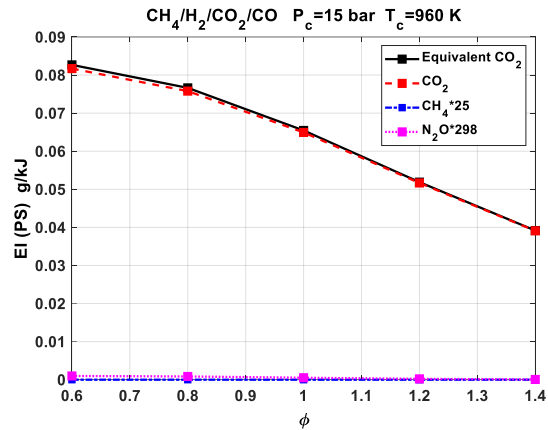


Figure 51: Emission index of total greenhouse gases in the function of the equivalent ratio

Therefore, Figure 51 shows that the concentrations of methane and N_2O are negligible compared to CO_2 emissions. Hence, the EI CO_2 equivalent referred mostly to the emissions of CO_2 .

These emissions depend mostly on the mixture composition and vary slightly with the end of compression temperature and pressure. The same applies to carbon monoxide emissions.

Influence of equivalence ratio

The emission indexes of the pollutant species: NO_x , equivalent CO_2 , and CO were calculated for four biofuel mixtures (at $T_c=960$ K and $P_c=15$ bar) for lean stoichiometric and rich conditions. Their evolutions with the equivalence ratio are represented in Figure 52.

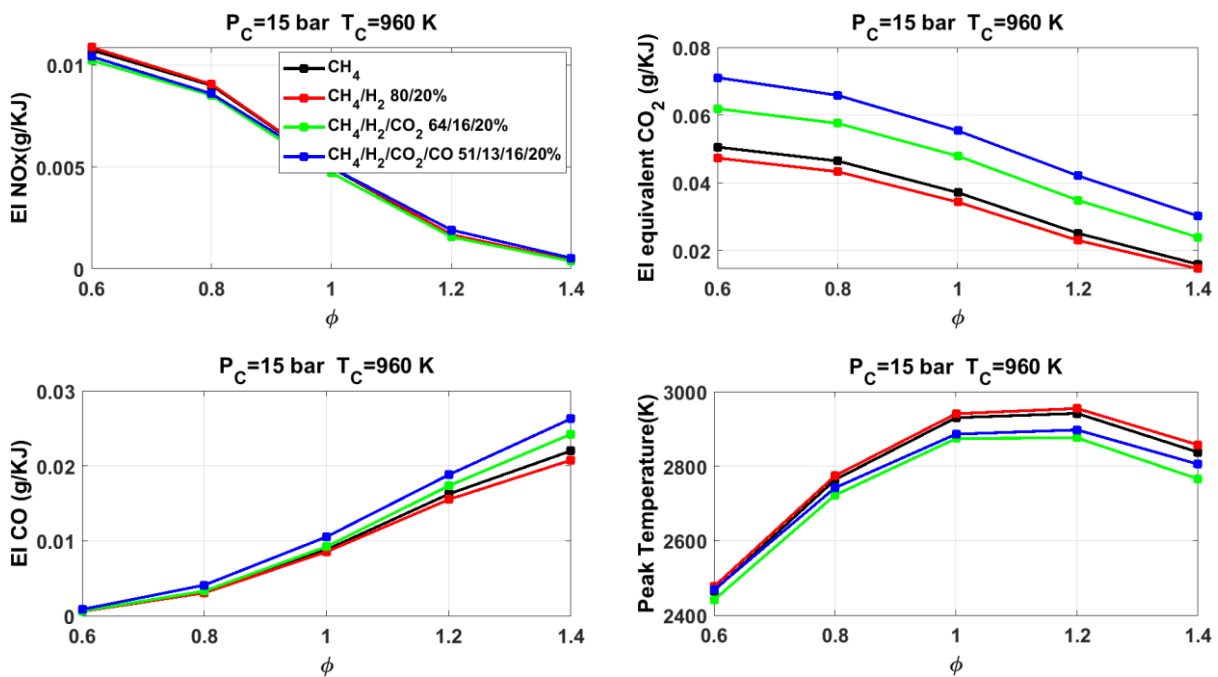


Figure 52: Influence of equivalence ratio on pollutant emission index for four biofuels without dilution

As the equivalence ratio increases, the concentrations of O_2 decrease; thus, not enough oxygen to transform carbon monoxide into carbon dioxide.

The lack of oxygen will then lead to the decomposition of carbon dioxide through (R99) reaction producing carbon monoxide. In fact, in normal lean conditions (R99) is considered as the most important reaction in the production of CO_2 . However, when the equivalence ratio increases, the air to fuel ratio decreases and the hydroxyl radical decreases because of the oxygen-deficiency. Thus, the reaction R99 will be reversed favoring the consumption of CO_2 and the production of CO:



According to the equation (IV.12), NO formation depends directly on the temperature and oxygen concentration. For the four biofuel mixtures, the maximal temperature during the combustion process is obtained for the equivalence ratio between 1 and 1.2. However, the maximal NO_x emissions are registered for an equivalence ratio of 0.6 and decrease as the equivalence ratio increase.

This trend is in contrast to what is presented in the literature, due to the fact that we are simulating an adiabatic combustion process. So, when the temperatures are high enough it is the O_2 concentrations that will control the NO formation.

To prove this assumption, the NO_x emission index and the maximal temperature of these biofuels were presented as a function of the equivalence ratio with a dilution ratio of 50 % CO_2 in Figure 53.

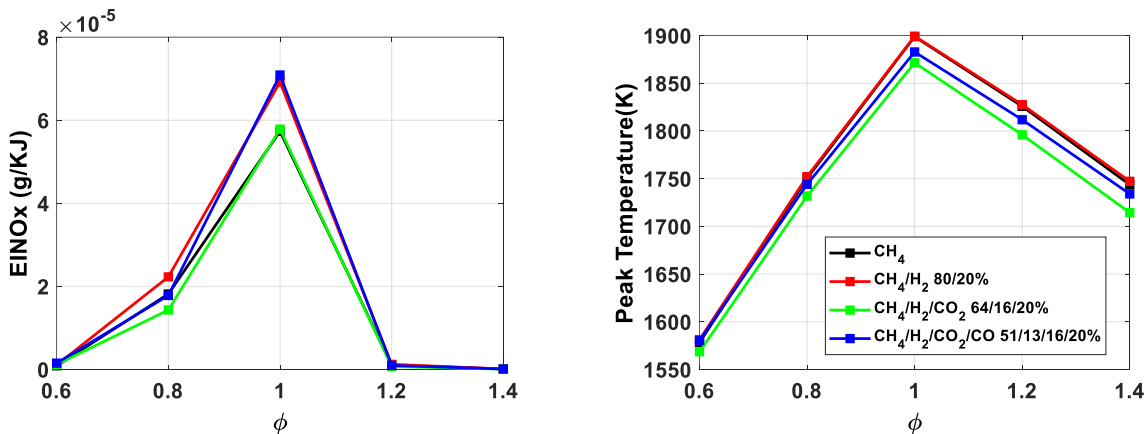


Figure 53: Influence of equivalence ratio on pollutant emission index for four biofuels diluted with 50 % CO_2

The CO_2 dilution rate reduces the maximal temperature. Therefore, for an equivalence ratio going from a value of 0.6 to 1, the temperature increases from 1700 to 2100 respectively. These temperature values are lower than those in case of no dilution (2500-2900 K). Hence, in this case, the emission indexes of NO_x are the highest for stoichiometric conditions and decreases in lean and rich mixtures.

This study highlights the importance of lean conditions in reducing pollutant emissions, in particular NO_x and CO. Their effect in reducing the reactivity of a certain mixture (studied in the previous section) can be improved by the selection of a relatively reactive biofuel mixture along with the temperature and pressure range. In particular, the reactivity of a biofuel mixture was shown

to increase by the addition of a certain quantity of hydrogen, and to mostly decrease with carbon dioxide. Thus, it is important to also study the effects of fuel composition on pollutant emissions.

Influence of fuel composition and dilution

The effect of fuel composition and dilution rate on the emission indexes of the pollutant species: NOx, equivalent CO₂, and CO were calculated at $T_c=960$ K and $P_c=15$ bar for different lean mixtures of CH₄/H₂, CH₄/H₂/CO₂, CH₄/H₂/CO₂/CO.

The evolutions of emission index of pollutant species of CH₄/H₂, CH₄/H₂/CO₂, and CH₄/H₂/CO₂/CO mixtures with respectively the percentage of hydrogen, carbon dioxide and carbon monoxide are represented in Figure 54, Figure 55 and Figure 56.

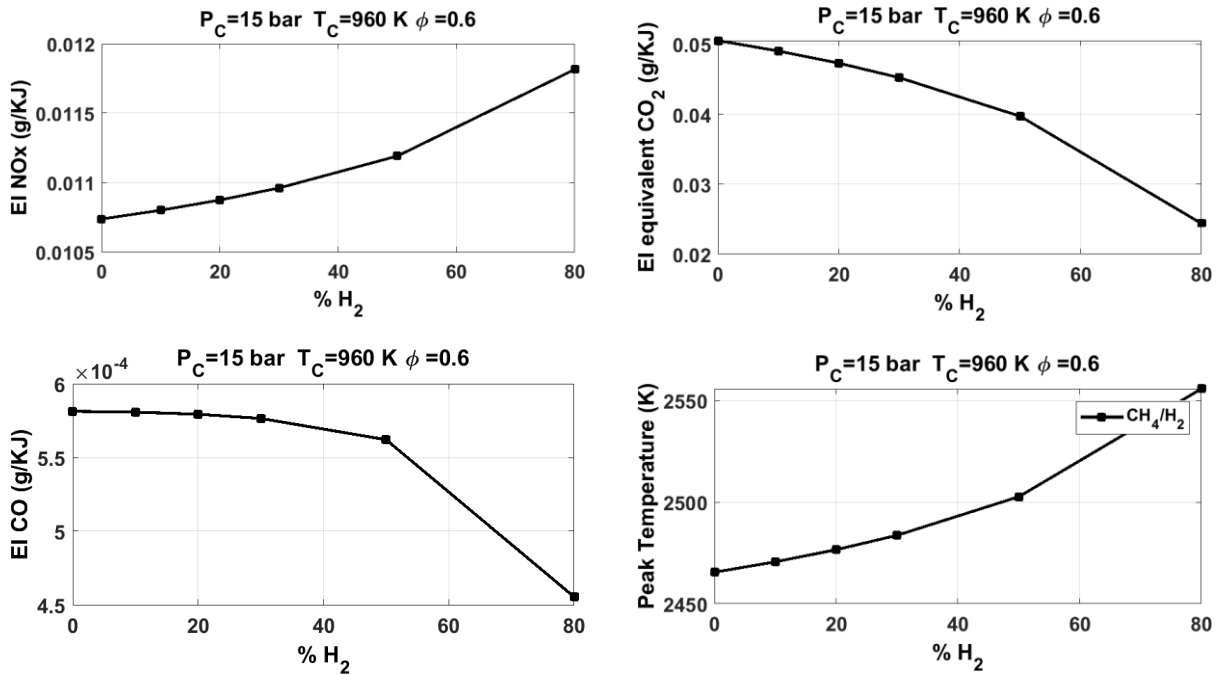


Figure 54: Influence of hydrogen on pollutant emissions index

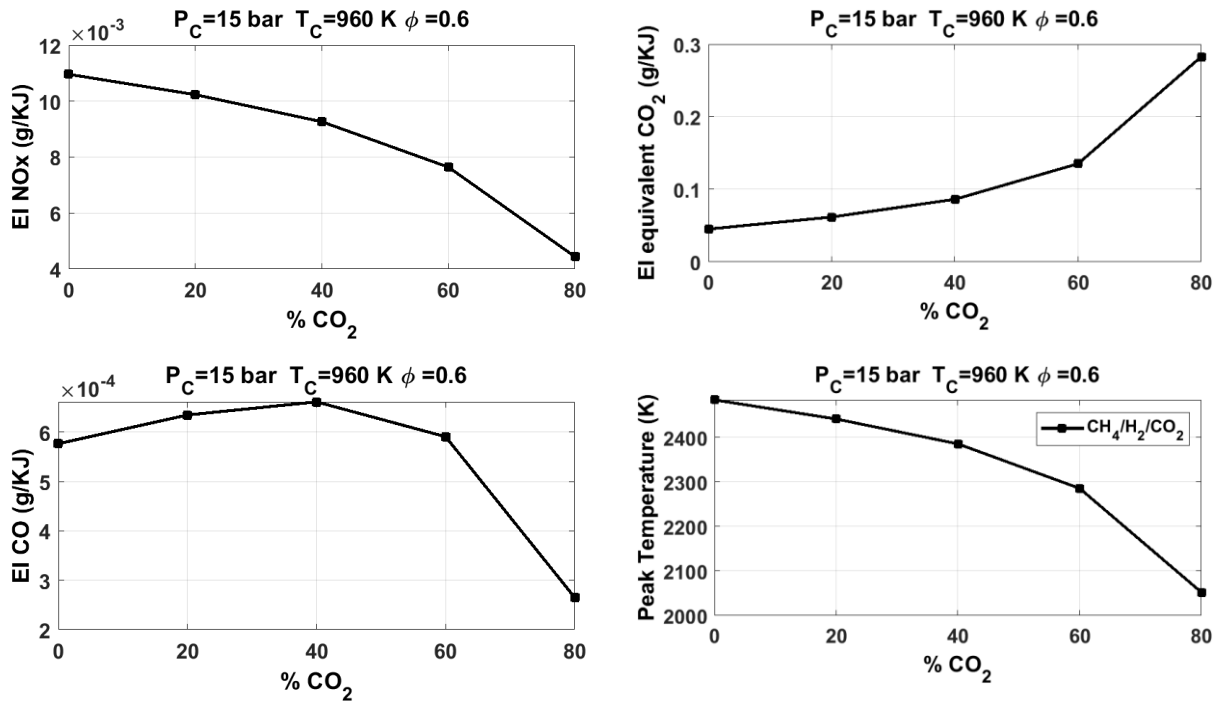


Figure 55: Influence of carbon dioxide on pollutant emissions index

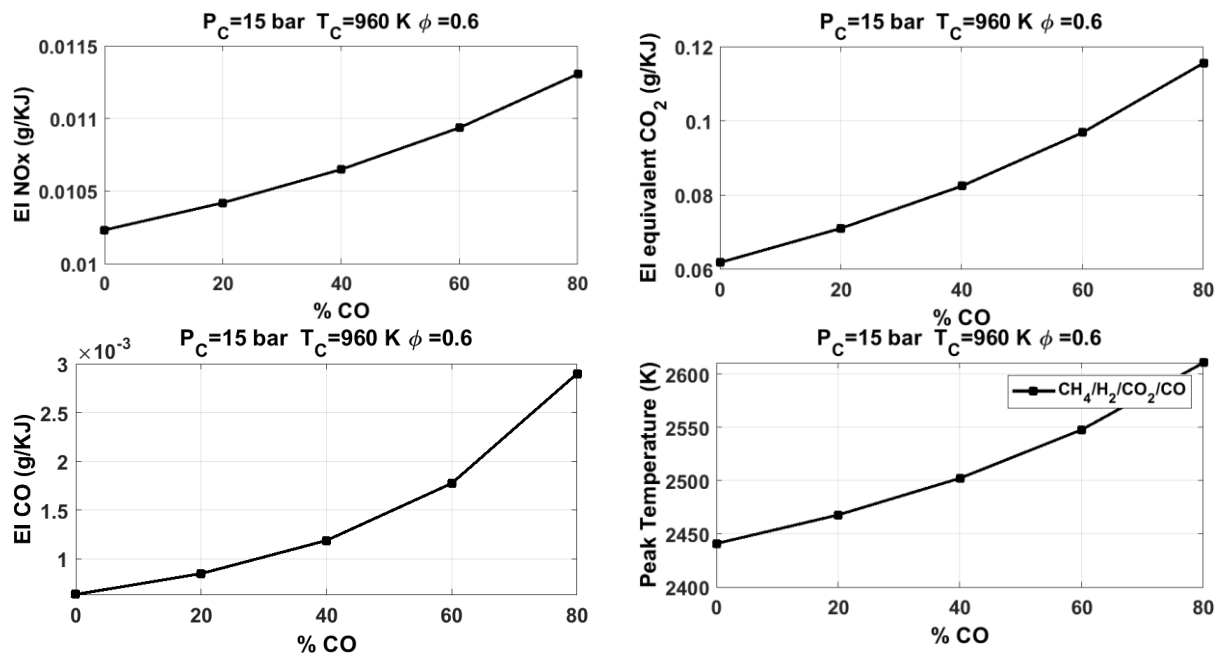


Figure 56: Influence of carbon monoxide on pollutant emissions index

Several studies were performed in the literature to determine the influence of hydrogen on the evolution of pollutants and greenhouse gases. Increasing hydrogen percentages in methane/hydrogen mixtures increases the peak temperature of the combustion. This will induce an increase in the emission index of NO_x; this increase is estimated to only 1% for a percentage of 10

% H₂ and 10 % for 80% H₂. Carbon monoxide exhibits similar effects on NO_x emissions as those observed for hydrogen mainly due to their effect on increasing the peak temperature.

On the other hand, increasing hydrogen percentage in the biofuel mixture means that a carbon component is replaced with hydrogen. Therefore, the total mass of carbon in the mixture will decrease, and so do the products containing carbon: CO₂ and CO. 10 % of H₂ was seen to reduce 2% of equivalent CO₂ and neglected effect on CO emissions. This impact becomes stronger at higher hydrogen percentages. For example, for a 50 % H₂, the CO₂ emissions are reduced by 20 % compared to 60 % for 80 % H₂.

In contrast, increasing the percentage of any of the carbon biofuel components CO₂, CH₄ or CO will surely increase the carbon mass emissions.

However, the emission index of carbon dioxide has a specific trend with the carbon dioxide percentage. It increases for the first 40% of added CO₂, then decreases as the percentage increase from 40 to 80 %. This can be explained by the chemical reaction R99 of the combination of CO with hydroxyl radical to produce CO₂ and radical hydrogen. When the concentrations of the products are high enough the reaction will occur backward, and the present CO₂ will decompose with H to produce CO and OH.

Because of its thermodynamic properties, it has an impact in reducing the peak temperature and therefore the emission index of NO_x.

The highest the concentrations of carbon dioxide, the more they reduce NO_x and carbon monoxide emissions. This can be illustrated by presenting the evolution of emission index with CO₂ dilution rate in the same conditions and for four biofuel mixtures. (view Figure 57).

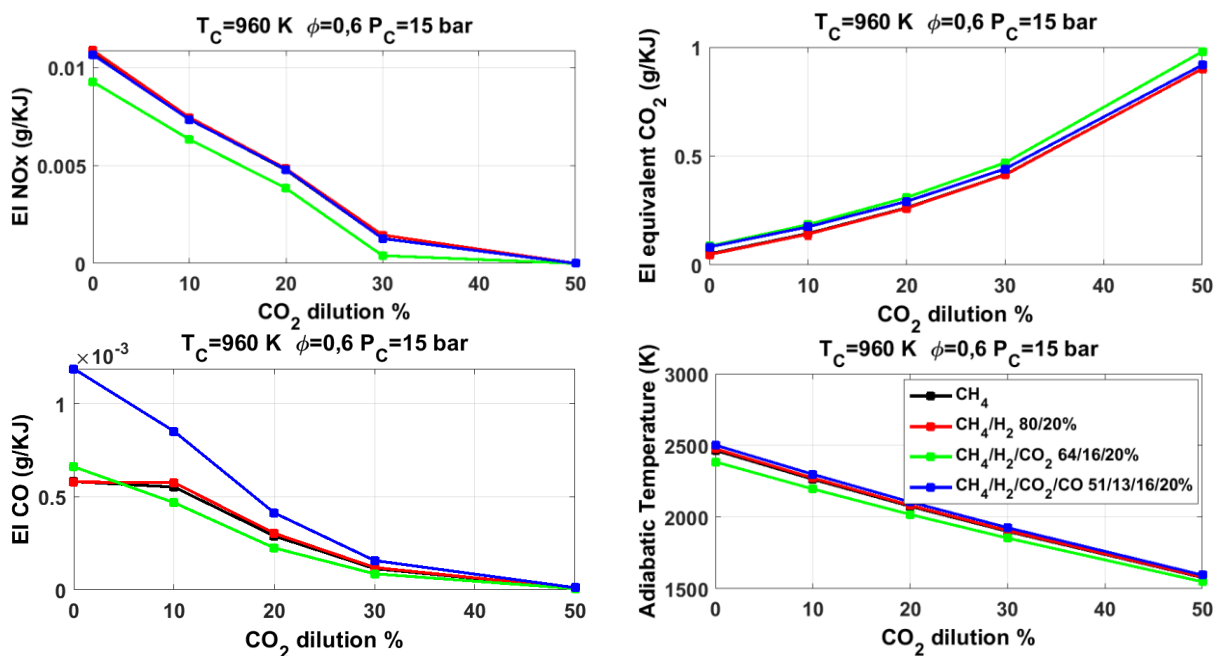


Figure 57: Influence of CO₂ dilution on pollutant emissions index of biomass-derived fuel mixtures

It is observed that the emission index of NO_x is reduced to 30 % for 10 % CO_2 dilution, 80% for 30 % dilution, and nearly 100% for 50% CO_2 dilution. CO emissions were also significantly reduced with carbon dioxide dilution. However, the problems of high dilution are the relatively higher CO_2 emissions as well as the decrease in the combustion reactivity as studied earlier.

It was shown earlier that the low reactivity could be improved by the addition of low hydrogen quantities. The effects of hydrogen on the pollutant emissions of highly diluted mixtures are presented in Figure 58.

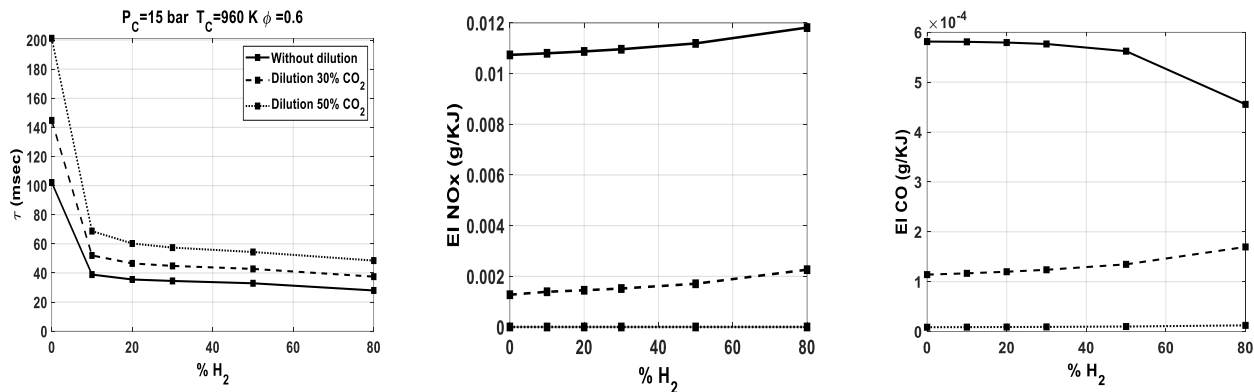


Figure 58: effect of hydrogen on biogas/syngas combustion process for different dilution rate

It is observed that a small amount of hydrogen (less than 10 %) is sufficient to control the reactivity of biofuel mixtures. And this applies to a dilution rate ranging from 0 to 50% of CO_2 . Furthermore, it is known that a higher percentage of hydrogen in the biofuel mixture decreases the mass of carbon in the mixture and, therefore, the mass of the produced CO_2 , with an increase in NO_x and CO as explained earlier in this chapter. However, as shown in Figure 58, in terms of CO and NO, a quantity of hydrogen lower than 30 % has a quite similar impact on these emissions.

the key ideas in this paragraph

- Emission index by energy units is selected in this study as it accounts for the energy contribution in emissions
- Increasing the percentage of hydrogen in the biofuel mixture means that a carbon component is replaced with hydrogen. Therefore, the total mass of carbon in the mixture will decrease, and so do the products containing carbon: CO_2 and CO
- CO percentage in the fuel will lead to an increase in the emissions of NO_x , CO_2 and CO
- As the equivalence ratio increases, carbon monoxide increases
- NO_x emissions with the equivalence ratio is in contrast to what is presented in the literature due to the assumption of an adiabatic combustion process; when the temperatures are high enough, the NO formation will be controlled by O_2 concentrations. This was validated by comparing the equivalence ratio effects on a diluted mixture with a reduced peak temperature.
- An increase of the end of compression pressure and/or temperature leads to higher NO_x emissions

- The effect of the pressure and temperature on carbon pollutant emissions can be neglected, as these emissions are mostly dependent on the composition of the mixture
- EI CO₂ equivalent referred mostly to the emissions of CO₂

4. Conclusions and discussions on optimal mixtures and conditions in auto-ignition point of view

In this section, the evolutions of auto-ignition delay time and/or temperature, as well as the pollutant emission indexes, were studied for different initial conditions of pressure (10,15 and 30 bar), temperatures (920-1040 K), equivalence ratio (0.6-1.4) and fuel compositions.

This study sheds light on the importance of lean conditions in reducing pollutant emissions, particularly NO_x and carbon monoxide. Furthermore, the equivalence ratio was found to affect the reactivity of the combustion; as ϕ increases, the reactivity of biogas/syngas mixtures increases. The lowest reactivity was found at lean conditions, except for pure methane mixtures, where the reactivity becomes higher at lean conditions. This was explained by the reduced effects of the most inhibiting reactions (R53) and (R98) of methane mixture in the studied conditions.

For all the studied mixtures, the pressure and temperature show a promoting effect on the combustion process. Compared to other parameters, they were shown to have the least effect on the carbon pollutant emission. However, they share the same effect in increasing NO_x emissions.

It was found that the auto-ignition delay time is mostly dependent on the fuel mixture and the dilution rate. It is also dependent on the air/fuel ratio, as well as the end-of-compression pressure and temperature. The general effect of each parameter on the combustion properties is summarized in Table 23.

Table 23: the general effect of each parameter on auto-ignition properties

| | CO ₂ Dilution rate (%) | $\phi < 1$ | H ₂ (%) | CO (%) | CO ₂ (%) | T _c (K) | P _c (bar) |
|---------------------------|---|------------|--------------------|--------|---------------------|--------------------|----------------------|
| NO _x reduction | +++ | +++ | - | - | +++ | -- | - |
| CO ₂ reduction | --- | - | ++ | --- | --- | - | + |
| CO reduction | ++ | +++ | + | --- | ++ | ++ | - |
| Reactivity | - | -- | +++ | - | - | +++ | ++ |

Compared to other parameters, temperature and pressure are found to have the least effects on pollutant emissions (CO and CO₂). However, the value of the initial pressure should be chosen according to the engine's operating range. For this study, we will consider a value ranging from 10-15 bar.

This study highlights the benefits of lean mixtures in reducing NO_x and CO emissions than rich or stoichiometric mixtures. Its inhibiting effect on the fuel reactivity and CO₂ emissions (except for methane as shown previously) can be offset by the addition of a certain amount of hydrogen.

In regards to NO_x emissions reduction, the CO₂ dilution rate, as well as the equivalence ratio, have the most influential effect. However, using CO₂ as a dilution specie, the dilution rate should be compromised so that it will not increase CO₂ emissions. Therefore, it was shown earlier that the NO_x emissions decrease significantly for a dilution rate higher than 30 %. The reduced reactivity caused by a high dilution rate can be fixed by adding a small amount of hydrogen (less than 10 %).

Since the increase in the carbon monoxide percentage leads to an increase in CO₂ and CO emissions and a slight decrease in the reactivity, it is better to reduce its quantity in the fuel mixture.

Hence, in a closed homogeneous reactor, a biogas/syngas mixture can be optimized by controlling carbon dioxide and hydrogen values. The former will serve as a diluent that will reduce NO_x and CO, and the latter will adjust the reactivity of the mixture and reduce the carbon emissions. However, we should not forget that we are working on biogas/syngas mixtures; therefore, the quantities of CH₄, H₂, CO₂, and CO are limited by the initial conditions of the methanisation and the gasification technique. If we consider X% biogas and (100-X) % syngas, the percentage of methane is related to carbon dioxide and that of hydrogen to carbon monoxide. As a result, in order to choose a fuel that meets the objectives mentioned earlier while respecting the composition percentages, a proposition is optimized and presented in Table 24.

Table 24: optimized fuel mixture in auto-ignition point of view

| | Φ (-) | H ₂ (%) | CO (%) | CH ₄ (%) | CO ₂ (%) | T _c (K) | P _c (bar) |
|--------------------------|-------------|--------------------|-----------|---------------------|---------------------|--------------------|----------------------|
| Biogas/Syngas mixtures | | B < (100-X) | (100-X-b) | a < X | (X-a) | [920-1040] | [10-15] |
| Auto-ignition phenomenon | Lean (<0.8) | b=10+b' | 90-X-b' | a | (X-a) | [920-1040] | [10-15] |

In this table, (a) represents the percentage of methane, ('b') represents the percentage of hydrogen in the mixture, and (b') the additional percentage of hydrogen knowing that 10% are already considered. The value of (b') depends on the percentage of carbon dioxide in the mixture; the highest is CO₂, the highest will be the value of (b'). These values can be chosen according to the qualitative diagram of Figure 59.

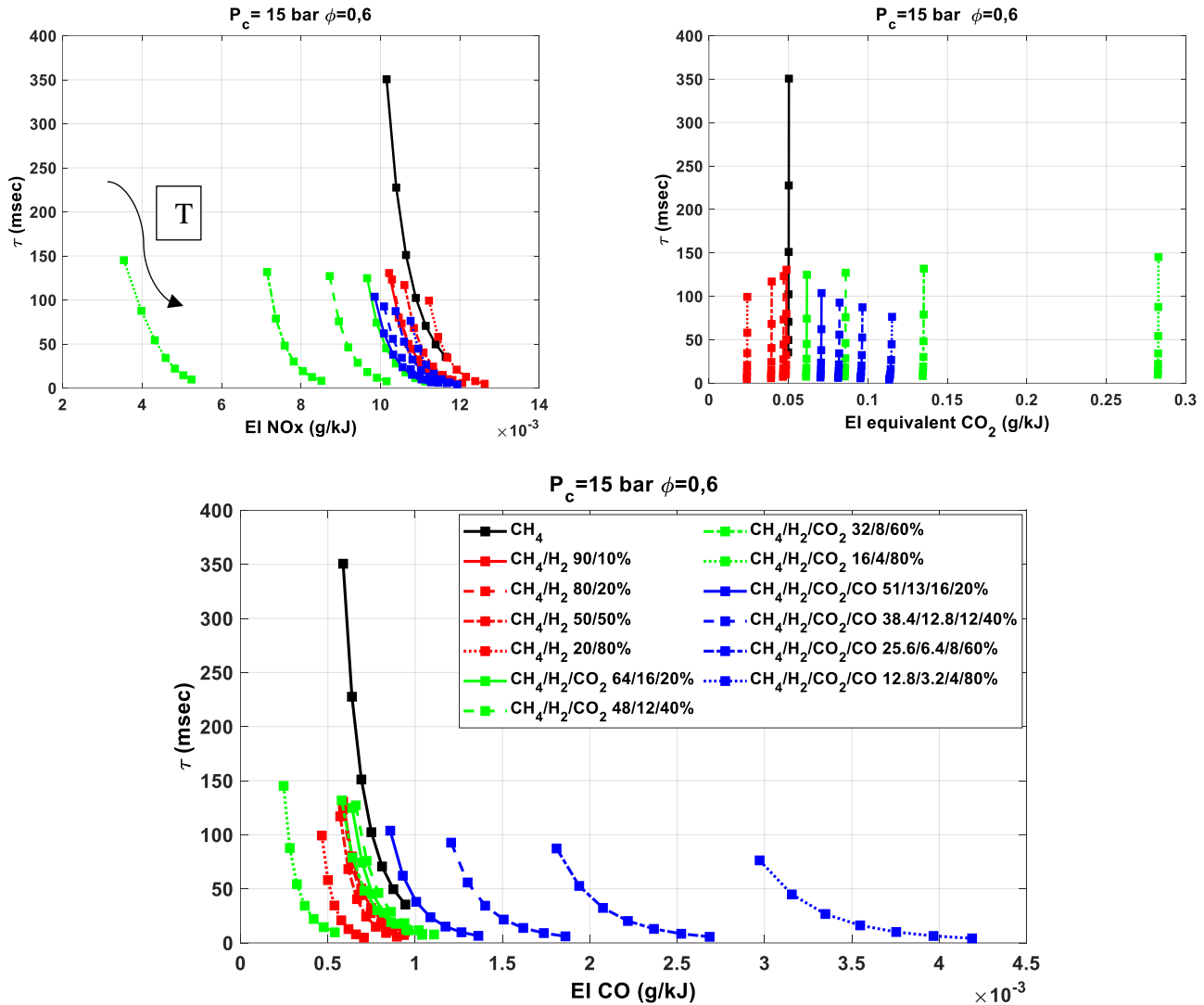


Figure 59: Auto-ignition delay times and pollutant emissions diagram (dilution 0% CO₂), T_c between 920 and 1040K

This diagram represents the ignition delay times and the pollutant indexes relative to several biogas/syngas mixtures at lean conditions and different end of the compression temperature. It is a qualitative diagram that can help determine the parameter to change to reduce the specific pollutant index or increase the reactivity.

The study presented in this section concerns the characterization of the combustion in the auto-ignition configuration. In the following section, the combustion will be studied in a propagating flame in order to have a full idea of the combustion process in lean homogeneous combustion.

Two major uncertainties are related to this study:

- Grimech3.0 predicts well the effects of the studied parameters in lean conditions, with an acceptable simulation time. One exception is the oxidation of carbon monoxide. Therefore, the first uncertainty concerns the fact that Grimech3.0 over-predicts the effects of carbon monoxide on the reactivity of biofuel mixtures. Therefore, only to study the effect of carbon

monoxide on the reactivity of biofuel combustion, AramcoMech1.3 was used to explain the chemical reactions induced by the addition of carbon monoxide. However, Grimech3.0 was used in the rest of the study majorly due to its low simulation time. The presented charts were all based on Grimech3.0.

- The second uncertainty concerns the assumption of adiabatic conditions due to which the highest NO_x emissions were shown for lean conditions. This is also not representable of the real applications, where the importance of lean conditions is majorly linked to its impact on reducing NO_x and CO emissions.

V. Approach II: Adiabatic premixed flame

Based on the simplified approach introduced at the beginning of this chapter, the combustion of biogas/syngas mixtures under lean conditions will be studied in this section in a propagating flame configuration.

Many practical combustors, including internal combustion engines, rely on premixed flame propagation; for premixed combustion to occur, the fuel and oxidizer must be sufficiently mixed before being introduced into the combustion chamber.

If the reactants are not fully mixed, partially premixed or non-premixed combustion will take place. Once completely mixed, ignition will occur if the ratio of fuel to oxidizer is within the flammability limits, and a sufficiently high local mixture temperature is present.

The initial heat required for the reaction to occur for spark-ignition engines is supplied via a spark from a spark plug. However, in gas turbines, the recirculation of hot burnt gases sufficiently raises the mixture temperature for the reaction to occur. On the other hand, in lean homogeneous combustion, the flame will more eventually propagate from one or multi-ignition sites.

Hence, studying the propagating flame phenomenon is essential to comprehend the physical aspects of lean homogeneous combustion.

In order to highlight these aspects, a numerical study will be carried out on Chemkin-Pro to analyze the characteristics of the premixed flame using a freely propagating flame. Thus, a parametrical study on the effect of the initial conditions and fuel composition on the combustion properties will be studied in the following section. The flame speed and flame stability are important characteristics of flame that account for the thermodynamic and transport phenomenon. Hence, the influence of the initial conditions and fuel mixtures on these parameters and on the produced pollutant emissions will be presented. At the end of this study, we will propose an optimized range of conditions that minimize pollutant emissions while maintaining flame stability and specific flame speed.

1. Simulated conditions and assumptions

Generally, flame front propagation is due to thermal and molecular diffusion of the radical species present in the fresh gases, which give rise to a multitude of chemical chain reactions.

The fresh gases in front of the flame are heated by the molecular heat conduction of the burnt gases, forming the preheating zone. When the flammable temperature of the mixture is reached, the heated

gases ignite; an exothermic reaction is created, producing locally reactive species, and forming the reaction zone.

These species, along with the released heat, diffuse towards the fresh gases leading to the propagation of the flame. The flame then consumes the reactants and leaves behind combustion products.

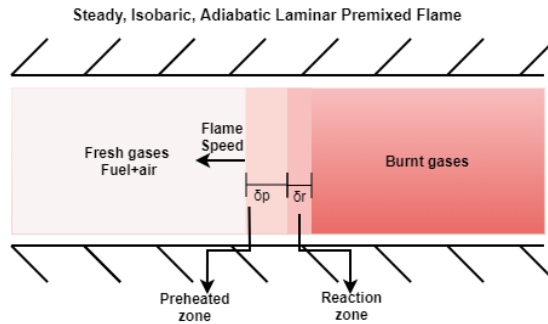


Figure 60: Model used in Chemkin for the calculation of laminar premixed flame speed

In our study, the premixed flame is simulated using a freely propagating premixed laminar flame in Chemkin-Pro. The simulated flame is considered steady, adiabatic, isobaric, quasi-one-dimensional, as shown in Figure 60.

We consider in this study, that the flame front propagation is defined when the chemical reaction is initiated at a certain nucleus independently of gas dynamic processes. Thus, the initial pressure and temperature are considered equal to the end of compression pressure (10, 15 and 30) and temperature (920:1040 K). The equivalence ratio is varied from 0.6 to 1.4. The fuel composition was also varied based on the experimental study.

The simulations accounted for multi-component transport as well as thermo-diffusion. The adaptive grid parameters (GRAD = 0.025 and CURV = 0.1) were suitably selected to obtain grid-independent values of laminar burning velocity.

2. Flame characteristics and properties

In premixed flame combustion, flame speed and thickness are important characteristics of flame ignition and propagation, while flame stability is more concerned with flame extinction. The burning velocity and the thickness of the flame front are controlled by transport processes in laminar flame. These processes are mostly influenced by the concurrence of thermal conductivity and species radical diffusion. Flame stability, on the other hand, is the result of the interaction of several physical phenomena.

Thus, these parameters (flame speed, thickness, and stability) are directly related to the physical aspects of the flame. Consequently, they will constitute the core of the parametric study in the premixed flame configuration.

5.1.2.1. Flame speed and thickness

In combustion research, one of the essential characteristics of premixed flames is the burning velocity determining both fuel consumption and heat release rates.

The laminar flame speed can be defined as the propagation speed of a flame front, normal to the front, as it moves relative to a stationary unburnt gas mixture.

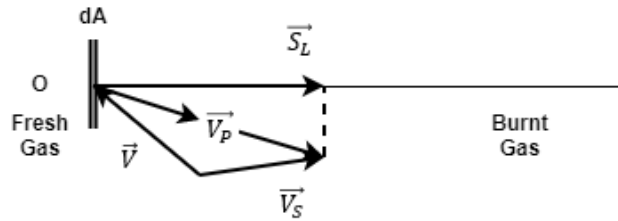


Figure 61: Flame Speed as described by Borghi and Destriau[123]

As described by Borghi and Destriau [123], the premixed laminar flame can be represented as a surface separating the fresh gases from the burnt gases. In the flame frame of reference, the fluid mixture propagates at the velocity of propagation V_p . The fresh gases are transported to the flame surface with a velocity V . Let dA be an element of the flame surface as shown in Figure 61. This element propagates with the space velocity noted V_s and centered on the point O [123] in the laboratory's reference frame.

However, the most representative quantity in the diagram shown in Figure 61, is the normal flame front component of velocity V_p , referred to as the laminar flame velocity S_L .

$$\vec{V}_p = \vec{V}_s - \vec{V} \quad (V.1)$$

In the case of a one-dimensional planar flame, the velocity of propagation is normal to the flame front and therefore equal to S_L . The relation (V.4) then becomes

$$\vec{S}_L = \vec{V}_s - \vec{V} \quad (V.2)$$

When the flame is not subjected to stretching, its laminar flame speed is written S_L^0 . This is particularly the case of a one-dimensional plane flame propagating in an open environment initially at rest ($V=0$). The stretch is precisely defined later.

Prior to computational methods, S_L was found using either experimental campaigns or simplified thermal theory first proposed by Mallard and Le Chatelier [124].

With the development of computational techniques for determining S_L , the dependence of laminar flame speed on pressure, preheating temperature, and mixture composition can more easily be determined, allowing for a more in-depth understanding of laminar structure flames and combustion in general.

Another essential characteristic of the flames is flame thickness; it is routinely used to normalize turbulent flame properties.

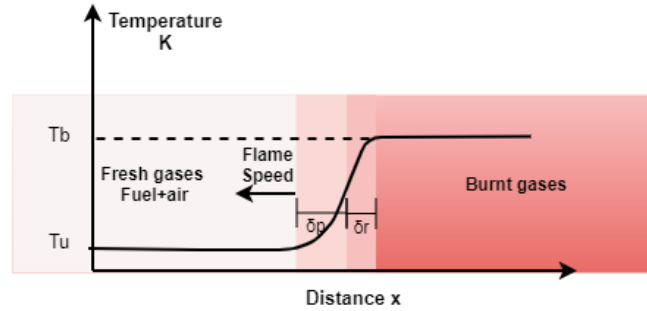


Figure 62: Flame thickness calculation

As can be seen in Figure 62, the flame region with a temperature gradient is often referred to as a one-dimensional laminar flame. This region is divided into two distinct zones:

- The preheating zone is characterized by the flame thickness δ_p in which the processes of diffusion and convection of mass and heat predominate. Chemical reactions are negligible in this zone.
- The reaction zone is characterized by the flame thickness δ_r , in which heat is released due to chemical reactions.

Thus, the front laminar flame thickness is defined as the sum of both the reaction and preheating zone thicknesses:

$$\delta_L = \delta_r + \delta_p \quad (V.3)$$

Therefore, to determine the thickness of the laminar flame, it is necessary to find the thicknesses of the reaction and the preheating zone.

The thickness of the reaction zone is deduced from the thickness of the preheating zone and the Zeldovich dimensionless number β , which measures the sensitivity of the reaction speed to temperature. It is given by the following relation:

$$\delta_r = \delta_p / \beta \quad (V.4)$$

Since the Zeldovich number β is infinitely large compared to the thickness of the preheating zone, the thickness of the reaction zone can be considered negligible [125].

The thickness of the preheating zone δ_p (commonly called Zeldovich thickness) is generally defined by the following relation:

$$\delta_p = \frac{\lambda}{\rho C_p S_L^0} \quad (V.5)$$

With λ the thermal conductivity of the reactive mixture, C_p the thermal capacity, ρ the density of the mixture and S_L^0 is the laminar flame velocity.

This definition is obtained by assuming that all the energy produced by combustion is used to raise the temperature of the fresh gases present in the preheating zone.

Spalding proposes another definition of the thickness of the laminar flame, assimilating it to the thickness of the heat release zone. It is then defined by the ratio of the difference between the burnt gas temperature T_b and the fresh gas temperature T_u to the maximum temperature gradient.

$$\delta_s = \frac{T_b - T_u}{\max(\text{grad}(T))} \quad (V.6)$$

This definition of the laminar flame thickness is the most convenient for determining the mesh resolution of numerical calculations since it can be measured locally along the flame front.

2.2.Flame Stability and types of instabilities

Flame stability is an important concept in flame combustion. It is concerned more with flame extinction phenomena rather than its ignition. It refers to the ability of an existing flame to stay ignited despite variations in the fuel and oxidizer flow rates, fuel quality, and turbulent shear.

Combustion instabilities are numerous. They result from the interaction of two or more physical phenomena. Some involve the properties of the system (instabilities due to gravity forces, for example); others are intrinsic to the flame front propagation mechanisms (hydrodynamic and thermo-diffusive instabilities). These instabilities modify both: the local equilibrium of the thermodynamic parameters and the local concentrations of the species and cause the deformation of the flame front[126].

In technological applications, flame instabilities can have both a damaging effect and a favorable effect, such as enhanced burning. It can arise from the interaction between the combustion field and the surrounding apparatus or intrinsic to the combustion field.

During the propagation of a premixed flame front, various instabilities can occur and influence the flame dynamics. These instabilities can induce heterogeneities of species concentration or temperature, leading to local imbalances between heat and species diffusion. These imbalances are then responsible for the deformation and displacement of the flame front.

Three types of instabilities will be presented in this study:

- Acceleration instabilities (due to gravity forces)
- Hydrodynamic instabilities
- Thermal instabilities

Each of these three phenomena can either have stabilizing effects that will bring the flame back to a stable state or accentuate the imbalances until the flame front extinction.

Hydrodynamic instabilities

A premixed flame is characterized by a high difference in density between fresh and burnt gases. Due to the strong temperature gradient on both sides of the flame front, the normal velocity of the flame front is multiplied by the expansion factor ρ_b/ρ_u during the transition from flue to fresh gas. Darrieus and Landau [127] have shown that a flame that is considered to be hydrodynamically unstable is unconditionally unstable. The change in velocity across the flame front induces the low lines to deviate towards the normal to the front on the flue gas side.

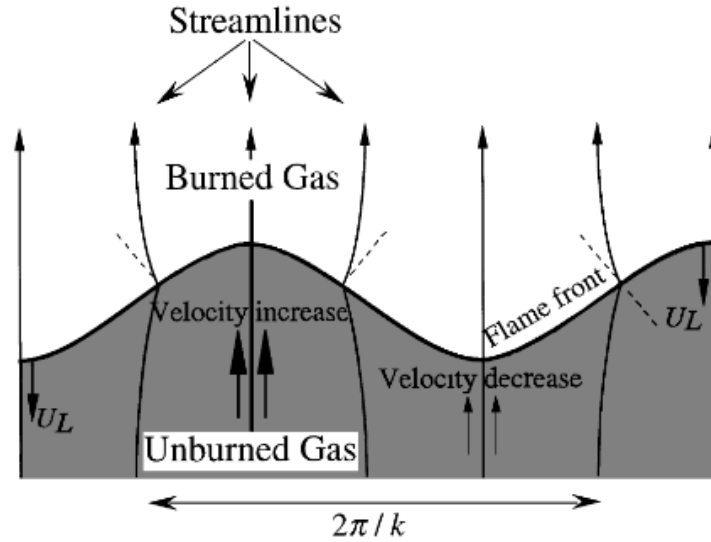


Figure 63: Deviation of flow lines leading to the Darrieus-Landau instability[127].

As a result, the flue gas flow converges downstream of the convex parts to the fresh gas. Conversely, the flue gas flow diverges downstream of the concave parts from the fresh gas Figure 63. Thus, the curvature of the flow lines causes the formation of a pressure gradient parallel to the flame front. Therefore, the change in the downstream flame front caused by these gradients is immediately reflected in the upstream flow. The fresh gas flow is slowed down in front of the convex parts and accelerated in front of the concave parts.

Thermal instability

Thermal instability appears when heat and species diffusion fluxes are perpendicular to the reactive areas of the flame but in opposite directions (Figure 64). This results in local enrichments of mass and temperature. The competition between these two diffusion phenomena is characterized by the Lewis number, which will be detailed in the following sections:

$$Le_i = \frac{\alpha}{D_i} \quad (V.7)$$

Where α is the thermal diffusion and D_i the mass diffusion coefficient.

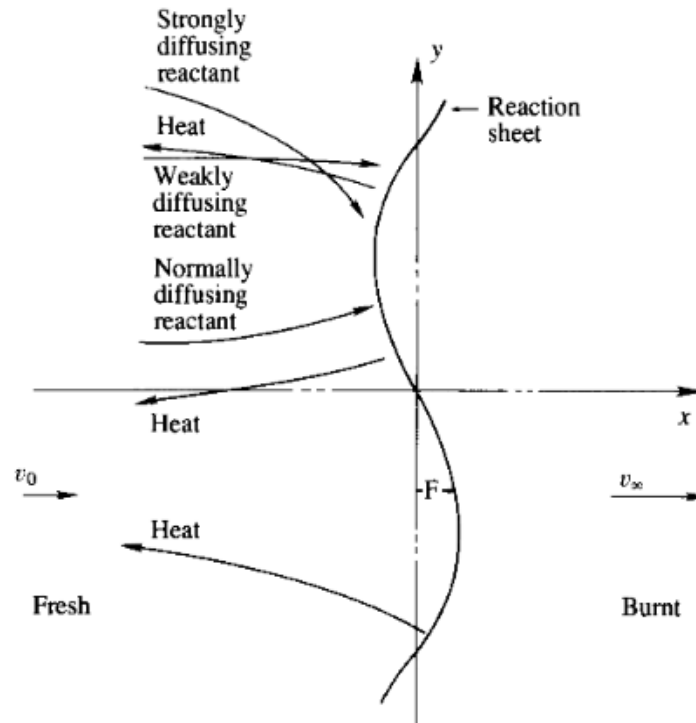


Figure 64: Schematic illustration of the mechanism of diffusive-thermal instability [128].

If the Lewis number is lower than the critical Lewis number of the mixture, the flame is unstable. The critical Lewis number is usually close to unity and depends mainly on the fuel through the activation energy and the adiabatic flame temperature. It can be defined by the following relationship proposed by Williams [128]:

$$Le_c = 1 - \frac{RT_b}{E_a} \frac{(2\sigma_d \ln \sigma_d)}{\int_0^{\sigma_d-1} \frac{1}{x} \ln(1+x) dx} \quad (V.8)$$

Where σ_d is the ratio of the density (burnt gas to fresh gas) and x the distance (mm).

The Lewis number thus appears as an important parameter of laminar and turbulent combustion with an influence on the stability, dynamics but also the structure of the flame. Therefore, three configurations can occur comparing Lewis number to the critical number:

- If $Le_i = Le_c$, the flame is stable and its wrinkling is mainly due to turbulent flow.
- If $Le_i > Le_c$, heat diffusion outweighs species diffusion, which has a stabilizing effect.
- If $Le_i < Le_c$, the instabilities increase due to species diffusion effects that outweigh thermal diffusion. Indeed, the mass diffusion has a destabilizing effect on the flame and this is visually translated by the appearance of "cells".

Thus, a numerical study will be carried out on Chemkin-Pro to study the premixed flame configuration using the freely propagate flame model. Thus, a parametrical study on the effect of the initial conditions on the combustion properties will be studied in the following section, on flame

speed, pollutant emissions, and flame stability. Prior to the parametric study, we note that when studying the effects of pressure, temperature or equivalence ratios, four biogas/syngas mixtures are normally considered: CH_4 ; CH_4/H_2 80/20 %; $\text{CH}_4/\text{H}_2/\text{CO}_2$ 64/16/20 %; and $\text{CH}_4/\text{H}_2/\text{CO}_2/\text{CO}$ 51/13/16/20 %. These mixtures correspond to the experimental study conducted on chapter 2, and using them will allow the homogenization of the studied data. In other words, we could eventually select other mixtures, but our purpose is to give qualitative database on the effect of each parameter

3. Parametric study of flame speed

In the following paragraph, the influence of the initial conditions (temperature, pressure and equivalence ratio), along with fuel composition on the flame speed will be discussed.

Pressure and equivalence ratio influence

As explained earlier, the flame propagation through the unburned mixture depends consists mainly of two zones: the preheating and the reaction zones. Both zones are equally crucial for the propagation process, and therefore one it is expected that the flame speed will depend on both transport and chemical reaction properties.

The effects of the initial pressure and temperature on the flame speed are represented in Figure 65 and Figure 66, respectively, for four different biofuel mixtures.

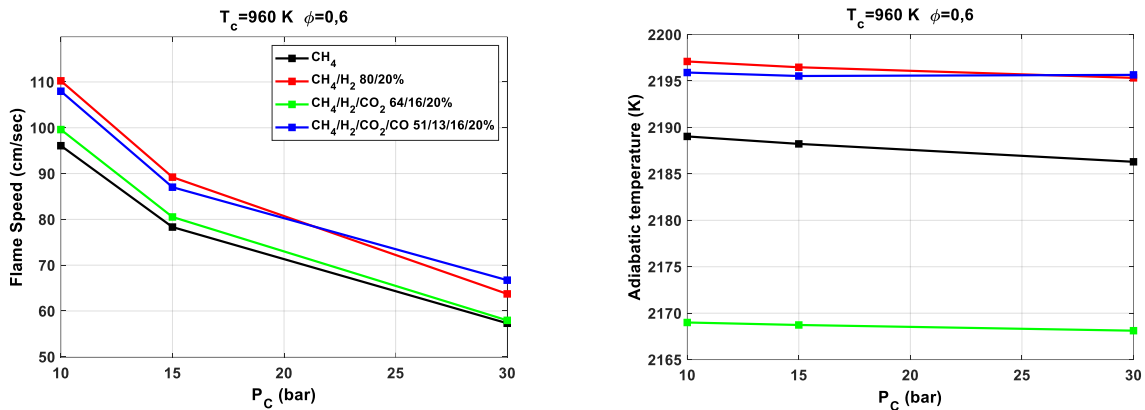


Figure 65 : Influence of pressure on the flame speed

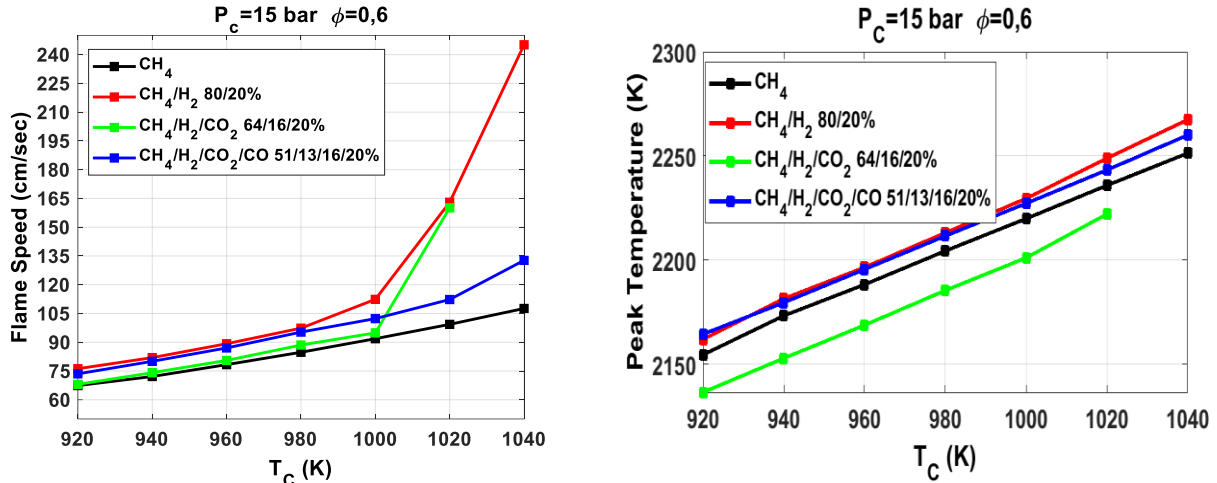


Figure 66: Influence of temperature on the flame speed

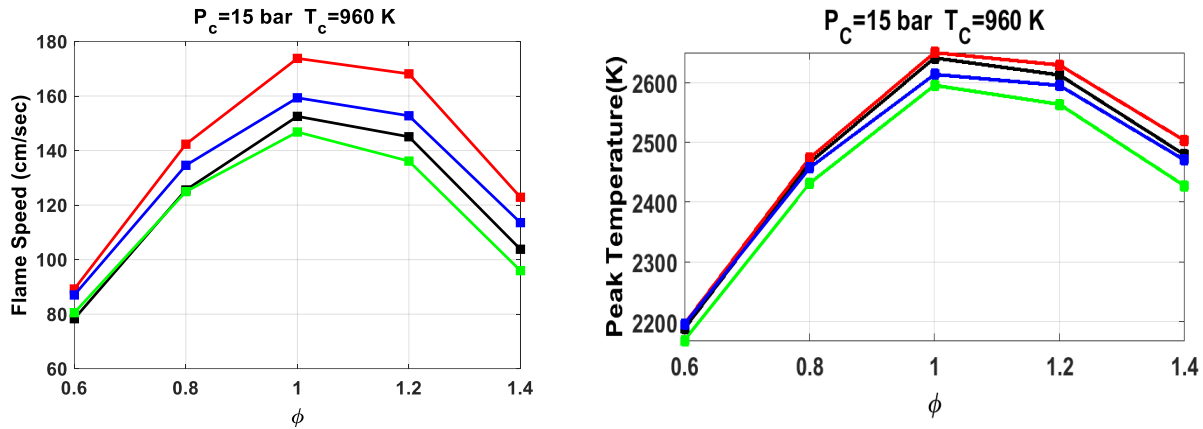


Figure 67: Influence of the equivalence ratio on the flame speed

It is observed that the flame speed increases with the fresh gas temperature for all the studied mixtures. On the other hand, the flame speed is shown to decrease with the initial pressure. Actually, increasing temperature leads to faster chemical reactions, which will reduce the chemical time, inducing an increase in flame speed. Besides, the thermal diffusivity for ideal gases can be written as:

$$\alpha = \frac{k(T)}{\rho C_p} = \frac{RTk(T)}{PC_p} \sim T^{1,5} P^{-1} \quad (V.9)$$

According to this equation, an increase in temperature will increase the thermal diffusivity, hence the flame speed. However, the pressure is inversely proportional to the thermal diffusivity; increasing pressure leads to a decrease in flame speed [129].

It is essential to note that flame speed is more sensitive to temperature than pressure for most hydrocarbon fuel mixtures. In other words, increasing the unburned gas temperature can offset the flame speed reduction due to pressure.

The effect of the equivalence ratio on the flame speed and temperatures for four biofuel mixtures is presented in Figure 67. It can be observed that the peak flame temperatures occur at a stoichiometry. The main reason for this is the relation between the combustion heat and the heat capacity of the products that decline when the equivalence ratio exceeds unity. It is expected that the flame speed dependency on the equivalence ratio will be similar to the temperature dependence on the equivalence ratio.

Thus, according to this study, the pressure can be chosen according to the engine application, and the temperature range can be adjusted to this pressure for a certain range of flame speed.

In lean combustion, the flame speed is relatively low compared to stoichiometry. However, it is shown to be higher for CH_4/H_2 mixtures and the lowest for pure methane mixtures, highlighting the effects of fuel composition on the flame speed.

Fuel composition influence

Because of the low flame velocity of CH_4 and its increased sensitivity to cyclic variations during operation, it cannot be used in the engine without being accompanied by another fuel having a higher flame velocity and low sensitivity to cyclic variations. Hence the importance of adding hydrogen with high flame velocity as an additive to improve the combustion of natural gas [73].

The evolutions of the flame speed with hydrogen, carbon monoxide, and carbon dioxide percentages are presented respectively in Figure 68, Figure 70, and Figure 72.

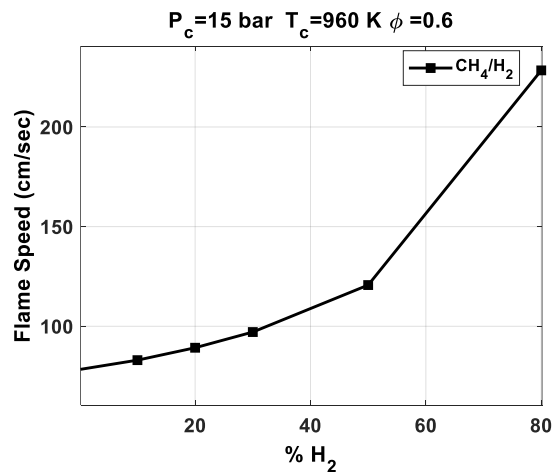


Figure 68: Influence of hydrogen percentages on the flame speed

Replacing methane with hydrogen increases the flame speed exponentially. The flame speed produced by a mixture of 50% of hydrogen is closer to that of methane than hydrogen, which means that unlike the auto-ignition phenomenon, the methane dominates the flame combustion for a percentage of hydrogen lower than 50%. Those results point out that methane, less reactive, strongly limits the flame velocity, even when mixed with an equal amount of the more reactive hydrogen. This effect of hydrogen on methane flame was studied and verified in the literature by several authors [68] [130] [131] [132].

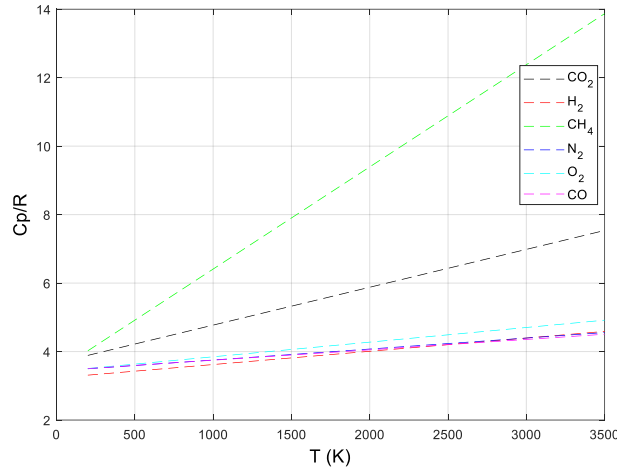
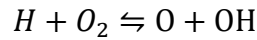


Figure 69: Specific heat capacity of biofuel components and air for different temperature

As explained in section IV, the addition of a certain amount of hydrogen boosts the reactivity of the mixture by increasing the rate of propagating chain reaction:



The heat release is also enhanced, which leads to an increase of the adiabatic flame temperature. Moreover, according to Figure 69, the replacement of methane with hydrogen will lower the heat capacity and therefore raise the thermal diffusivity. The increased reactivity and thermal diffusivity lead to an increase in laminar flame speed.

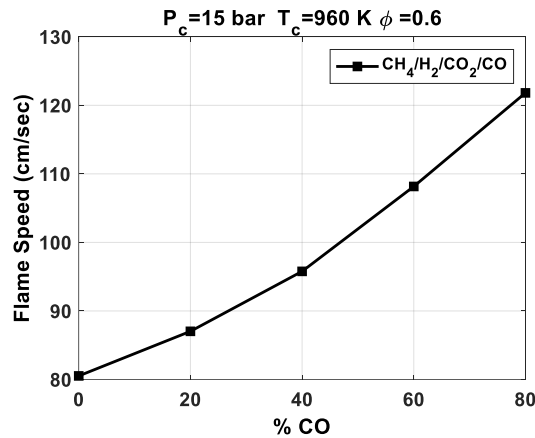


Figure 70: Influence of the carbon monoxide percentages on the flame speed

Carbon monoxide displays a similar effect as hydrogen on the flame speed [130]. However, CO is shown to be less influential on the laminar flame than hydrogen. This can be explained by the higher reactivity of hydrogen compared to carbon monoxide.

The effects of hydrogen, methane, and carbon monoxide can be viewed by the work of Lieuwen et al.[133] on the flame speed characteristics of syngas mixtures with different percentages of co-firing methane. The dependence of the flame speed on fuel composition at two fixed adiabatic flame temperatures (1500 and 1900 K) as shown in Figure 71.

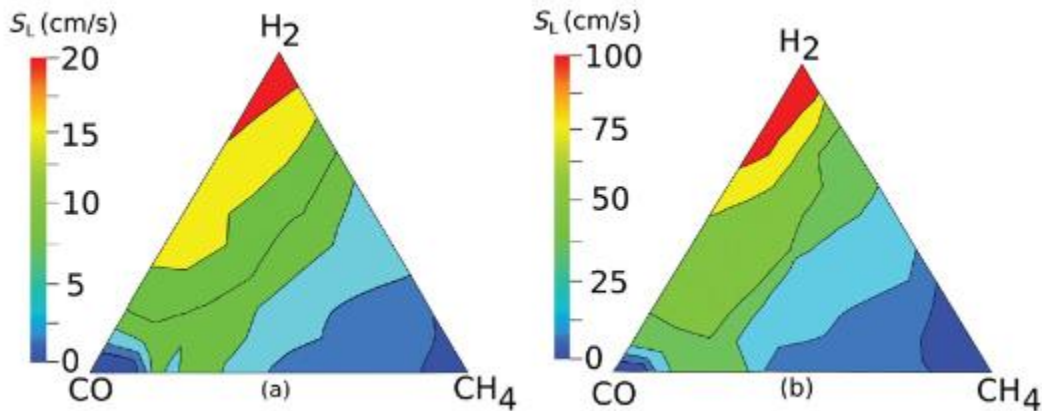


Figure 71: Laminar flame speed (cm/s) as a function of fuel composition at fixed 1500 K (a) and 1900 K (b) adiabatic flame temperature at 4.4 atm with 460 K reactant temperature[134]

The volumetric fuel composition is given by the location within the triangle, where the three vertices denote pure CO, H₂, or CH₄. The mixture equivalence ratio was adjusted at each point such that the mixture has the given flame temperature. The largest flame speed is shown for high H₂ mixtures; methane predominates the flame combustion for a certain percentage. Pure carbon monoxide is shown to have similar effects to pure methane; however, a small amount of hydrogen can control carbon monoxide's flame speed.

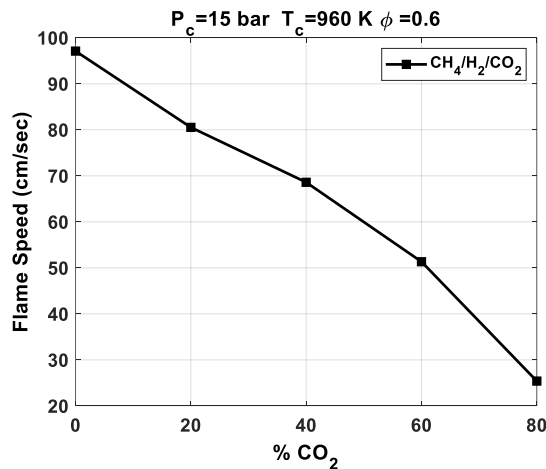


Figure 72: Influence of carbon dioxide percentages on the flame speed

On the other hand, carbon dioxide reduces the flame speed values, as shown in Figure 72. Several studies [135], [136] have been conducted on CO₂ diluted flames. These studies showed that an increase in the amount of CO₂ in the mixture decreases the laminar flame velocities.

Figure 69 clearly shows that carbon dioxide has a high heating capacity compared to the other biofuel components. Thus, when the percentage of CO₂ increases in the mixture, the thermal diffusivity decreases and, therefore, the flame speed.

Conclusions

- Flame speed depends on both transport and chemical reaction properties.
- Increasing temperature leads to faster chemical reactions; thus, the ignition time is shorter, and the flame speed is higher.
- The pressure is inversely proportional to the thermal diffusivity. For most hydrocarbon fuels, increasing pressure leads to a decrease in flame speed.
- The hydrogen and carbon monoxide have the same effect on the flame speed; when their percentage increases, the heat capacity of the biofuel mixture decreases, leading to an increase in thermal diffusivity. The increased reactivity and thermal diffusivity lead to an increase in laminar flame speed.
- CO is shown to be less influential on the laminar flame compared to hydrogen
- The carbon dioxide has a high heating capacity in comparison to the other biofuel components. Thus, when the percentage of CO₂ increases in the mixture, the thermal diffusivity decreases and, therefore, the flame speed.

4. Parametric study of pollutant emissions

The evolutions of the pollutant emissions produced in a closed reactor with the temperature, pressure, equivalence ratio, and fuel composition were studied in the previous section.

The same parametric study of the pollutant emissions is carried out on the laminar premixed flame and is presented in the following. The emissions indexes of pollutant emissions (NO_x, equivalent CO₂, and CO) were also calculated as gram per released energy units.

The pressure, temperature, and equivalence ratio show the same effects on the pollutant emissions as those shown in the auto-ignition study (Figure 73, Figure 74, and Figure 75 respectively).

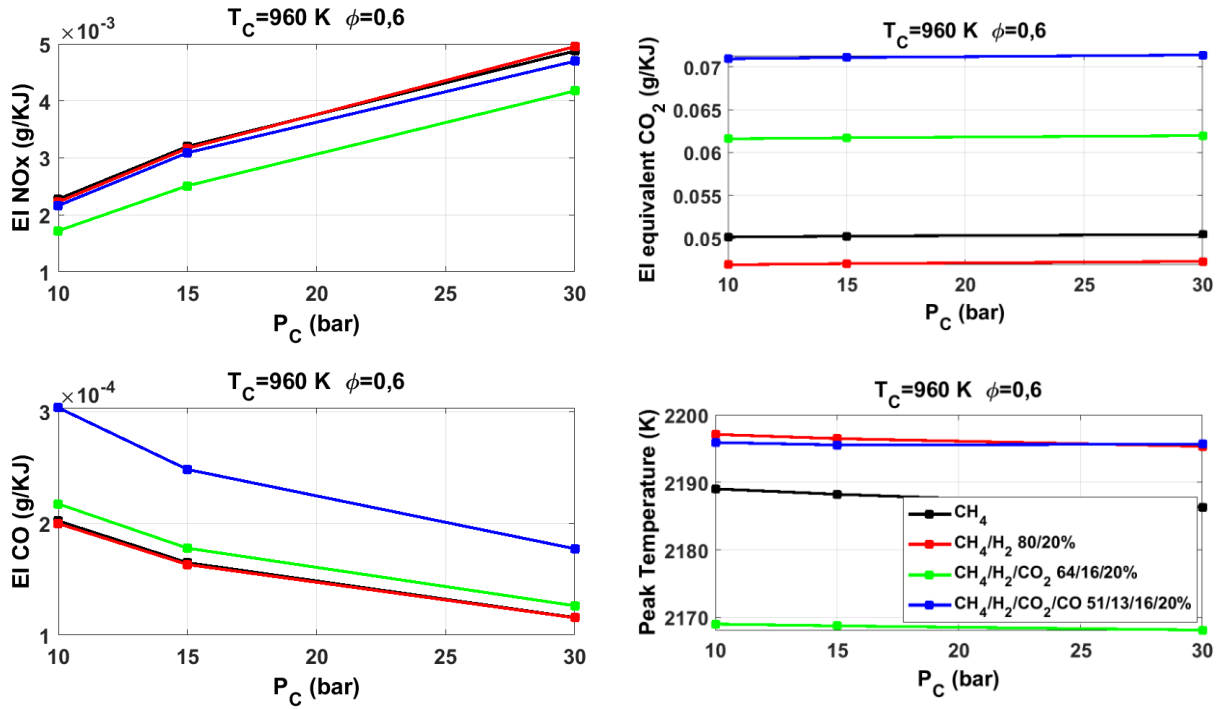


Figure 73: Influence of the pressure on the pollutant emissions index

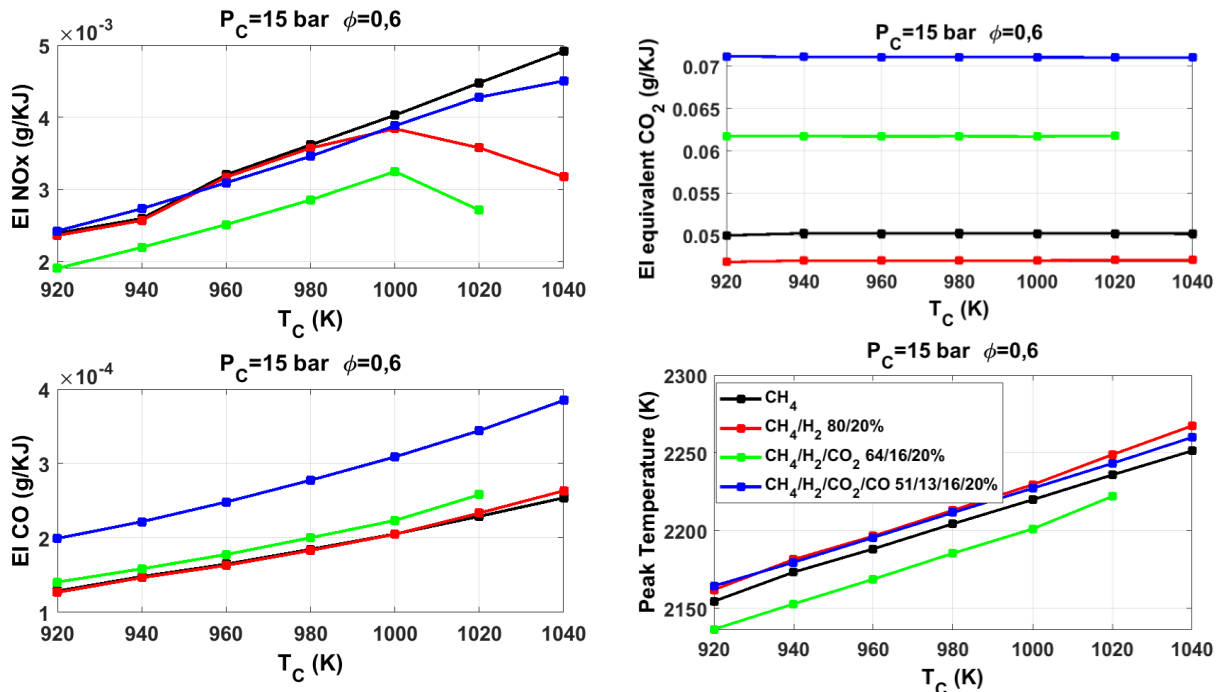


Figure 74: Influence of the temperature on the pollutant emissions index

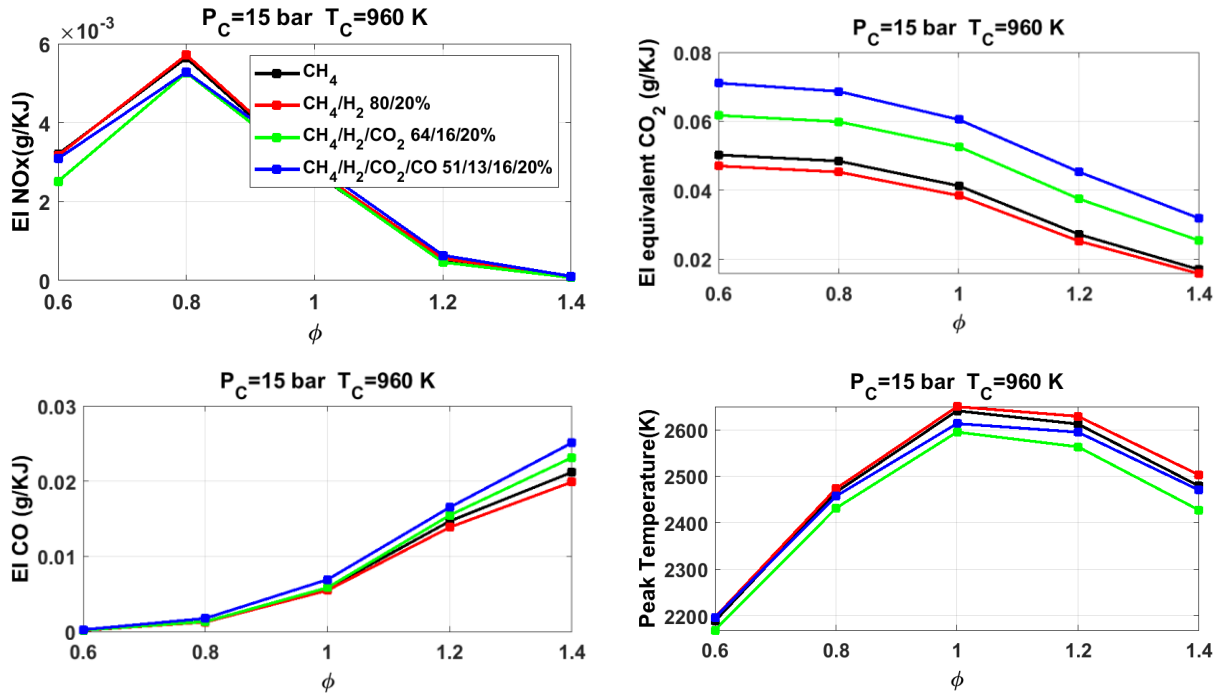


Figure 75: Influence of the equivalence ratio on the pollutant emissions index

However, the study of flame showed a relatively low emission index compared to the auto-ignition process. This can be explained by the higher energy produced in the isochoric closed reactor compared to the isobaric free flame. Therefore, the combustion peak temperature is highest in the closed reactor than in the flame configuration. The highest NO_x emissions are seen for lean mixtures of 0.8 compared to 0.6 in the closed reactor. As explained earlier, the normal effect of equivalence ratio on the NO_x emissions (as studied in literature) will be obtained for reducing peak temperature, in other words, by CO₂ dilution.

The effect of the fuel composition, as well as the dilution rate, was represented in Figure 76, Figure 77 and Figure 78. The closed reactor showed similar effects; the only difference resides in the hydrogen effect on the NO_x emissions.

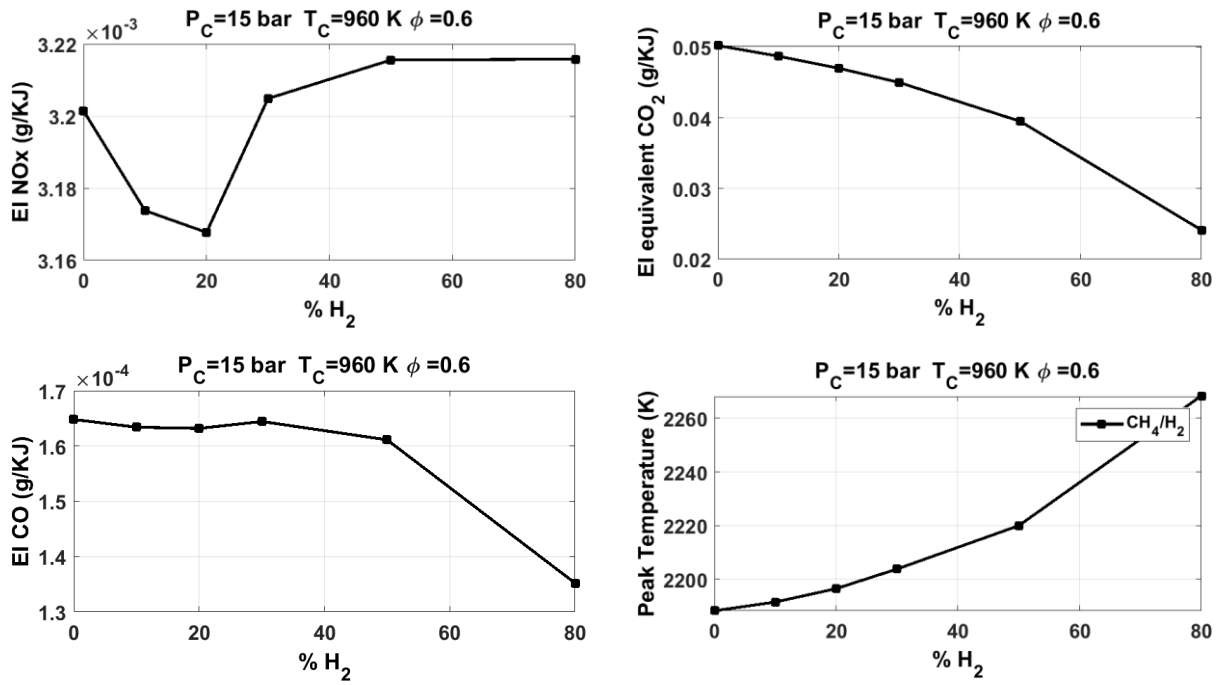


Figure 76: Influence of the hydrogen percentages on the pollutant emissions index

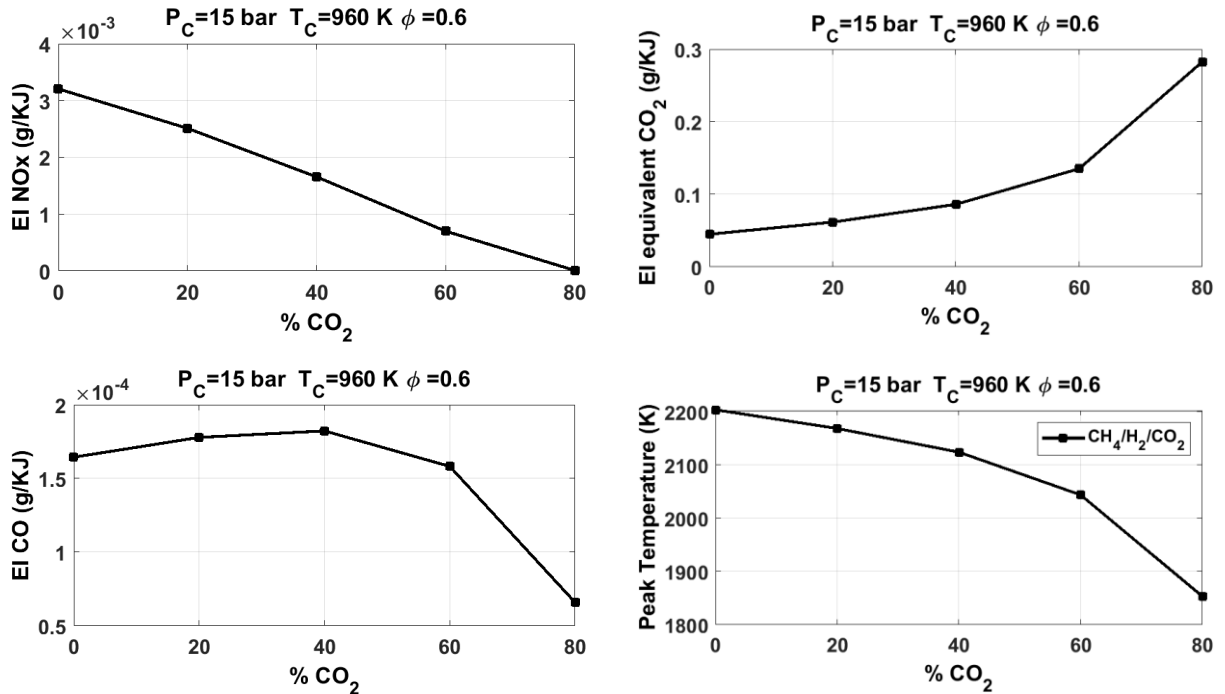


Figure 77: Influence of the carbon dioxide percentages on the pollutant emissions index

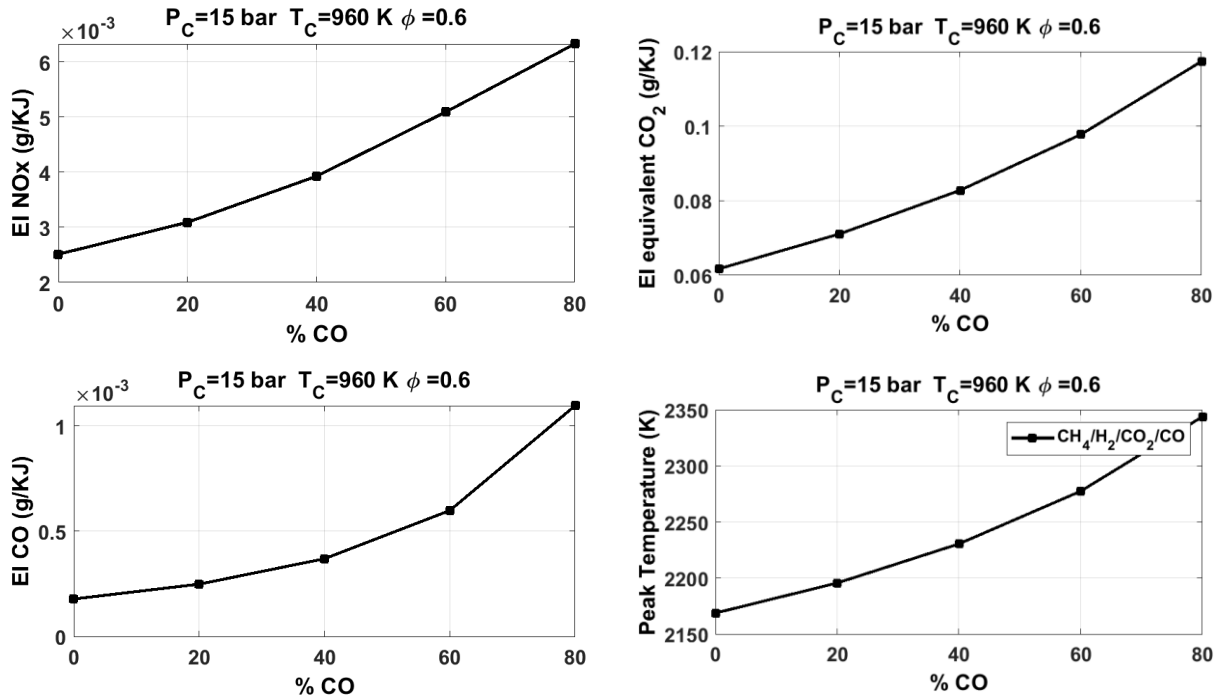


Figure 78: Influence of the carbon monoxide percentages on the pollutant emissions index

Nevertheless, Figure 76 indicates that adding small amounts of hydrogen (less than 20%) decreases NO_x emissions. For a higher value, NO_x emissions increase with hydrogen.

Conclusions

- The effect of the pressure and temperature of the pollutant emissions in flame point of view are the same as the auto-ignition case
- The emissions values are higher in the study of auto-ignition than those in flame configurations. This can be explained by the higher energy produced in the isochoric closed reactor compared to the isobaric free flame. Therefore, the temperature at the end of the combustion process is highest in the closed reactor than in the flame configurations.
- The highest NO_x emissions are seen for lean mixtures of 0.8 compared to 0.6 in the closed reactor.
- The effect of the fuel composition of the pollutant emissions in flame point of view are the same as the auto-ignition case

5. Parametric study of flame stability

As explained earlier, the stability is a highly important parameter in flame characterization. In this section, we will study the effects of each parameter of the thermal instability of premixed flames. This can be done by comparing the Lewis number of the mixture with the critical Lewis number.

5.2. Calculation of Lewis number and critical Lewis number

Lewis number is the ratio of the thermal diffusion coefficient to that of the mass diffusion. It is used to measure the balance of these two diffusion phenomena and to determine which diffusion has more influence on the combustion process. A Lewis number lower than unity indicates a higher thermal effect than the mass scattering, and a Lewis number greater than unity indicates a higher diffusion effect.

Lewis number is frequently assumed as unity, in order to simplify the energy conservation equation for simple combustion problems. However, in the present work, it is of interest to study more realistic cases, for which Lewis number differs from one, and to evaluate how this physical quantity affects the flame parameters.

Lewis number is usually defined as:

$$Le_i = \frac{\alpha}{D_i} \quad (V.10)$$

α is the thermal diffusion and D_i the mass diffusion coefficient.

The thermal diffusion coefficient is defined as the ratio of the thermal conductivity λ of the mixture and the product of mass density and specific heat capacity:

$$\alpha = \frac{\lambda}{\rho_u C_p} \quad (V.11)$$

The thermal conductivity of the mixture λ is defined as:

$$\lambda = \frac{1}{2} \left(\sum_{k=1}^N X_k \lambda_k + \frac{1}{\sum_{k=1}^N \frac{X_k}{\lambda_k}} \right) \quad (V.12)$$

The empirical formula of mass diffusivity is given by:

$$D_{i,j} = \left(\frac{1,8583e - 3}{P \sigma_{i,j}^2 \Omega_D} \right) T^{3/2} \sqrt{\left(\frac{1}{M_i} + \frac{1}{M_j} \right)} \quad (V.13)$$

Where:

- M is the molecular weight of the component;
- P is the pressure in (atm);
- j is the major species in the mixture (generally nitrogen);
- $\sigma_{i,j}$ is the characteristic diameter of the molecules called the collision diameter;
- Ω_D is a dimensionless quantity called the collision integral and is a function of dimensionless temperature;

For a mixture of two or more fuels, three definitions of Lewis number can be used for lean and stoichiometric mixtures [137]:

Lewis number based on heat release base:

$$Le_H = 1 + \frac{\sum_{i=1}^n Q_i (Le_i - 1)}{\sum_{i=1}^n Q_i} \quad (V.14)$$

Lewis number on a volume-base:

$$Le_V = \sum_{i=1}^n X_i Le_i \quad (V.15)$$

Lewis number on a diffusion-based:

$$Le_D = \frac{\alpha}{\sum_{i=1}^{nb} X_i D_{i,j}} \quad (V.16)$$

Where:

- X_i is the mole fraction of the component “i” of the fuel;
- Le_i the Lewis number of each component;
- Q_i the amount of heat release;
- nb the total number of components;
- $D_{i,j}$ the mass (or molecular) diffusivity of each component for the major specie (in our study, it is nitrogen or carbon dioxide in case of high dilution rate).

For rich mixtures, the same formulations of Lewis number can be used by replacing fuel components by oxidant O_2 . Thus, the Lewis number calculation through each of the presented methods is nearly the same.

In contrast, the values are widely dependent on the calculating method for lean mixtures. And, since hydrogen has an overwhelming effect on CO regarding the stability of the flame, the most suitable approach will be the Lewis number on diffusion basis [137].

In the previous section, a critical Lewis number was defined to determine the thermal stability of the premixed flame. However, using asymptotic analysis for an adiabatic flame, the instability was found to occur below unity:

$$Le_c = 1 - \frac{2}{\beta} \quad (V.17)$$

Where β is the Zeldovich number defined as:

$$\beta = \frac{E_a T_b - T_u}{R T_b^2} \quad (V.18)$$

The activation energies E_a can be obtained from single-step reaction rate parameters; according to Westbrook et al. [138], a value of 30 kcal/mol is sufficient to have good agreement between computed and experimental results for the reaction rate of hydrocarbons. Thus, this value will be used in our study.

However, according to Clark et al. [139], as the flame front was considered to be an infinitely thin density discontinuity, the asymptotic analysis under-predicts the critical Lewis number by an amount of the order of $(\frac{1}{\beta})^{18}$. Hence, for this study, the critical Lewis number should be considered as:

$$Le_{c-2} = 1 - \frac{1}{\beta} \quad (V.19)$$

This critical Lewis number will be used in the following paragraph to characterize the effects of parameters on flame stability.

5.3.Parametric study

The evolution of diffusive based Lewis number and critical Lewis value with the temperature, pressure and the equivalence ratio for different biofuels is represented in Figure 79.

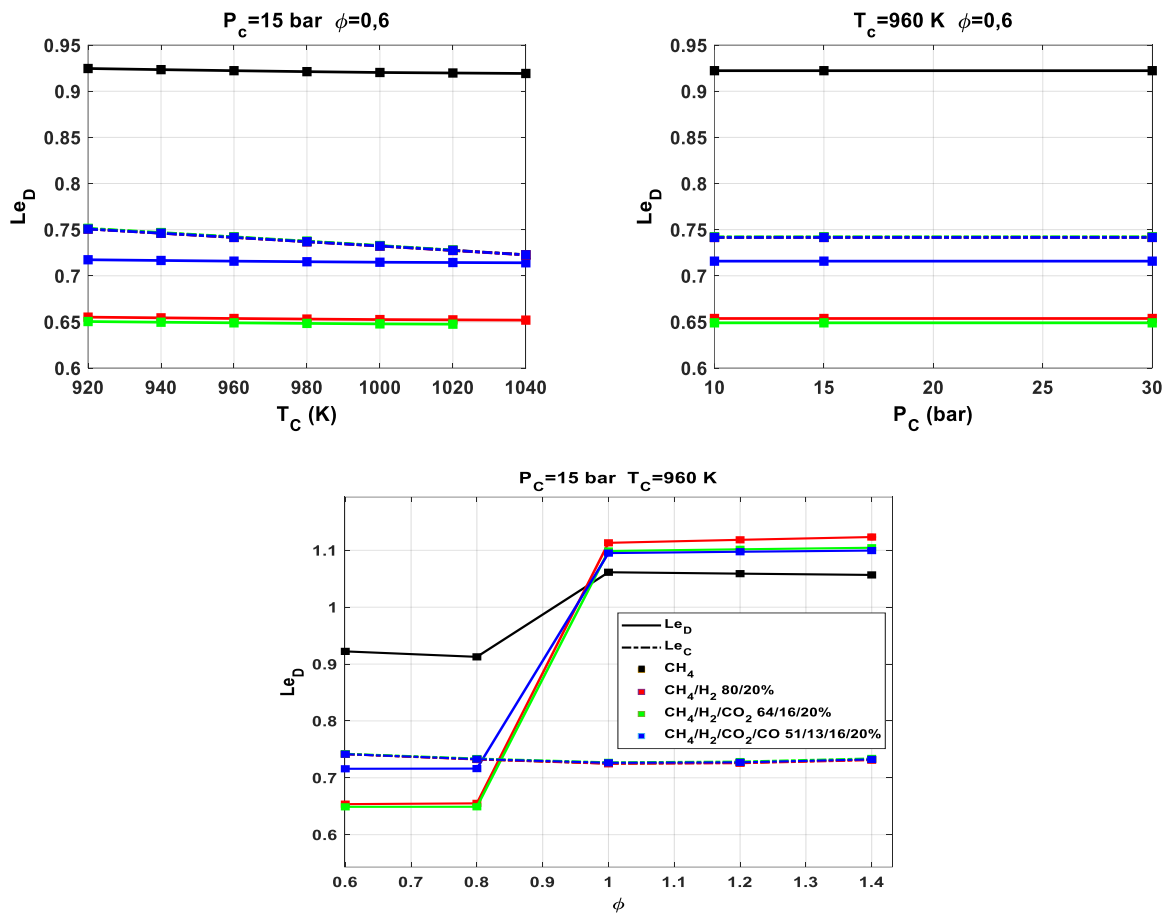


Figure 79: Evolutions of Lewis number diffusive based with the pressure, temperature and equivalence ratio of different types of biofuel

As can be seen in the figure above, the pressure and temperature do not have any effect on the Lewis number value, and therefore on the flame stability.

As explained in the parametric study of the flame speed, the increase in temperature leads to the increase of thermal diffusivity as well as the rate of chemical rate; in other words, the thermal and mass diffusion coefficient increase. As a result, the balance of these two diffusion phenomena is not affected by the temperature change and therefore Lewis number is shown to be constant.

In contrast, the equivalence ratio is an important factor in the flame stability calculations. Lewis numbers are the lowest for lean mixtures and they increase as the mixture becomes richer. For all stoichiometric and rich mixtures, Lewis numbers are higher than the critical Lewis values, which indicates a stable flame. However, for lean conditions ($\phi = 0.6$ and 0.8), the Lewis numbers of methane/hydrogen and methane/hydrogen/carbon dioxide mixtures are lower than their critical ones. This means that these mixtures are not stable.

The evolution of Lewis number with the fuel compositions is represented in Figure 80.

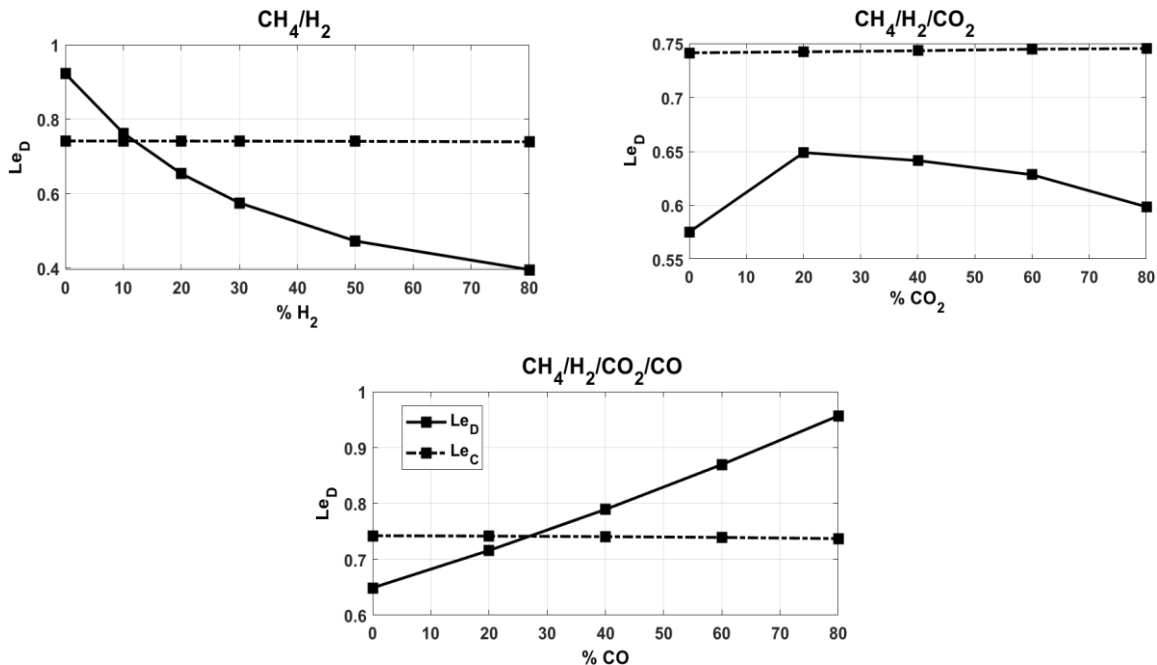


Figure 80: Evolutions of Lewis number with the fuel percentages at $P_c=15$ bar, $T_c=960$ K, and $\phi=0.6$

As can be seen, the hydrogen addition decreases the stability of methane flame. This stability can be fixed by the addition of carbon monoxide.

Several studies were made on syngas mixtures. It was demonstrated that H₂ increases thermal instabilities especially for lean mixtures. On the other hand, the presence of CO decreases hydrodynamic and thermo-diffusive instabilities [140], [141].

The carbon dioxide is the most destructive of the flame stability. As its concentration increases, the thermal diffusivity decreases and so does the Lewis number.

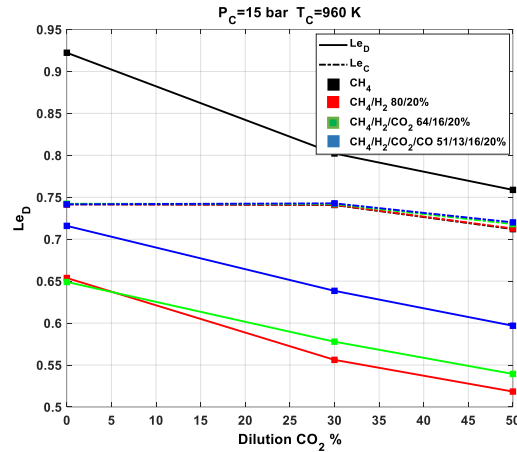


Figure 81: Evolutions of Lewis number with the dilution rate

As shown in Figure 81, for lean conditions, as CO_2 dilution rate that exceeds 30 %, all the presented biofuel mixtures except methane show a Lewis number under the critical value, thus indicating unstable flame.

Zhen et al [142] studied the effect of hydrogen addition under stoichiometric conditions on flame stability of three different biogas compositions (CH_4/CO_2 40/60), (CH_4/CO_2 50/50), (CH_4/CO_2 40/60). The results of the flame stability study showed that pure biogas flames without any hydrogen addition are not stable; thus, the flames will be stabilized at the burner when a certain minimum amount of hydrogen is introduced. The same results were obtained for lean, stoichiometric and rich mixtures and led to the same results made previously [143].

Since carbon dioxide has a destructive effect on flame front stability, its concentration in the mixture should be chosen wisely in lean conditions. Additionally, as shown previously, for a dilution rate that exceeds 30 % CO_2 , and at lean conditions, the flame for all the presented biofuels is unstable. The Lewis numbers for different biofuel mixtures and dilution rate are presented in Figure 82.

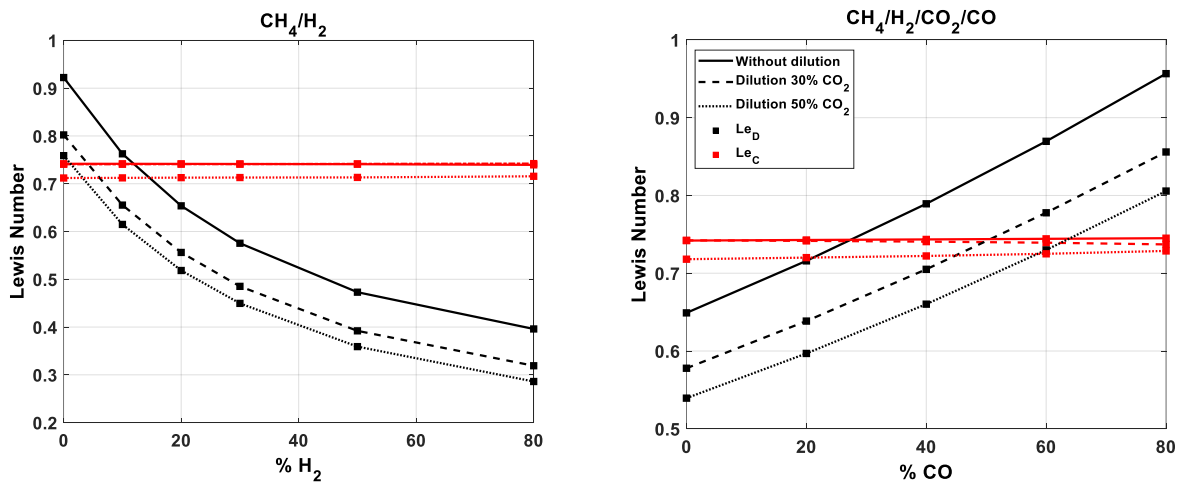


Figure 82: effect of hydrogen and carbon monoxide addition on biofuel mixtures stability for different dilution rate

As the dilution rate of CO₂ increases, the flame becomes more sensitive to hydrogen concentrations at lean mixtures. A mixture containing 10 % of hydrogen is stable in case of no dilution, and unstable for a dilution rate of 30 %. The CO on the other hand, has a stabilizing effect on flame front. However, the 30 % CO sufficient for the stabilizing of non-diluted flame, become 60 % for a dilution of 30 %.

This study highlights the importance of carbon monoxide of biogas/syngas mixtures as an important component in maintaining the stability of the fuel mixture. It also shows a negative side of hydrogen that was not present in the auto-ignition approach. This means that the composition of hydrogen, carbon monoxide and carbon dioxide should be chosen very wisely.

Conclusions

- The pressure and temperature do not affect the Lewis number and therefore the flame stability
- The equivalence ratio is an important factor in the flame stability calculations. Lewis numbers are the lowest for lean mixtures and they increase as the mixture becomes richer.
- For all stoichiometric and rich mixtures, Lewis numbers are higher than the critical Lewis values, which indicates a stable flame.
- For lean conditions ($\phi=0.6$ and 0.8), the Lewis numbers of methane/hydrogen and methane/hydrogen/carbon dioxide mixtures are lower than their critical ones. This means that these mixtures are not stable.
- As the hydrogen percentages increase in the mixture, the flame stability decreases
- The addition of carbon dioxide to biofuel mixture have a negative effect on the flame stability.
- As the carbon dioxide percentages increase in the mixture, the thermal diffusivity decreases and so does the Lewis number.
- Carbon monoxide on the contrary has a stabilizing effect on the front flame

6. Conclusions on optimal mixtures and conditions in premixed flame point of view

The presence of heterogeneities in the combustion chamber causes combustion to be initiated by a self-ignition core that is more reactive than the rest of the mixture and develops in a non-uniform or deflagrating manner. The propagating flame front is particularly influenced by these heterogeneities: turbulence phenomena, temperature fluctuations, shock wave interactions, etc.

Hence, the same numerical study carried out on closed homogeneous reactor in the previous section was carried out on laminar premixed flame model.

The parametrical study was performed on the effect of initial conditions on the combustion properties: flame speed, pollutant emissions and flame front stability.

It was shown that flame speed depends on both transport and chemical reaction properties. Therefore, increasing temperature leads to faster chemical reactions, thus the ignition time is shorter and the flame speed is higher. The increasing of pressure however leads to a decrease in

flame speed. The hydrogen and carbon monoxide were found to have the same promoting effect on the flame speed, the former being more influential. The carbon dioxide on the other hand has a high heating capacity in comparison to the other biofuel components. Thus, when the percentage of CO₂ increases in the mixture, the thermal diffusivity decreases and therefore the flame speed.

In brief, the effects of all these parameters on the pollutant emissions are similar to the one studied for the auto-ignition process. The values of the emissions are however higher in the study of auto-ignition than those in flame configurations. This can be explained by the higher energy produced in the isochoric closed reactor compared to the isobaric free flame.

Because of the similarity in both configurations, the same analysis done in the optimizing of fuels and conditions in auto-ignition process can be applied here.

However, influence of each parameter on Lewis number and therefore on thermo-diffusive stability was also studied.

It was shown that unlike rich or stoichiometric conditions, the stability of flame propagating in lean conditions is strongly dependent on the studied biofuel mixture.

As the dilution rate of CO₂ increases, the flame becomes more sensitive to hydrogen concentrations at lean mixtures. A mixture containing 10 % of hydrogen is stable in case of no dilution, and unstable for a dilution rate of 30 %. The CO on the other hand, has a stabilizing effect on flame front. However, the 30 % CO sufficient for the stabilizing of non-diluted flame, become 60 % for a dilution of 30 %. As a result, according to this study, the dilution rate should be limited to a value smaller than 30 %, and the hydrogen percentages should not exceed 20 %. A percentage of carbon monoxide higher than 30 % is required to stabilize the effect of CO₂ dilution as well as the hydrogen concentrations on the stability of flame front.

However, these percentages depend highly on the adiabatic assumption in this configuration that leads to higher burn gas temperature and therefore lower critical Lewis number. On the other hand, the qualitative behavior of H₂, CO₂, and CO on the thermal stability is similar.

Hence, in the premixed flame configuration, the biogas/syngas can be optimized by controlling the percentage of these three components in a way to reduce pollutant emissions while maintaining flame stability, and a certain flame speed. As a result, in order to choose a fuel that meets the objectives mentioned earlier, while respecting the composition percentages, a proposition is optimized and presented in Table 25.

Table 25: optimized fuel mixture in auto-ignition point of view

| | Φ (-) | H ₂ (%) | CO (%) | CH ₄ (%) | CO ₂ (%) | T _c (K) | P _c (bar) |
|------------------------|------------|------------------------|------------------------------|---------------------|---------------------|--------------------|----------------------|
| Biogas/Syngas mixtures | | $b < (100-X)$ | $(100-X-b)$ | $a < X$ | $(X-a)$ | [920-1040] | [10-15] |
| Premixed-flames | Lean (<1) | $b = \text{limit-} b'$ | $100 - \text{limit-} X + b'$ | a | $(X-a)$ | [920-1040] | [10-15] |

In this table, (a) represents the percentage of methane, (b) represents the percentage of hydrogen in the mixture, and (limit) represents the maximum amount of H₂ for which thermal instability does not exist. In our study, this limit was found to be 10% for non-diluted mixtures; for higher dilution rates, this value tends to zero. However, it is important to note that the value of critical Lewis is based on an adiabatic approach, and will be higher in real configurations, allowing for higher percentages of hydrogen. The value of (b') depends on the percentage of carbon dioxide in the mixture; the highest is CO₂ the highest will be the value of (b'). The percentage of carbon monoxide is important in flame configurations to assure thermal stability. The values of (a) and (b') can be chosen according to the qualitative diagram of Figure 83.

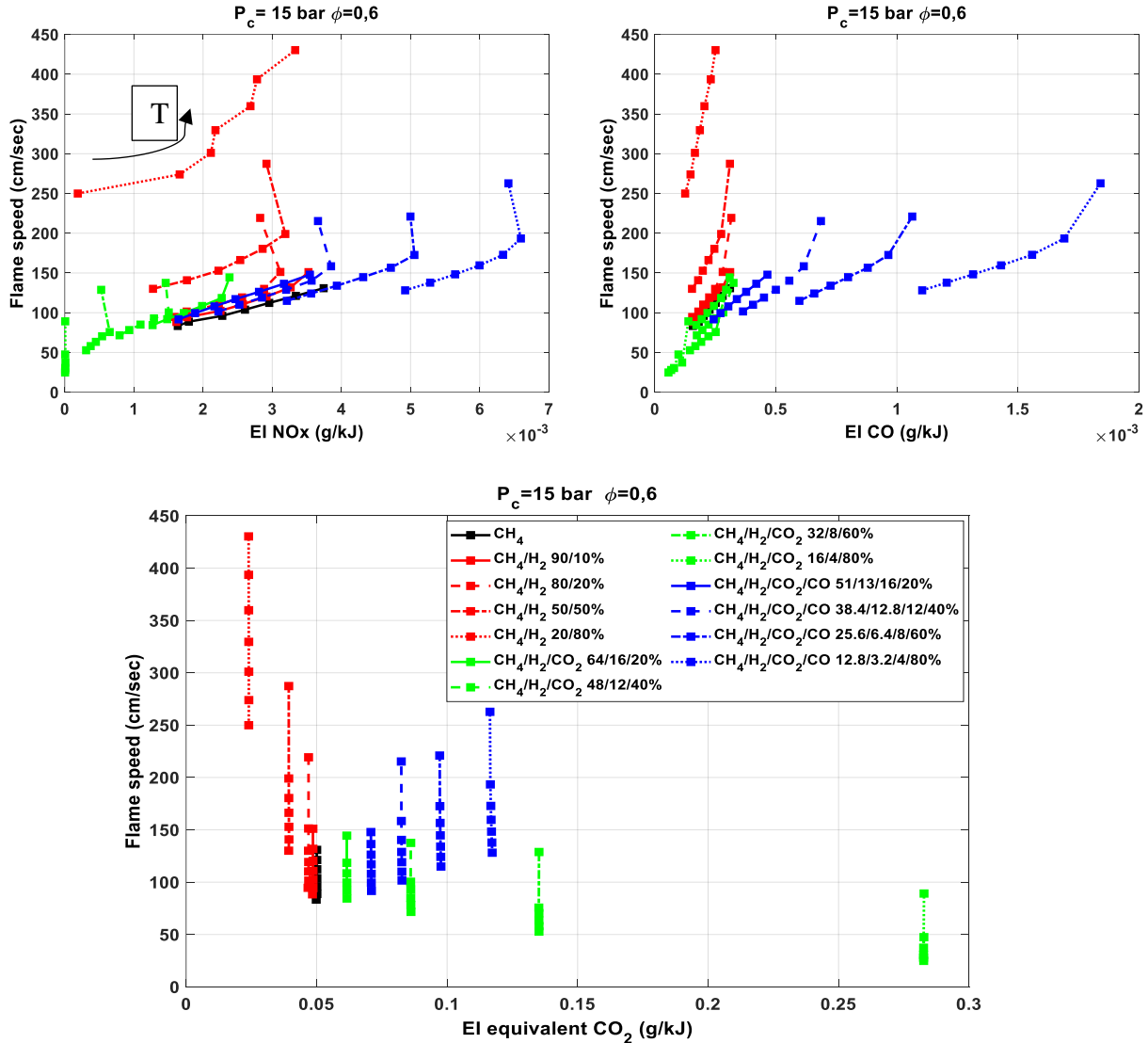


Figure 83: Flame speed and pollutant emissions diagram (dilution 0%), T_c between 920 and 1040 K

VI. Optimization on the simplified approach

The combination of lean homogeneous technology with renewable energy is an alternative process that can lead to minimizing the emissions and maintaining a high thermal efficiency. In order to benefit from its advantages, characterizing the combustion of biogas/syngas under HCCI

conditions and understanding the effect of initial conditions and fuel composition was of a high priority. Hence, an experimental study was conducted on the SU RCM in the previous chapter to study the effects of fuel composition on the ignition delay times. In this chapter, the purpose was to extend the studied field to cover up more parameters.

However, due to the physical and chemical phenomena that can occur in this combustion mode, it was modeled on Chemkin-Pro with a simplified approach that consists of studying the combustion in two configurations: closed homogeneous reactor and premixed flame configuration.

The effects of each component as well as the initial conditions on the ignition delay time, flame speed, flame stability and pollutant emissions were studied in both configurations.

Based on the closed homogeneous reactor study, it was found that the biogas/syngas mixtures can be optimized mainly based on carbon dioxide and hydrogen mixtures. A minimum amount of 10% of hydrogen is required in order to keep up a certain reactivity of the combustion. This percentage was validated on the experimental study. The same study was conducted on the second configuration; however, the optimization should also consider the percentage of carbon monoxide as an important factor in maintaining the thermal stability of the flame (Figure 84).

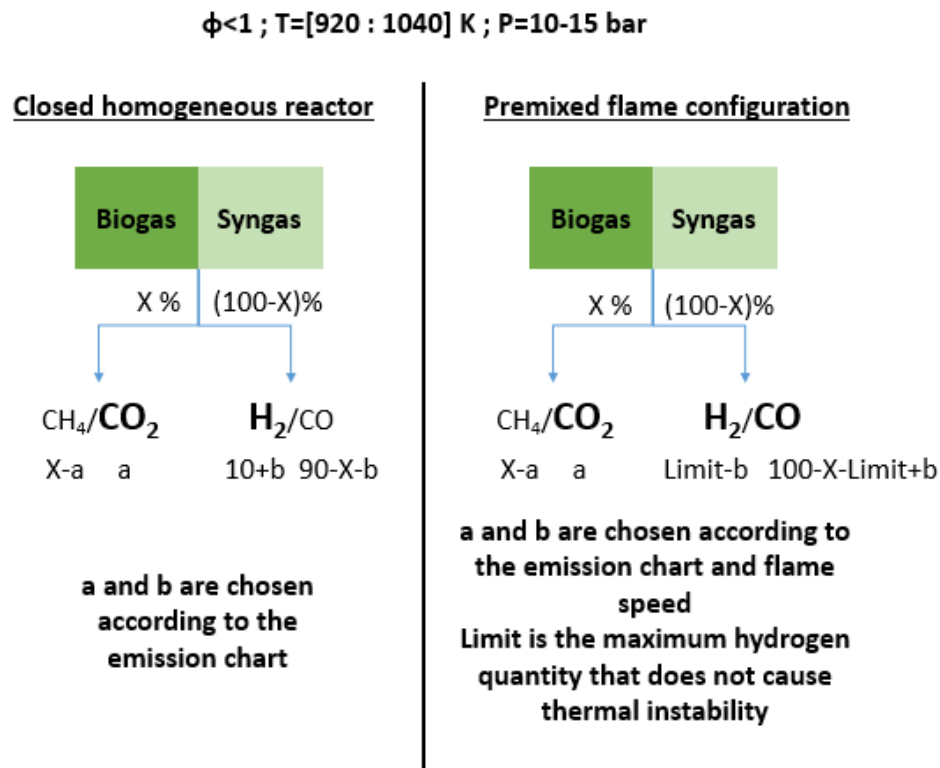


Figure 84: Range of optimized conditions in an homogeneous reactor approach and premixed flame configuration

In lean homogeneous combustion, both: auto-ignition and flame propagating modes are likely to occur; the combustion can start with one or more auto-ignition sites and then continue with a flame propagating. Hence, another simplified approach will be considered to account for the turbulence

phenomenon in the combustion process. This approach will be used to detect the effect of each parameter on the combustion mode. The qualitative method for the prediction of the combustion phenomenology consists of the construction of the combustion diagram and is described in the following section.

VII. Turbulent combustion

Propagation of the premixing flame front may occur in laminar or turbulent flows. However, experimental studies on HCCI mode on rapid compression machines, which is a direct application to the internal combustion engine, have shown that the flames and flows are quite turbulent. Guibert et al. [144] prove that due to heterogeneities and turbulence levels in the RCM chamber, two distinct regimes may govern the auto-ignition of reactive mixtures in RCM: either a purely volumetric ignition or a reaction front followed by a volumetric ignition. Thus, understanding the physical phenomena that induce these combustion regimes is very important in characterizing self-ignition. To identify these phenomena, the properties of turbulent flames and the different turbulent combustion regimes, as well as the characteristic magnitudes of turbulence, will be discussed in the following section.

A direct approach to model the mean reaction rate based on the series expansion of the Arrhenius law cannot be retained because of the large number of unclosed quantities (correlations between species concentrations and temperature fluctuations) and of the large truncation errors due to high non-linearities;

Therefore, the derivation of models must be based on physical analysis and comparisons of the various time and length scales involved in the combustion phenomena. These analyses lead to the so-called "turbulent combustion diagrams" where multiple regimes are identified and delineated, introducing non-dimensional characteristic numbers. These diagrams are mainly based on intuitive arguments and present magnitude arguments rather than actual demonstrations.

1. Non-dimensional numbers in turbulent combustion

The physical characteristic quantities that exist in the combustion chamber are shown in Figure 85.

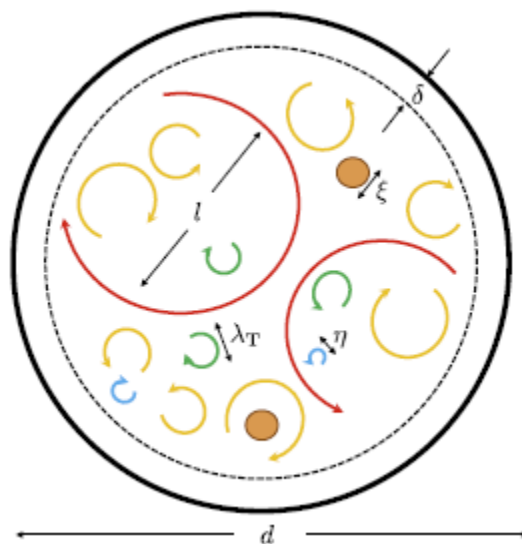


Figure 85 : Schematic of turbulent field within a combustion chamber[145]

Length scales include:

- Chamber length L ,
- Foucault's integral scale l_t ,
- Taylor's Microscopic Scale λ_T ,
- The thickness of the deflagration flame δ_T

To characterize turbulent velocity and scalar fields, dimensionless parameters are introduced.

The turbulent Damköhler number represents the intensity of the chemical reaction. It compares the characteristic time of the turbulence $\tau_t = \frac{l_t}{u'}$ with the characteristic time of the chemical reaction

$$\tau_c = \frac{\delta_L}{S_L^0} \quad [145]:$$

$$Da_t = \frac{\tau_t}{\tau_c} = \frac{l_t/u'}{\delta_L/S_L^0} \quad (VIII)$$

With u' the fluctuating turbulent velocity.

The Damköhler number makes it possible to differentiate between two configurations:

- ($Da_t \ll 1$): the time of the turbulence is negligible compared to the time of the chemical reaction. This configuration is equivalent to that of a perfectly mixed reactor; reagents and products are mixed by the turbulent motion, so the overall reaction rate is controlled by the chemistry.
- ($Da_t \gg 1$): the chemical reaction time is negligible compared to the time of turbulence. So, the effects of turbulence do not influence the inner structure of the flame, therefore, the flame in this configuration is close to the laminar flame folded by the turbulent movements.

The Damkohler number (mixing number) is defined as the ratio between the characteristic time of the chemical reaction τ_c and the characteristic time of the heat dissipation τ_{λ_T} [146].

$$Da_\lambda = \frac{\tau_{\lambda_T}}{\tau_c} \quad (VII.2)$$

If $Da_\lambda < 1$ temperature fluctuations are dissipated before self-ignition.

The turbulent Reynolds number is also a dimensionless number that represents the ratio of the intensity of the turbulence to that of the viscosity forces. It is defined from u' , l_t and kinematic viscosity ν .

It can be interpreted as the ratio of the characteristic time of viscous dissipation τ_v ($\tau_v = \frac{l_t^2}{\nu}$) and the characteristic time of turbulence τ_t [145]:

$$Re_t = \frac{\tau_v}{\tau_t} = \frac{u'l_t}{\nu} \quad (VII.3)$$

When the Reynolds number is greater than one ($Re_t > 1$), it is a turbulent flow. Then, this dimensionless number makes it possible to differentiate two types of flames:

- $Re_t < 1$: laminar premix flames

- $Re_t > 1$: turbulent premix flames

Another dimensionless number, the Karlovitz Ka number, which compares the characteristic time of the chemical reaction with the characteristic stretch of the reactive zone. It is defined as the ratio between the characteristic time of the chemical reaction and the Kolmogorov time scale $\tau_k = \frac{\eta_k}{u'(\eta_k)}$

$$Ka = \frac{\tau_c}{\tau_k} = \left(\frac{u'}{S_L^o}\right)^{-0,5} \left(\frac{l_t}{\delta_L}\right)^{3/2} \quad (VII.4)$$

The Karlovitz number allows to differentiate between the case when the phenomena of flame stretching exist or not:

- $Ka < 1$: Kolmogorov's characteristic time is more important than the reaction time. Then, local flame extinction phenomena do not exist since the combustion rate is high enough to compensate for the stretching undergone by the reaction zone.
- $Ka > 1$: the flow can produce stretches on the flames that can lead to extinguishing phenomena and the small structures of the flow can penetrate the reaction zone.
- $Ka = 1$: limit between the flame regime and the regime of folded and thickened flames

2. Combustion diagram

Diagrams defining combustion regimes in terms of length and velocity scales ratios have been proposed by Barrere, Bray, Borghi, Peters, Williams, Abdel-Gayed and Bradley, Borghi and Destriau and Peters[147]. Between all these diagrams, the following study will be based on the combustion diagram of Borghi.

The Borghi diagram is based on Reynolds, Damkohler and karlovitz dimensionless numbers and the length terms u'/S_L^o et l_t/δ_L used to characterize premixed combustion of a reactive mixture. (The diagram is shown in Figure 86).

Several cases can be distinguished:

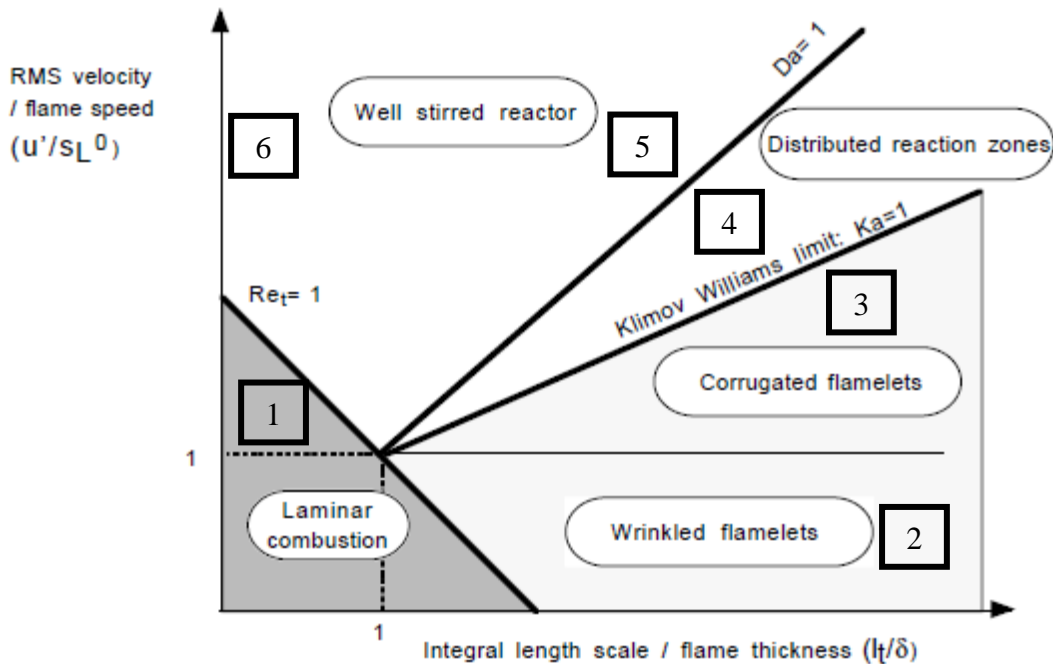


Figure 86: The combustion diagram of Borghi

- If $Re_t < 1$: the characteristic time of viscous dissipation is shorter than that of turbulence, then laminar flames are involved. (Zone 1)
- If $Ka < 1$ and $Da > 1$: the characteristic time of the chemical reaction is shorter than the characteristic time of the turbulence as well as the smallest turbulent scale: Kolmogorov scale. In this domain, two flame regimes dependent on the ratio u'/S_L can occur:

-If $u' < S_L^0$: the laminar velocity is high in front of the turbulent intensity. Then the turbulence does not affect the flame structure; the flame front is wrinkled by the velocity gradients it encounters. This regime is identified as "folded flame regime" (Zone 2);

-If $u' > S_L^0$: the turbulent intensity is sufficiently important in front of the laminar combustion speed so that the large vortices strongly deform the flame front until it breaks. This break in the flame front then gives rise to pockets of fresh gas and/or flue gas. This regime is called "folded flame regime with pockets" or "corrugated flames" (zone 3).

- If $Ka > 1$ and $Da > 1$: the characteristic time of the turbulence is always greater than that of the chemical reaction, which in turn is greater than the Kolmogorov scales. The turbulence structures are fast enough to stretch the flame front creating local extinctions. This regime is defined as a "pleated-thickened flame regime" or "distributed combustion regime". (Zone 4)
- If $Da < 1$: two flame regimes depending on the report $\frac{l_t}{\delta_L}$ can occur:
 - If $\frac{l_t}{\delta_L} > 1$, turbulent movements have shorter characteristic times than those of chemical reactions: the mixing of the reagents is ensured by turbulence and the reaction speed is controlled by the kinetics of the reaction. The flame is said to be "thickened"; (zone 5)

- If $\frac{l_t}{\delta_L} < 1$ the flame front occupies the entire volume of the fireplace. This regime is also called a "homogeneous reactor" (zone 6).

3. Positioning of optimal mixtures on combustion diagram

The turbulence is characterized through its RMS velocity u' and its integral scale l_t . This approach is used in turbulent combustion models to quantify the velocity fluctuations in a flame using RMS velocities. This assumption shows that the kinetic turbulent energy is not well defined except far from the flame front. Therefore, this has no theoretical basis in a premixed flame even though this is used in most existing codes.

The positioning of mixtures on the diagram of Borghi requires the determination of $\frac{u'}{S_L^0}$ and $\frac{l_t}{\delta}$. Knowing the turbulence characteristics (integral length scale, turbulent kinetic energy and its dissipation rate among other characteristics), this diagram indicates whether the flow contains flamelets (thin reaction zones), pockets or distributed reaction zones. This information is essential to build a turbulent combustion model. A continuous flame front, without holes, cannot be modeled in the same way as a flame which is broken into many small pockets, and where combustion does not take place along a sheet but in a more distributed manner.

The laminar flame speed was calculated by the "the premixed flame speed" module on Chemkin – Pro, and the flame thickness was calculated as explained in the previous section.

The turbulent integral length scale is defined as [148]:

$$l_i(x) = \int_0^{\infty} C_{uu,y}(x, dy) dy$$

Where:

$$C_{uu,y} = \frac{\overline{u(x)u(x+dy)}}{u'(x)u'(x+dy)}$$

Here u denotes the instantaneous velocity fluctuation, the overbar represents a time average and dy is the separation distance.

In turbulent premixed combustion, eddies are turbulence that has sizes ranging from the Kolmogorov to the integral scales. Their characteristic speeds are ranging from the Kolmogorov called u'_k to the integral RMS u' velocities.

With the assumption of homogeneous and isotropic turbulence, the speed $u'(r)$ and the size r of any eddy participating in the turbulence cascade are linked by the following equation:

$$\frac{u'(r)^3}{r} = \varepsilon_d \quad (VII.5)$$

ε_d is the local dissipation rate of turbulent kinetic energy.

In Pounkin's study on the SU RCM [53], the aerodynamic conditions in the combustion chamber were examined. The tests were performed with Rhodorsil liquid particles first at a constant end compression temperature of 665 K and two different loads: 140 and 180 mol/m³. Later on, the tests were carried out at a constant load and two different end-of-compression temperatures.

The loads are calculated at the end of compression according to:

$$c = \frac{n}{V} = \frac{P_C}{RT_C} \quad (VII.6)$$

The load is modified by changing the inlet pressure from 0.30 to 0.39 bar for loads of 140 and 180 mol/m³ respectively. It should be remembered that the inlet temperature remains constant and equal to 343 K.

The evolution of the aerodynamic structures over time was similar in all the studied tests. The evolutions of kinetic and turbulent kinetic energies were also represented for all these tests and for different geometric configurations and without grids.

In general, there were small deviations or no clear trend, suggesting that the load on the energy has little influence on the average kinetics. The same applies for the evolution of turbulent energy. It appears that the load has also little influence on its evolution and the results from one charge to another are quite similar.

Therefore, Pounkin [53], showed that the influence of the load and the end of compression temperature on the aerodynamic conditions was not a phenomenon of the first order. Whether it is on the aerodynamic field, kinetic and turbulent energies or integral scales, no trends can be identified from the study carried out.

In brief, the main objective of the following study is to determine the effects of the different combustion parameters on the non-dimensional number and so the physical phenomena of the turbulent premixed flame. In other words, the values of integral length and RMS velocities, measured and calculated by Pounkin[53], in the configuration without grid, are used to calculate $\frac{u'}{s_L^0}$ and $\frac{l_t}{\delta_L}$. The non-dimensional numbers will be deduced, consequently, from these two values according to the equations presented in the previous paragraph.

Using average value of RMS velocities of 2.25 m/sec and length scale of 4.95 mm[53], the average values of the Damköhler and Karlovitz characteristic numbers are calculated over the combustion process.

The effect of the temperature, the equivalence ratio as well as the hydrogen and carbon monoxide concentrations on the two non-dimensional numbers Da and Ka are presented in Figure 87, Figure 88, Figure 89, and Figure 90, respectively.

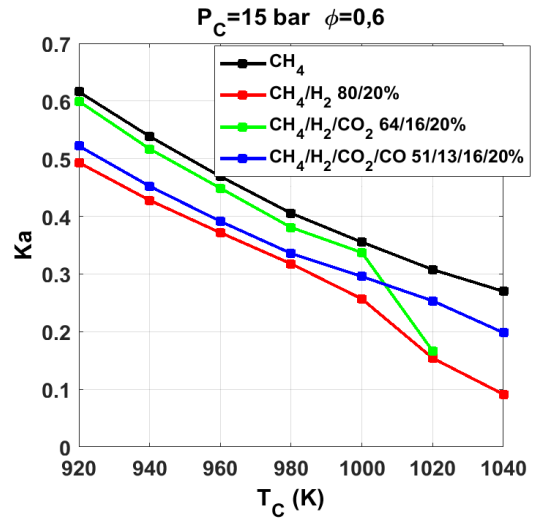
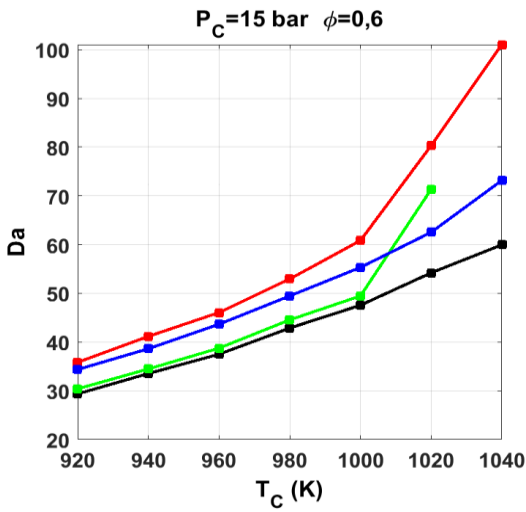


Figure 87 : Da and Ka as a function of temperature for different types of biofuel

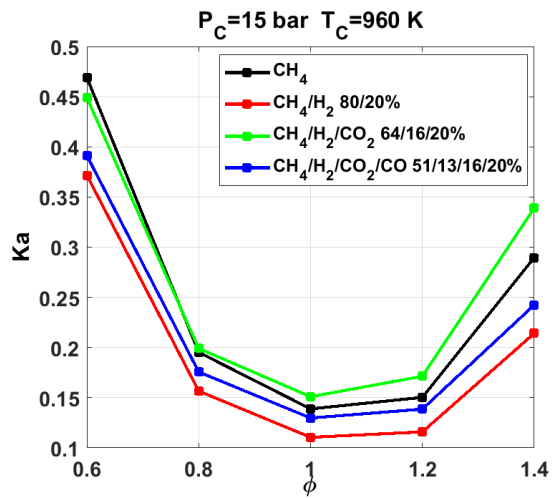
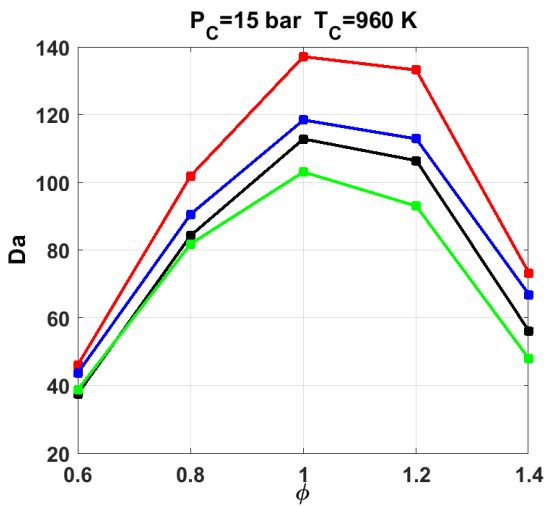


Figure 88: Da and Ka as a function of the equivalence ratio for different types of biofuel

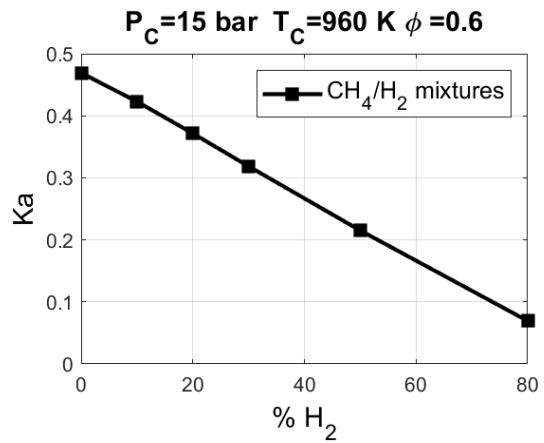
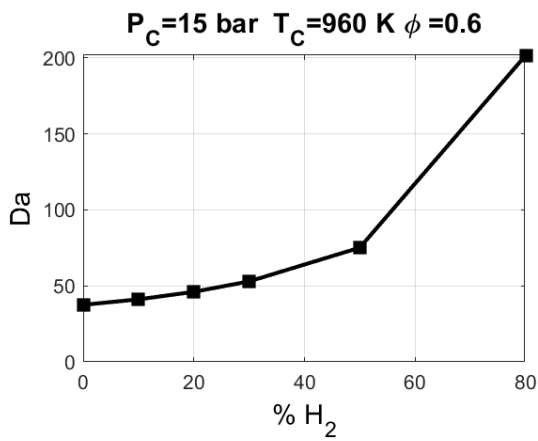


Figure 89 : Da and Ka as a function of the hydrogen percentage

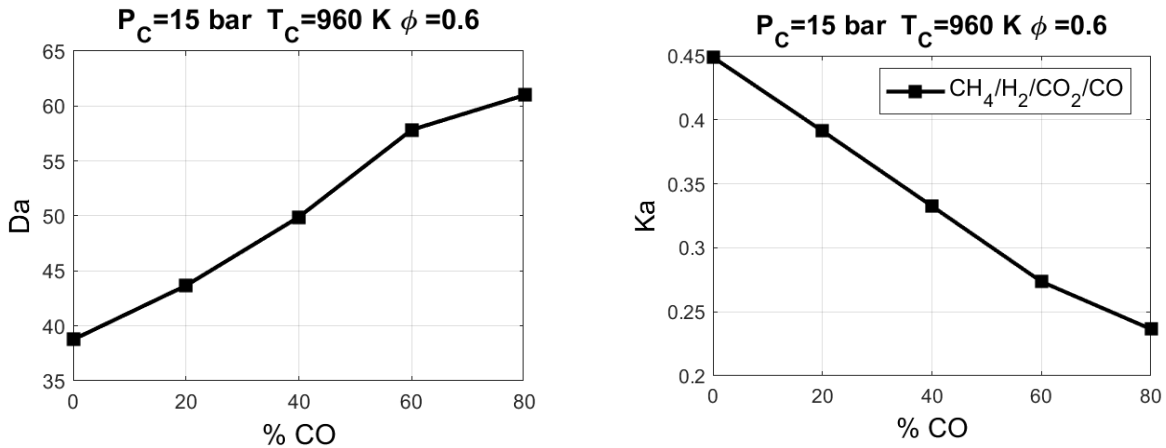


Figure 90: Da and Ka as a function of the carbon monoxide percentage

As can be seen, all studied biofuel mixtures presented a Damkohler number that is higher than unity. Which means that all along this study, the combustion occurs in zones 2, 3 and 4 in the diagram of Borghi.

The temperature, the concentrations of hydrogen and carbon monoxide as well as the equivalence ratio share similar effects on the two studied non-dimensional numbers.

As one of these studied parameters increases, the Damkohler number increases while the Karlovitz number decreases, the same applies to when the equivalence ratio get closer to stoichiometry. In other words, the combustion process will more likely occur with the presence of corrugated or wrinkled flamelets regime. Note that, it is the ratio u'/S_L that will decide between these two flamelets regime.

However, as discussed earlier in this chapter, these parameters have a significant effect on the flame speed value. Thus, when either the temperature or the concentration of H_2 or CO increases or when the equivalence ratio gets closer to stoichiometry, the flame speed increases. For a constant value of u' , the ratio u'/S_L decreases and the combustion initially occurring in zone 3 will get closer to zone 2.

In other words, the characteristic time of the mixture is therefore much more important than the characteristic time of chemistry. Turbulent structures, therefore, have very little influence on the combustion process. In addition, the Karlovitz number is less than 1, which means that the chemical characteristic time is shorter than any turbulent time scale and the flame thickness is smaller than the smallest turbulent scale; the Kolmogorov scale. In this regime, the flame front is thin, with an inner structure close to that of a laminar flame, and is simply wrinkled by the velocity gradients it encounters. This is the flamelet regime.

Furthermore, the pressure and the concentrations of carbon dioxide in the mixture have different effects on Da and Ka numbers. These effects are presented in Figure 91 and Figure 92 respectively.

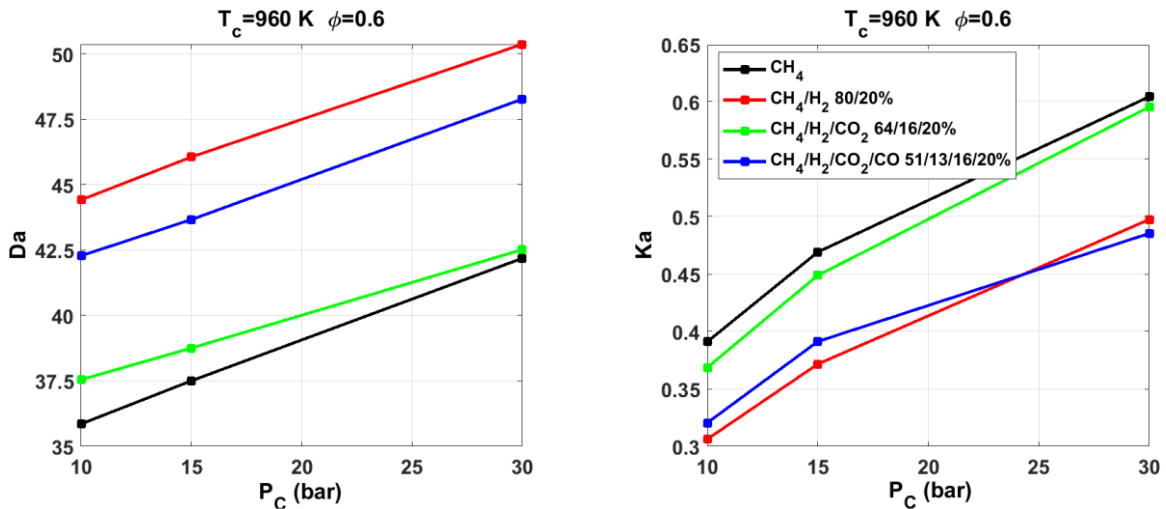


Figure 91: Da and Ka as a function of pressure for different types of biofuel

As the pressure increases, Da and Ka numbers increase. Therefore, as the pressure goes higher, the combustion will more likely occur in the “distributed reaction zone”. The characteristic time of the turbulence is always greater than that of the chemical reaction, which in turn is greater than the Kolmogorov scales. The turbulence structures are fast enough to stretch the flame front and thus create local extinctions.

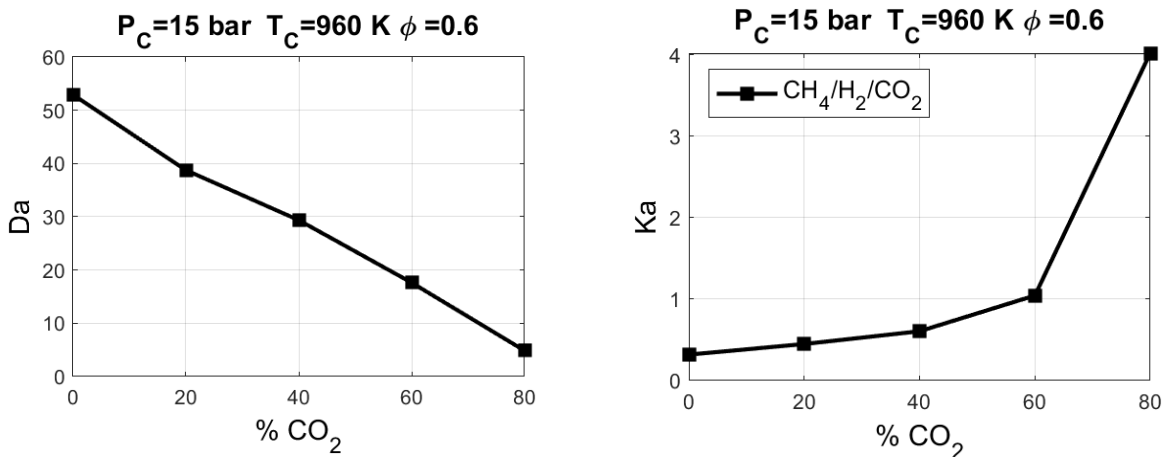


Figure 92 : Da and Ka as a function of the carbon dioxide percentage

As for the concentration of CO₂, its increase leads to the decrease of Da number and the increase of Ka number. For a number of Damkohler number higher than unity, the combustion will occur in zone 4. However, when it gets under unity, the combustion regime will come closer to the homogeneous reactor; zone 5 or zone 6.

The effects of all these parameters on the non-dimensional numbers of Da and Ka are summarized and presented in Table 26.

Table 26: Effect of parameters on the non-dimensional numbers Da and Ka

| Parameter | Da | Ka | Combustion gets closer to |
|--|------------|------------|--|
| T \nearrow or CO \nearrow or H ₂ \nearrow or Φ getting closer to stoichiometric conditions | \nearrow | \searrow | Zone 2 or Zone 3 Corrugated or wrinkled flamelets |
| P \nearrow | \nearrow | \nearrow | Zone 4 Distributed reaction zones |
| CO ₂ \nearrow or Dilution rate \nearrow | \searrow | \nearrow | Zone 4 or zone 5 or zone 6 |

The results shown in Table 26, highlight the effect of the dilution on homogeneous combustion; when the percentage of dilution increases, the combustion mode gets closer to zone 4, then 5 and 6 that are the most representative of the auto-ignition model.

4. Conclusions and proposed experimental study

This study's observations and analyses illustrate essential details that give rise to non-intuitive and nonlinear behavior with biogas/syngas mixtures. It was shown that the behavior of fuel mixtures could be significantly different than that of the individual constituents. Hence, behaviors such as flame speed or ignition delay time may behave in a highly nonlinear manner as fuel mixtures change. Furthermore, the effect of hydrogen was shown to provide many unique impacts on the behavior of the studied mixtures. The simplified approach of the turbulent combustion depends on the turbulent characteristics in the combustion chamber. Therefore, for a different level of turbulence and thermal heterogeneities, the velocity fluctuation, as well as the length scale, will change, which means the combustion of the mixture will occur in a different zone.

However, this simplified approach highlights the effect of parameters on the combustion regimes and this for the different characteristics of the combustion chamber.

It was shown that higher CO₂ dilution and leaner mixtures tend to decrease the Da and increase Ka numbers and, therefore, get closer to the homogeneous reactor (distributed reaction zones). This highlights the importance of dilution and lean conditions in HCCI combustion as it favors the auto-ignition phenomena. On the other hand, the increase in carbon dioxide and monoxide quantity makes the combustion closer to the wrinkled zone.

Because of the complexity of the lean homogeneous combustion, a last experimental study on the characterization of biogas/syngas mixtures will be addressed on the SU RCM. The direct visualization of a certain range of mixtures can validate the simplified approaches qualitatively studied in this chapter.

However, when studying by direct visualization, the quartz chamber will be used. It is highly essential to wisely choose the studied mixtures not to exceed the maximum allowed pressure of 40 bars. For all the studied mixtures, the end of compression pressure was selected from 10-15 bars. Also, while choosing the studied conditions, it is important to mention that the quartz chamber is more affected by heat transfer than the chamber used in the experimental study of chapter 2.

Therefore, twelve mixtures were selected from the numerical and experimental study. The effect of the initial conditions and fuel composition on the combustion behavior will be highlighted:

- First of all, the effect of the equivalence ratio will be addressed. It was shown in this chapter that lean mixtures have an effect in reducing the flame speed and increasing the ignition delay time. Also, according to the turbulent combustion approach, it was shown that as the equivalence ratio decreases in lean mixtures, the combustion becomes closer to the distributed reaction zones. For these reasons, three lean mixtures were chosen to be studied in direct visualization in order to verify the studied effects and visualize the physical phenomenon. Therefore, the fuel composition ($\text{CH}_4/\text{H}_2/\text{CO}_2$) and the initial conditions are fixed, and only the equivalence ratio was varied from 0.4; 0.6 and 0.8 with an end of compression temperature of 1000 K to allow the leanest mixture to burn.
- Although we are more concerned with the characterization of lean combustion, it could be interesting to compare the behavior in a lean, stoichiometric, and rich mixture. In particular, in mixtures containing carbon monoxide, as we have studied earlier that thermal instability is more likely to occur in lean mixtures, and carbon monoxide has a stabilizing effect. Therefore, we choose a biogas/syngas mixture $\text{CH}_4/\text{H}_2/\text{CO}_2/\text{CO}$ at a low temperature of 940 K.

The rest of the mixtures will be studied at an equivalence ratio of 0.6.

- The effect of temperature will be studied on the mixture $\text{CH}_4/\text{H}_2/\text{CO}_2$ at both temperatures, 1000 K and 970 K.
- In the experimental study of chapter 2, it was observed that a percentage of hydrogen of 10-20% was sufficient to predominate the auto-ignition phenomenon. The same result was obtained in the numerical study and was due to the low activation energy of the reaction of hydrogen decomposition. The percentage, however, was found to be less than 5%. Thus, the following mixtures to be studied are CH_4 and CH_4/H_2 , with a small percentage of hydrogen (5%) at 970 K.
- In both configurations, the carbon dioxide was viewed as a diluent specie that does not participate in chemical reactions. It is normally present in biogas. Hence, CH_4/CO_2 will also be studied at 970K to allow the comparison with methane mixture.
- The final parameter to be studied is carbon monoxide. Chapter 2 shows that carbon monoxide has no to a slight effect in increasing the ignition delay time. In the flame configuration, it was shown to increase the laminar flame speed of a certain mixture. And for both configurations, leads to increase the temperature peak. The turbulent combustion approach showed that with the highest volume percentage of carbon monoxide, the combustion would be more likely to occur in the corrugated flame configuration. Thus, the final mixtures are $\text{CH}_4/\text{H}_2/\text{CO}_2/\text{CO}$ with 20 and 40% of carbon monoxide at 1000 K.

The twelve mixtures are summarized in the following table.

Table 27: Mixtures to study by direct visualization

| | Mixture | CH ₄ (% vol.) | H ₂ (% vol.) | CO ₂ (% vol.) | CO (% vol.) | P _c (bar) | T _c (K) | φ (-) | Da | Ka |
|------------------------------------|---------|--------------------------------|-------------------------------|--------------------------------|-------------------|-------------------------|-----------------------|----------|--------|-------|
| Effect low equivalence ratio | 1 | 48 | 12 | 40 | 0 | 11 | 1000 | 0.4 | 25.14 | 0.56 |
| | 2 | 48 | 12 | 40 | 0 | 11 | 1000 | 0.6 | 36.58 | 0.37 |
| | 3 | 48 | 12 | 40 | 0 | 11 | 1000 | 0.8 | 64.34 | 0.20 |
| Effect equivalence ratio | 4 | 38.4 | 9.6 | 12 | 40 | 15 | 940 | 0.6 | 42.93 | 0.31 |
| | 5 | 38.4 | 9.6 | 12 | 40 | 15 | 940 | 1 | 111.29 | 0.11 |
| | 6 | 38.4 | 9.6 | 12 | 40 | 15 | 940 | 1.2 | 115.81 | 0.11 |
| Effect fuel composition | 7 | 100 | 0 | 0 | 0 | 11 | 971 | 0.6 | 38.06 | 0.36 |
| | 8 | 95 | 5 | 0 | 0 | 11 | 971 | 0.6 | 42.10 | 0.33 |
| | 9 | 55 | 0 | 45 | 0 | 11 | 971 | 0.6 | 1.49 | 11.42 |
| | 10 | 51.2 | 12.8 | 16 | 20 | 11 | 1000 | 0.6 | 52.91 | 0.24 |
| | 11 | 38.4 | 9.6 | 12 | 40 | 11 | 1000 | 0.6 | 59.34 | 0.21 |
| Effect temperature | 12 | 48 | 12 | 40 | 0 | 11 | 970 | 0.6 | 47.78 | 0.27 |

VIII. Conclusions

In this chapter, an advanced study that provides a better understanding of the physical-chemical phenomena of biofuel combustion was carried out numerically on Chemkin-Pro. The numerical database completed the experimental one built in the previous chapter on the SU RCM. All the numerical study was carried out using the chemical mechanism of Grimech3.0, except for the effect of carbon monoxide studied on Aramco1.3.

Due to thermal heterogeneities and turbulence levels in the combustion chamber, the lean homogeneous combustion is more likely to occur in one or multi-sites and to propagate throughout the chamber. Because of the complexity of this type of combustion, it was modeled using a simplified approach.

The simplified approach consists of dividing the combustion process into two configurations; an Auto-ignition process on a closed homogeneous reactor and a laminar premixed flame on a freely propagating flame configuration.

This approach is essential in comprehending the impact that can have the end of compression conditions and the fuel composition on the chemical and physical aspects of combustion, particularly in HCCI conditions. It aims to build a qualitative study to characterize the

biogas/syngas combustion to define at the end, a range of optimized conditions and fuel compositions.

Both configurations highlight the importance of lean combustion in reducing pollutant emissions such as NO_x and carbon monoxide. The pressure and temperature were shown to have the least effects on the CO and CO₂ emissions. Their effects can be adjusted according to the engine application.

The importance of biogas/syngas mixtures was also highlighted in reducing pollutant emissions and maintaining a specific reactivity.

An addition of a small quantity (less than 10%) of hydrogen was shown to control the auto-ignition phenomenon and to boost the reactivity of the different biofuel mixtures, including methane and methane diluted with carbon dioxide. This statement was also validated in the experimental study of the previous chapter. In a pure auto-ignition configuration, hydrogen and carbon dioxide were shown to form a good combination.

Carbon dioxide serves as a dilution specie that reduces the temperature of the mixture and, therefore, NO_x emissions and carbon monoxide. Its negative impact on the reactivity can be boosted by a small quantity of hydrogen that will also reduce the mass carbon emissions. On the other hand, carbon monoxide has a negative effect on the pollutant emissions and slightly increases the ignition delay times of biofuel mixtures. The importance of this species is mainly highlighted in the flame configuration, where it was shown to maintain the thermal stability of the combustion. As hydrogen and carbon dioxide decrease the thermal stability drastically, a certain amount of carbon monoxide could adjust the combustion stability.

In order to understand the lean homogeneous combustion duality auto-ignition/flame, another simplified approach concerning the turbulent combustion was considered. The non-dimensional numbers were calculated in order to see the impact of different conditions on the combustion process. It was shown that for lean diluted conditions, the combustion process tends towards the distributed reaction zone, which corresponds to the homogeneous reactor. However, for a higher amount of hydrogen or carbon monoxide and higher temperatures, the combustion tends to occur in the wrinkled flame zone, which corresponds to the premixed-flame configuration.

Some mixtures were selected to be studied by rapid cinematography on the SU RCM to visualize the combustion behavior by highlighting the effects of the equivalence ratio, end of compression temperature, as well as fuel composition. This study will be detailed in chapter 5 to validate the different aspects discussed in this chapter.

Chapter 4:
Biomass combustion

Chapter 4

I. Introduction

As described previously, lean homogeneous combustion is an alternative technology that integrates the advantages of both types of conventional engines. Combining this technology with renewable energy like biomass is a promising alternative to reduce pollutant emissions. The combustion of biogas/syngas mixtures under lean homogeneous conditions was studied both experimentally and numerically in the previous chapters 2 and 3.

However, to benefit from lean homogeneous combustion advantages, it has to overcome some challenges mainly related to ignition timing control.

Based on the dust explosion principle, the combustion is likely to occur if the combustible powder is dispersed in a confined site at the explosive concentration with a simultaneous presence of an ignition source.

This sheds light on the diphasic combustion gas/solid and its possible effect in controlling the ignition timing and the lean homogeneous combustion stability.

Thus, the second main objective of this thesis is to answer this question:

How will the solid particles affect the lean combustion of a reactive mixture?

Two possible configurations come to mind: The ignition of solid particles initiates the combustion (Figure 93), or it is the gaseous mixture that starts to ignite, and the combustion propagation subsequently burns the particles (Figure 94).

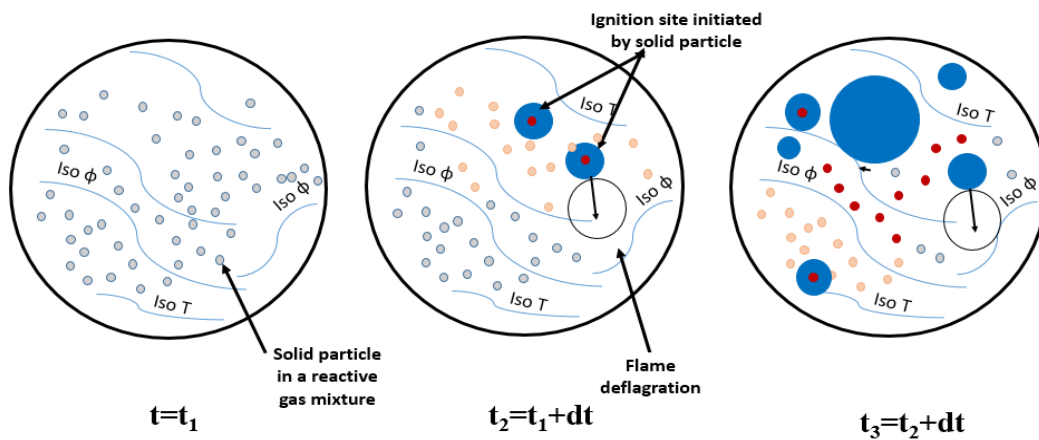


Figure 93 : First possible result of the diphasic combustion gas/particle

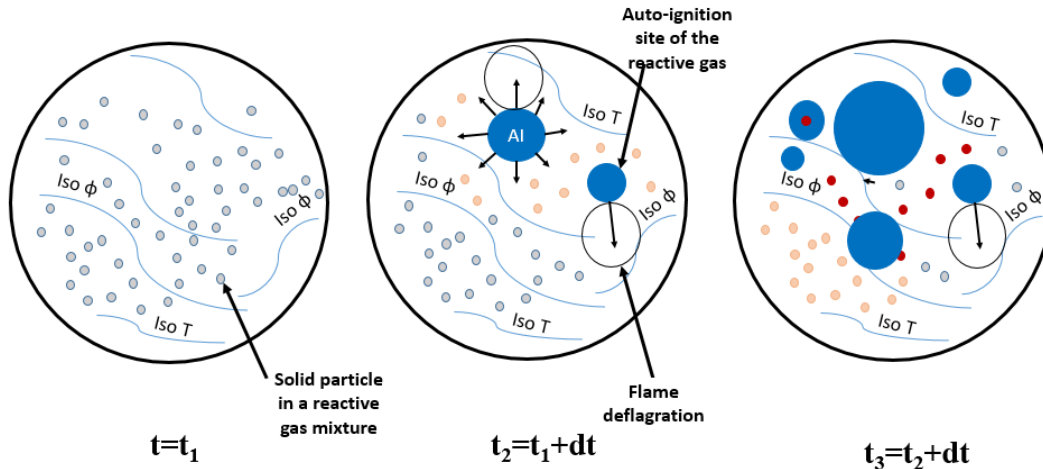


Figure 94 : Second possible result of the diphasic combustion gas/particle

In order to answer these questions, a particle injector is conceived to inject solid particles into the reactive mixture of the SU RCM chamber.

The combustion of diphasic combustion gas/solid under lean homogeneous conditions will be studied to determine the effects of particles on the initiation and control of the ignition process. In order to stay in a renewable energy approach, solid particles will be of lignocellulosic biomass.

Before proceeding with the diphasic combustion study, it is essential to characterize first the conceived particle injector and then the solid particle combustion.

Thus, this chapter is divided into two main sections. Section 1 describes the experimental setup used for the particle injection into the combustion chamber. The first practical tests were conducted to determine the crucial characteristics of the particle injector, such as the injection time, duration, jet cone angle, and the penetration depth of particles. PIV measurements were also performed to study the internal aerodynamics induced by the particle injection. The interest of the particle flow analysis lies in the control of the particle kinematics and the ability to predict the particle density and the shape of the stream.

In section 2, lignocellulosic biomass composition and the chemical structure of its principal components will be reviewed. The combustion and pyrolysis processes and the influences of various factors on biomass pyrolysis, including temperature, heating rate, particle size, and shape, are presented. The biomass char oxidation processes, char reactivity, and related issues are also presented. The experimental dispositive described in section 2 is set up on the rapid compression machine to study solid biomass combustion. This study is vital to characterize the biomass combustion in inert mixtures to control and characterize its combustion with gaseous biofuel more precisely. Several parameters were shown to have influences on the combustion, such as the injection time and pressure, as well as the pressure and temperature of the inert mixture.

II. Particle injection system

Based on a gaseous reactive mixture, the quasi-homogeneous species' concentration will provide the optimal conditions for the non-production of soot. The introduction of particles and gas vector during injection will have several consequences: the seeded particles will be as many ignition points of the reactive mixture in the chamber's whole volume, the inert gas in an inert hypothesis will bring turbulence during the initiation and development of combustion. Depending on the case, combustion will be by self-ignition and/or deflagration. In a reactive hypothesis, it will have, besides, the role of diffusion of the reactivity. The low equivalence ratio of the reactive mixture will limit the production of NO_x by low adiabatic temperatures.

The ability for direct injection of powder can reduce powder losses in the oil and improve combustion phasing, which leads to the possibility of reaching traditional engine efficiencies. These results allow the start of a conversation on an alternative option to existing biofuels:

Rather than transforming solid biomass to liquid or gaseous drop-in fuels, modifications to an engine that can allow the use of minimally-refined fuels. By simplifying the biofuel production process, higher system efficiencies may be attainable, along with allowing portability at smaller scales.

On this basis, an injector system was designed and conceived in IJLRA. Its main purpose is to introduce solid particles into the combustion chamber of the SU RCM. A first study was conducted on this system to determine information such as the injection time and duration, the particle jet angle, and the penetration depth.

1. Description of the experimental setup

The particle injection system is majorly composed of a mixture tank, a hydraulic system to control the injection valves, and the injection tube. A scheme describing the injection system is presented in Figure 95.

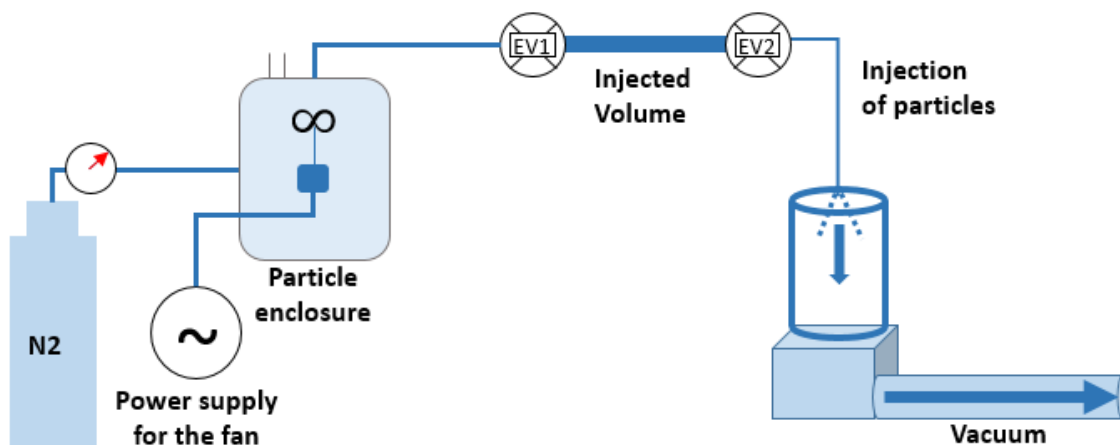


Figure 95 : Scheme describing the experimental setup of the particle injection system

The particles are suspended in a closed chamber that can be pressurized. It includes a mini-blower used to assure the blending of particles and avoid their agglomeration on the enclosure wall. The particles are introduced into the combustion chamber as an atomized powder in a carrier gas.

A sampling tube will take the particles in suspension, which will be in a homogeneous concentration from the enclosure into the combustion chamber via an injection circuit. A safety valve will open if the pressure in the chamber exceeds 35 bar. The second port is connected to the first solenoid valve, and the last port is connected to the vacuum cleaner to clean and evacuate the residential particles. A by-pass must be opened to allow the particles to go through this last port.

The size distribution of particles will be adapted to allow rapid volatilization. The chamber's pressure adjustment must allow the injection in the combustion chamber, which can be a few bars or pressure beyond a hundred bars.

A pressure sensor is used to measure the carrier gas pressure in the vessel, and a thermocouple to measure the chamber's heating temperature. A hydraulic group is used to command the two solenoid valves necessary for the particle injection. The injected volume can be defined as the volume of particles occupying the line between these valves (EV1 and EV2).

According to this definition, two modes of injection can be determined: Continuous and discontinuous injection. The first mode can occur when both solenoid valves are open simultaneously for a certain period. However, for the latter mode to happen, EV1 must be opened first to fill the injection volume while EV2 is closed. Once filled, EV1 is closed, and EV2 is opened to allow the charged volume injection into the porthole.

It is important to note that there is a delay between the command of the injection valve, its opening, and the real start of injection. These different definitions are illustrated in Figure 96.

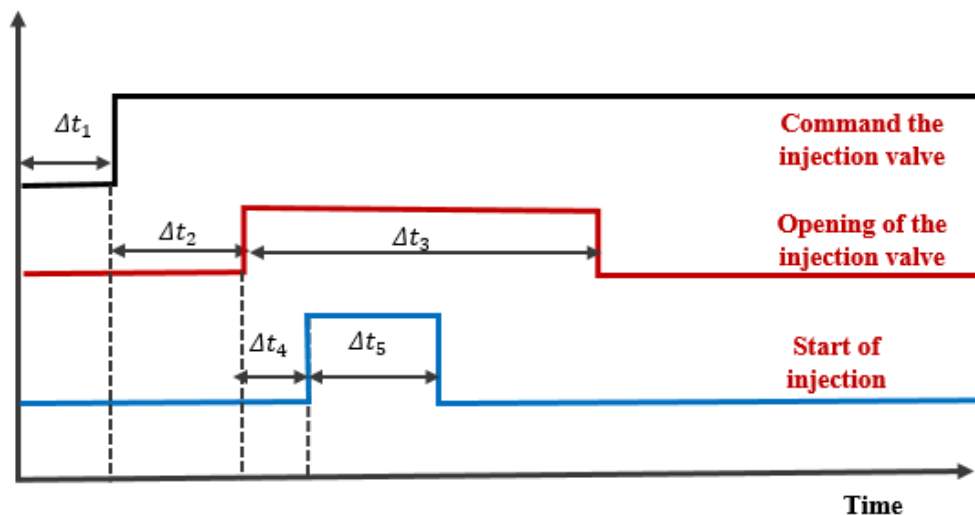


Figure 96: Chronogram of the injection valve command, opening, and start of injection

Where:

- Δt_1 is the time corresponding to the command of the injection valve.
- Δt_2 is the real and effective opening of the valve; it represents the necessary time for the injection valve to open after its command.
- Δt_3 is the opening duration of the injection valve.

- Δt_4 is the effective start of injection. This period depends on the injection pressure, as well as the pressure of the gas mixture in the chamber.
- Δt_5 : is the effective duration of injection: This period depends on several parameters, including the injection pressure and volume, as well as the shape and size of injected particles.

In the following study, the start of injection refers to the opening of the injection valve ($\Delta t_1 + \Delta t_2$). This value will be determined in this section while characterizing the injection system.

The pressure of the carrier gas, as well as the number of particles introduced, will define the dilution rate of the injected particles. Like a liquid injection, the system will be able to control the start of the injection, the number of injected particles as well as the volume of the carrier gas.

The injection nozzle volume will be a control parameter allowing in particular to obtain the angles of jet, penetration, and the turbulence that could result from the injection of carrier gas. It can be considered that an injection device diluted by gas can cause a loss of power, but in the claimed process, it is precisely this dilution that will allow a limitation of polluting emissions at the source.

The objective of this primary study is to make a first characterization of the gas/particle mixture infused by the injector. To do so, a configuration to perform PIV measurements is set up. Nevertheless, this first study only concerns image acquisition to determine information such as the injection time and duration, the jet angle, and the penetration depth.

The laser system Nd: YAG at 532 nm consists of two IR laser heads combined in a single package with a second harmonic generator and one discrete power supply. It is designed for Particle Image Velocimetry (PIV).

Both heads were set to the same frequency of 15 Hz. Before starting the PIV measurements, the mirrors and lenses in the laser beam were adjusted. The alignment is optimized by adjusting the beam from laser 2 to overlap the beam from laser 1. The beam from laser 1 is fixed and cannot be adjusted, so beam overlap is optimized by steering the beam from laser 2. This is an iterative process, switching between overlap measurements at the laser head and at a distance several meters from the head.

A Dantek Dynamics camera acquires the images. The camera's triggering is synchronized with the two laser beams' triggering, so there are two images acquired at each shot at a time t and $t+\Delta t$. Once switched on, the two laser beams are superimposed. A part of the beam is infrared and, once refracted, becomes a green laser. The field depth was adjusted to obtain a good focus on particles close to the centerline of the stream.

Direction Y was along the flow direction, and direction X was the transverse perpendicular direction in the plane of observation.

As explained earlier, we are more interested in characterizing the diphasic combustion solid/gas using lignocellulosic biomass. However, this manuscript aims to characterize the particle injector system and the parameters that can generally impact the gas/solid biomass combustion. Thus, the study of the injector characterization in this section, and the combustion of solid biomass and gas/solid biomass, in the following sections, will be conducted on cornstarch. The major features of the injector system and the experimental conditions are summarized in Table 28.

Table 28: Summary of the injection system proprieties

| | |
|--------------------------------|-----------------------|
| Nature of particles | Cornstarch |
| Particle density | 673 Kg/m ³ |
| Particle diameter | ~15μm |
| Time between two images | 15 μsec |
| Injection pressure | 2-2.5 bar |
| Injected volume | 2 mm ³ |
| Number of injection holes | 1 |
| Diameter of the injection hole | ϕ=2 mm |

The input parameters that can be modified are the following:

- the pressure of the chamber and the counter-pressure;
- the injected volume;
- particle density (number of particles/cm³);
- the nature of the particles;
- the shape of the injection nozzle;
- the injection type: continuous injection (the two solenoid valves are open) or discontinuous injection (the valves are opened one after the other).

The leading information that should be sought is as follows:

- the jet angle;
- the depth of penetration;
- the start, duration, and end of the injection;
- the density of the particles once injected into the volume;
- the settling time of the particles;
- velocity, turbulence, and entrainment of the flow.

2. Determining the start and duration of the particle injection process

As revealed in the experimental setup description, the solenoid valves are controlled by a hydraulic group system. In other words, a time delay exists between the command and the real opening of the valves.

Thus, an important step preceding the analysis of the jet angle and the penetration depth of the injected particles is to determine this delay and the injection duration. To do so, images of particle injection were registered with tens of delays generated between the command of the injection solenoid valve and the camera acquisition with the laser shot.

A delay generator varied these time laps from 15.5 to 24.5 milliseconds. Table 29 below shows the number of acquired images for each delay time.

Table 29: The number of acquired images for each delay time

| Test | 1 | 2 | 3 | 4 | 5 | 6 | 7 | 8 | 9 | 10 |
|--------------------|------|------|------|------|------|------|------|------|------|------|
| Delay (msec) | 24.5 | 23.5 | 22.5 | 21.5 | 20.5 | 19.5 | 18.5 | 17.5 | 16.5 | 15.5 |
| Acquisition number | 20 | 20 | 20 | 20 | 20 | 20 | 20 | 20 | 20 | 20 |

According to the registered images, the injection starts 24.5 msec after the injection valve's command, and it lasts for 7 msec (for the studied conditions).

We note that the duration of the injection is not relevant for all conditions. It depends on various parameters such as the injected volume, the injection pressure, the particle properties (shape and diameter), and the injection nozzle structure.

3. Determining the particle jet characteristics

3.1. Definition and calculations

The image processing technique based on MATLAB was used to determine the jet characteristics: the particle jet angle, the penetration depth, and the jet area.

Various methods were used in the literature to determine the jet angle (θ). In this study, the same method used by Du et al. [149] was utilized to determine the particle jet angle; θ is defined as the angle created by the two lines surrounding the jet from the injector's tip till the mid-length of the jet as can be seen in Figure 97.

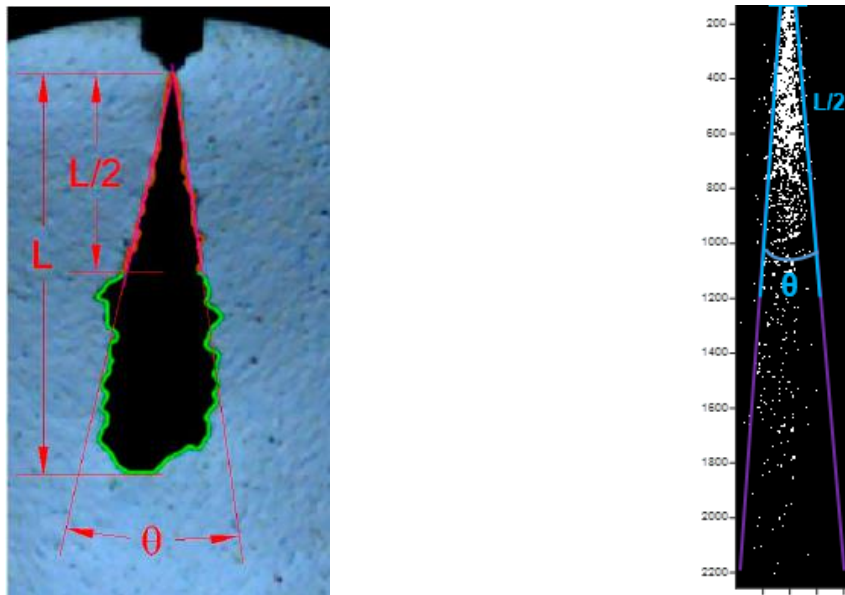


Figure 97: Definition of the jet penetration length L and the jet cone angle (θ) at $L/2$ [150].

It is calculated according to the following Equation:

$$\theta = 180 - \cos^{-1} \left(\frac{V_1 V_2}{d_1 d_2} \right) * \frac{180}{\pi}$$

V_1 and V_2 represent the vectors along the jet boundaries, and d_1 and d_2 are the lengths of V_1 and V_2 , respectively.

This method is commonly used to determine the angle of the liquid jet. For particle jets, however, the vectors V_1 and V_2 determination is more complicated due to the random distribution of particles around the jet. Thus, to determine these vectors, the jet's width was determined in the binarized images from the injector's tip until the jet's mid-length. Then, vectors V_1 and V_2 were determined by applying polynomial fit from the minimum to the maximum width on both sides of the jet.

The jet penetration length d is defined as the distance from the injector's tip to the very end of the jet, as shown in Figure 98. It is calculated using the following equation:

$$d = (d_{injector\ tip} - d_{spray\ end}) * P_{size}$$

Where: $d_{injector\ tip}$ is the pixel address at the end of the injector tip; $d_{spray\ end}$ is the pixel address at the end of the jet, and P_{size} is the dimension of the pixel (mm/pixel).

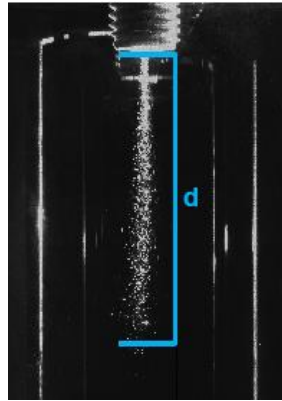


Figure 98 : Jet depth determination

The jet area is defined as the area covered by the particle jet. Actually, because of the randomly distributed particles around the jet boundary, the calculation of this parameter may represent some errors. However, it will be determined for a qualitative study of the jet coverage with the injection time.

3.2. Results

The evolution of the average jet angle $\bar{\theta}$ is presented as a function of the injection time in Figure 99. The angles measured from 7 msec onwards are no longer relevant since the injection is already complete.

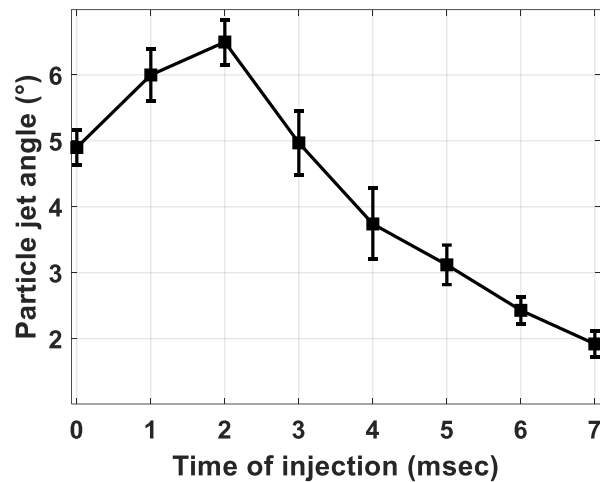


Figure 99: The evolution of the average jet cone angle $\bar{\theta}$ with the injection time

The measured jet angles are between 2 and 7°; it is more significant in the middle of the injection process than at the beginning or at the end. It is still relatively narrow, the jet is quite directed, and the particles do not seem to be enough dispersed throughout the enclosure.

The multi-hole nozzles could be used to better particle dispersion in the enclosure and improve their quick distribution in space. Several studies were conducted on the advantages of this type of nozzle in the homogenous distribution of the injected fuel (particles in our case) in the combustion chamber [150,151]. Weclas et al. [153] conducted several studies on the effects of multi-hole fuel nozzles in the conventional combustion engine. They found that the fuel surface area was increased compared to a free diesel injection, and the jet penetration length and jet velocity were decreased.

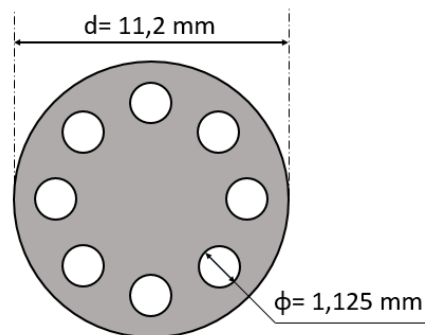


Figure 100 : Scheme representing the multi-hole injection nozzles

Thus, in the injection tests presented later in this chapter, the single nozzle will be replaced by multi-hole nozzles of eight cylindrical holes, as represented in Figure 100. This will allow greater dispersion of particles in the chamber, a larger jet angle, and homogeneous particle distribution.

Figure 101 represents the percentage of penetration depth over the image's length as a function of the injection time. The distance between the outlet nozzle and the bottom of the image is 9 cm. Since the penetration depth can no longer be determined when the particles are outside the camera's visual field, no information has been determined.

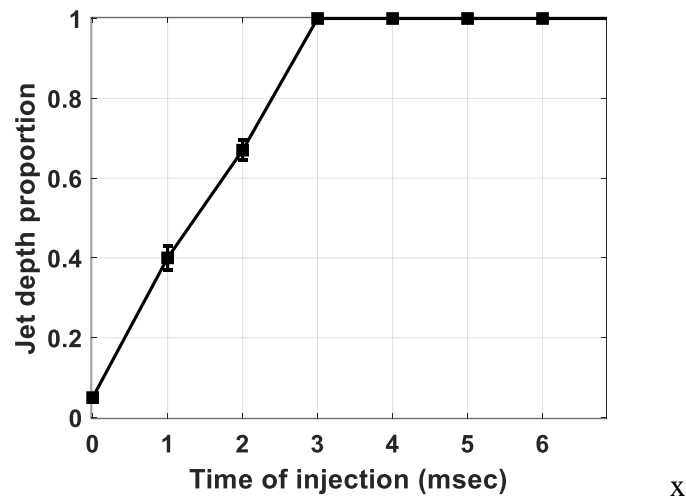


Figure 101: The evolution of the field depth proportion with the injection time

The penetration depth increases quickly; it is no longer measurable after 3 msec, with the view set up. The particles are, therefore, quickly injected into the enclosure. Since the nozzle is pointing downwards, the time during which the particles are in suspension is reduced; the particles fall rapidly due to gravity. At 10 msec, few suspended particles are visible.

The magnitude jet area can indicate the jet's overall expanding capability and the powder-air mixing quality, both of which are determined mainly by the distribution and the properties of the particle jet. The jet area is represented in Figure 100 as a function of the injection time.

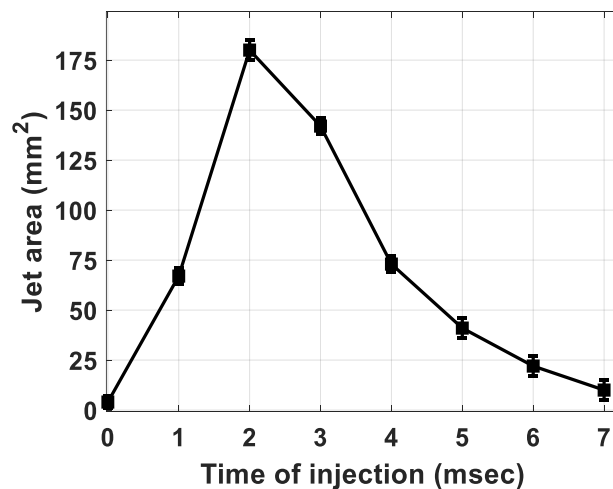


Figure 102: The evolution of the jet area with the injection time

As can be seen, the surface area increases after injection from 0 to 2 msec and decreases afterward. This means that the highest surface area is attained for 2 msec after the start of injection and when the jet penetration percentage is no more than 60%.

These results can indicate that when the injection starts, the particles are injected with a higher flow rate and, therefore, higher velocities; the particles were highly concentrated, and therefore, their area was relatively higher. After 2 msec of injection, the flow rate seems to decrease (the particles are more spaced one from the other) because, at this stand, there is less mass to be injected. As explained earlier in this chapter, the injected volume is a well-determined mixture of particles and compressed nitrogen.

In order to verify this assumption, PIV measurements will be held in the following section to characterize the velocities distribution and kinetic energies induced by the particle jet.

4. PIV measurements

4.1. Definition and calculation

The study of the internal aerodynamics was carried out using the PIV (Particle Image Velocimetry) method. Particular attention was paid to the study of the evolution and development of the global motion in the cylinder after the injection, as well as the evolution of the mean and turbulent kinetic energy.

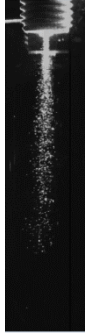
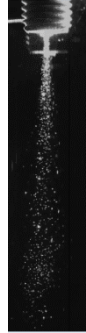
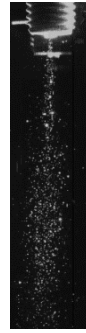
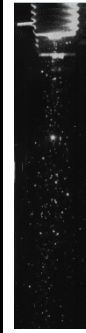
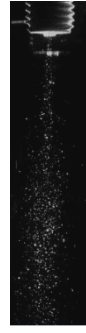
PIV consists of measuring the displacement of small particles (solids or liquids) that follow the fluid under the study's movement. The local velocities of fluid are thus assimilated to the velocities of the particles carried by this flow. By a statistical approach, this displacement is measured during an interval of time noted dt , making it possible to deduce the flow's local speed.

The processing is carried out by statistical inter-correlations applied to portions of these two images, called query windows. This makes it possible to calculate the particles' average velocity in this window during the interval dt . By dividing the Mie scattering images into several query windows, the velocity field's projection in the measurement plane is then reconstructed. Thus, the fluid's local velocity is determined by knowing the optical system's magnification, represented by the distance, the actual travel time, and the time interval dt between the two images.

The two heads laser is fired twice, and therefore, at each acquisition, two successive images are recorded with a delay of $\Delta t = 15\mu\text{sec}$.

For each delay, only one example of the registered images obtained is represented in Table 30 below. Image 1 is used to indicate the image registered by the first laser head at time t and Image 2 by the second head at $t+\Delta t$.

Table 30 : Registered images for each delay by the two laser heads

| Time (msec) | 1 | 2 | 3 | 4 | 5 | 6 | 7 | 8 | 9 | 10 |
|-------------|--|--|--|--|--|--|---|--|--|--|
| Image 1 |  |  |  |  |  |  |  |  |  |  |
| Image 2 |  |  |  |  |  |  |  |  |  |  |

4.2. Results

The PIVLAB tool is a time-resolved particle-image velocimetry software based on the commercial MATLAB software [154]. It was used in our study to analyze the vector velocities induced in the cylinder.

In order to carry out a complete statistical study, 20 reproducibility tests were carried out for each time after the injection. The average velocity magnitude of the particles detected at each position and for the various time after injection is presented in Figure 103.

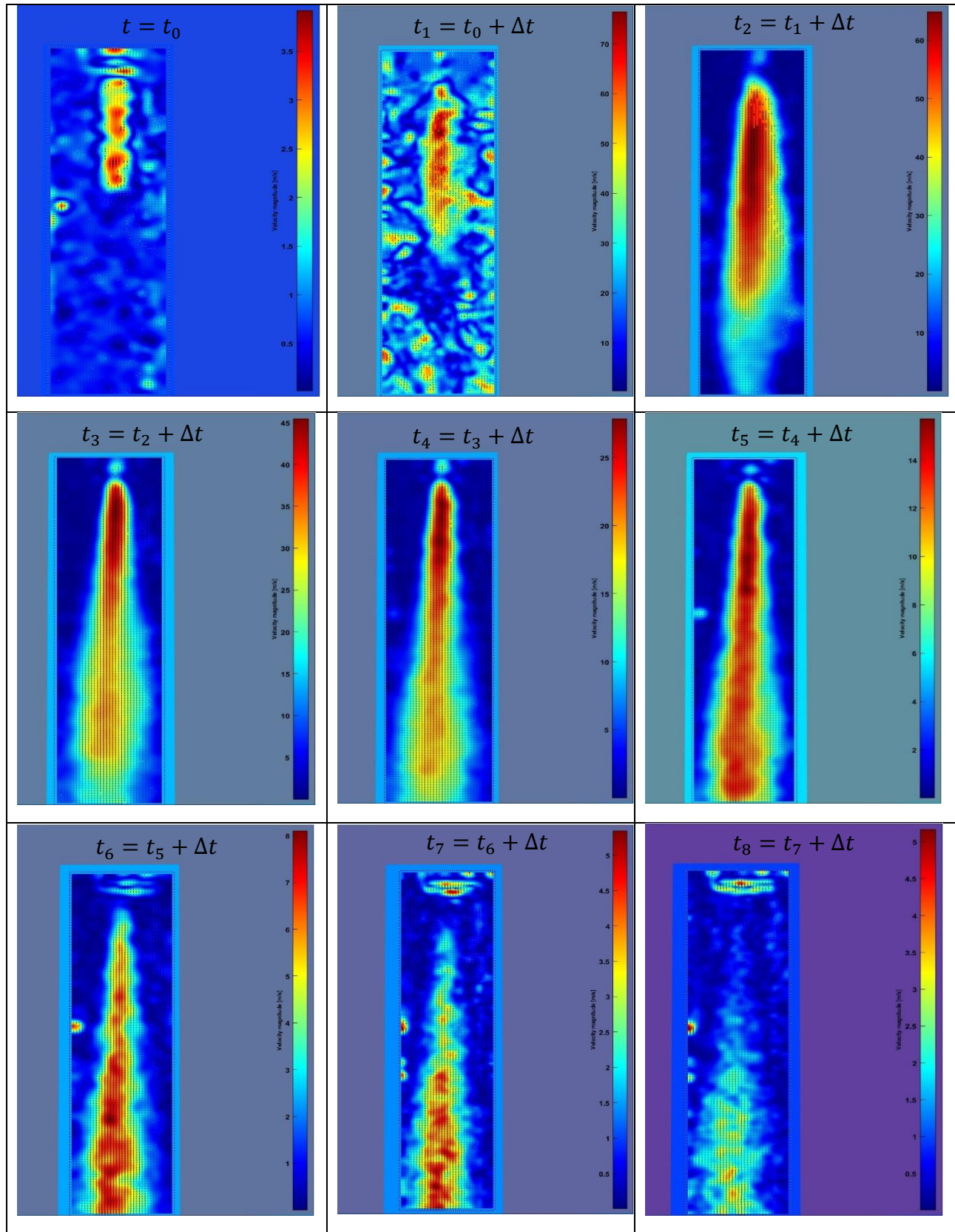


Figure 103: PIV measurement of the particle jet at different injection time

In jet flow engineering, the jet ahead of the nozzle is described by a turbulent behavior. Figure 104 shows the structure of the turbulent jet [155]. A potential core region is formed near the nozzle exit. In this region, the velocity is usually assumed to be constant. A mixing region surrounds this potential core region until the jet becomes fully developed, forming the developed region. The region surrounding the potential core region is called a mixing region. Over the distance from the nozzle, the jet becomes fully developed and forms the developed region.

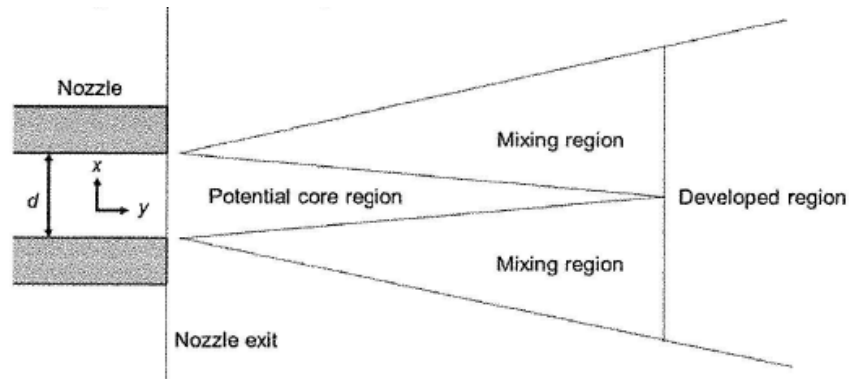


Figure 104: Turbulent jet flow from nozzle exit [155]

When the injection starts at t_0 , a small velocity potential is induced at the nozzle's exit. More discrepancies and turbulence structures are later created after 1 msec. This can be due to the difference in pressure between the injected particles and the mixture in the cylinder.

The aerodynamics, however, become more stable 2 msec after the start of injection. Between 2 and 6 msec, the velocity of the jet of particles is shown to be minimal at the exit of the nozzle; then, it accelerates ahead. This stream resembled the turbulent jet observed in fluid mechanics ahead of a nozzle. However, the higher potential core is shown for t_2 , where according to the previous section, represents the highest flow rate than other injection times.

As we get closer to the end of the injection, the velocity core is displaced from the nozzle tip to the mid-cylinder till its end at t_7 , where the injection is completed. In other words, the distribution is high towards the high energies at t_2 ; after that time, the distribution of high energies decreases in favor of an increase towards lower speeds.

The horizontal and vertical velocities in the injector system's cylinder at t_2 are presented in Figure 105.

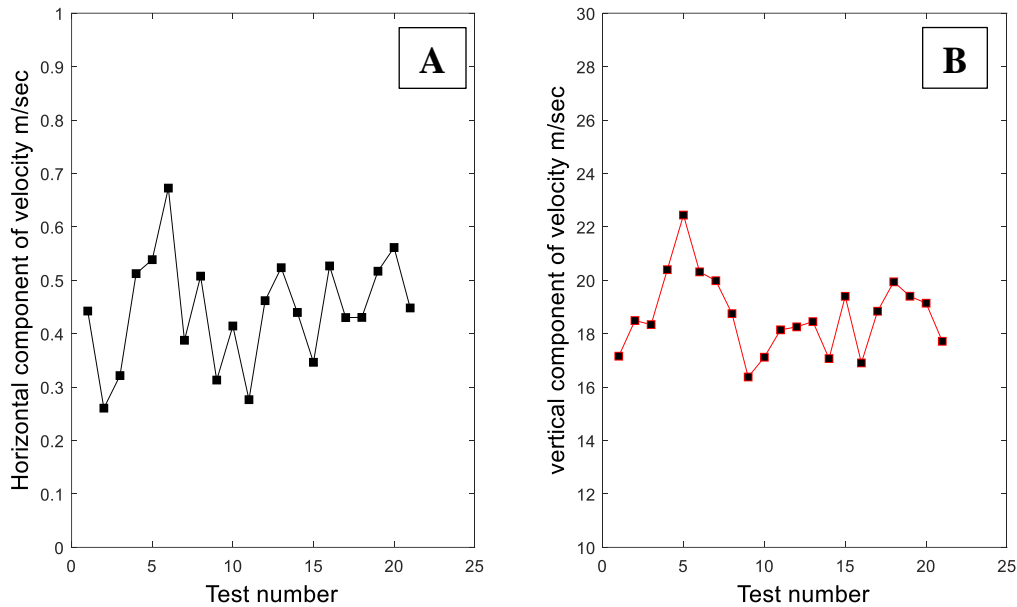


Figure 105: Horizontal and vertical components of average velocity at t_2 for different acquired tests

Because the injection is vertical, the horizontal velocities' values are considerably smaller than the vertical velocities. There are negligible discrepancies in horizontal velocities from one test to another (in order of 0.225 m/sec). Higher variations exist for the vertical velocities, but the values are relatively close to the average with a maximum discrepancy of 3.25 m/sec, representing 17% of the average value.

5. Conclusions on this section

In this section, the conceived particle injector system was described briefly, and primer tests were performed to characterize its injection characteristics.

The acquired image analysis shows that under the studied conditions where particles were injected at 2-2.5 bars into stagnant air at ambient pressure, the injection starts at 24.5 msec after commanding the injection valve, and it lasts for 7 msec. We note that particles' distribution in the chamber depends on various parameters such as the injected volume, the injection pressure, the shape and the size distributions in particles, and the injection nozzle structure.

It was also observed that the highest surface area covered by the particle jet was attained for 2 msec after the start of injection; meanwhile, the jet length percentage was no more than 60%. This indicates that the particles are injected with a higher flow rate at this time and, therefore, higher velocities. This can be explained by the duality of particles/ N_2 in the injected volume: when the number of particles increases, the nitrogen quantity decreases, but the injected volume is always the same. The experiments presented here were carried out with cornstarch, so it remains to know the dispersion when the particles' nature is different (change in shape, size, and density).

The primary purpose behind the conception of particle injector was to directly inject particles into reactive mixtures in the combustion chamber to allow the study of diphasic combustion (gas/solid) and see whether or not particle injection can control the timing of the ignition. According to the

study conducted in this section, the injection process's reproducibility was validated by the analysis of 200 acquired images. This validation is crucial to qualify the effects of solid particles better.

During the whole injection process, the jet was relatively narrow; It diffuses quickly from top to end (after 3 msec), but it only covers a small cylinder area. Thus, a different nozzle geometry with eight-holes will be used in the following sections to allow better dispersion of particles in the chamber.

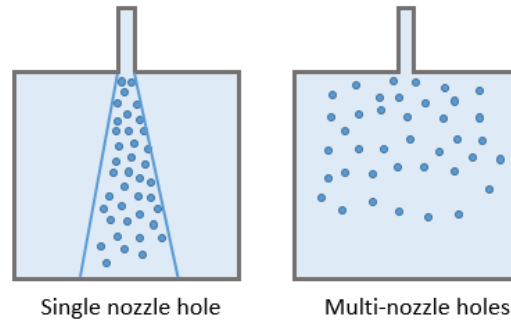


Figure 106 : Particle dispersion in the chamber using : a single nozzle and multi-hole nozzles

The particles will be injected into a reactive biofuel mixture compressed at certain pressure; a higher injection pressure will be required to allow the injection of particles in the combustion chamber and eliminate the backflow phenomenon. Therefore, the real injection time after the command of the valves, as well as the injection duration, will be different. The injection of particles/ N_2 into the reactive mixture will have several consequences: the well-dispersed particles will be as many ignition points of the reactive mixture in the whole volume of the chamber while the inert gas (N_2 in this study) will bring turbulence during the initiation and development of combustion.

Before studying the effect of solid particles on the lean homogeneous combustion of biofuel, it is crucial to study and characterize the combustion of solid biomass particles and to highlights the essential parameters that affect its combustion. Thus, the following section will be dedicated to studying the combustion and the chemical composition of lignocellulosic biomass.

Key ideas of this section

- The reproducibility of the injection process was validated by the analysis of 200 acquired images (velocities, jet angle, and field depth).
- With a single hole nozzle, the jet is narrow; another nozzle geometry should be used for a better particle dispersion.
- In the following study, multi-nozzle holes will be used for a better distribution of particles
- When injected into ambient air at 2-2.5 bars, the injection starts at 24.5 msec after commanding the injection valve, and it lasts for 7 msec.
- The start and duration of injection depend on the injected volume and pressure, as well as the pressure of the gas mixture in the chamber.
- In the following study, we refer to the opening of the injection valve by the start of the injection.

III. Biomass Composition

In this manuscript, the study is limited to cornstarch because our purpose is to study the effects of solid biomass on the reactive gas qualitatively. Even though it is not considered as lignocellulosic biomass, cornstarch is a white, granular, organic powder produced by all green plants. It is a polysaccharide comprising glucose monomers joined in α -1,4 linkages. Its chemical formula, similar to cellulose, is $(C_6H_{10}O_5)_n$. The simplest form of starch is the linear polymer amylose; amylopectin is the branched form. However, in future studies, we will use lignocellulosic biomass.

Lignocellulosic material is the non-starch, fibrous part of plant materials that represents a major part of the biomass. Because it does not take part in the human food chain, its use for biofuel does not threaten the world's food supply [156].

Lignocellulosic biomass has a complex internal structure. It is comprised of several significant components that have, in their turn, also complex structures. It is primarily composed of macromolecular substances (cellulose, hemicellulose, and lignin) with smaller amounts of low molecular weight substances: extractives and inorganics (salts or minerals). Extractives are organic compounds, and inorganics are the species that form the ashes. Biomass has a porous structure and consists of cells. In a typical lignified cell, cellulose represents an important structural element surrounded by other substances that function as a matrix (hemicellulose) and encrusting (lignin) materials.

The composition of lignocellulosic biomass highly depends on its source. There is a significant variation of the macromolecular components of biomass, depending on whether it is derived from hardwood, softwood, grasses, or, Nutshells [157]. The composition of lignocellulose encountered in the most common sources of biomass is summarized in Table 31.

Table 31: Composition of lignocellulose in several sources on a dry basis[158]

| Lignocellulosic materials | Cellulose (%) | Lignin (%) | Hemicellulose (%) |
|----------------------------------|----------------------|-------------------|--------------------------|
| Hardwoods stems | 40–55 | 18–25 | 24–40 |
| Softwood stems | 45–50 | 25–35 | 25–35 |
| Nut shells | 25–30 | 30–40 | 25–30 |
| Corn cobs | 45 | 15 | 35 |
| Grasses | 25–40 | 10–30 | 35–50 |
| Paper | 85–99 | 0–15 | 0 |
| Wheat straw | 30 | 15 | 50 |
| Sorted refuse | 60 | 20 | 20 |
| Leaves | 15–20 | 0 | 80–85 |
| Cotton seed hairs | 80–95 | 0 | 5–20 |
| Newspaper | 40–55 | 18–30 | 25–40 |
| Waste papers from chemical pulps | 60–70 | 5–10 | 10–20 |
| Primary wastewater solids | 8–15 | 24–29 | NA |
| Swine waste | 6.0 | NA | 28 |
| Solid cattle manure | 1.6–4.7 | 2.7–5.7 | 1.4–3.3 |
| Coastal Bermuda grass | 25 | 6.4 | 35.7 |
| Switchgrass | 45 | 12 | 31.4 |

As shown in this table, the cellulose contained in wood generally ranges from 40 to 55%. On the other hand, hemicellulose usually represents between 24 and 40% of the total wood, while the usual proportions of lignin are 18–25% for hardwood and 25–35% for softwood.

Leaves, however, have more hemicellulose and lower cellulose content, more extractives, and inorganic species. In herbaceous and agricultural biomass, the content of inorganic species in herbaceous and agricultural biomass is, on average, higher than in wood. Cellulose is usually the most abundant, while lignin is the least abundant macromolecule. However, many exceptions exist, such as the high content of lignin in some shells. Vassilev et al. [157] have reviewed the precise values of the cellulose, hemicellulose, and lignin contents for several species, covering a wide range of biomass.

In this section, the analysis of each principal component's structure is examined and described. In other words, the physical properties of each of the components of lignocellulose and how each of these components contributes to the complex structure's behavior as a whole will be addressed.

1. Cellulose

The cellulose component is considered the most abundant organic compound in the biosphere. It is a primary structural component of cell walls; it gives chemical stability and mechanical strength to plants. Solar energy absorbed throughout the process of photosynthesis is stored in the form of cellulose. The latter is a polysaccharide β -1,4-polyacetal of cellobiose (4-O- β -D-glucopyranosyl-D-glucose). Therefore, it is considered as a polymer of glucose as cellobiose consists of two molecules of glucose. The chemical formula of cellulose is $(C_6H_{10}O_5)_n$, including covalent bonds,

hydrogen bonds, and Van Der Waal forces within the polymer. The structure of one chain of a single polymer of cellulose is presented in Figure 107.

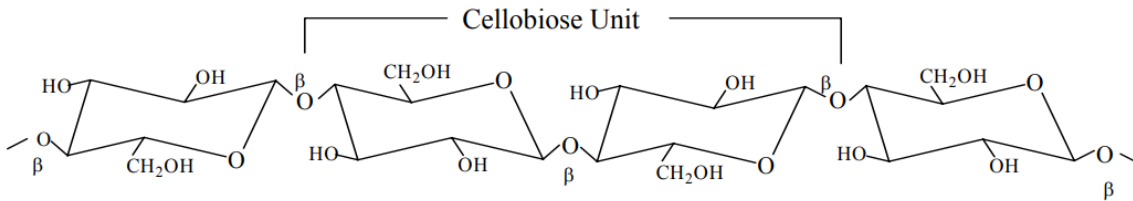


Figure 107: Structure of a single cellulose molecule

As can be seen, the polymer is arranged in long straight chains because of the nature of the bond between the glucose molecules (β -1,4 glucosidic). This arrangement of molecules, along with the fact that hydroxides are evenly distributed on both sides of monomers, allow for hydrogen bonds forming between cellulose molecules. In turn, the hydrogen bonds result in forming a compound comprised of several parallel chains attached [159].

The main functional groups of cellulose are the hydroxyl -OH functions; they have the property of forming hydrogen bonds with the -O, -N, and -S atoms, and also with the -OH functions of other cellulose chains. The linear chain polymer has an aldehyde function at one of its ends (denoted C₁), which in turn has an aldehyde function at the other end (denoted C₂), which in turn has an aldehyde function at one of its ends (denoted C₃). Confers reducing properties.

The -OH functions contribute significantly to the hydrophilic properties of cellulose. Cellulose is relatively hygroscopic, capable of absorbing 8 to 14% of its mass of water under pressure and temperature's normal conditions (20°C, 60% relative humidity). Though, despite the presence of -OH functions, cellulose is totally insoluble and swells in the presence of water.

Moreover, the repetition of the cellobiose pattern and the homogeneous distribution of -OH functions on linear unbranched chains favor the formation of hydrogen bonds between chains, leading to the formation of a three-dimensional structure consisting of several cellulose chains in parallel.

Consequently, cellulose exists in two structural states: amorphous cellulose and crystalline cellulose, where the polymers are organized in the form of a crystalline mesh whose cohesion is ensured by hydrogen bonds. The crystalline mesh consists of several parallel chains.

An illustration of the cellulose molecules' arrangement in parallel chains and the accompanying hydrogen bonding is given in Figure 108.

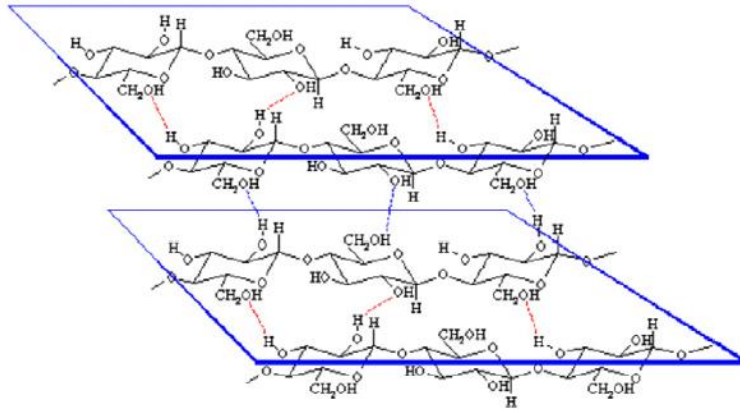


Figure 108: Demonstration of the hydrogen bonding that allows the parallel arrangement of the cellulose polymer chains [160]

The degree of polymerization (DP) represents the number of glucose units that make up one polymer molecule. It is an important parameter on which depends many properties of cellulose.

The DP of cellulose depends on the source of biomass. Its value is more commonly a number between 800-100000. It can, however, extend to a value of 17000.

2. Hemicellulose

The total polysaccharide fraction in biomass is mainly composed of cellulose and hemicellulose, as the latter is a complex polysaccharide composed of pentose (xylose and arabinose) and hexose sugars (mannose, galactose, glucose, rhamnose, or glucuronic acid). However, unlike glucose, hemicellulose is not considered a polymer as it has no consistently recurring monomer unit, and it is much shorter, with a polymerization degree (DP) between 100~200. It could be preferentially hydrolyzed under relatively mild conditions, known as pre-hydrolysis.

The chemical structure of significant hemicelluloses found in softwood includes glucomannan, galactoglucomannans, and arabinoglucuronoxylan. Hardwood can also be consistent with low amounts of glucomannan. However, the hemicellulose in hardwood is more represented with Xylan [161], whose chemical structure appears in Figure 109.

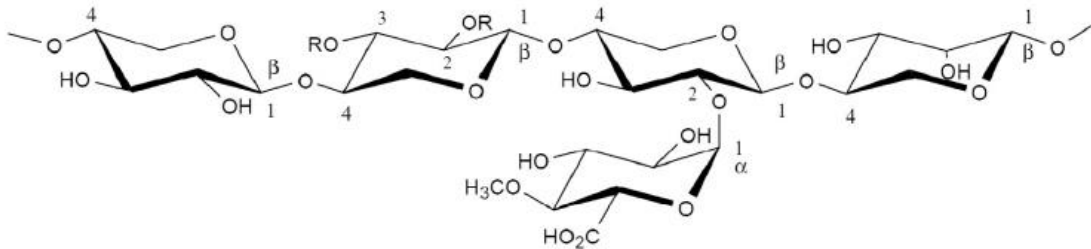


Figure 109: Chemical structure of Xylan (Hemicellulose)

Xylan is the most commonly used model compound for hemicellulose in previous mechanistic studies, as it is the basic building block of hemicellulose. It primarily consists of xylose, arabinose, and galactose, whose amounts depend on the biomass species [162].

3. Lignin

Lignin is a branched, long-chain molecule comparable to polymers, except that it has various monomer components. It is an amorphous three-dimensional polymer mostly derived from phenylpropane units as the predominant building blocks. Particularly, most commonly encountered are p-coumaryl ($C_9H_6O_3$), coniferyl ($C_{10}H_{12}O_3$), and sinapyl ($C_{11}H_{14}O_4$) alcohol. Their chemical structures are presented in Figure 110.

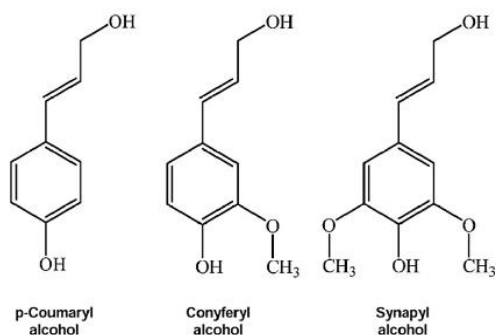


Figure 110: Chemical structures of the dominant building blocks of the three-dimensional polymer lignin P-Coumaryl-, Coniferyl-, and Sinapyl alcohol

The properties of lignins depend on the extraction or isolation techniques used. Thus, the ratio of phenols in lignin depends on plant species and ecosystems [163]. For example, normal softwood lignins are usually associated with "guaiacyl lignins" because the structural elements are derived principally from trans-coniferyl alcohol (more than 90%). The remains consist mainly of trans-p-coumaryl alcohol. Lignin is more abundant and polymeric in softwoods than in hardwoods.

In contrast, hardwood lignins, generally termed "guaiacyl-syringyl lignins," are mainly composed of trans-coniferyl alcohol and trans-sinapyl alcohol-type units in varying ratios (about 50% of trans-coniferyl alcohol and about 50% of trans-sinapyl alcohol). The primary linkage in lignin, the arylglycerol- β -aryl ether substructure, comprises about half of the total inter-unit linkages. These lignin model compounds' oxygen content ranges between 12-29 wt%, much lower than cellulose or hemicellulose. One chemical structure model of softwood and another one of hardwood lignin are presented in Figure 111 and Figure 112, respectively.

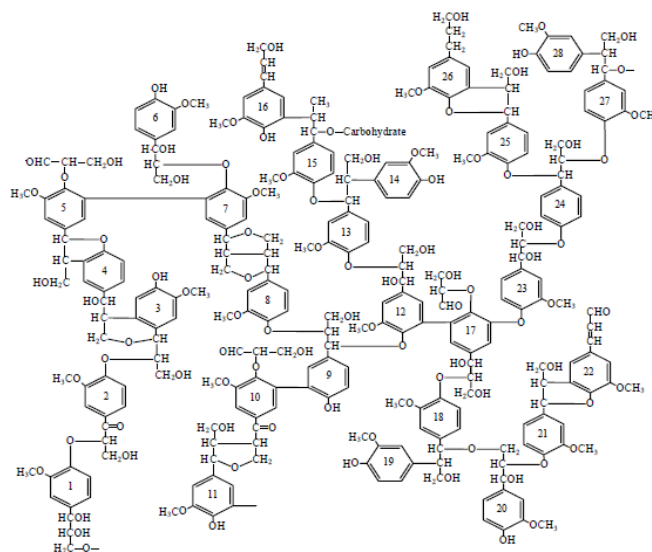


Figure 111: A model of the chemical structure of softwood lignin

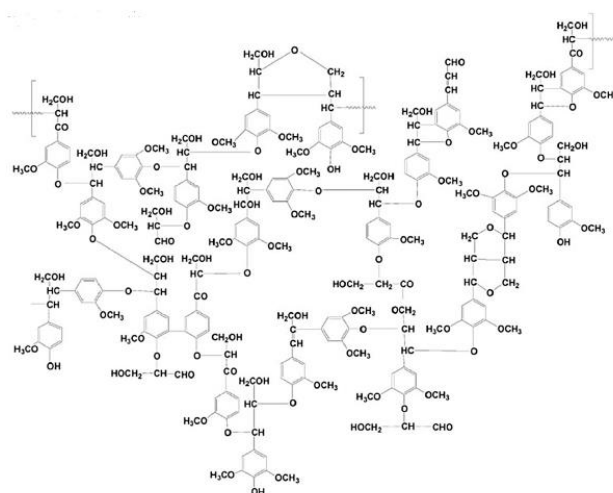


Figure 112: A model of the chemical structure of hardwood lignin

4. Extractives, inorganic, and moisture contents

Extractives are organic compounds that can be separated by successive treatments of the biomass with solvents, and recovered by evaporation of these solvents. These substances contribute to the characteristic properties of biomass, such as color, odor, taste, and the wood's decay resistance.

The extractives are categorized according to their lipophilic and hydrophilic constituents [164].

Inorganic elements are the species present in biomass that form the ash. They usually exist in lower concentrations compared to organic elements. In decreasing order of abundance in mass, the major

elements found are commonly C, O, H, N, Ca, K, Si, Mg, Al, S, Fe, P, Cl, Na, Mn, and Ti [157]. The macromolecular compounds cellulose, hemicellulose, and lignin are formed of C, O, and H, and N is organically bonded to them. The other elements are present in water-soluble, ion-exchangeable (salts or organically bound compounds), or mineral forms.

Ashes are formed of inorganic matter as phosphates, carbonates, silicates, chlorides, sulfates, oxyhydroxides, nitrates, or hydroxides. Therefore, inorganics are ash, forming elements[165].

Moreover, moisture can also be present in biomass and can be found in three forms [166]:

- The bound or hygroscopic or adsorbed water (M_b) is mainly composed of hydrogen-bonded to the hydroxyl groups of cellulose and hemicellulose, and to a lesser extent of lignin. It is found in the cell wall and is limited by the number of available sorption sites and the number of water molecules that can be held on a sorption site.
- Free or capillary water (M_c): It is found in liquid form in the lumens or void areas of biomass when sorption sites are no more available. Weak capillary forces only hold it without hydrogen bonds.
- Water vapor (M_v): It is found in the gas phase.

The Moisture content (M) is the quantity of moisture existing within the biomass. It is equal to the sum of the three types of moistures:

$$M = M_b + M_c + M_v$$

IV. Biomass combustion

1. Introduction

The process of biomass combustion involves several physical and chemical aspects of high complexity. The nature of this process depends on the fuel properties and the combustion application. Biomass fuels generally have a high moisture content between 50-65% by weight in fresh woody biomass. The water starts to evaporate when the fuel is introduced into a hot environment. The solid particle's conversion experiences four different stages: heating and drying, devolatilization (pyrolysis), combustion of gases, and char burning. These stages are shown in Figure 113.

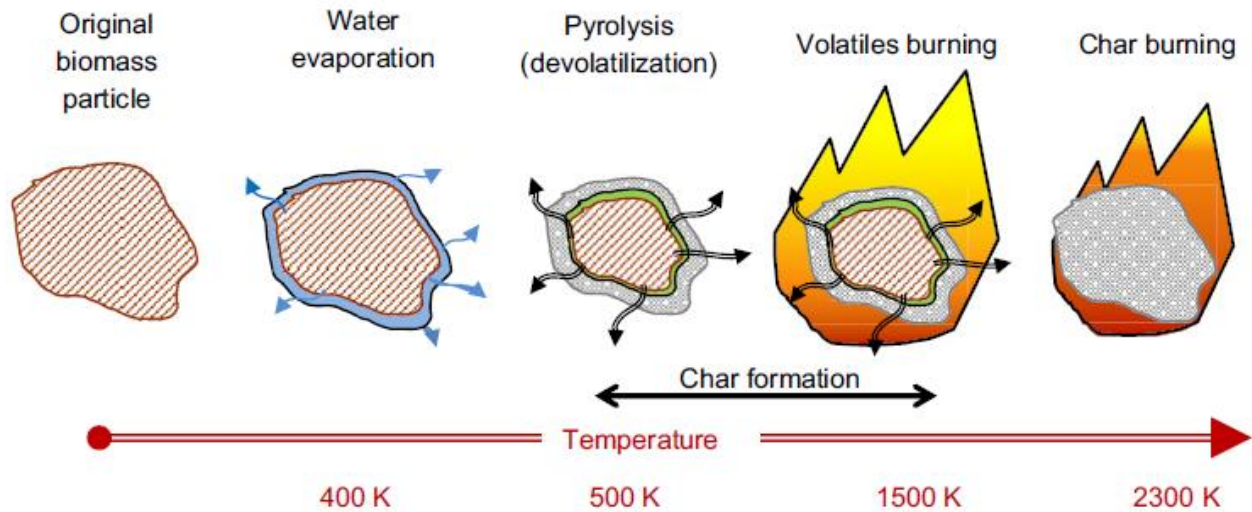


Figure 113: Combustion steps of a biomass particle in the 10e100 micron size range[167].

Drying and pyrolysis/gasification will always be the first steps in a solid fuel combustion process. These stages' importance will depend on the combustion technology implemented, the fuel properties, and the combustion process conditions.

Each stage has its own characteristics[168] :

- Heating and drying represent the first stages where the biomass moisture is evaporated by the heat supplied by the radiation of flames and the stored heat in the body of the combustion unit.
- Pyrolysis can be defined as thermal degradation (devolatilization) in the absence of an externally supplied oxidizing agent. When the dry biomass temperature reaches between 200°C and 350 °C, the volatile gases (CO, CO₂, CH₄) and high molecular weight compounds (tar) are released.
- Combustion of gases is a self-sustaining process; during this stage, the volatile gases and tars produced from the particle pyrolysis are combusted in the presence of oxygen, and the heat released from burning gases is used to dry the fresh fuel and release other volatile gases. The produced char remains the only material after all the volatiles are burnt out.
- Char burning or oxidation is the stage that generally starts after the release of volatile (at about 800 °C), and takes the longest time. The char reacts with oxygen to form mainly CO and CO₂. At the end of the biomass combustion, inorganic ash remains.

Figure 114 shows several conversion stages differentiated with time and increasing temperature.

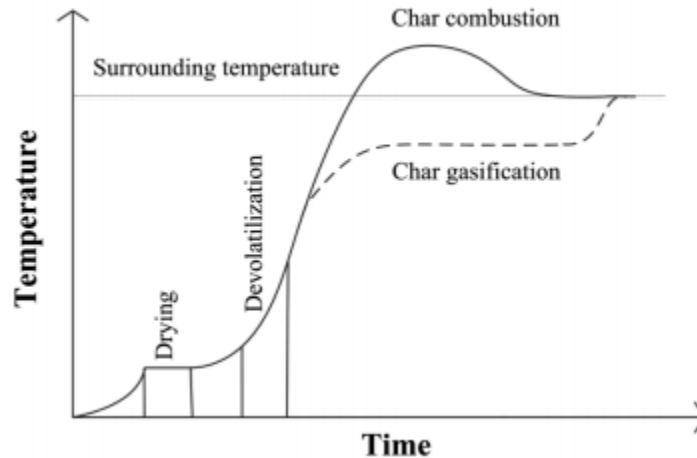


Figure 114: Different stages of biomass combustion versus temperature and time [169]

2. Ignition mechanism

Similar to gas combustion, the ignition temperature and delay time are key parameters in studying solid combustion. Generally, the particle ignition requires reaching the auto-ignition temperature of particles to trigger the chemical reactions. With sufficient time and a good mixture of reactants, chain formation of radicals and subsequent heat release enables the reaction to proceed in a self-sustained way.

Three modes of ignition can be identified for biomass or coal particles according to the timing of the ignition onset[170]:

- Homogeneous ignition characterizes by sequential combustion of volatiles and char. The ignition first occurs in the gas phase (volatile matter) around the particle, resulting in a flame envelope formation preventing oxygen from reaching the surface of the particle. This results in a delay in the char ignition till the end of the devolatilization stage.
- Heterogeneous combustion where the ignition first occurs in the solid residue (char) at the surface of the particle resulting in simultaneous combustion of volatiles and char.
- Hetero-homogeneous ignition where the ignition first occurs in the gas phase near the particle surface without forming a flame envelope.

Several parameters influence the ignition process of solid biomass, including the initial pressure, temperature, and composition of the reactant mixture, as well as its thermal and transport properties, velocity, and turbulence.

However, unlike gaseous fuels, which react with an oxidizer agent through well-studied mechanisms, solid fuels must first pyrolyze before the occurrence of any subsequent ignition. Thus, in the following paragraph, the biomass pyrolysis will be introduced; the factors that influence pyrolysis products will also be determined for better control of the solid biomass combustion.

3. Biomass Pyrolysis

Pyrolysis is an endothermic thermochemical process that occurs in the total absence of oxidizing agents. It can also occur with a limited supply that does not permit gasification. It consists of

decomposing the large complex hydrocarbon molecules of biomass into relatively smaller and simpler gas, liquid, and char molecules[156].

Pyrolysis of biomass is generally carried out in a relatively low-temperature range of 300 to 650 °C and can take the form of mild pyrolysis, slow pyrolysis, or fast pyrolysis.

The products of pyrolysis are a complex mixture of volatiles and solid char. Volatile compounds are mainly composed of permanent gases (CO, CO₂, CH₄, and H₂), liquid compounds, and water vapor. Their composition depends on many factors described in the following section.

3.1. Factors Affecting Biomass Pyrolysis

Several parameters influence the pyrolysis characteristics of biomass. Some are related to biomass's chemical and physical properties, such as the fuel composition and inorganic content, density, thermal conductivity and heat capacity, particle size, and shape. Others are related to the operating conditions such as temperature, pressure, and the heating rate.

Chemical and physical properties of biomass (Composition and particle shape and size)

The composition of the original biomass mainly determines pyrolysis yields and product distributions. In lignocellulose biomass, cellulose is the primary source of condensable vapor, while hemicellulose yields more non-condensable gases and less tar than that released by cellulose. However, both cellulose and hemicellulose are considered the main sources of volatiles.

Usually, cellulose and lignin produce the lowest and highest char yield, respectively; the char produced by hemicellulose lay between these two. The effects of the composition on the pyrolysis products can be found in various references in literature[171, 172, 173, 174, and 175].

As for particle's physical properties, several studies were conducted to study the influence of particle shape, size and physical structure on biomass pyrolysis. Jalan and Srivastava [176] investigated the particle size and heating rate's effects on the pyrolysis of a single cylindrical biomass particle. In pyrolysis models, there exist a geometric particle factor that accounts for the particle size, and shape.

Janse et al. [177] conducted simulations to investigate the influence of particle shape on wood flash pyrolysis. Three shapes were used for this study: spherical, cylindrical, and flat particles. Results show that the spherical particles react quicker for a factor comparable to the minimum particle size than other particle shapes. This tendency was explained by the higher surface-area-to-volume ratio of spherical particles; flat particles, however, react most slowly. Thus, it is more convenient to use spherical particle shape assumptions in modeling work.

With small particle diameters (generally less than 200 micrometers), the reaction rate becomes predominant, and the different particle shapes display almost equal conversion times. An increase in particle diameter (or conversion time) caused no change in bio-oil yield, a slight decrease in gas yield, and a slight increase in char yield (as can be seen in Figure 115). This trend might be due to the decrease in average particle temperature as a result of different heat penetration for the various shapes.

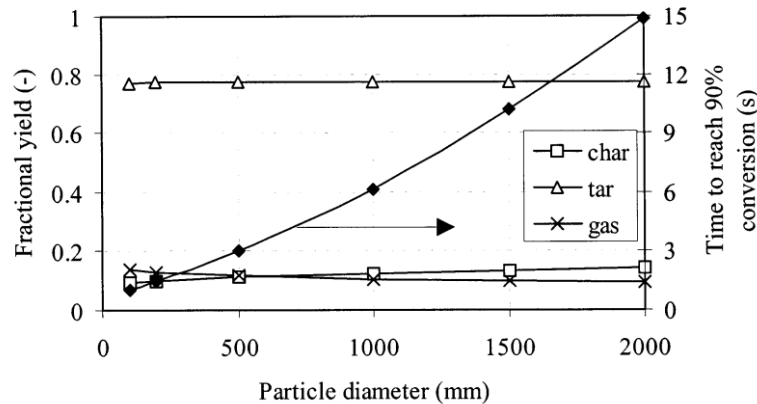


Figure 115: Time to reach 90% conversion and yields of tar, gas, and char at an imposed surface temperature of 823 K [177]

Temperature and Heating Rate

The pyrolysis temperature is defined as the maximum temperature to which the biomass particle is heated during pyrolysis. It is an important parameter that affects the composition and yield of the products [156].

As presented in Figure 116, the release of pyrolysis gas products changes with temperature variations. The same applies to the release of char, as the amount of produced char is higher at low temperatures.

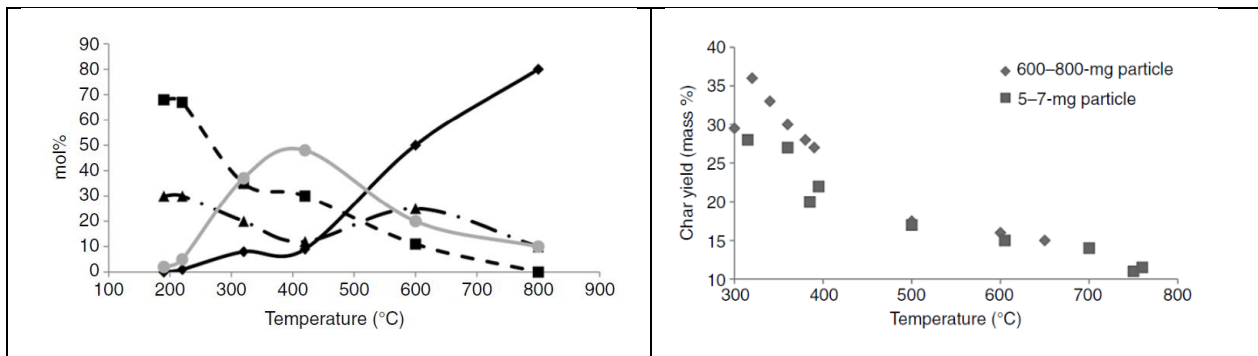


Figure 116: Pyrolysis gas release and char yields as a function of temperature [156]

Porosity

Another parameter affecting the pyrolysis behavior is the initial porosity of the biomass, as it is directly related to the particular biomass specimen under consideration.

The effect of the initial porosity on the char yields and conversion times was studied by Miller and Bellan [178], as shown in Figure 117. Results showed that char yields for both cellulose and wood remain nearly constant over the entire range of considered porosities due in part to the fixed initial particle mass. The conversion time, on the other hand, shows an increasing trend with initial porosity for both cellulose and wood. As a consequence, the effective heating rates of the particles are being decreased with increasing porosity.

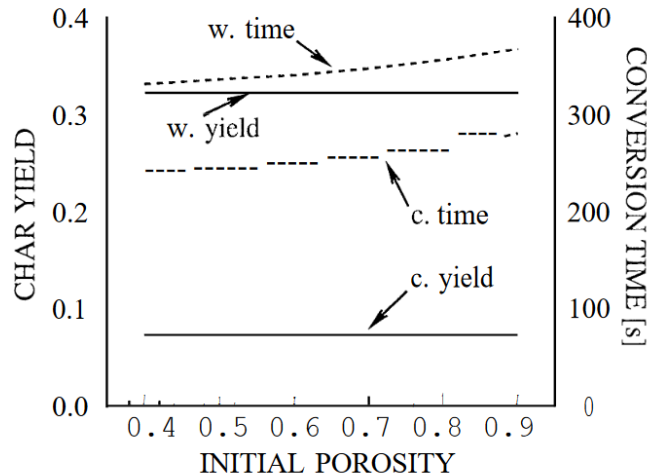


Figure 117: Char yield and conversion time as a function of the initial porosity for $T=900\text{K}$ [178]

3.2. Modeling the pyrolysis process

The exact pyrolysis mechanisms of biomass are currently not precise, although substantial literature sources on biomass devolatilization kinetics and mechanisms are available. Cellulose thermal decomposition models, together with phase changes and tar production, provide a framework from which many investigators have developed mathematical descriptions of biomass devolatilization.

Several pyrolysis kinetic models were modeled in the literature; however, they can be grouped into three major categories:

- One-step reaction, successive reactions, or two-stage models;
- Chemical structure-based models;
- Superposition models based on the kinetics of individual components of biomass (cellulose, hemicellulose, and lignin) [163].

Broido and Nelson proposed a competitive reaction model for the devolatilization of large cellulose samples. This was followed by other multi-step models by Bradbury, Sakai, and Shafizadeh. These models were usually used to describe low- or medium-temperature and low-heating-rate pyrolysis conditions [163].

More recently, Debiagi et al. [179] proposed a multi-step kinetic mechanism of biomass pyrolysis that leads to a better characterization of yields and compositions of residual bio-char.

This model is by far the only model able to describe the chemistry of the whole process from biomass to thermochemical conversion products in a comprehensive and predictive way. It provides interesting details with a little computational cost.

The model describes the solid residue as a mixture of pure carbon and lumped metaplastic compounds, representing the entire range of oxygenated and hydrogenated groups bonded to the carbonaceous matrix. These metaplastic species, released to the gas phase with their kinetics, describe the change of both mass loss and elemental composition of the bio-char [180]. These comprehensive predictions of bio-char composition are crucial for an accurate description of the successive oxidation and gasification processes.

The first step of biomass thermochemical conversion is pyrolysis. The material is heated under an inert atmosphere, releasing the raw material's volatile matter, yielding solid biochar, condensable tar, and gas [181]. Slow pyrolysis, in particular, is a suitable alternative when high yields of solid products are requested. At temperatures not higher than 650 K, with slow heating rates and long residence times (hours), this process yields up to 50 wt.% of biochar. Biomass isolated compounds produce biochar in different amounts. The lowest yield is for cellulose, followed by hemicellulose and lignin, which reaches up to 50% of its initial weight [182]. Because of a catalytic effect, inorganic matter in more massive amounts increases solid and gas yields, consequently reducing bio-oil yields [183].

3.3. Conclusions of this section

Understanding the combustion process of solid biomass is essential to characterize their impact on biofuel combustion better.

Pyrolysis is the thermochemical process that occurs at the early stage of solid combustion. It highly affects the combustion phenomena as it controls the yields of volatiles, tars, and char. Many models were introduced to simulate the pyrolysis process. However, the most commonly used pyrolysis model is still the single kinetic rate model.

Many factors influence the pyrolysis process, such as the composition, humidity, diameter, porosity. Knowing these parameters and their effects on the pyrolysis process are essential to study solid biomass combustion and its interaction with reactive gas.

In our study, we will only work on cornstarch whose chemical composition is similar to cellulose. The size, humidity, and porosity of the particles are not homogeneous; however, the mean size of particles can be estimated to 15 μm . Based on these physical and chemical properties, the reaction rate predominates the thermal aspects; the char yields are relatively high and decrease with temperature.

Biomass particles will be injected with nitrogen as a carrier gas into the reactive/inert mixture of the combustion chamber. The solid particle travels through the combustion chamber with the carrier gas; it exchanges energy by both radiation and convection and potentially provides an energy source or sink through reactions.

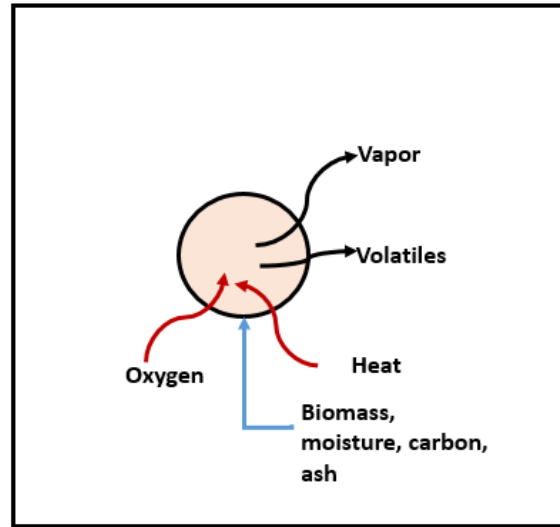


Figure 118: Biomass particle combustion process

At different residence times, biomass particle undergoes the following processes: drying, devolatilization, volatiles combustion, and gasification and oxidation of char (Figure 118). The combination of volatiles and char combustion will characterize the mode of ignition, whether it is homogeneous, heterogeneous, or both. These processes may occur individually or simultaneously depending on particle properties and the chamber conditions: particle type, density, size, shape, porosity, injection pressure, as well as the thermodynamic and chemical properties of the gaseous mixture (temperature, pressure, and composition).

4. Experimental study of biomass combustion

Before studying the diphasic combustion gas/solid, it is vital to characterize each combustion apart. A better comprehension of the main factors that affect the combustion of biomass powder is required to predict its effect on gas combustion.

The main objective of this study is to present the fundamental process of biomass powder combustion in the RCM chamber. As explained previously, the parameters that can affect the combustion process can be grouped as follows:

- The physico-chemical properties of the studied biomass (the type, shape, moisture and size distribution of studied particles)
- The temperature distribution of the mixture
- The injected volume (particle density)
- The pressure difference between the injected particles and compressed gas mixture
- The oxygen concentrations

We will only be able to study the influence of specific parameters related to the injector and RCM systems.

4.1. Experimental tests and conditions of the combustion of solid biomass

The particle injection system described and characterized earlier in this chapter is integrated into the rapid compression machine; the injector nozzle is implemented at the center of the combustion

chamber's top cylinder. The combustion process was studied by rapid cinematography by the mean of a rapid processing camera. The experimental setup is presented in Figure 119.

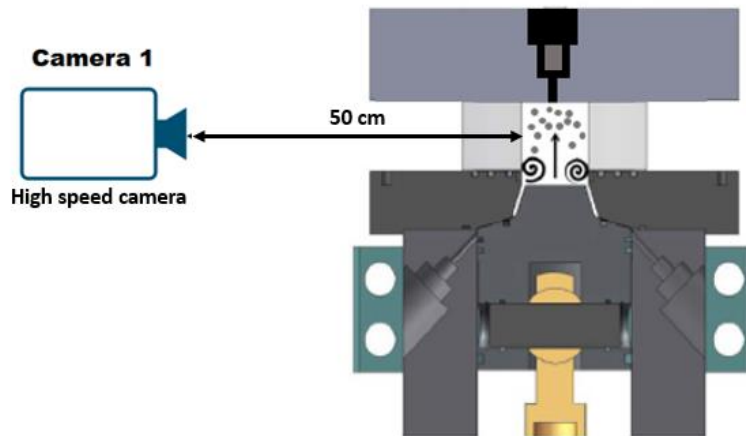


Figure 119 : Experimental setup for the study of particle combustion

In the present work, a CMOS high-speed Phantom camera is used to record the ignition events. No filter is used, and therefore, the visualized signal corresponds to the visible light intensity. It is important to remark that the captured signal includes black body emission and chemiluminescence emission. The exposure time is set to 99 μsec and the frame rate to 10000 Hz, yielding a resolution of 640 \times 480 pixels, which proved to be sufficient for proper visualization of the particles.

This study was only carried out on one type of biomass: cornstarch. Its combustion was tested for three temperatures varying from 955 to 1155 K, with different injection timing.

The particles were injected in an inert gas mixture of Ar/O₂. The mixture's temperature in the chamber was controlled by changing the proportion of Argon to oxygen, as shown in the following table.

Table 32: Argon and Oxygen proportions for different end of compression temperatures

| End of compression temperature (K) | Ar (Volume %) | O ₂ (Volume %) |
|------------------------------------|---------------|---------------------------|
| T _c =1155 K | 70 | 30 |
| T _c =1050 K | 57 | 43 |
| T _c =955 K | 43 | 57 |

As mentioned previously, in this study, the ‘start of injection’ refers to the opening of the injection valve. It was found in the first part of this chapter that the valve opens 24.5 msec after its command. For example, if we command the valve to inject after 5 msec, the start of injection is considered 29.5 msec, but the real injection remains unknown (depends on the injection pressure and counter pressure).

Thus, several injection timings were defined (Figure 120);

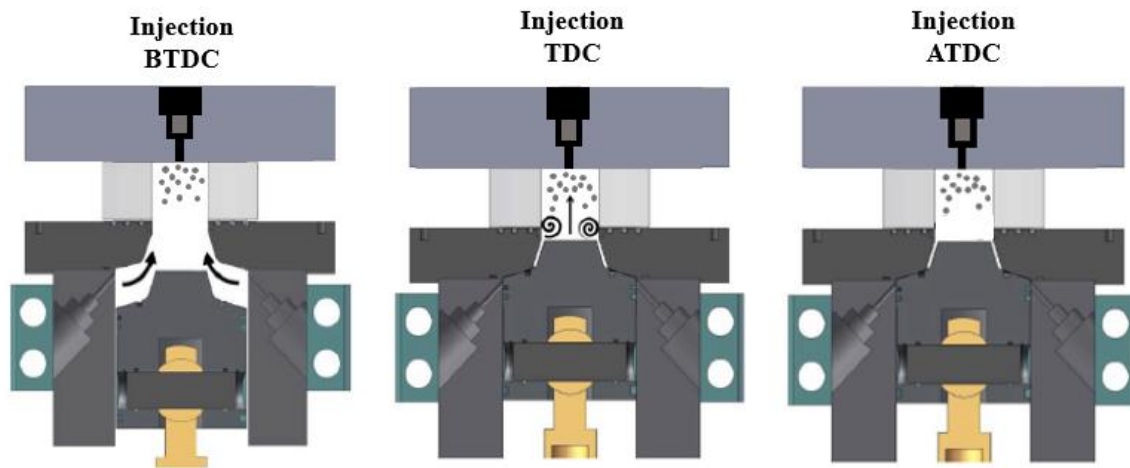


Figure 120 : The experimental tests of solid biomass combustion

- Injection 5.5 msec before the top dead center BTDC; the pressure at this location is close to the end of compression pressure. The advantage of the injection at this time is to inject particles while the pressure is still increasing. Therefore, this will help us see the effect of the increasing pressure on particles' ignition time.
- Injection at the top dead center TDC: this location represents the higher pressure (the end of compression pressure and the highest temperature in the cycle).

- Injection several milliseconds after the top dead center ATDC: At this position, the pressure and, therefore, the temperature is decreasing in the chamber. This injection will be mainly tested on the higher end of compression temperature.

The test conditions of this work are presented in Table 33. This table represents the command and the injection timing of all tested conditions. Three gas temperatures were studied: $T_c=1155$ K, $T_c=1050$ K, and $T_c=955$ K. For the latter, three different injection times were tested compared to only one for the formers. The O_2 concentration is constant for tests exhibiting the same end of compression temperature and varies from one temperature to another because the temperature is set by changing Ar/ O_2 proportions. Thus, the heat capacity of each mixture is also presented in Table 33.

Table 33 : Experimental test conditions of the combustion of solid biomass

| Tests | T_c (mixture) (K) | Injection command timing (msec) | injection timing (msec) | P injection (bar) | O_2/Ar | Heat capacity of the mixture (J/(mol.K)) |
|---------|---------------------------|--|-------------------------------|-------------------------|----------|--|
| Test 1a | 1155 | 30 | 24.5 ATDC | 20 | 0.43 | 28.059 |
| Test 1b | 1155 | 30 | 24.5 ATDC | 20 | 0.43 | 28.059 |
| Test 1c | 1155 | 30 | 24.5 ATDC | 20 | 0.43 | 28.059 |
| Test 2 | 955 | 30 | 24.5 ATDC | 20 | 1.32 | 32.366 |
| Test 3a | 955 | 0 | -5.5 BTDC | 20 | 1.32 | 32.366 |
| Test 3b | 955 | 0 | -5.5 BTDC | 20 | 1.32 | 32.366 |
| Test 4 | 1050 | 0 | -5.5 BTDC | 20 | 0.75 | 30.459 |
| Test 5 | 955 | 5.5 | TDC | 20 | 1.32 | 32.366 |

4.2. Ignition delay time and ignition temperature

The ignition of solid particles may occur homogeneously, heterogeneously, or under a combination of both modes. Homogeneous ignition occurs when particles generate volatiles that ignites before the solid residue. On the other hand, heterogeneous ignition happens when the particle ignites by direct oxygen attack on the solid surface before the flammability limit is achieved, and the auto-ignition temperature for that mixture is attained in the gas phase.

Several methods were identified in the literature to determine the ignition time of the solid combustion. However, methods based on optical diagnostic techniques are the most widely used. According to the study of Molina and Shaddix [184] on the combustion of bituminous coal diluted

particle jets in an entrained flow reactor, the start of the ignition is defined based on the CH* chemiluminescence emissions. Yuan et al.[185] determined the ignition characteristics of diluted coal particle jets using the residence time when the intensity reached 10% of the maximum peak intensity value. More recently, Khatami et al. [186] and Riaza et al. [187] studied the ignition delay time of coal particles in a drop tube reactor under different conditions. They defined the ignition delay time as the time between the initial entrance of a particle in the reactor and the first appearance of luminous combustion. It is this definition that will be used in our work. Rapid cinematography will be used to study the combustion of the injected solid particles in the RCM chamber. The ignition delay time is determined between the start of injection and the first appearance of luminous combustion, either a volatile flame or char surface oxidation.

Thermogravimetric analysis (TGA) is a traditional and important analysis method to obtain the ignition and combustion characteristics of fuel particles. It consists of measuring the mass of the sample with time or temperature while subjecting the sample to a controlled temperature program in a controlled atmosphere [188]. However, some authors consider this temperature to be the auto-ignition temperature, while others consider it the start of the pyrolysis process.

In our case, the cornstarch is used as solid biomass. Several studies in the literature used the TGA method to determine the thermal stability and decomposition of cornstarch; The decomposition temperatures found in some references are presented in Table 34.

Table 34: Temperature decomposition of cornstarch in literature

| Studied cornstarch | T max (°C) |
|---------------------------------------|------------|
| Cornstarch [189] with air | 308.9 |
| Cornstarch [190] with nitrogen | About 265 |
| Cornstarch [191] with air | 305 |
| Cornstarch [192] with dry nitrogen | 325 |

As can be seen, the temperature decomposition of cornstarch is around 600 K, which is consistent with our studied temperature range 900-1200 K.

4.3. Assumption calculations and experimental challenges

The temperatures were calculated based on the polytropic compression assumption in the compression phase, as explained in chapter 2, and a constant volume when the piston is at the top dead center.

Our purpose is not to give appropriate temperature values but to provide temperature to be compared together. As seen earlier, while characterizing the combustion process in the injector, the particle density is very low (in order of 673 kg/m^3)

This means that the proportion of solid particles in the gas mixture can be neglected, and the mixture can be considered mainly consistent with gaz.

The combustion of particles will indeed produce heat locally. However, due to the particles' small size and the low density, the heat rate will primarily affect the zones next to particle combustion. The temperature in the chamber will be considered unchangeable.

As explained in a previous section, for the same injected volume (2 mm^3), the proportion of N_2 /particles can be changed.

According to this statement, the evolution of load variations induced in the combustion chamber for different possible N_2 /particles quantities with the injected volume is represented in Figure 121.

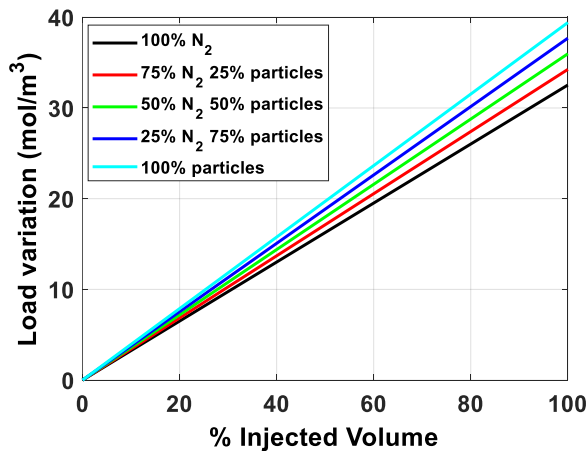


Figure 121: Load variations as a function of the injected volume for different possible N_2 /particles proportions

It is observed that the injection of the total volume into the combustion chamber increases the load of the mixture of about 33 mol/m^3 in case the volume contains only nitrogen and 40 mol/m^3 in case of 100% of particles. Note that load variation is an important parameter that can change the ignition delay times of a certain gaseous mixture. This is mainly due to the constant volume combustion; as the load increases, the pressure of the mixture also increases. The evolution of pressure increase due to the injection of the total volume is represented in Figure 122, with the volume percentage of the injected particles. Load and pressure variations were calculated for an injection pressure of 20 bars.

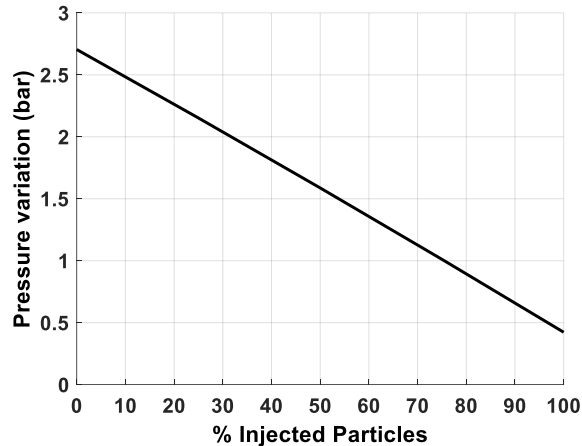


Figure 122: Pressure variations as a function of the injected particles volume

It can be seen that in our experimental conditions when all the volume is injected into the combustion chamber, the maximum pressure increase is estimated to 2.5 bars.

Another assumption concerns the ignition delay times. We have mentioned that these delays will be determined from the start of injection until the appearance of the first luminous particle. However, because the real injection time is not precisely known for each test, the opening of the injection valve will be used instead. Even though it cannot be directly transposed to real conditions ignition delays, as the injection timing is different for test conditions, but it can be a way to compare among samples.

4.4. Effect of temperature, injection time, aerodynamics

Test 1, 2, and 3

Although the particle injection was shown to be reproducible if repeated in the same conditions, the particle size, porosity, and moistures are changeable, affecting the products of pyrolysis. Therefore, it is essential to determine if the combustion process is reproducible as well.

The first study (Test 1a, b, and c) was conducted on a mixture heated to 1155 K. The injector was commanded at the TDC, which corresponds to a start of injection 24.5 msec after the TDC. This corresponds to the time where the pressure drops due to the heat transfer.

The experimental conditions were alike for all three tests in order to study the reproducibility of biomass combustion in these conditions. The evolution of the pressure curve for these tests with time is presented in Figure 123 (the blue squares represent the start of injection, the pink, red, and orange squares represent the viewed range from which the presented images are extracted).

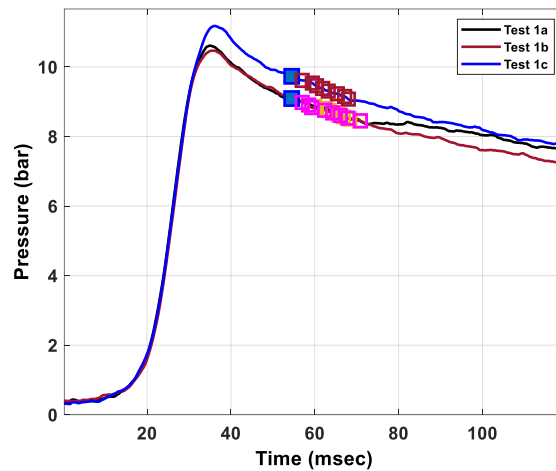


Figure 123: Pressure curves of Test 1a, b, and c of particle injection, with the end of compression temperature of 1155 K and an injection timing of 24,5 msec ATDC (the blue squares represent the start of injection)

The first presented image for each test corresponds to the first image, where the ignition of one or several particles is visible (first visible luminosity). The color black signifies no combustion, and the color white represents the combustion of particles. The time on the top of each image is referenced to the time at the TDC.

| Test 1a | | | |
|--------------|----------------|----------------|----------------|
| 30 msec ATDC | 32.6 msec ATDC | 35.6 msec ATDC | 38.3 msec ATDC |
| | | | |
| Test 1b | | | |
| 28 msec ATDC | 29.3 msec ATDC | 34.3 msec ATDC | 37.9 msec ATDC |
| | | | |

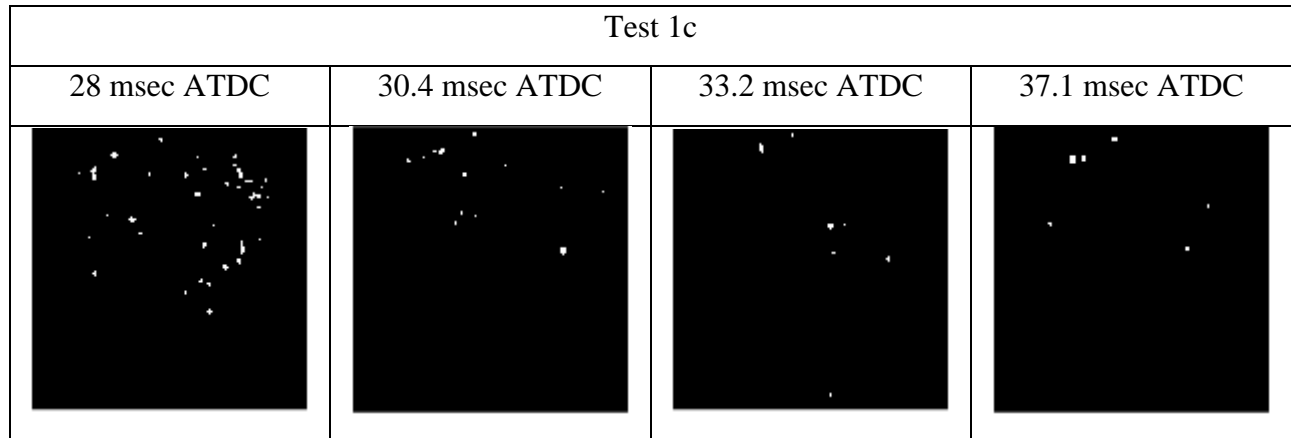


Figure 124: Acquired images (binarized) of the particle's combustion for Test 1a, b, and c

According to these images, the combustion of the first particle is visible 3.5 msec after the start of injection for Test 1a and 2.5 msec for tests 1b and c. This corresponds to when the temperature of the mixture decreases due to heat loss. These tests highlight the high reproducibility of the ignition of injected particles at high temperatures; the ignition delay time is between 2.5 and 3.5 msec.

The particles are injected with high pressures (20 bars) into the mixture, when the pressure and temperature are decreased to nearly 8 bar and 1000 K, respectively. Thus, once injected, the particles are first heated until all the moisture is evaporated, then start to decompose (pyrolysis) as their decomposition temperature determined by the thermogravimetric analysis is about 600 K. At the end of the pyrolysis, the volatile gases or the char are seen to ignite. The combustion of each particle produces local energy that heats its surrounding; thus, particles are shown to burn successively from a random point in the particle jet to the particles at the exit of the injection nozzle.

The same injection timing was conducted with a mixture compressed to 955 K (Test 2). In this test, the concentrations of oxygen in the mixture, as well as the thermal heat capacity, are higher than in test 1. However, contrary to the first study results, the particles could not burn under these conditions. The temperature at the start of injection is about 880 K. This temperature is high enough to heat up and dry particles and even start the pyrolysis process. However, by the time the pyrolysis ends, the temperature of the mixture will be even lower; therefore, neither the volatiles nor the char can be burned.

Choosing the right conditions of injection is essential to control the combustion.

The characteristic parameters of the combustion of particles for tests 1a, b, and c and test 2 are summarized in Table 35.

Table 35: Characteristic parameters of particle combustion for Test 1 (a, b, and c) and Test 2

| Tests | Command timing (msec) | Start of injection (msec) | Temperature of the mixture at the start of injection occurs (K) | time corresponds to the combustion of the first particle (msec) | P_{start} (bar) | T_{start} (K) | Ignition delay time (msec) |
|---------|-----------------------|---------------------------|---|---|-------------------|-----------------|----------------------------|
| Test 1a | TDC | 24.5 ATDC | 995 | 28 ATDC | 8.86 | 995 | 3.5 |
| Test 1b | TDC | 24.5 ATDC | 1009 | 27 ATDC | 8.98 | 1009 | 2.5 |
| Test 1c | TDC | 24.5 ATDC | 1000 | 27 ATDC | 9.61 | 1000 | 2.5 |
| Test 2 | TDC | 24.5 ATDC | 800 | - | - | - | - |

Another study (Test 3 a, b, and c) was conducted on a mixture heated to 955 K to validate the combustion reproducibility at lower temperatures. The injector in test 3 was commanded -30 msec BTDC, which means that the injection will start -5,5 msec BTDC.

The evolution of the pressure curve for these tests with time is presented in Figure 125 (the blue square represents the start of injection, the pink, and red squares represent the viewed images in the studied tests). The acquired images for different times after the start of injection are presented in Figure 126.

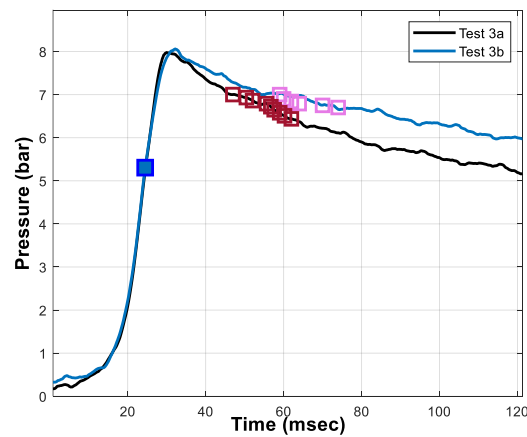


Figure 125: Pressure curves of Test 3a and 3b before and at the TDC for a mixture compressed at 955 K. the blue square represents the theoretical injection timing, the red and pink squares represents the registered images of test 3a and 3b, respectively

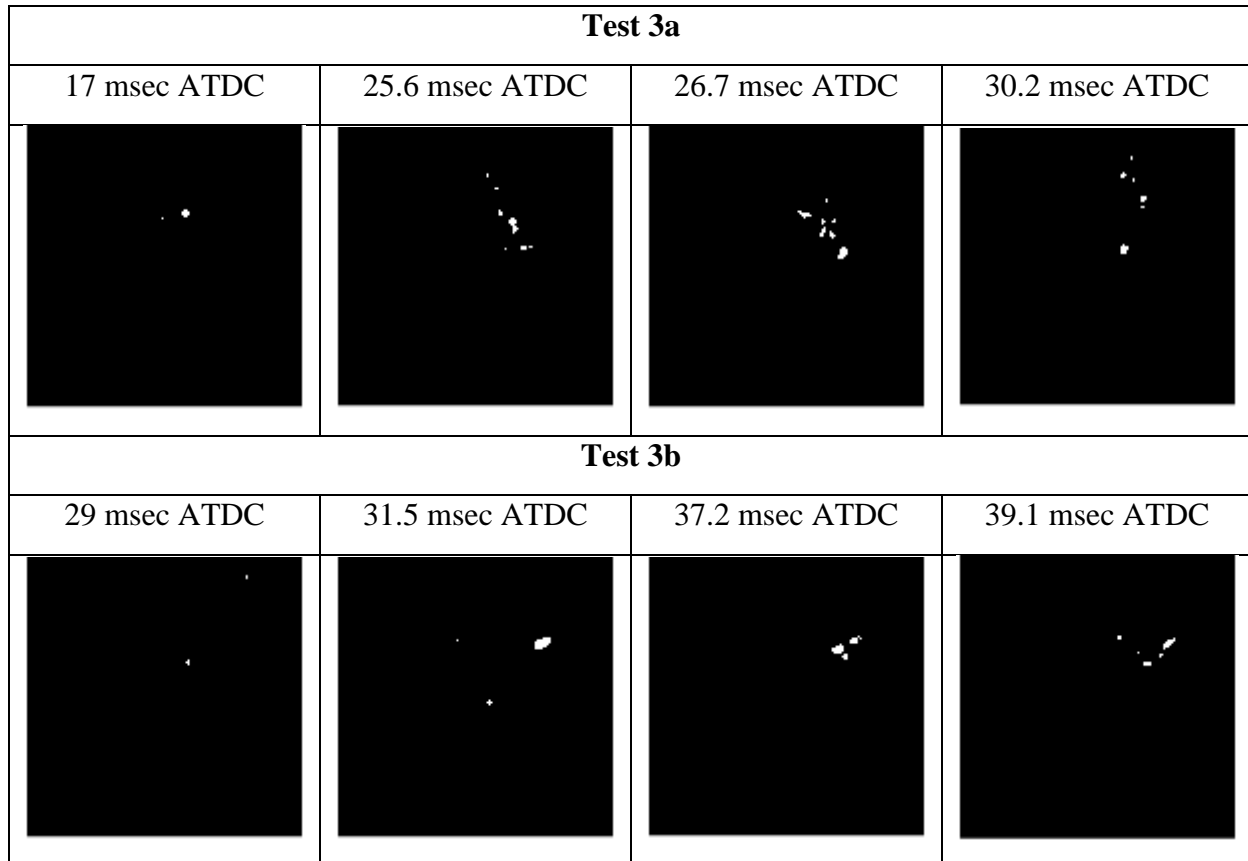


Figure 126: Combustion images of particles at 955K for test 3a and 3b

It can be observed that for the same experimental conditions, the particles do not start to burn simultaneously: the first luminosity appears 17 msec ATDC for test 3a and 29 msec ATDC for test 3b; This corresponds to an ignition delay time of 22.5 msec and 34.5 msec, respectively. We have seen in chapter 2 that gas combustion is less reproducible at temperatures lower than 960 K due to heat loss at the wall of the enclosure. This seems to apply to solid particles as well. However, in order to better study the reproducibility of particle injection at lower temperatures, more tests are required. The combustion time, pressure, and temperature for Test 3a and b are summarized in *Table 36*.

Table 36 : Characteristic parameters of particle combustion for Test 3 (a and b)

| Tests | Command timing (msec) | Start of injection (msec) | Temperature of the mixture at the start of injection occurs (K) | time corresponds to the combustion of the first particle (msec) | P_{start} (bar) | T_{start} (K) | Ignition delay time (msec) |
|---------|-----------------------|---------------------------|---|---|-------------------|-----------------|----------------------------|
| Test 3a | 0 | 24.5 | 848 | 47 | 7 | 835 | 22.5 |
| Test 3b | 0 | 24.5 | 848 | 59 | 7.16 | 813 | 34.5 |

Tests 4 and 5

For the same injection timing, test 4 was performed at the end of compression temperature of 1050 K. Similar to temperature 1155 K, the combustion reproducibility was validated. On the other hand, test 5 was performed for the same end of compression temperature (955 K) but with an injection at the TDC.

The evolution of the pressure curves for these tests with time is presented in Figure 125. The acquired images for different times after the start of injection are presented in Figure 126.

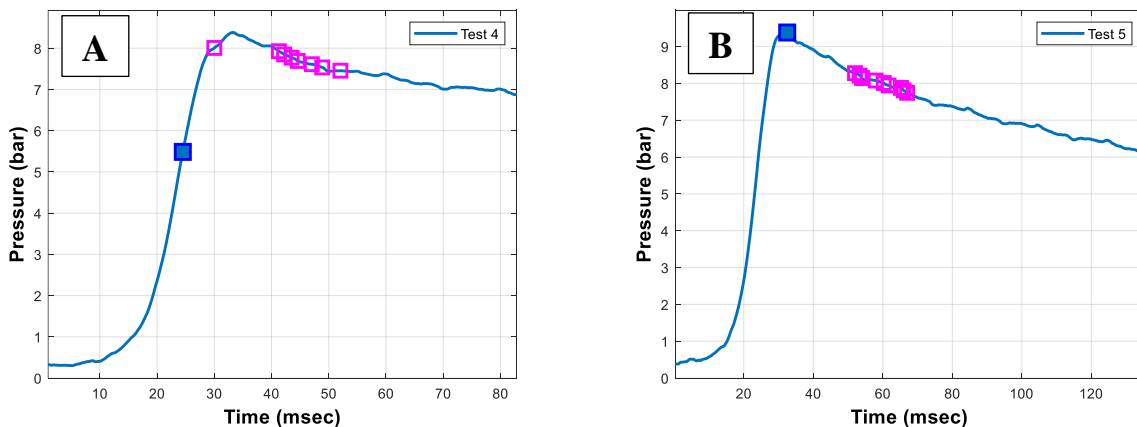


Figure 127: Pressure curves for **A.** Tests 4, injection -5,5 msec BTDC, $T_c = 1050$ K and **B.** Test 5 injection at the TDC, $T_c = 955$ K. the blue square represents the injection timing, the pink squares represent the registered images of tests 4 and 5

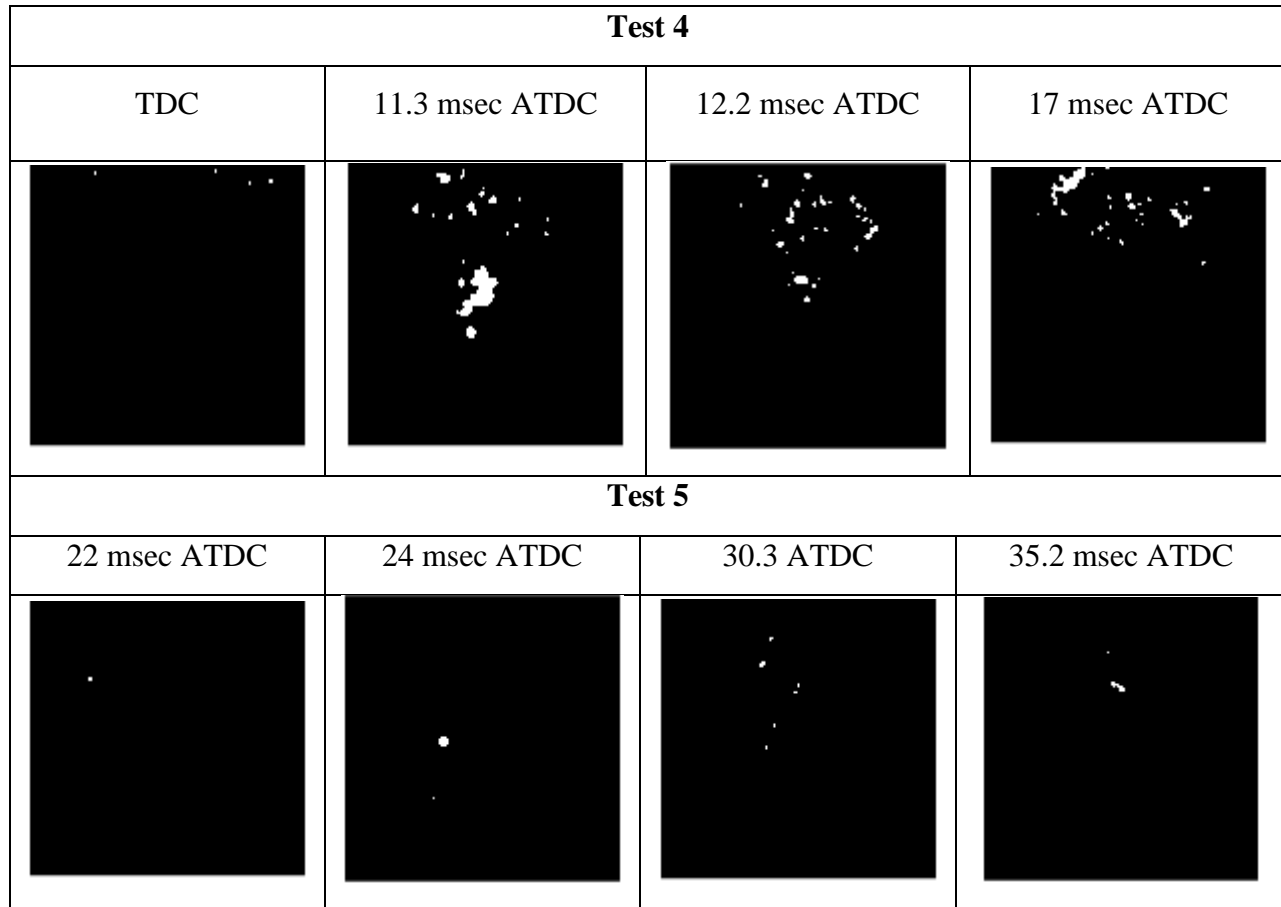


Figure 128: Combustion images of particles at 955K for tests 4 and 5

For test 4, the combustion of the first particle appears at the top dead center, which is equivalent to 5.5 msec after the start of injection, compared to a range of [22.5-33] msec for test 3. Thus, for the same injection timing the ignition delay time decreases with temperature.

This effect of temperature was investigated by several authors in the literature[170]. For test 5, the onset of combustion appears 22 msec ATDC, which is equivalent to 22 msec after the start of injection. This result is similar to that in test 3; however, we cannot conclude on the effect of injection timing, on the combustion of particles, because more tests with different temperatures are required to do so.

The location of the first burnt particles is changeable from one test to another due to the continuous change in the internal aerodynamics due to the flow movement. The particles can also be dependent on the temperature distribution inside the combustion chamber, but this assumption has to be verified. The particle injection may induce a change in the chamber aerodynamic fields and thus have an influence on the temperature distribution in the chamber. However, PIV measurements are inquired in future studies to measure to quantify the level of change in the aerodynamic fields.

The combustion time, pressure, and temperature for test 4 and 5 are summarized in Table 10.

Table 37 : Characteristic parameters of particle combustion for Test 4 and Test 5

| Tests | Command timing (msec) | Start of injection (msec) | Temperature of the mixture at the start of injection occurs (K) | Time corresponds to the combustion of the first particle (msec) | P_{start} (bar) | T_{start} (K) | Ignition delay time (msec) |
|--------|-----------------------|---------------------------|---|---|--------------------------|------------------------|----------------------------|
| Test 4 | -30 BTDC | -5.5 BTDC | 900 | TDC | 8 | 1030 | 5.5 |
| Test 5 | -24.5 BTDC | TDC | 952 | 22 ATDC | 8.27 | 840 | 22 |

Key ideas of this section

- Rapid cinematography was used to study the combustion of injected particles in the SU RCM
- The biomass combustion was studied in an inert mixture Ar/O₂ with three different temperatures, and three different injection timing
- The ignition delay time of particles is defined as the time between the start of injection and the appearance of the first luminosity (char or volatile combustion)
- The temperature is a key parameter in solid combustion. It decreases the ignition delay time for the same injection conditions
- The reproducibility of the powder combustion is validated especially for temperatures higher than 1050 K
- For an end of compression of 955 K, the heat transfer with the chamber walls affects the value of the ignition delay time for the same injection conditions
- For tests displaying similar experimental conditions, the slight differences in the ignition delay time might be due to the difference in size, humidity, and porosity of each particle
- The particles can burn at any point in the chamber as long as the thermal conditions are sufficient for burning the products of devolatilization; a future study on the particle and temperature distributions in the chamber can be good

V. Conclusions

In this chapter, an injector system was conceived to directly inject solid particles into a reactive gas mixture and study the effect of the injected powder in controlling the ignition timing of HCCI combustion.

In the first part of this chapter, tests were performed to characterize different aspects of the system (injection time, duration, jet angle, penetration depth, and field velocities). A multi-hole nozzle was used for a wider injection range allowing a better distribution of particles in the chamber.

Prior to gas/solid combustion, the combustion of solid biomass was characterized to study the different factors that can affect its ignition.

In this section, the solid biomass combustion was conducted on the SU RCM by implementing the injector nozzle of the injection system described earlier at the combustion chamber center.

The temperature of the mixture, the injection time, and the presence or not of aerodynamic fields were the parameters studied in this section that affect the combustion process. This study was carried out on cornstarch. Its combustion was tested for three temperatures varying from 955-1155 K, with different injection pressure and injection times.

The particles were injected in an inert gas mixture of Ar/O₂. It can be seen that in our experimental conditions when all the volume is injected into the combustion chamber, the increase in pressure is estimated to a maximum value of 2.5 bars.

The injected particles are heated and start to burn only when their temperature is equal to their decomposition temperature determined by the thermogravimetric analysis. The combustion of each particle produces local energy that heats its surrounding; thus, particles are shown to burn successively from a random point in the particle jet to the particles at the exit of the injection nozzle. After that, particles are immediately heated at the time of their injection.

When a particle burns, it releases energy that will be used to heat the surrounding, which causes the combustion of other particles in the chamber. Combustion of higher concentrations can increase the mixture's pressure by producing a high level of heat release.

For mixtures heated to 1155K, particles injected 24.5 msec after the top dead center were burnt. However, for the same injection time but at lower temperature of 955 K, particles injected after the top dead center could not burn. However, for this temperature (955 K) and for an injection before the top dead center, particles were able to burn; Nevertheless, the time delay needed for the first particle to burn depends on the particles and temperature distribution in the chamber. The comparison of the ignition delay time is not accurate as the real start of injection is unknown. Also, the temperature and pressure are varying during the process. However, for the same start of injection, the ignition delay time decreases with the overall temperature.

The reproducibility of the combustion was validated for higher temperatures 1050-1155 K. At lower temperatures, the biomass combustion is affected by the heat transfer at the chamber walls. Therefore, the tests were less reproducible with a wider range of ignition delay times.

A good choice of the injection time with temperature is essential to better control the combustion of the mixture; injecting particles after the end of compression in the heat transfer phase needs a higher temperature to burn.

Chapter 5:

Diphasic combustion gas/solid

Chapter 5

I. Introduction

The purposes of this chapter are to highlight the different possible behaviors related to biofuels and diphasic gas/solid combustion.

Several authors in literature have shown that combustion in HCCI mode can lead to mass combustion coexistence with the propagation flame front. These authors explained that this coexistence is linked to the different properties of fuels and the levels of temperature and concentration heterogeneities in fuel, accompanied by a certain turbulence level in the chamber [193], [144] [53].

The combustion of gaseous biofuel mixtures was studied both experimentally and numerically under lean homogeneous conditions in the previous chapters. The experimental results were issued from the pressure curve of the combustion process.

However, the pressure signal analysis does not allow access to the combustion process's phenomenology. That's why an experimental study of the phenomenology of combustion by direct visualization will be conducted next.

This chapter's objectives will be as followed:

First, to highlight the different possible behaviors related to biofuels in lean homogeneous conditions. The experimental studies performed through direct visualization of the combustion process on SU RCM are described in detail throughout this chapter. The effects of parameters such as fuel composition, the temperature on the combustion behavior were studied experimentally. The results were then compared to those studied in the numerical study.

Second, to give a first study on the effects of biomass injection on biofuel combustion. As shown in chapter 4, the biomass powder combustion was carried out on the rapid compression machine. The particles were then injected at non-reactive Ar/O₂ mixtures and under different temperatures to identify the particle combustion properties. However, in this chapter the particles are injected into the reactive biomass gas mixtures studied in the previous section for the same conditions. In other words, we aim to study the two-phase interaction of solid biomass particles on a reactive gaseous mixture. This study will show whether or not particles have a positive effect on the reactivity, control and stability of gaseous combustion.

II. The fundamentals of direct visualization

Whether it is an auto-ignition or a propagating flame front or both, the combustion, in general, is characterized by high radical concentrations and chemical reactions. The thermodynamic imbalance that occurs during the combustion process is reflected by the electronically excited particles, relaxing into state energy savings, mainly through the emission of ultra-violet or visible radiation. These emissions are the characteristic of transitions between the electronic levels. The energy variation corresponding to each transition is quantized, leading to a band emission. This phenomenon is known as chemiluminescence. It describes the emission of electromagnetic radiation from chemical reactions, which can occur when an excited state relaxes to its ground state[194].

In order to exhibit this process, the chemical reaction must first provide sufficient energy for the excitation to occur. The products of this reaction must be capable of excitation to an electronically excited state, and the reaction rate must be sufficiently high. Also, the reaction coordinates must favor the production of excited-states.

In our case of study, the chemiluminescence of combustion can be observed starting from the ignition initiation phase until its end. The chemical species are excited by the chemical reaction's energy and emit photons when they are de-excited. Each species emits at particular wavelengths depending on the electronic transition of relaxation. Spectral filtering can be used to separate the contributions of these different species.

Therefore, the chemiluminescence phenomenon is good information of the combustion process; it will be used in this chapter to experimentally study the combustion of gaseous biofuel and gas/solid biomass via direct visualization.

III. Experimental Setup

The combustion process is studied by direct visualization using two intensified cameras Phantom Fastcam. These two cameras are located in a way that allows the vision of two perpendicular sides of the combustion chamber, which covers a big part of the combustion process. This installation is presented in the figure below (Figure 129):

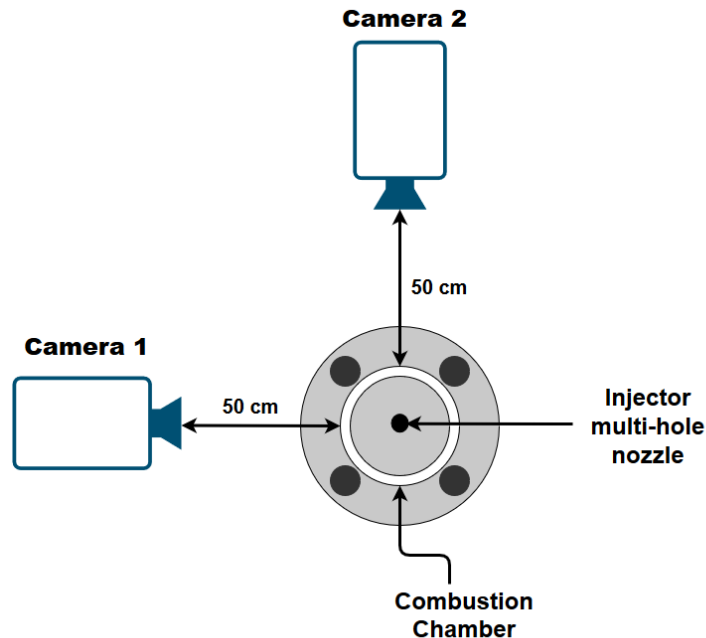


Figure 129: Experimental setup of the cinematography process on the rapid compression machine. It shows how both cameras are located to allow a wider vision of the combustion process.

The same properties were set up for both cameras: the images were acquired with a resolution of 640x480 pixels. The greyscale is set to 8 bits, which is equivalent to 256 shades of grey. The exposure time is the period during which the camera's sensor is exposed to the light to record a picture.

This exposure time and the frequency of acquisition must be chosen wisely [195]. For example, low frame rate images give bright flame images. However, it is not adequate to resolve the fast-oscillating components due to its low temporal resolution. On the other hand, high frame rate images provide much better performance on the frequency analysis but limit the possible exposure time. Thus, all images were registered with a frequency of 10000 Hz. The exposure time determines the incidental light quantity. As a result, only a precisely defined light quantity leads to the correct exposure.

In our cases, the relation between luminosity, the reactivity and the heat release of the mixture combustion should be taken into consideration. In other words, the exposure time will be lowered when the luminosity (the heat release) is high. Thus, it was varied between 30 and 99 microseconds for both cameras according to the studied mixture.

The acquired images are filtered and binarized using the image processing toolbox (MATLAB) allowing the extraction of several parameters. Thus, the combustion phenomenology of gaseous biofuel mixtures and gas/solid biomass is treated and presented in the following paragraphs.

IV. Chronograms of direct visualization

The direct visualization process is triggered by a signal related to the position of the RCM piston. In our study, the signal is sent at the start of the compression phase, when the piston leaves the position of the top dead center.

A chronogram is presented in Figure 130, describing the start time and period of processes of each component used in direct visualization.

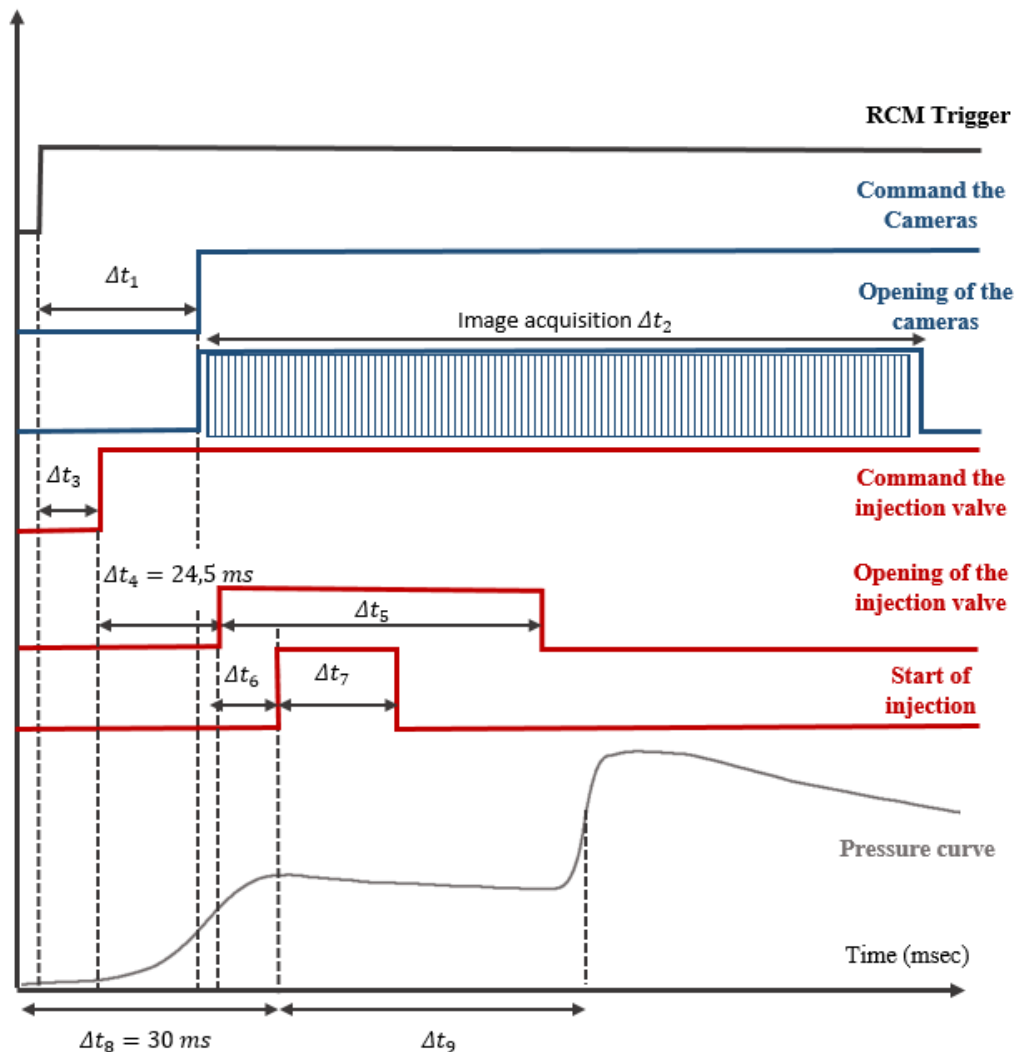


Figure 130: Chronogram of image acquisition for direct combustion viewing

The different periods of time presented in this diagram are defined as follows.

- Δt_1 is the time between the RCM signal and the commanding of the two cameras. In this study, this period of time was varied according to the reactivity of the studied mixture: 20 msec for mixtures with an auto-ignition delay time lower than 100 msec and 70 msec for the other mixtures.
- Δt_2 is the acquisition duration of the combustion phenomenon by the cameras. This time duration depends on the total number of images as well as the frequency of acquisition:

$$\Delta t_2 = \frac{\text{Total number of images}}{\text{Frequency}}$$

In our study, $\Delta t_2 = 300 \text{ msec}$

- Δt_3 is the time between the RCM trigger and the command of the injection valve. This time was also varied depending on when we want to inject particles in a specific mixture.
- Δt_4 is the real and effective opening of the valve; it represents the necessary time for the injection valve to open after its command. This time was determined in the previous chapter to be 24.5 msec.
- Δt_5 is the duration of the opening of the injection valve.
- Δt_6 is the effective start of injection. This period depends on the injection pressure, as well as the pressure of the gas mixture in the chamber
- Δt_7 : is the effective duration of injection: This period depends on several parameters, including the injection pressure and volume, as well as the shape and size of injected particles.
- Δt_8 is the compression phase duration equal to 30 msec in SU RCM
- Δt_9 is the auto-ignition delay time that depends on each studied mixture

V. Biofuel combustion

1. Experimental mixtures and conditions of biofuel combustion

As mentioned earlier, the first part of this chapter aims to complete the experimental and numerical studies of biomass gaseous combustion. Accordingly, direct visualization will be conducted on the twelve different biofuel mixtures introduced at the end of chapter 3 to visualize the influence of parameters on the combustion behavior. The observed results will be compared to the experimental and numerical results obtained in previous chapters.

The composition and experimental conditions at the end of compression of the studied mixtures are presented in Table 38.

Table 38: Studied mixtures with direct visualization

| Mixture | CH ₄ | H ₂ | CO ₂ | CO | P _c | T _c | ϕ | AI delay time (msec) | Combustion duration (msec) | Pressure rate MPa/msec |
|---------|-----------------|----------------|-----------------|----|----------------|----------------|--------|----------------------|----------------------------|------------------------|
| 1 | 48 | 12 | 40 | 0 | 11 | 1000 | 0.4 | 20 | 10.9 | 0.082564 |
| 2 | 48 | 12 | 40 | 0 | 11 | 1000 | 0.6 | 20 | 8.5 | 0.1236 |
| 3 | 48 | 12 | 40 | 0 | 11 | 1000 | 0.8 | 16 | 6.9 | 0.24365 |
| 4 | 38.4 | 9.6 | 12 | 40 | 15 | 940 | 0.6 | 133 | 29.45 | 0.11525 |
| 5 | 38.4 | 9.6 | 12 | 40 | 15 | 940 | 1 | 110 | 16.364 | 0.162019 |
| 6 | 38.4 | 9.6 | 12 | 40 | 15 | 940 | 1.2 | 100 | 12.545 | 0.23298 |
| 7 | 100 | 0 | 0 | 0 | 11 | 971 | 0.6 | 51 | 7.9 | 0.2772 |
| 8 | 95 | 05 | 0 | 0 | 11 | 971 | 0.6 | 36 | 8.6 | 0.2374 |
| 9 | 55 | 0 | 45 | 0 | 11 | 971 | 0.6 | 95 | 21.1 | 0.0549 |
| 10 | 51.2 | 12.8 | 16 | 20 | 11 | 1000 | 0.6 | 20 | 6.545 | 0.3031 |
| 11 | 38.4 | 9.6 | 12 | 40 | 11 | 1000 | 0.6 | 24 | 6.591 | 0.2920 |
| 12 | 48 | 12 | 40 | 0 | 11 | 970 | 0.6 | 53 | 14.1 | 0.0858 |

2. Law of heat release and chemiluminescence

Before proceeding with the combustion process analysis, the validity of the registered images is evaluated in this paragraph. This can be done by comparing the images light intensity in both cameras 1 and 2 with the apparent heat release calculated from the pressure curve.

These quantities were extracted and presented in Figure 131A for mixture 2.

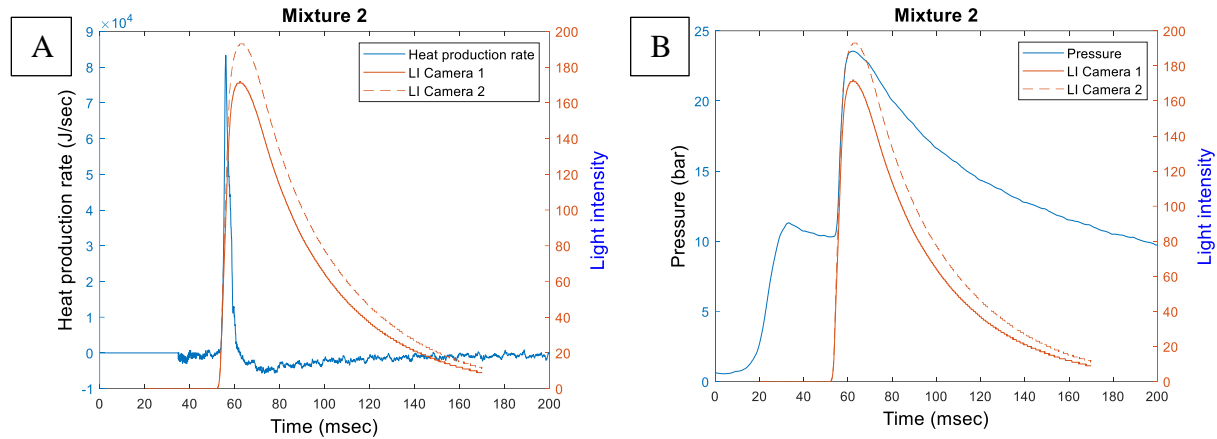


Figure 131: Luminous intensities of camera 1 and 2 with A. heat production rate B. pressure curve

A good correlation between heat release and image brightness for both cameras can be observed at the start of combustion; the brightness of the image starts to increase with the increase of heat release rate.

However, while the heat release decreases fast and becomes zero, the brightness decreases gradually and tends towards zero after a relatively long time. Also, a slight phase shift is observed between the peaks of heat release and the brightness. On the other hand, the pressure curve is shown to correlate better with the heat release, as shown in Figure 131B. This means that the highest light intensity is shown for the highest pressure in the combustion chamber instead of the heat release.

Similar trends were observed for other studied mixtures. However, and despite the slight shift between the heat release and light intensities, it can be considered that chemiluminescence will provide a good examination of the combustion process.

It is important to note that this assumption is valid when using a filter; in this study, no filter is used, and therefore, the visualized signal corresponds to the visible light intensity. Hence, the combustion process will be studied qualitatively in the following section. Only two parameters were extracted from the registered images: the location of the first ignition site, and the percentage of luminous area.

3. Extracting of combustion properties

The experimental combustion of each mixture was performed nine to ten times to verify the reproducibility of the combustion before the parametrical study. For each test, the combustion process was registered by the mean of both cameras. For some mixtures, the combustion behavior was similar in all tests, while for others, there were exceptions. However, in this section, the most accurate behavior of each mixture will be presented.

3.1. Auto-ignition sites

Due to heterogeneities in the chamber during the ignition process, the combustion can occur with different modes, as seen in the previous section. To better understand the combustion behavior of biofuel mixtures, the acquired images by both cameras are treated to extract several quantitative data. In Figure 132, we present the direction of x, y, and z-axis according to the cameras' positions.

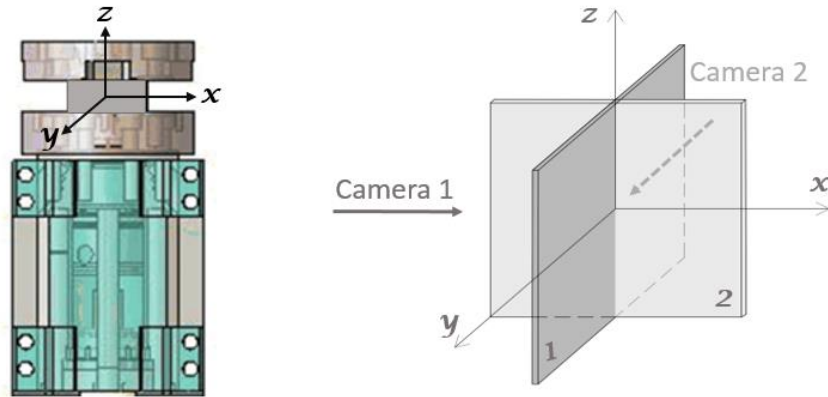


Figure 132 :The registered planes viewed by camera 1 and camera 2 in 3D

The first extracted parameter is the location of the initial nuclei. The latter is considered as a zone of higher concentration of radicals or promoter additives. Hence, it represents the center of a luminous zone in the acquired images and can be determined by the image binarization.

The locations of the initiation ignition sites are presented in (x, y, and z) directions in Figure 133 and planes (x, y) and (x, z) in Figure 134.

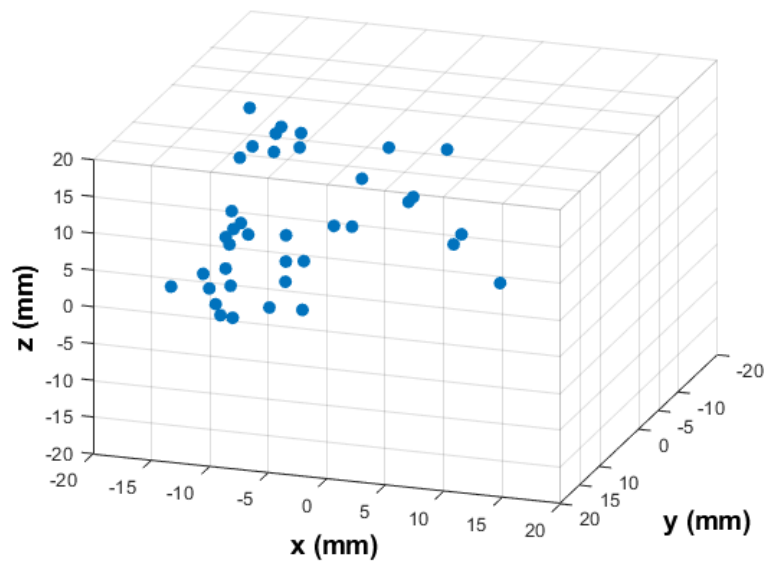


Figure 133: The locations of auto-ignition initiation sites in the combustion chamber (x, y and z)

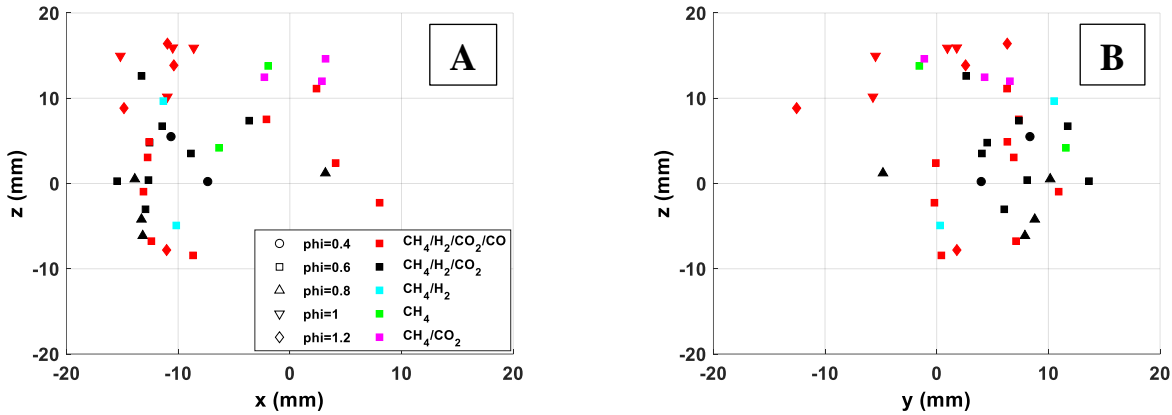


Figure 134: The locations of auto-ignition initiation sites in the combustion chamber (x, z) and (y, z)

These figures show that self-ignition sites are spread throughout the chamber. However, there is a higher concentration in the upper part of the chamber to the left front plane.

The accuracy of combustion at the upper part of the chamber means that the gases in the chamber's central region are colder than those in contact with the heated cylinder head. The hot gases are thus concentrated in the upper part of the chamber. This trend was also observed with the mixtures studied by Pounkin [53] on the SU RCM. He referred to Tran's LIF technique measurements to explain the connection of this trend with temperature heterogeneities in the chamber. Tran conducted and produced a mean temperature map at different times after the compression end. It should be noted that the LIF measurements were performed with inert mixtures whose behavior is identical to that of reactive mixtures up to the start of combustion. The fields are represented at times 17 and 25 msec after the end of compression, as these are the closest to the time when the combustion of the tests performed begins. It was observed that the highest temperature levels are well located in the upper part of the chamber, which corroborates self-ignition sites with the highest density in this area. The same results can be observed in the work of Neuman [196] on the development of rapid compression machine.

3.2. Apparent surface and combustion speed

The development of the combustion area can be a good indicator of the rapidity of the combustion process. Thus, studying the evolution of the ratio between the apparent surface occupied by the combustion development and the total surface of the combustion chamber will be performed in this section.

This evolution is presented in Figure 135 as a function of the time following the combustion initiation.

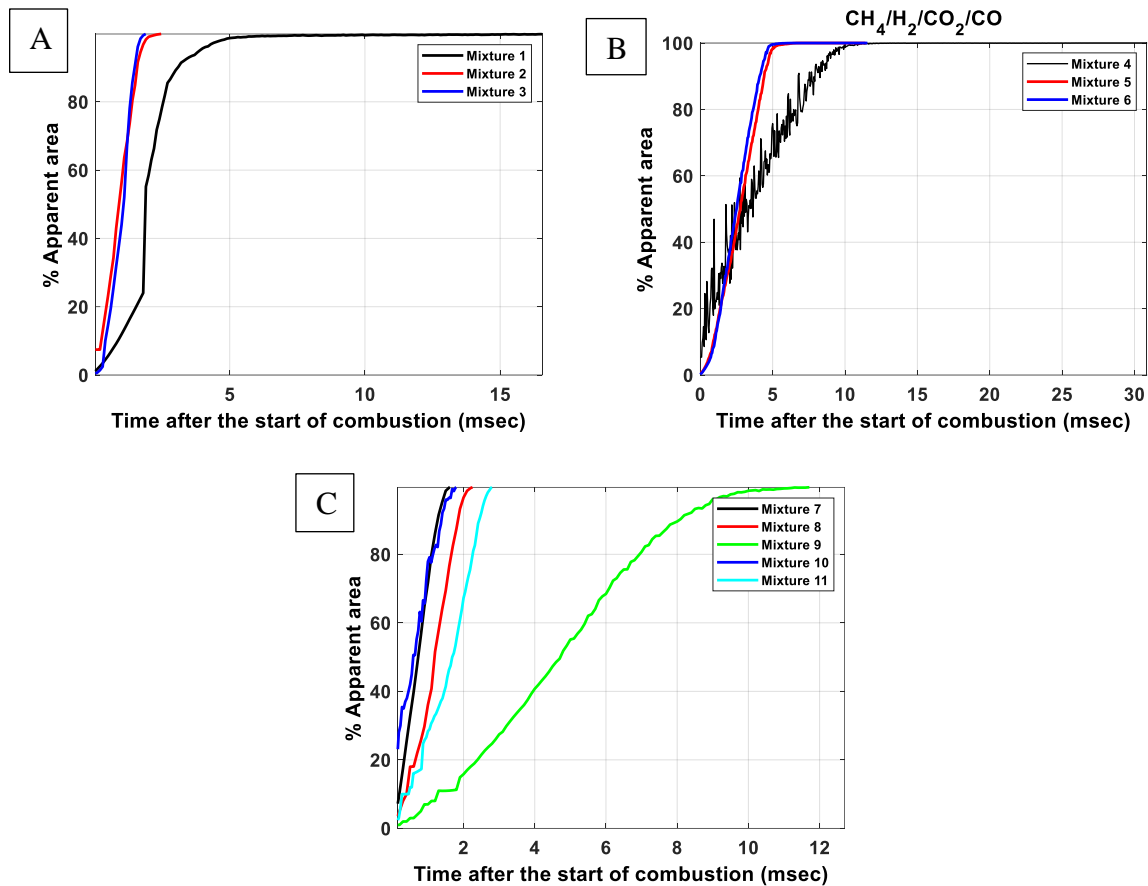


Figure 135: % Apparent area with time for various mixtures a. the effect of lean equivalence ratio, b. the global effect of equivalence ratio, c. Fuel composition effect

As can be seen from Figure 135A, the combustion of mixture 3 ($\phi=0.8$) is the most rapidly occupied by the combustion, followed by that of mixture 2 ($\phi = 0.6$) then mixture 1 ($\phi=0.4$). This result can be directly related to the combustion rapidity; the combustion becomes faster when fuel concentrations in the mixture increase. This tends to prove that at $\phi=0.8$, the combustion seems closer to a mass development compared to other lean mixtures.

This effect of the equivalence ratio can also be seen in Figure 135B; the ratio of the apparent surface area occupied in the chamber increases rapidly for rich mixtures exceeding stoichiometric mixtures (1 msec) and lean mixtures (5 msec).

It can be observed in Figure 135C that the development of the combustion area of mixture 9 (CH_4/CO_2) is significantly slower than all the other mixtures (12.4 msec). Mixture 7 (CH_4) and mixture 10 (20% CO), on the other hand, are the fastest to occupy the combustion chamber.

These results extracted from visual combustion images seem to be in good correlation with the combustion duration extracted from the pressure and presented in Table 38 for the studied mixtures.

However, we should clarify that even though the ratio of the apparent combustion area seems to be in good correlation with the combustion duration, these two parameters are not similar. For example, according to the pressure curve, mixtures 10 and 11 dispose of the same combustion duration time. However, the combustion of mixture 11 (with 40% CO) occupies the entire chamber

a little slower than that of mixture 10 (with 20% CO). According to the study of Yu et al. [197] on the effect of turbulence and thermal stratification on the HCCI combustion process, a high level of temperature inhomogeneity leads to an increase in the duration of combustion. Thus, mixtures containing higher CO₂ level seems to be more influenced by temperature inhomogeneities due to its higher heat capacities and thermal conductivity.

Hence, to better understand the obtained results, the acquired images representing the combustion process of the studied mixtures, are treated and will be presented next. It would be interesting to compare the visualized phenomenon by the numerical results on the turbulent approach conducted in chapter 3.

4. Visualization of the combustion process by chemiluminescence

During the combustion process, each point of the combustion chamber has a different value of the fluctuating velocity u' and integral length scale l_t . In chapter 3, we have calculated non-dimensional numbers based on the average values of these scales (u' and l_t). We have stated it is not correct to present a mixture in Borghi's diagram with one point, but it is enough to carry on the qualitative study of the effects of parameters on combustion.

In this section, however, the average values of u' and l_t , as well as their standard deviation, are used to calculate the non-dimension numbers of Damkohler and Karlovitz. These values extracted from the PIV measurements conducted by Pounkin on the SU RCM are represented in Table 39.

Table 39: Average and standard deviations of u' and l_t

| Average length scale (mm) | Standard deviation of length scale (mm) | Average fluctuating velocity (m/sec) | Standard deviation of fluctuating velocity (m/sec) |
|---------------------------|---|--------------------------------------|--|
| 4.95 | 3.06 | 2.25 | 1.15 |

This will allow the positioning of different configurations of each mixture on the diagram of Borghi. The corresponding non-dimensional numbers are calculated and presented in Figure 136 for the twelve mixtures.

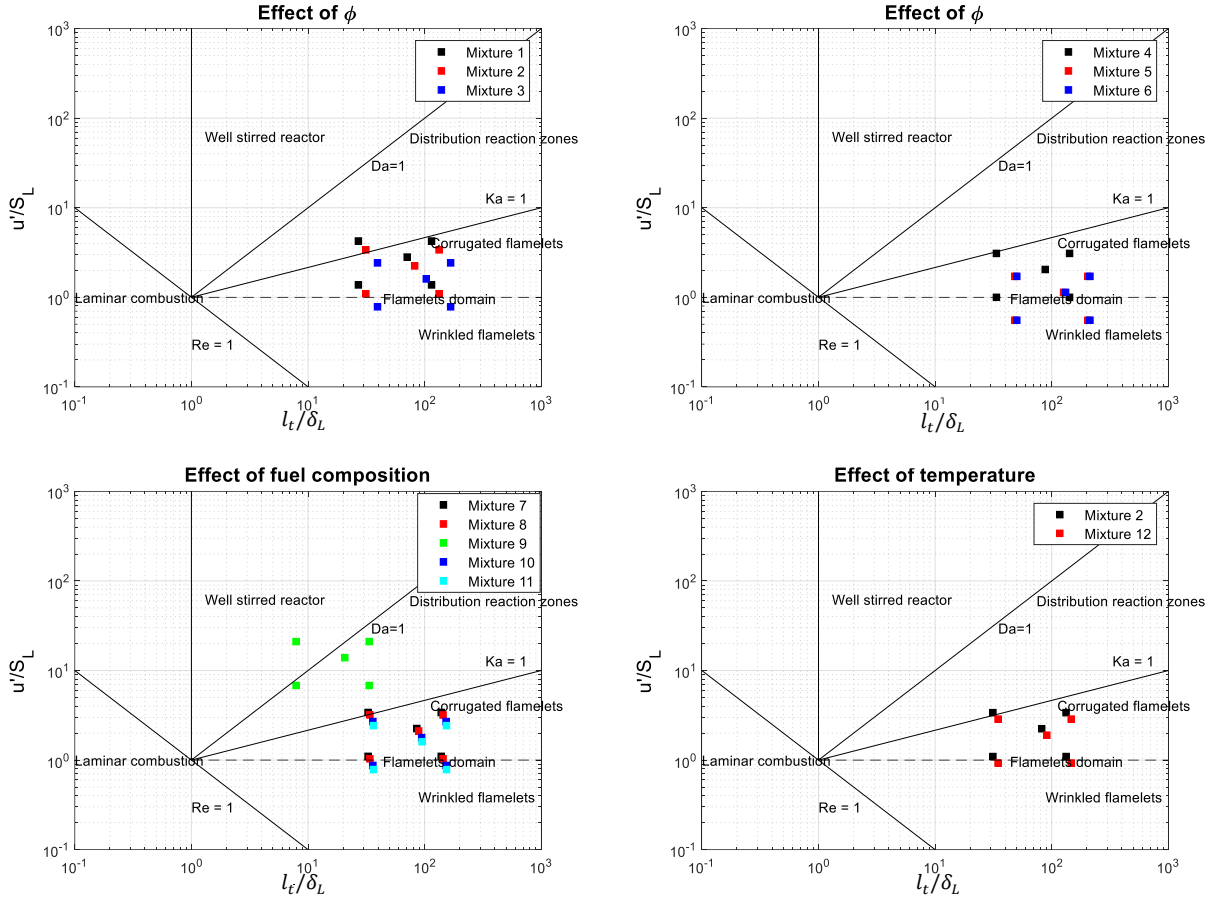


Figure 136: Mixtures 1-12 on the diagram of Borghi

The combustion process for the different studied configurations is illustrated by eight images on each camera. The images were chosen between the start of combustion, where the pressure is P_{start} , and the image where the pressure is maximum in the chamber (P_{max}); They are evenly spaced and distributed according to the pressure difference between the start of combustion and the maximum pressure reached:

$$P_{image} = \frac{P_{start} - P_{max}}{8}$$

The images and the pressure curves of the twelve studied mixtures are presented from Figure 138 to Figure 149.

We note that only for mixture 1 and 9, only the images of camera 1 were presented to allow visualization of 16 images instead of 8 (Figure 138 and Figure 146).

The exhibited area in each image is equal to the area of the combustion chamber (40 x 40 mm), and the color level is scaled based on the intensity and the shade of grey of each pixel; the color blue indicates no combustion while the color red indicates complete combustion. The color intensity depends on the brightness of the mixture; therefore, for each biofuel mixture, the gain was adjusted to have better brightness.

Effect of low equivalence ratio : Mixture 1, 2 and 3

The effect of a low equivalence ratio on the combustion process, was studied for CH₄/H₂/CO₂ mixtures at T_c=1000 K, P_c=11 bar, and three equivalence ratios (0.4, 0.6 and 0.8). The operational conditions of the acquired images are given in Table 40.

Table 40: Operational conditions of Mixtures 1,2, and 3

| | Mixture 1 ($\phi=0.4$) | Mixture 2 ($\phi=0.6$) | Mixture 3 ($\phi=0.8$) |
|-----------------------------------|--------------------------|--------------------------|--------------------------|
| Exposure time (μsec) | 99 | 99 | 45 |
| Gain (-) | 8 | 1 | 1 |

The acquired images and the corresponding pressure curves for mixtures 1, 2 and 3 are represented in Figure 138, Figure 139, and Figure 140, respectively.

The first thing to note in the combustion images is that the heat release and the mixture's brightness increase with the equivalence ratio due to higher fuel concentrations in the mixture. The combustion behavior of lean mixtures ($\phi=0.4$) seems to be similar to that at $\phi=0.6$. However, the brightness of the images does not allow the validation of this assumption. For lean CH₄/H₂/CO₂ mixtures ($\phi=0.6$), the combustion appears to be consistent with the instantaneous auto-ignition of a certain load in the upper part of the chamber; it spreads quickly to cover only the upper part of the chamber. However, the CH₄/H₂/CO₂ mixture combustion with an equivalence ratio 0.8 exhibits further behavior; the combustion is initiated by two sites in the chamber's upper and bottom parts. These then combine and spread into the entire chamber pretty quickly. Its combustion is more similar to volumetric combustion.

According to the numerical study of chapter 3, as can be seen from Figure 136, as the equivalence ratio decreases, the combustion will more likely exhibit volumetric combustion. On the other hand, according to the direct visualization: the combustion of mixture 2 is similar to volumetric combustion in the upper part of the chamber and in the entire volume for mixture 3. As for mixture 1, due to the low brightness of images, we cannot state clearly the type of the combustion.

Effect of equivalence ratio: Mixture 4,5, and 6

The equivalence ratio effect on the combustion process was studied for CH₄/H₂/CO₂/CO mixtures at T_c=940 K, P_c=15 bar, and three equivalence ratios (0.6, 1, and 1.2). The operational conditions of the acquired images are given in Table 41.

Table 41:Operational conditions of Mixtures 4,5, and 6

| | Mixture 4 ($\phi=0.6$) | Mixture 5 ($\phi=1$) | Mixture 6 ($\phi=1.2$) |
|-----------------------------------|--------------------------|------------------------|--------------------------|
| Exposure time (μsec) | 71 | 15 | 10 |
| Gain (-) | 4 | 1 | 1 |

The acquired images and the corresponding pressure curves for mixtures 4, 5, and 6 are represented in Figure 141,

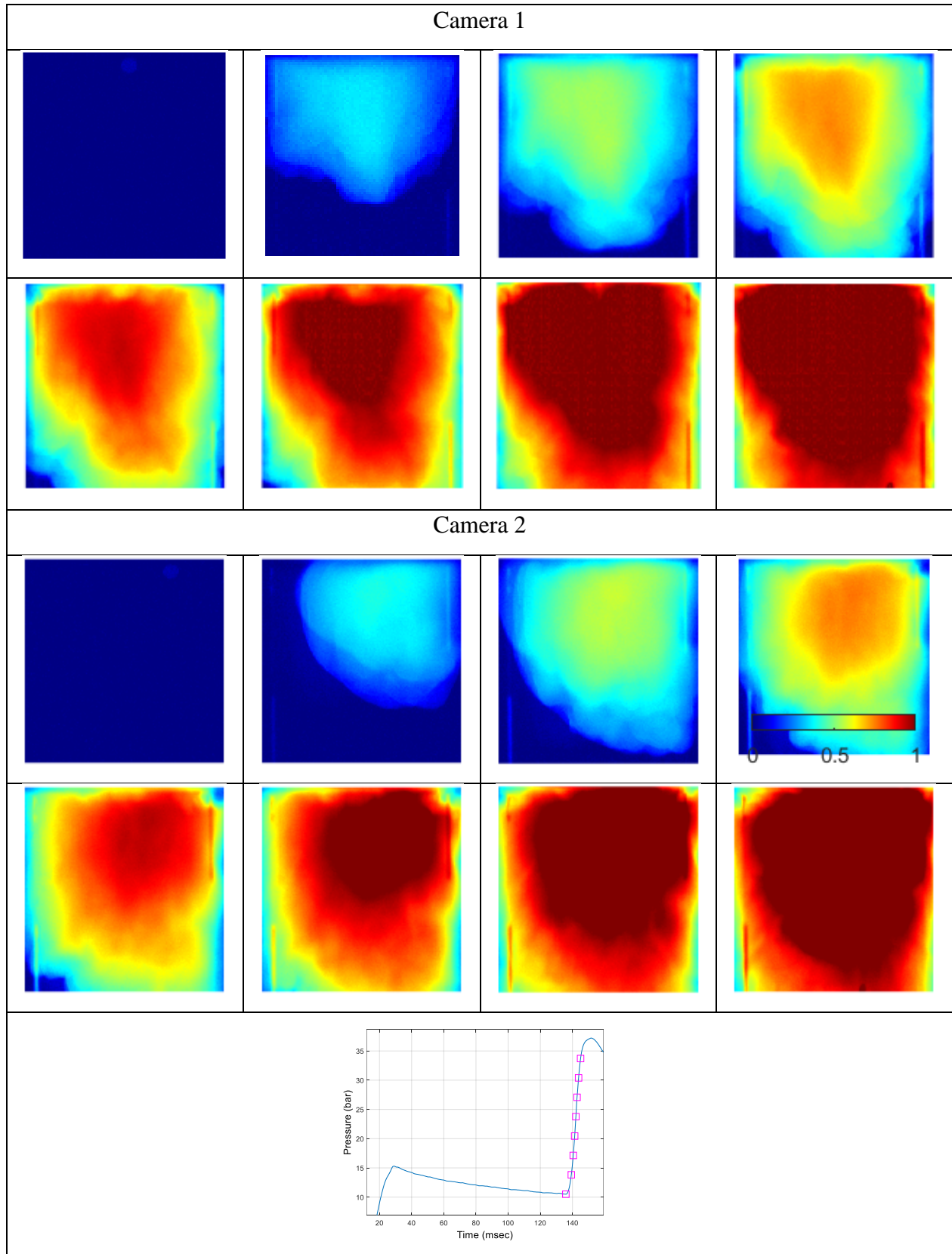


Figure 142, and Figure 143, respectively.

The combustion of lean $\text{CH}_4/\text{H}_2/\text{CO}_2/\text{CO}$ mixtures is, in general, similar to lean $\text{CH}_4/\text{H}_2/\text{CO}_2$ mixtures; it is initiated in one site of the combustion chamber, then spreads to cover the upper part of the chamber. However, for $\text{CH}_4/\text{H}_2/\text{CO}_2/\text{CO}$ mixtures, the combustion seems more of a propagating flame, primarily due to carbon monoxide in the mixture. The same propagating flame is shown for stoichiometric $\text{CH}_4/\text{H}_2/\text{CO}_2/\text{CO}$ mixtures; however, the combustion spreads and covers up the entire chamber and not only the upper part. For rich $\text{CH}_4/\text{H}_2/\text{CO}_2/\text{CO}$ mixtures, the combustion is more likely to be mass combustion in the entire chamber; a specific load is ignited simultaneously in the center of the chamber than spread to cover up the whole chamber. However, errors can occur in analyzing the stoichiometric and rich mixtures due to the camera sensor's saturation. According to the numerical study, as the equivalence ratio increases, the points move slightly to the wrinkled flames, representing the cases of mixtures 5 and 6.

Effect of fuel composition: Mixtures 7- 11

Concerning the effects of fuel compositions on the combustion behavior, mixtures 7, 8, 9, 10, and 11 were studied to determine the influence of hydrogen, carbon dioxide, and carbon monoxide on biofuel combustion. The operating conditions of mixtures 7,8,9,10 and 11 are presented in Table 42.

Table 42: Operational conditions of Mixtures 7-11

| | Mixture 7 (CH_4 100%) | Mixture 8 (CH_4/H_2 95/05%) | Mixture 9 (CH_4/CO_2 55/45 %) | Mixture 10 ($\text{CH}_4/\text{H}_2/\text{CO}_2/\text{CO}$ 20 % CO) | Mixture 11 ($\text{CH}_4/\text{H}_2/\text{CO}_2/\text{CO}$ 40% CO) |
|-----------------------------------|---------------------------------------|--|--|--|---|
| Exposure time (μsec) | 15 | 15 | 99 | 20 | 20 |
| Gain (-) | 1 | 1 | 3 | 1 | 1 |

The combustion of pure lean CH_4 mixtures (mixture 7) is shown to be high-speed; The combustion is shown to be well developed. Two or more sites appear in the chamber's central area and then spread to the rest of the chamber. The self-igniting of many sites in the chamber increases the combustion luminosity. So, we seem to be dealing with multi-sites combustion.

In his study on the combustion of methane and n-heptane, Fukushima et al. [198] found out that the coexistence of different combustion regimes is related to the fuel properties, temperature stratification, and the level of turbulence in the cylinder. As shown in Figure 137, for a temperature fluctuation of 12K in the case of methane, the combustion regime is purely self-ignition. The combustion becomes mostly flame propagation for temperature fluctuations of more than 90K.

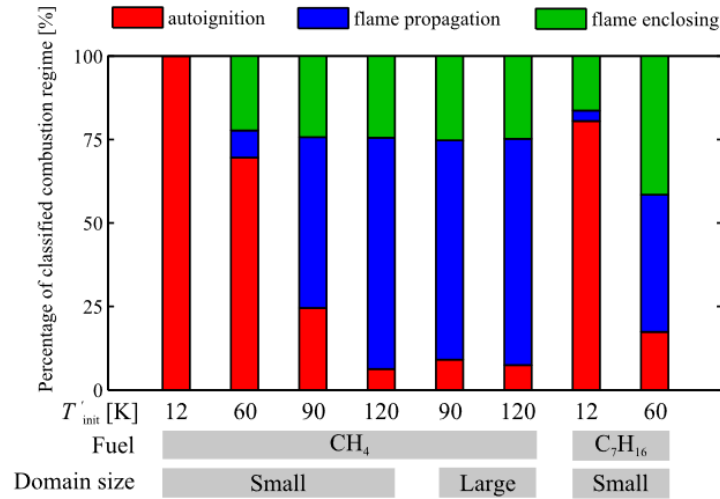


Figure 137: Ratio of combustion regimes represented by the fluid elements[198]

The temperature fluctuations in the RCM chamber for 20 msec after the top dead center are near 40 K. However, the ignition delay of the studied methane is about 50 msec after the top dead center, which can imply higher temperature fluctuations. Whether it is higher or not, methane's combustion is shown to be similar to volumetric combustion.

The combustion of methane mixtures with minimal hydrogen (5%) (mixture 8) exhibits similar behavior than for mixture 7. However, the combustion is ignited earlier in the presence of hydrogen. This confirms the experimental and numerical studies on the effects of hydrogen on methane combustion. It was explained earlier that a small quantity of hydrogen is sufficient to predominate methane reactivity. However, more than 50 % of hydrogen is required to predominate its flame velocity. Hence, the presence of hydrogen provides radical (H) that initiate earlier the decomposition of methane via reaction R53:



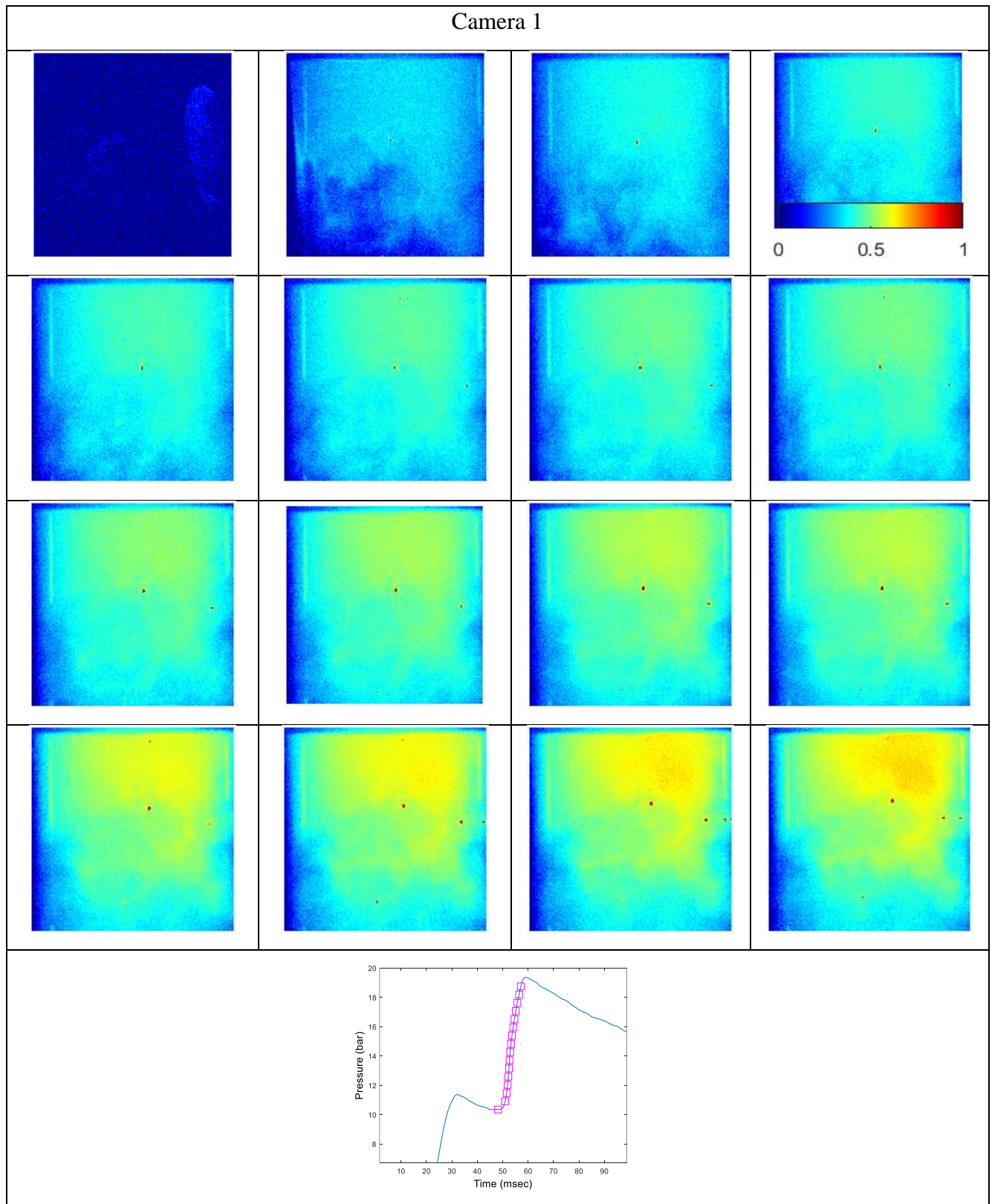
The effects of carbon dioxide on biogas/syngas mixtures are also confirmed in this study through mixture 9. CO₂ was always considered as a dilution gas with high heat capacities that do not usually participate in chemical reactions. Because of its dilution effect, the initiation phase is belated, then the combustion spreads slowly to cover only the upper part of the chamber. Due to its high capacity and thermal conductivity properties, it increases the heat transfer with the chamber wall and therefore reduces the capacity of the flame to propagate in the entire chamber. The effects of CO₂ are also confirmed in this study. The combustion of methane mixtures with 45% of carbon dioxide exhibits similar behavior to mixture 2 (CH₄/H₂/CO₂ at $\phi=0.6$); The ignition initiation is belated due to the dilution and high heat capacities effects of carbon dioxide. Once ignited, the combustion spreads slowly but only covers the upper part of the chamber. Due to its high capacity, it increases the heat transfer with the chamber wall and therefore reduces the flame's capacity to propagate in the lower part of the chamber. The combustion always occurs in the upper top of the chamber because it has a higher temperature as it is connected to the heating collar.

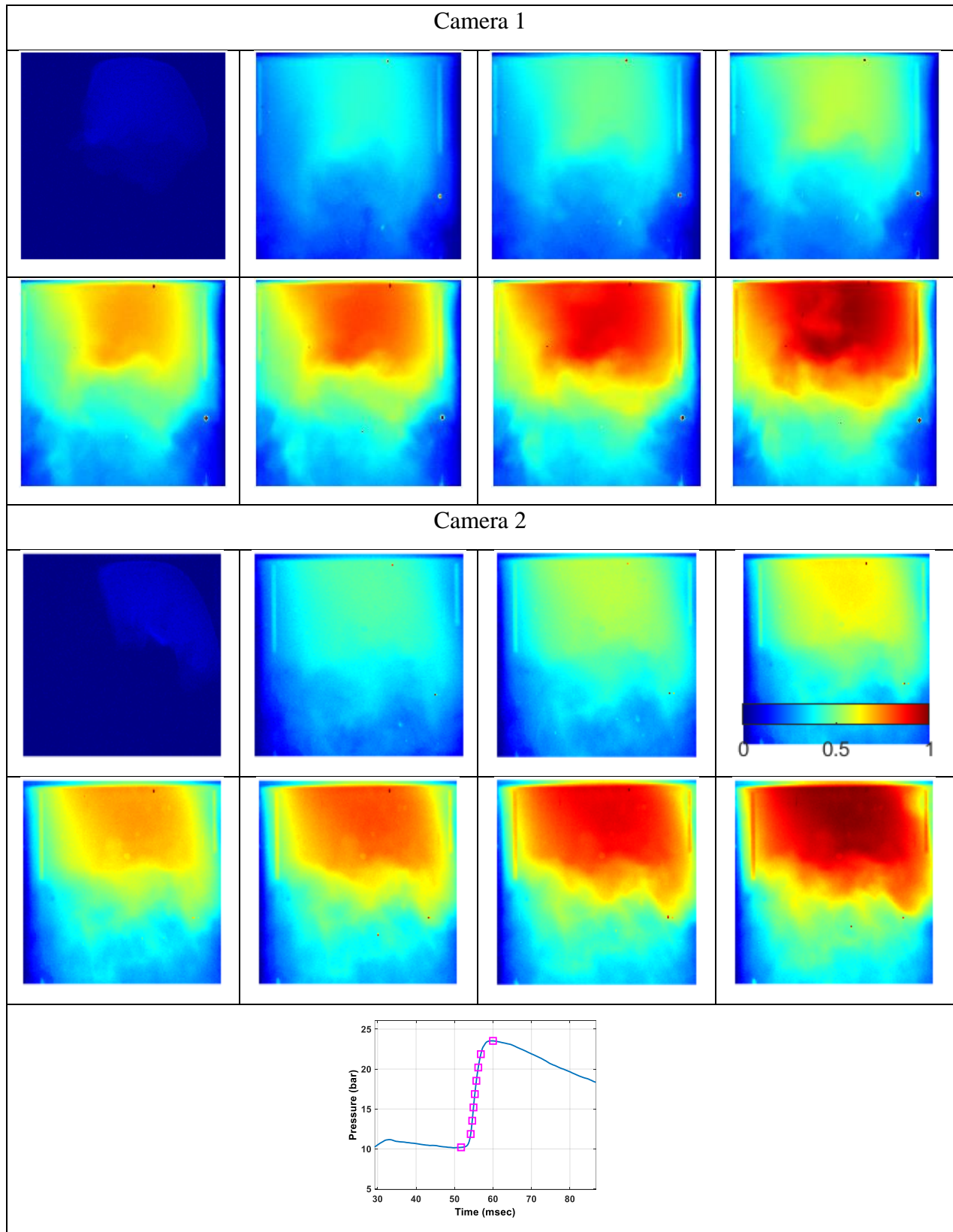
The combustion of biogas/syngas mixtures with small (20%) and higher (40%) quantities of carbon monoxide are presented in Figure 147 and Figure 148.

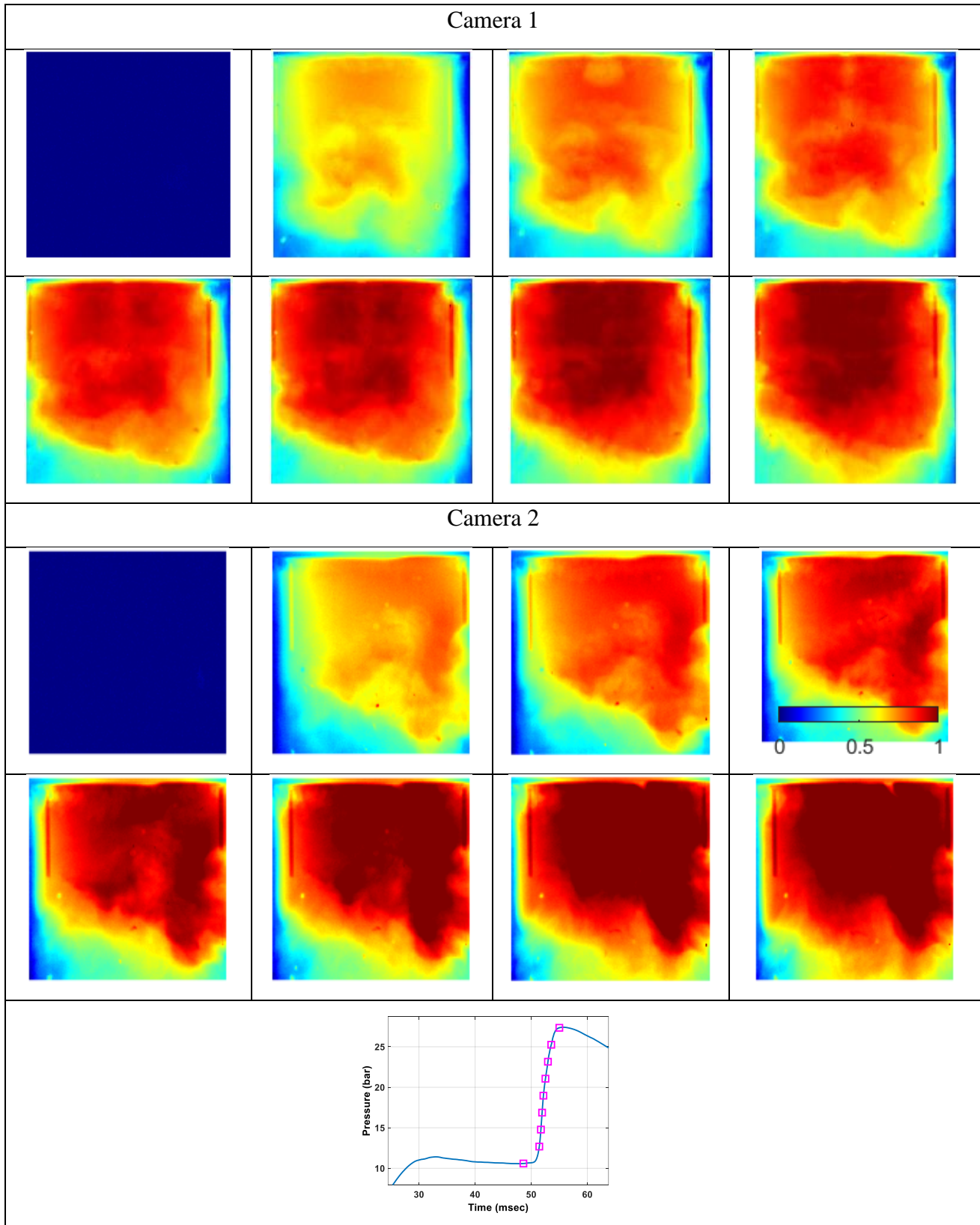
Both mixtures exhibit comparable combustion; the combustion ignites in the combustion chamber's upper part, then spreads to cover the entire chamber. The initiation and propagating phase of the combustion are quite similar to $\text{CH}_4/\text{H}_2/\text{CO}_2$ mixtures. However, near the combustion end, another ignition site appears in the lower part of the combustion chamber. This combustion behavior also confirms the earlier study on the effects of carbon monoxide on biogas/syngas combustion; carbon monoxide in the studied conditions does not exhibit a significant change in the combustion process.

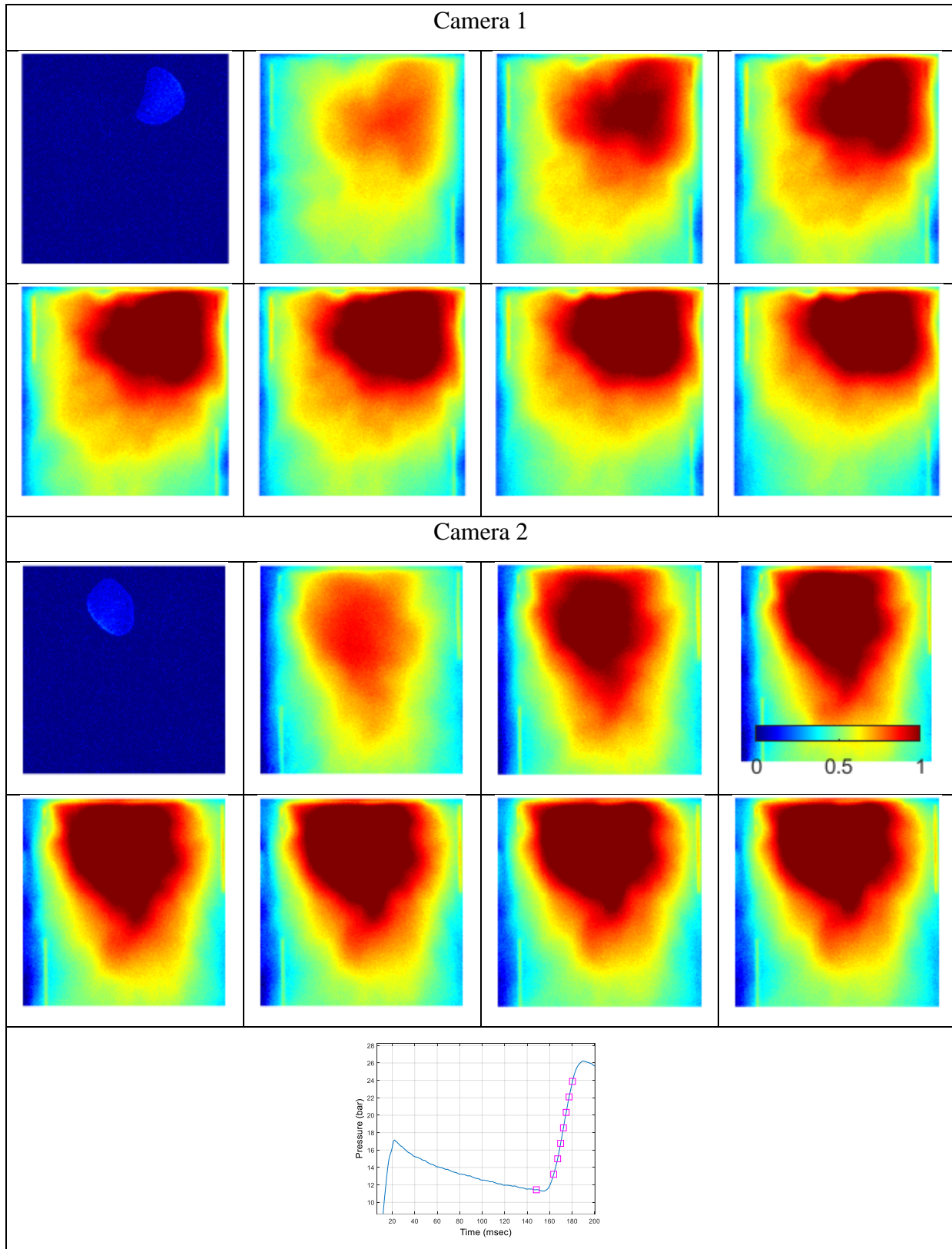
Effect of temperature: Mixtures 2 and 12

Lastly, mixtures 2 and 12 were used to determine the effects of temperature on the biofuel combustion. However, a higher temperature difference is needed to spot the combustion behavior differences after the initializing phase.

Figure 138: Images acquired for the combustion process of mixture 1 ($\phi=0.4$)

Figure 139: Images acquired for the combustion process of mixture 2 ($\phi=0.6$)

Figure 140: Images acquired for the combustion process of mixture 3 ($\phi=0.8$)

Figure 141: Images acquired for the combustion process of mixture 4 ($\phi=0.6$)

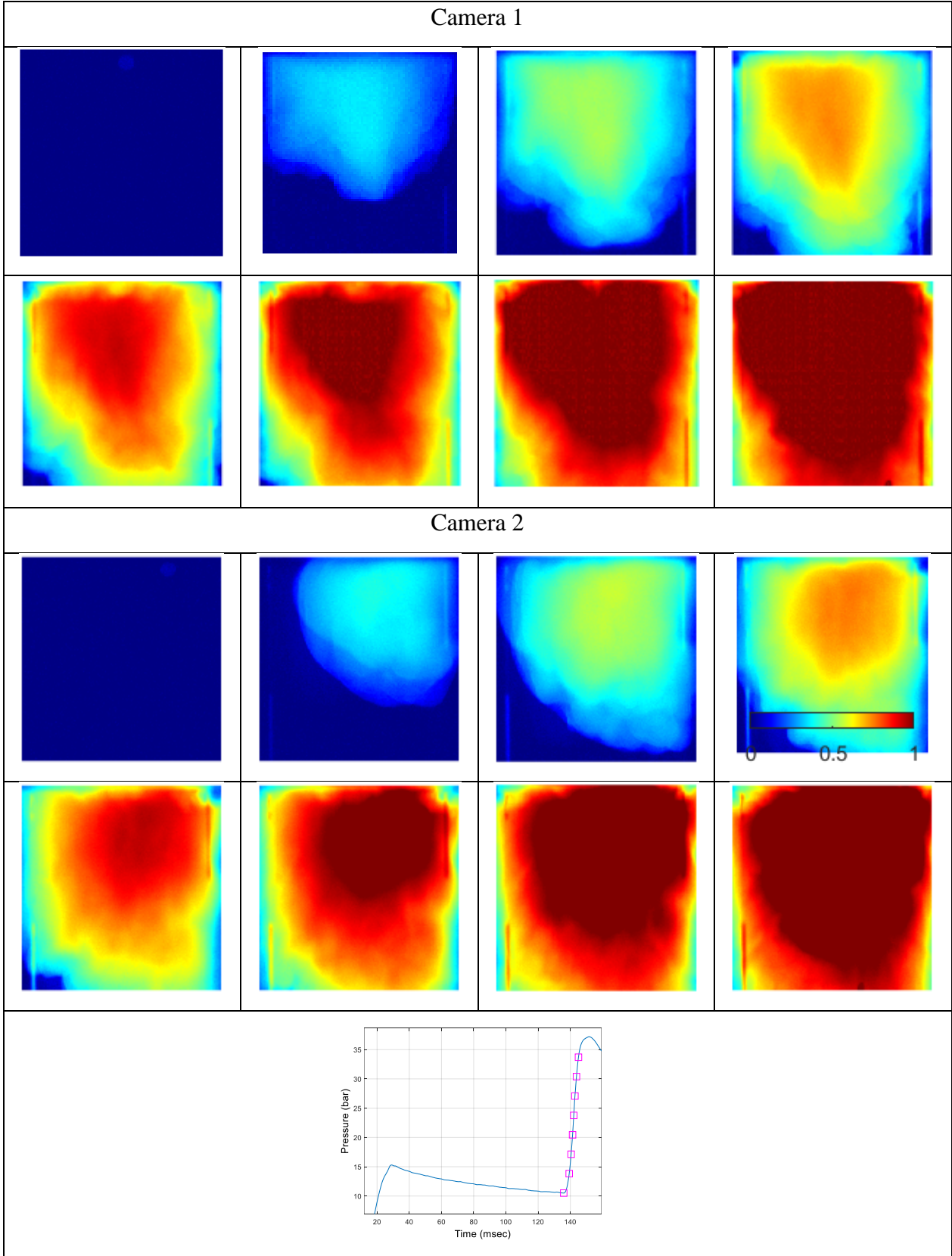
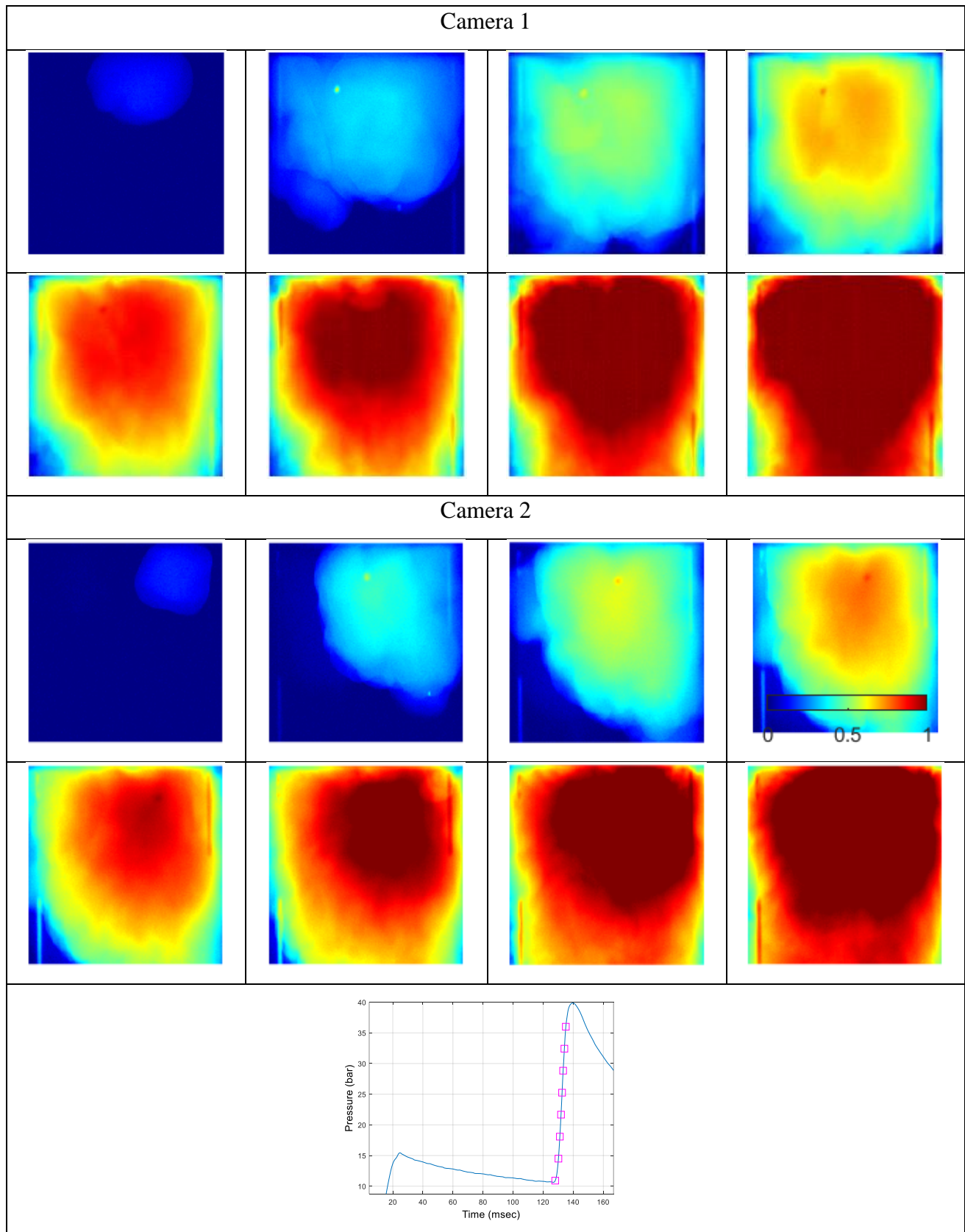


Figure 142: Images acquired for the combustion process of mixture 5 ($\phi=1$)

Figure 143: Images acquired for the combustion process of mixture 6 ($\phi=1,2$)

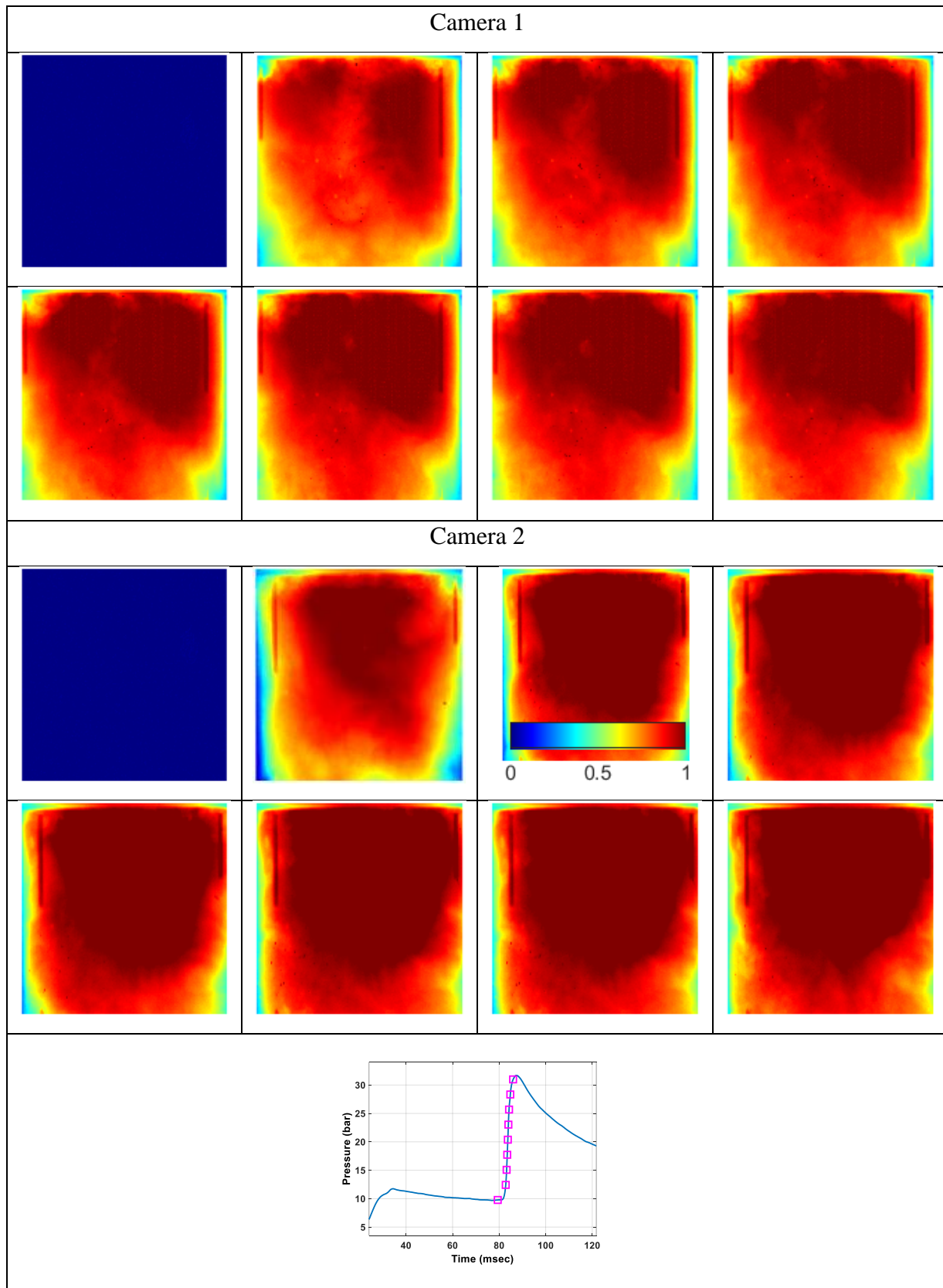


Figure 144: Images acquired for the combustion process of mixture 7

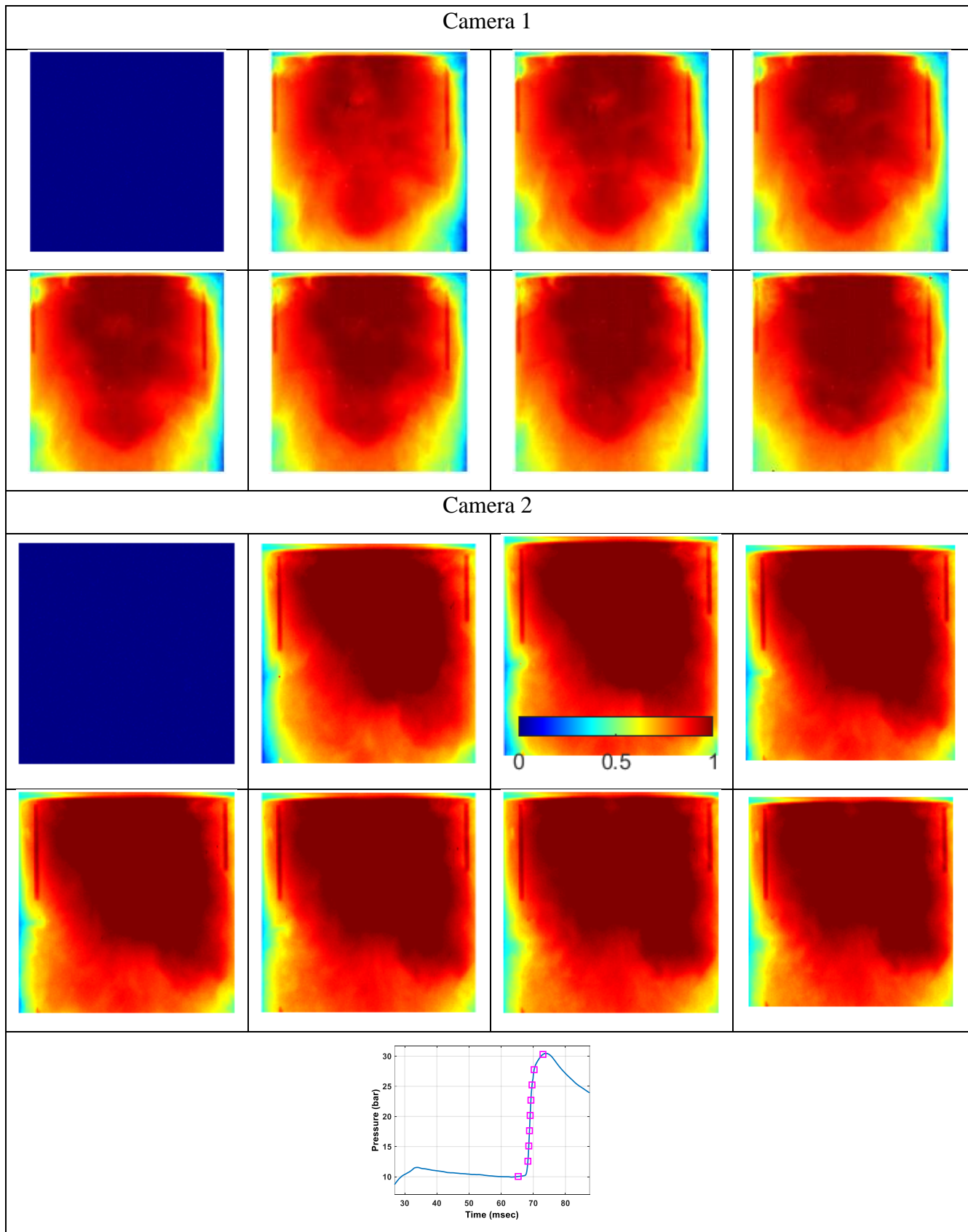


Figure 145: Images acquired for the combustion process of mixture 8

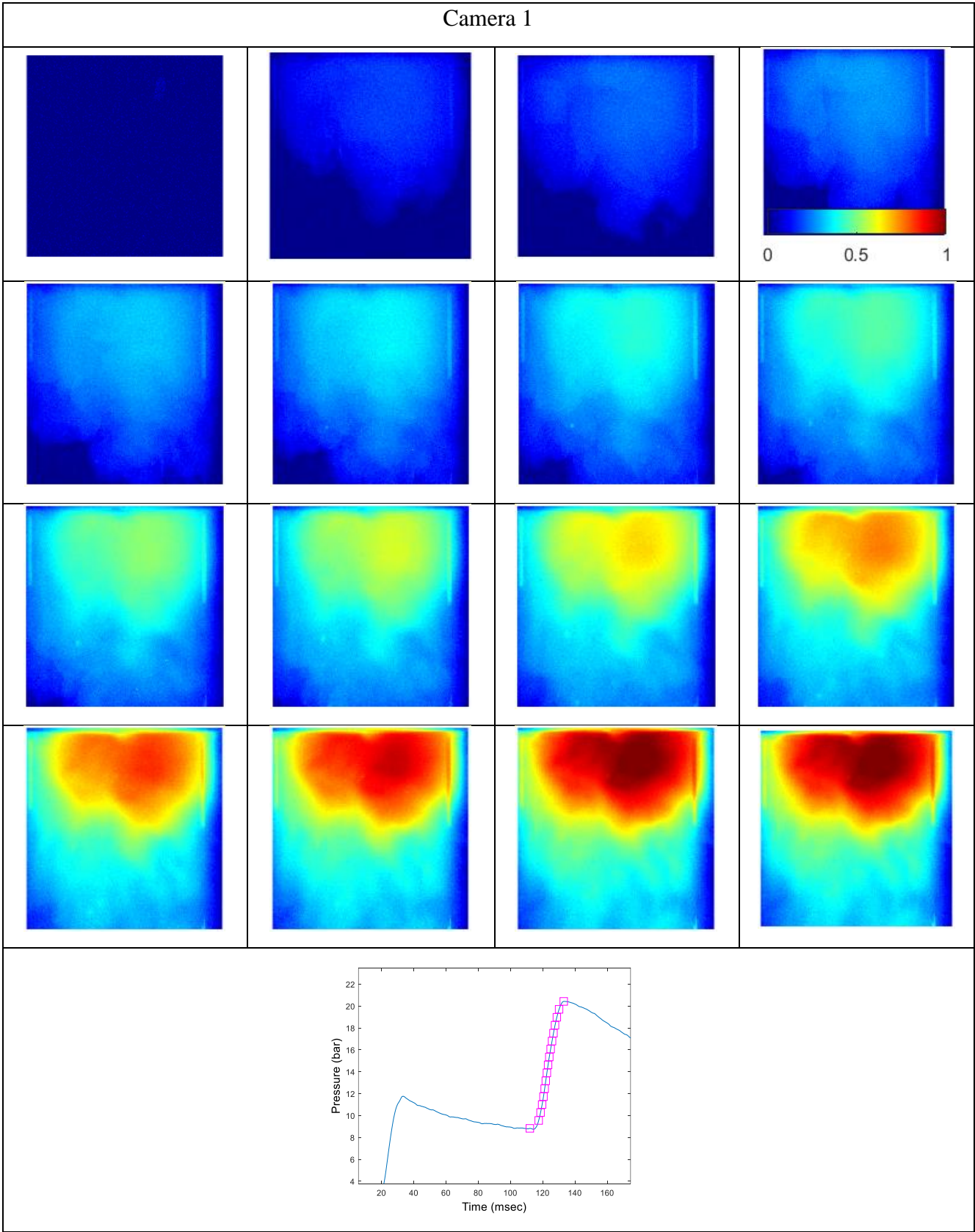


Figure 146: Images acquired for the combustion process of mixture 9

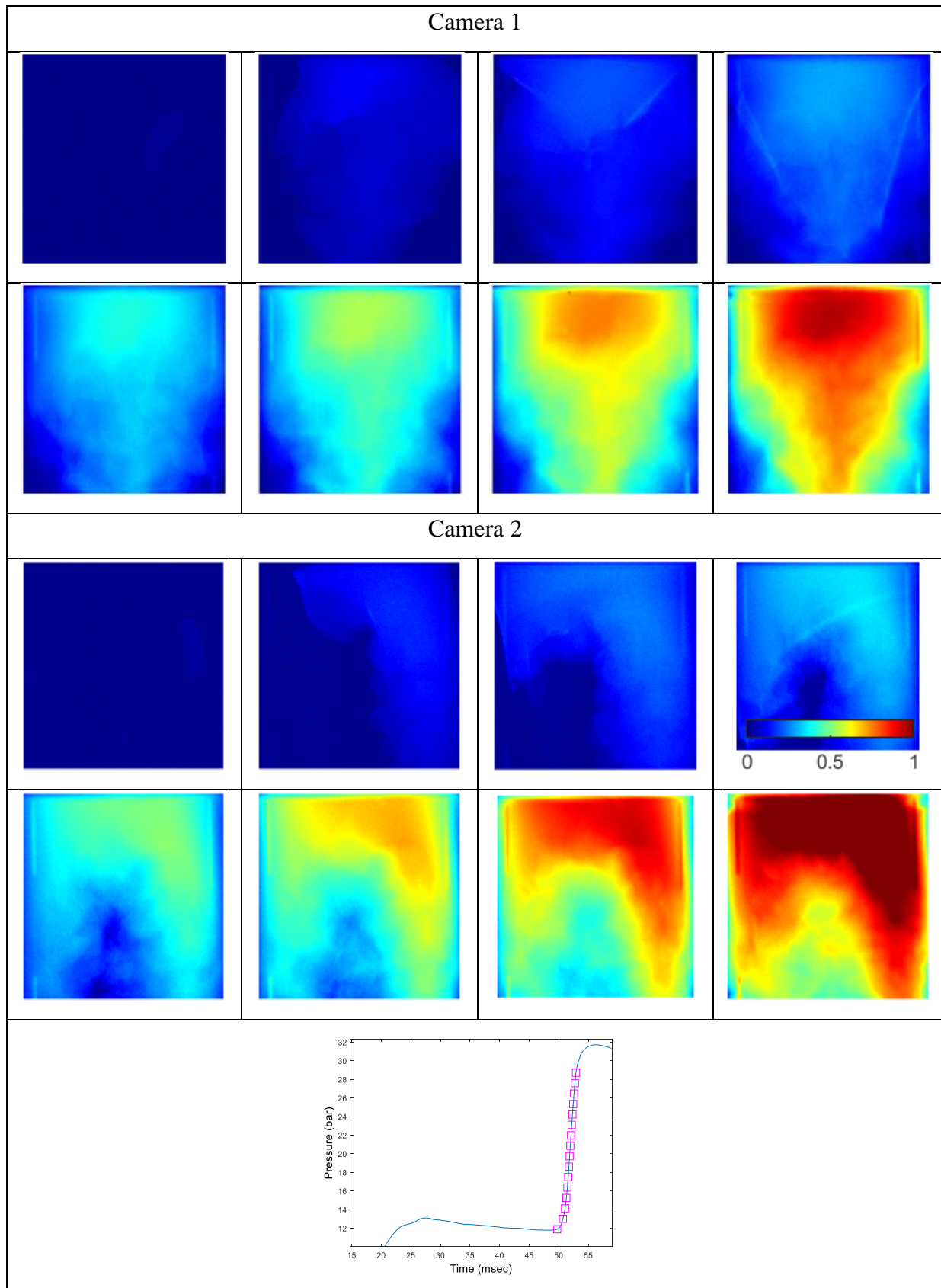


Figure 147: Images acquired for the combustion process of mixture 10

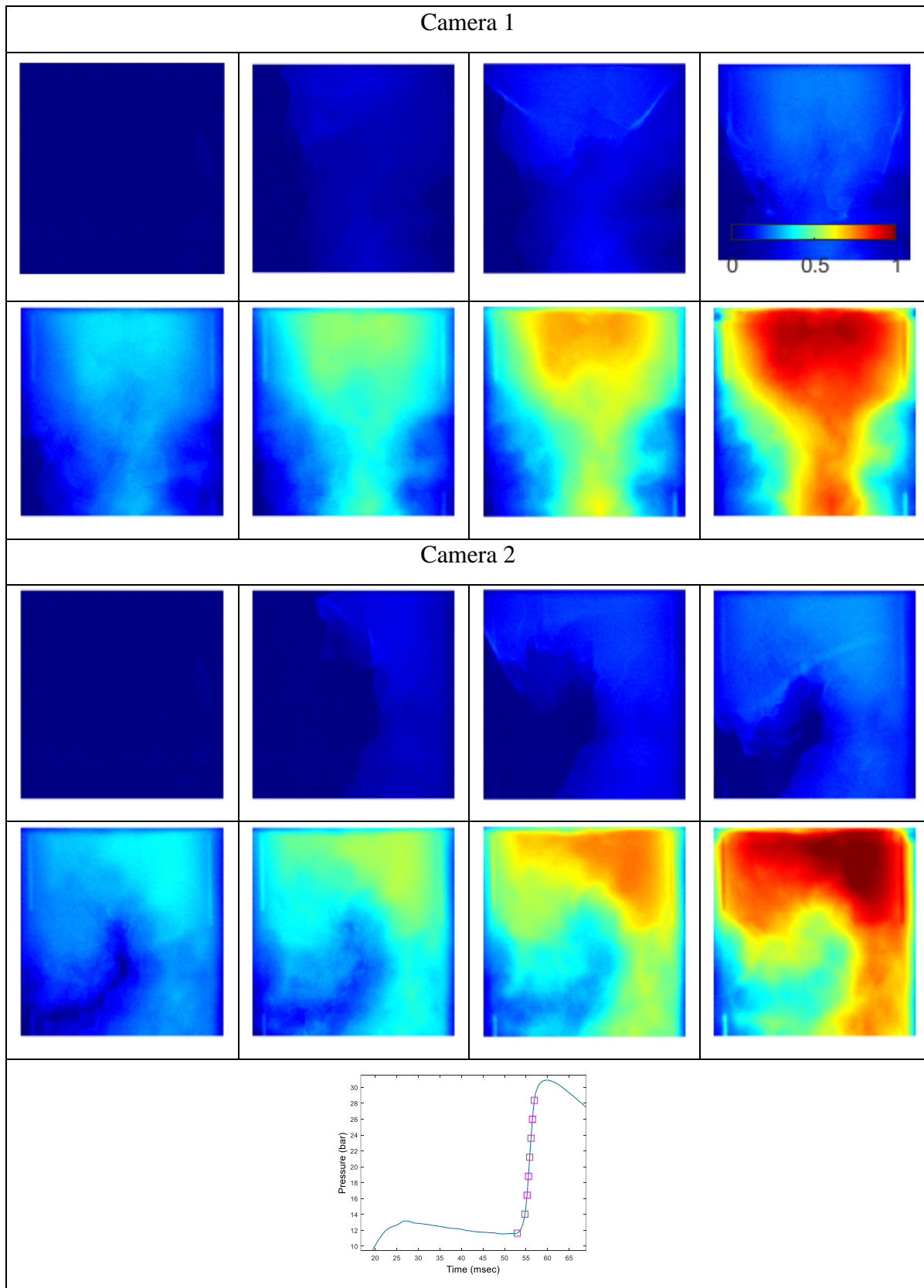


Figure 148: Images acquired for the combustion process of mixture 11

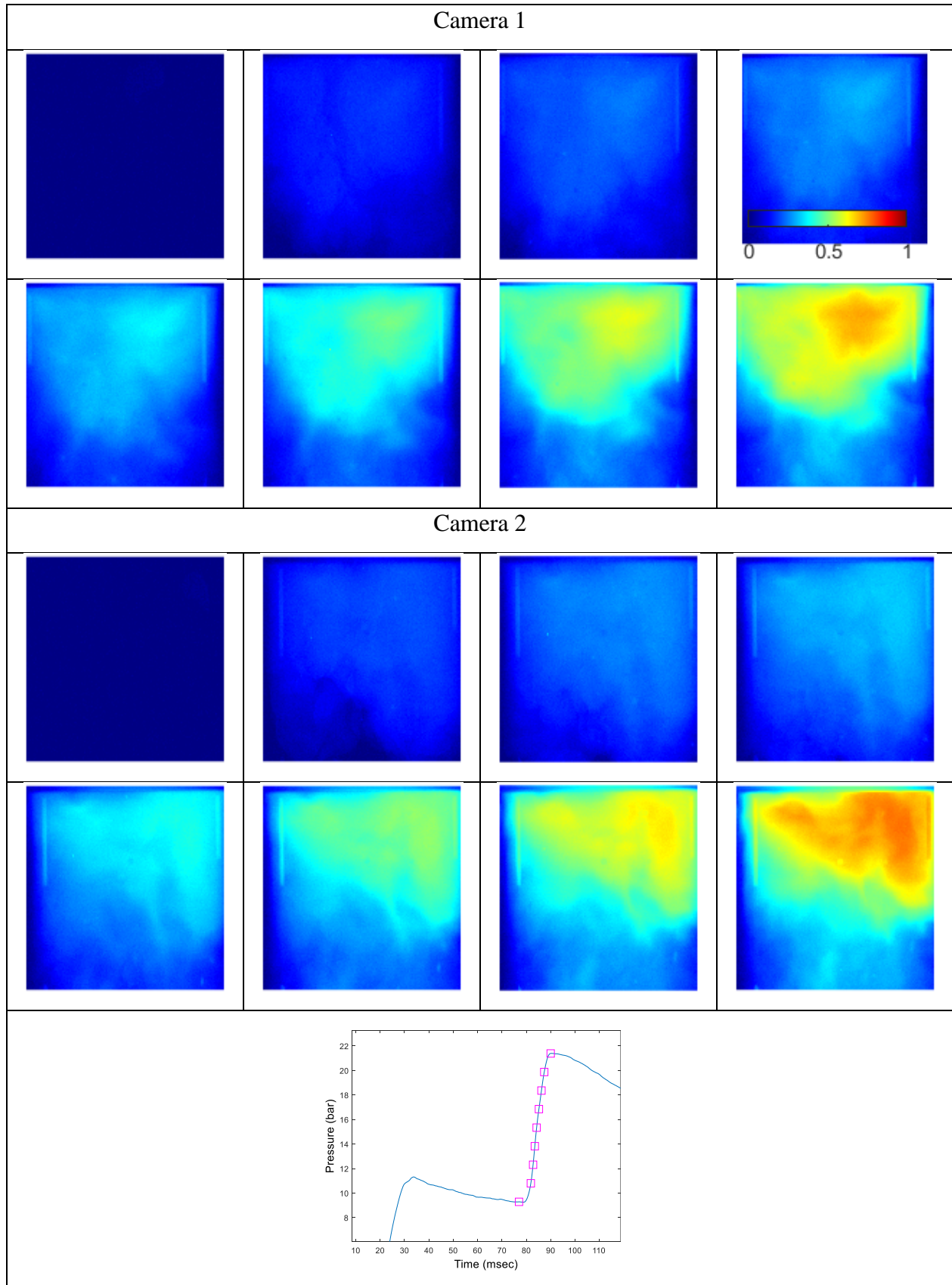


Figure 149: Images acquired for the combustion process of mixture 12

5. Conclusions

In this section, rapid cinematography was performed to directly visualize the combustion behavior of the twelve mixtures selected in chapter 3.

This study was necessary to understand the combustion of biogas/syngas mixtures in our experimental conditions fully and to confirm and complete the previous studies.

Hence, through this study of the direct visualization of chemiluminescence combustion, different mixtures' combustion phenomenologies were highlighted.

Thus, the coexistence between auto-ignition and flame propagation of combustion is highlighted for all the studied mixtures. The ignition starts where the thermodynamic conditions are favorable for the initiation of self-ignition wave fronts. Thus, depending on the mixture's reactivity and the distribution of thermodynamic properties, several ignition sites can appear and then spread in the chamber.

Some results from the numerical data were validated in this study.

For example, a low amount of hydrogen, 5%, was observed to control the combustion of methane by initiating the mixture earlier; the rest of the combustion process was shown to be similar.

Furthermore, the dilution effect of carbon dioxide was observed when added to pure methane mixtures. The carbon dioxide delays the initiation of combustion and increases temperature stratification due to its high heat capacity. Also, carbon monoxide showed again that it has no significant effect on the ignition delay time.

However, in terms of the effects of parameters on the combustion behavior, it is to mention that the comparison of the numerical expectations and experimental visualization was not easy. This was mainly due to the camera's saturation for high luminous combustion and the difficulty in detecting the combustion process for mixtures with low luminosity.

To conclude, this study is a qualitative observation of the combustion process; it allows the validation of some aspects studied numerically. However, a quantitative observation is required in future studies to better distinguish the effects of parameters on the combustion behavior.

In the second part of this chapter, the first effects of biomass injection on the combustion of biogas/syngas mixtures will be presented.

Fundamental ideas of this section

- Rapid cinematography was performed to directly visualize the combustion behavior of the twelve mixtures selected in chapter 3.
- A low amount of hydrogen, 5%, was able to control the combustion of methane by initiating the mixture earlier. However, the rest of the combustion process is similar.
- The dilution effect of carbon dioxide was observed when added to pure methane mixtures. The carbon dioxide reduced the temperature of the chamber significantly.
- Also, for mixtures containing a certain amount of carbon dioxide (40%), the combustion seems to be more localized in the chamber, possibly due to the high heat capacity of carbon dioxide.
- Carbon monoxide showed again that it has no significant effect on the ignition delay time or the combustion process.
- The comparison of the numerical expectations and experimental visualization was not easy, due to the saturation of the camera's sensor for high luminous combustion, and the low luminosity for some mixtures.
- Some of the numerical data were validated; however, for other parameters, further analysis and treatment of the images should be done to validate or not the effect of parameters on the combustion's behavior as explained in the turbulent combustion approach.
- This study is a qualitative observation of the combustion process; a quantitative observation could be made in future studies by using a filter with chemiluminescence to validate the numerical study.

VI. Gas/solid biomass combustion

The gaseous and solid biomass combustion processes were studied separately on a rapid compression machine in previous sections. The parameters that affect their combustion were mentioned, and some of them were studied in detail.

In this section, on the other hand, more interest is drawn on the effects of solid particles on the combustion of gaseous mixtures; in other words, this study will show whether the particles promote the combustion of biofuel mixtures or the inverse. The same experimental setup described previously will be used to study the diphasic combustion gas/solid in this section; our purpose is to make a first study on the effects of biomass injection on the combustion of different gaseous biomass mixtures.

In order to reduce the quantity of the residual particles in the combustion chamber, for each test with particle injection, there will be another test without injection. This will give particles time to burn before injecting a new amount.

1. Experimental mixtures and conditions of gas/solid biomass combustion

Therefore, the study of diphasic combustion gas/solid biomass will be addressed. Rapid cinematography is also used to view the effects of the particle injection on the combustion behavior of the mixtures.

Thus, it will be more interesting if the study covers different combustion zone, therefore, different combustion behavior. For this reason, three mixtures were chosen from three zones in the Borghi diagram, as shown in Figure 150. Mixture 13 corresponds to the distributed reaction zones (zone IV), mixture 14 to the corrugated flamelets (Zone III), and mixture 15 lay between these two.

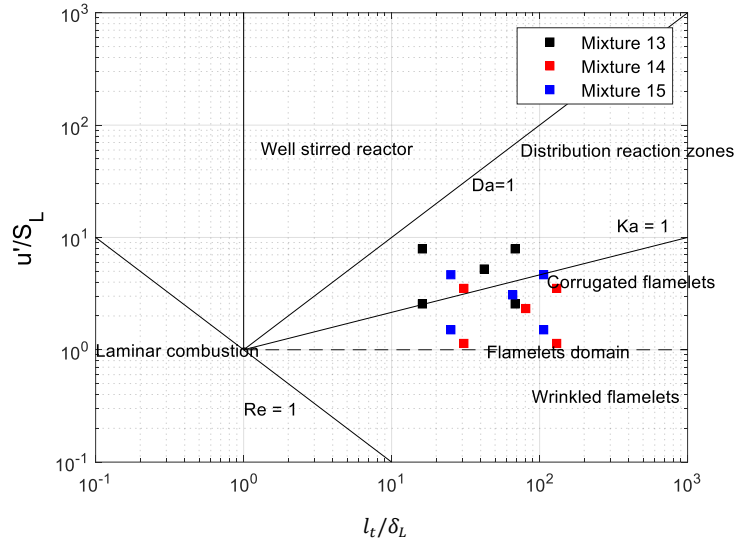


Figure 150: Borghi diagram for mixture 13, 14 and 15

These experimental conditions related to these mixtures are presented in Table 43.

Table 43: Biogas/syngas mixtures studied with solid biomass particles

| Mixtures | Composition | percentages | ϕ | Pressure (bar) | Temperature (K) |
|------------|--|--|--------|----------------|-----------------|
| Mixture 13 | CH ₄ /H ₂ /CO ₂ | 24/6/70 | 0.6 | 8 | 940 |
| Mixture 14 | CH ₄ /H ₂ /CO ₂ | 48/12/40 | 0.6 | 8 | 990 |
| Mixture 15 | CH ₄ /H ₂ /CO ₂ + dilution 5% CO ₂ | 48/12/40 + dilution 5% CO ₂ | 0.6 | 11 | 990 |

2. Results on the effect of solid biomass over biofuel combustion

Several injection tests were studied for each of the three mixtures. The same experimental setup described earlier is also used in this part of the study. However, this time only camera 1 was used to visualize the results. The operating conditions of each test will be presented.

The same assumption of the start of injection explained in chapter 4 is used in this study. Furthermore, we distinguish between the ignition delay time of the gas/solid mixture, which is the time between the end of compression pressure and the time of the peak heat release, and the ignition time of solid particles. The presented images in the following study correspond to this range (start of ignition till the end of the combustion process).

2.1. Mixture 13

The first mixture to be studied is mixture 13, whose combustion, according to the study made in chapter 3, corresponds to the distributed reaction zones (zone IV). This mixture is composed of CH_4/H_2 (80/20%) diluted with 70% of CO_2 and compressed at a temperature of 940K and 8 bars.

However, this mixture was not reactive enough to ignite with these conditions and even higher initial concentrations. The importance of this mixture is to see if the particles can promote its combustion or not.

Several injection experiments were performed on this mixture, and the combustion occurs after a certain period of time for all of them. This can be the first proof of the positive effect of particles in promoting combustion.

From all the injection experiments performed on mixture 13, only three of them will be presented in the following study; the first injection (injection 1) occurs before the top dead center (-5,5 msec before the top dead center), and the other two at the top dead center.

The evolution of the pressure curve for the combustion with and without particles are presented in Figure 151.

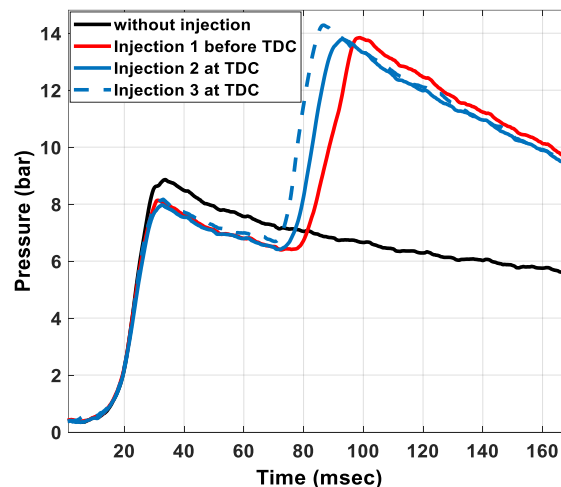


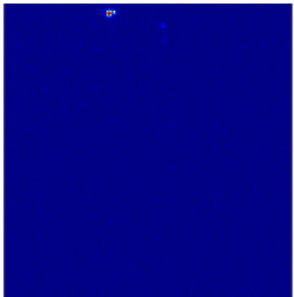
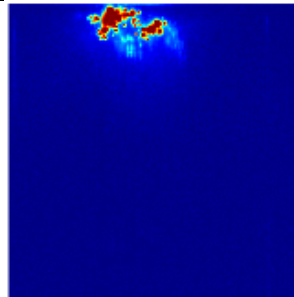
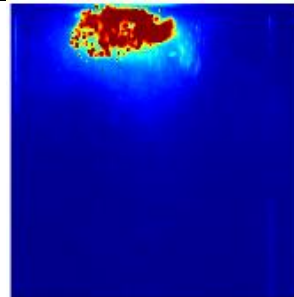
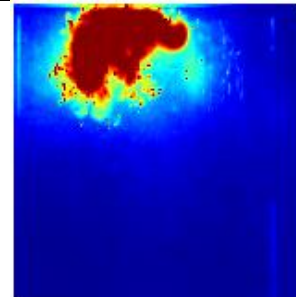
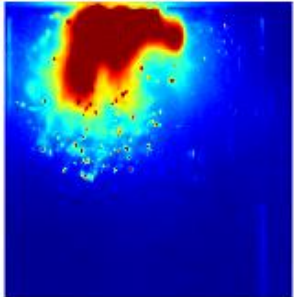
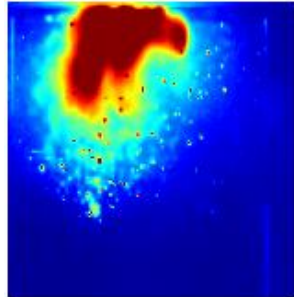
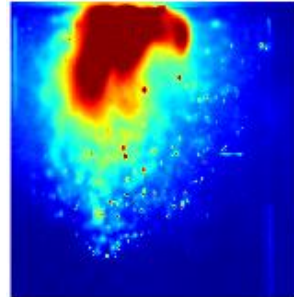
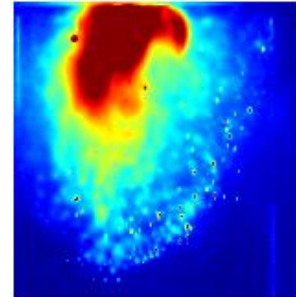
Figure 151: Pressure curve of mixture 13 with and without injection

It is observed that the ignition delay values are close for the three tests (between 46-56 msec); the same applies to the maximum pressure. However, the heat release relative to injection 3 at TDC is the highest among them, and its combustion is the fastest. Further information on the pressure increase and combustion duration is presented in Table 44.

Table 44: Combustion characteristics of the three injection tests

| Test | Auto-ignition delay times (msec) | Combustion duration (msec) | The velocity of pressure rises (MPa/msec) |
|-------------|----------------------------------|----------------------------|---|
| Injection 1 | 56 | 23.8 | 0.03116 |
| Injection 2 | 50 | 22.4 | 0.03275 |
| Injection 3 | 46 | 17.9 | 0.041956 |

The time delays are further from the start of the studied injection times, which indicates that the injected particles were heated before initiating the combustion. This can be seen from the combustion images of these experiments presented in Figure 152.

| Injection 1 BTDC | | | |
|---|---|--|---|
| 45 msec ATDC | 45.6 msec ATDC | 46.3 msec ATDC | 48.1 msec ATDC |
|  |  |  |  |
| 50.6 msec ATDC | 51.9 msec ATDC | 53.1 msec ATDC | 54.4 msec ATDC |
|  |  |  |  |
| Injection 2 at TDC | | | |
| 40.5 msec ATDC | 41.7 msec ATDC | 42.9 msec ATDC | 44.2 msec ATDC |
|  |  |  |  |

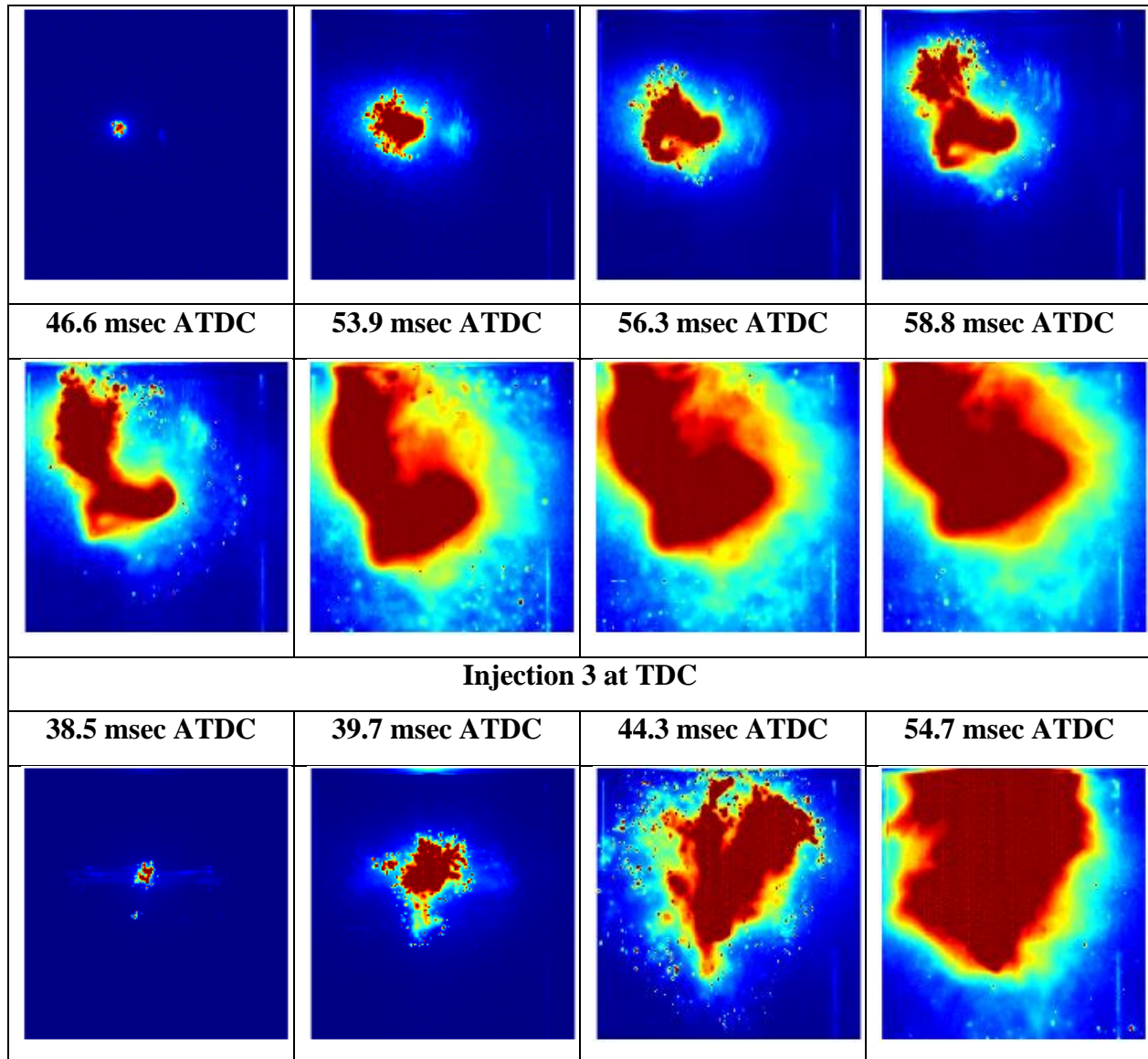


Figure 152 : Combustion of mixture 13 with three particle injection tests

For each injection test, the combustion is initiated by the ignition of one to several particles in the upper, lower, or center part of the chamber. The propagation of the combustion is highly dependent on the distribution of the particles in the enclosure. For example, for the first injection test, the particles located in the upper part of the chamber start to ignite and initiate the combustion of the gas mixture; the combustion then propagates throughout the enclosure but stays somehow concentrated in the upper part of the chamber. For injection test 2, the combustion is initially initiated by particles in the center of the enclosure. Other particles start to ignite after a certain time; then, the sites were reunited and propagate in the chamber while also staying closer to the upper part. The behavior of the combustion in injection test 3 is particularly similar to that of injection test 2. Moreover, for the three tests, particles initiated the combustion.

The evolution of the percentage of the luminous surface of combustion for the three injection tests is presented in Figure 153.

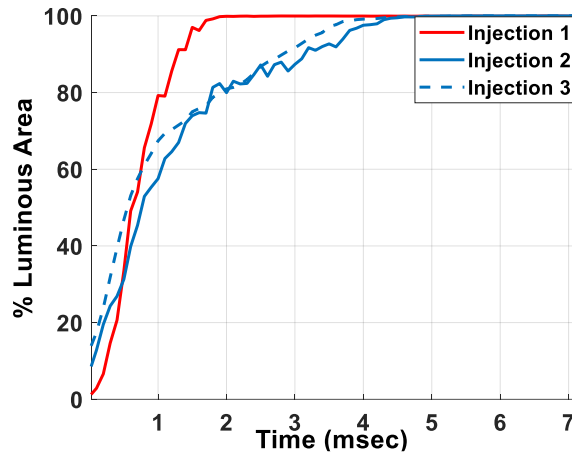


Figure 153: Percentage of the luminous surface of combustion versus time after the start of combustion for the three injection tests

It is observed that the surface is completely illuminated after 4 msec for tests 2 and 3, and 2 msec for test 1. However, as shown in Table 44, the combustion duration is the longest for test 1, and the pressure increase velocity is the shortest. The fast occupation of the chamber by combustion test 1 can be explained by particle distribution in the chamber; in test 1, particles were injected before the top dead center, which means they were mixed longer with the gas mixture and therefore distributed differently in the chamber.

The initial gas mixture (without solid particles) does not burn due to the lack of energy for pursuing the chemical reactions. The injection of solid particles was shown to have a positive effect on promoting combustion. In order to explain this promoting effect, two configurations are possible:

- After the heating, drying, and devolatilization of the injected particles, the produced volatiles (mainly consistent with CO_2 , CH_4 , and CO) or char burn with oxygen. The combustion is exothermic, and it will provide the gas mixture with sufficient activation energy for the chemical reactions to occur.
- The produced volatiles changed the composition of the gas mixtures by creating locally rich mixtures, which will activate the chemical reactions and provoke the combustion of the mixture.

However, either way, the injected particles into mixture 13 initiated the gas/solid combustion. The most critical points to be highlighted:

- The chemical and thermal effects of particles promote the combustion, not the injection pressure effects (because the gas mixture did not ignite even with higher initial pressure)
- The ignition delay times of the gas/solid mixtures are similar for all the studied tests. This means that the particles can control gas combustion.

Furthermore, the effects of particles on the combustion behavior of mixtures 14 and 15 will also be studied in the following section.

2.2. Mixture 14

The combustion of mixture 14 corresponds to the corrugated flame zone (Zone III). This mixture is composed of $\text{CH}_4/\text{H}_2/\text{CO}_2$ (48/12/40%) and compressed at a temperature of 990 K and 8 bars.

The images acquired for the combustion process of mixture 2 without injection are presented in Figure 154.

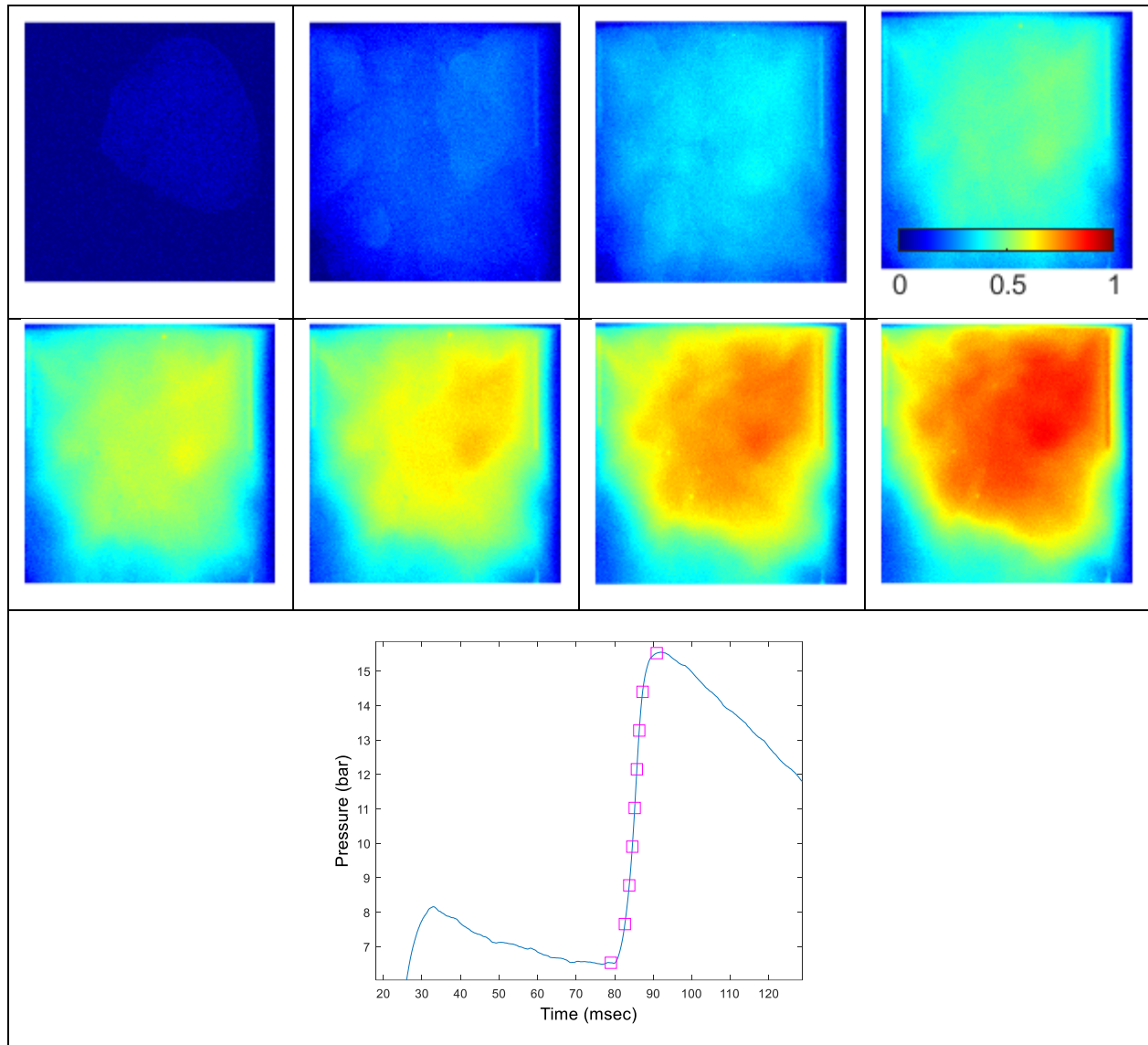


Figure 154: Images acquired for the combustion process of mixture 14 without injection

The combustion process is surely similar to the combustion behavior of lean $\text{CH}_4/\text{H}_2/\text{CO}_2$ mixtures ($\phi=0.6$) (mixture 2), studied in the first part of this chapter with a temperature of 1000 K. The combustion appears to be consistent with the instantaneous auto-ignition of a certain load in the upper part of the chamber; it spreads quickly to cover only the upper part of the chamber.

Several injection experiments were performed on this mixture, and two of them are presented in the following study; the first injection occurs before the top dead center (-5.5 msec BTDC) and the second one at the top dead center.

The evolution of the pressure curve for combustion with and without particles is presented in Figure 155.

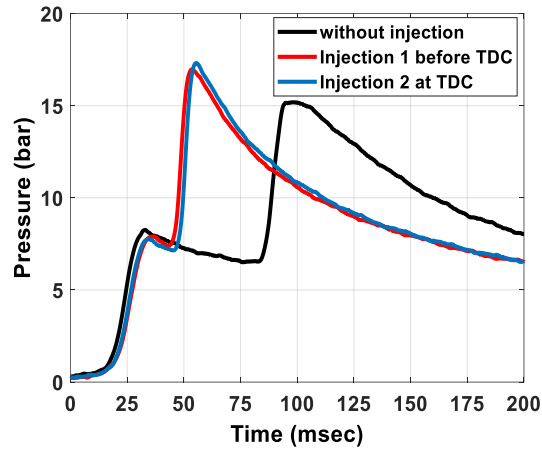


Figure 155: Pressure curve of mixture 14 with and without injection

Similar to mixture 13, the pressure curves indicate that the particle injection promotes the combustion of the gas mixture.

The ignition delay time is significantly reduced from 53 msec in gas combustion to less than 20 msec in gas/solid combustion. Injection tests 1 and 2 exhibit the same effects on pressure and heat release curves. Moreover, the pressure curve analysis shows that the combustion duration is similar for all mixtures (~14 msec), despite the differences in the ignition start (as can be seen in Table 45).

Table 45: Combustion characteristics of the mixture 14 with two injection tests

| Test | Auto-ignition delay times (msec) | Combustion duration (msec) | The velocity of pressure rises (MPa/msec) |
|-------------------|----------------------------------|----------------------------|---|
| Without injection | 53 | 13.7 | 0.0658 |
| Injection 1 | 13 | 14 | 0.0665 |
| Injection 2 | 16 | 14 | 0.07145 |

The images of the combustion process of tests 1 and 2 are presented in Figure 156.

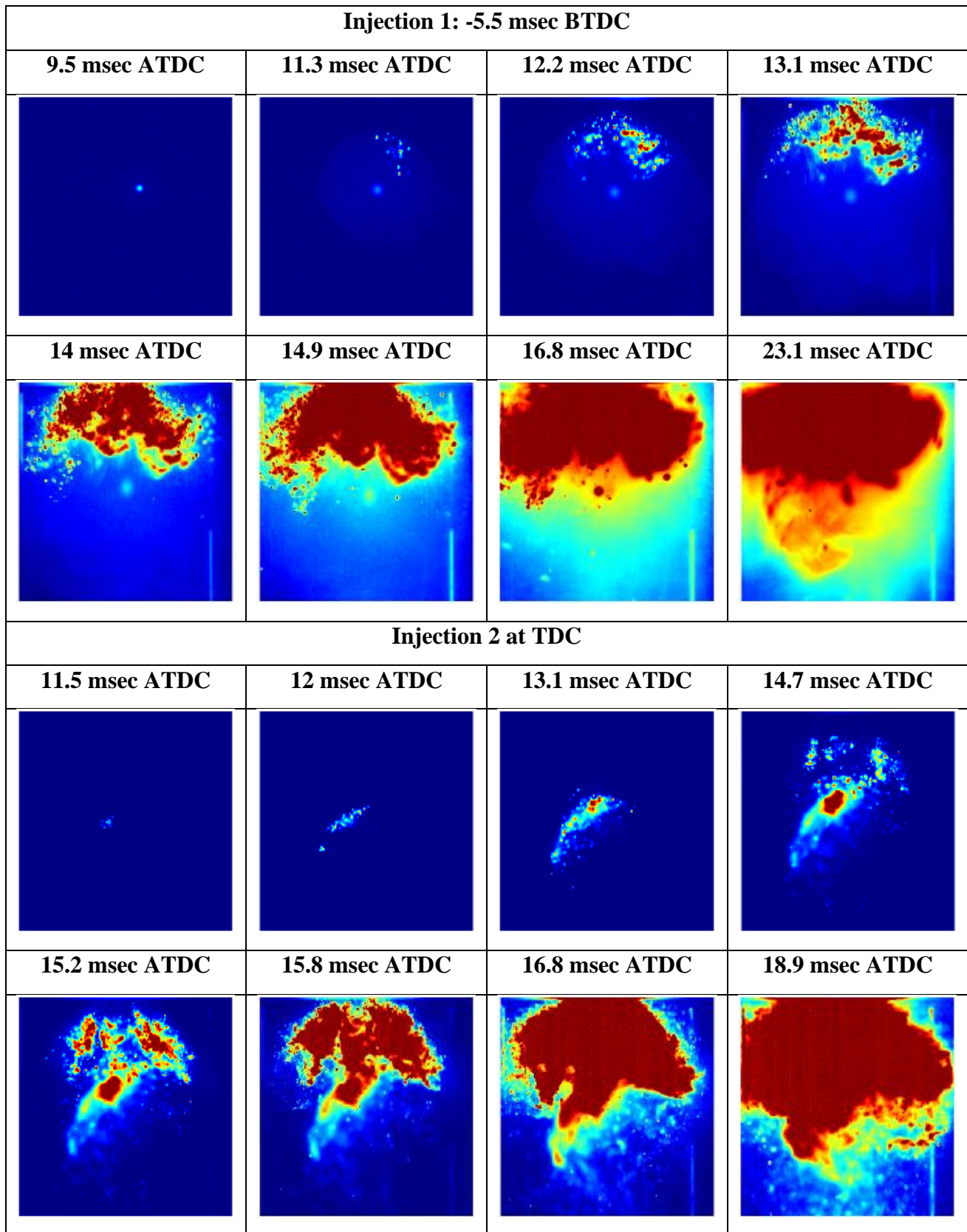


Figure 156: Combustion of mixture 14 with two particle injection tests

For injection test 1, the first ignition site is initiated by a particle combustion 15 msec after the start of injection. The produced energy, along with the thermodynamic conditions in the chamber were sufficient to trigger the combustion of particles at the exit of the nozzle. The heat released from the combustion of the concentrated particles in the upper part of the chamber accelerates the chemical reactions in the gas combustion. Thus, the combustion in injection test 1 is similar in concept to mass combustion in the upper part of the chamber because several multi-sites were initiated and propagates in the chamber. For test 1, the combustion was initiated by particles at the exit of the injection nozzle; therefore, the combustion mainly occurs in the chamber's upper part.

As for test 2, the particles were ignited 11.5 msec after the start of the injection. The combustion exhibits similar behavior than in test 1 with fewer particle concentrations; several sites appear around the initiation nuclei, and the multi-sites combustion propagates mostly in the upper part of the combustion chamber.

The evolution of the percentage of luminous area with the time after the start of combustion is presented in Figure 157. Similar to the results of mixture 13, the combustion chamber is illuminated faster in combustion test 1 than in combustion test 2, which can be due to the particle distribution in the chamber.

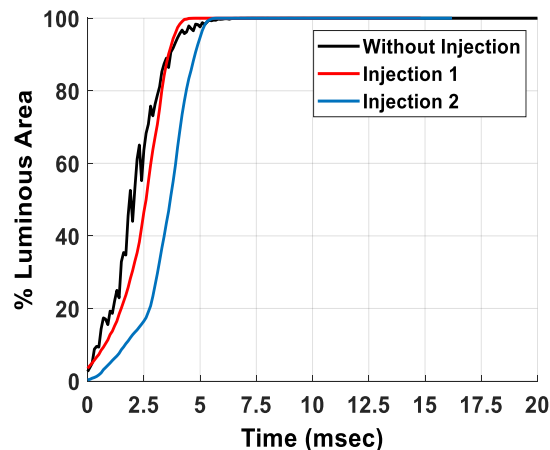


Figure 157: Percentage of the luminous surface of mixture 14 with two particle injection tests

To summarize, the solid particles not only promote the ignition of mixture 14 but also induce a change in combustion behavior. Without injection, the combustion was shown to ignite and to propagate in the upper part of the combustion chamber, whereas, with particle injection, the multi-sites combustion is favored for all the injection tests. The main difference occurs in the particle distribution in the combustion chamber, so the way the combustion propagates.

Essential points to be highlighted:

- The injection of particles promotes the reactivity of the mixture
- The studied injection times (BTDC and at TDC) are shown to have more impact on the propagation of the combustion than the initiation phase.

2.3.Mixture 15

The combustion of mixture 15 occurs in the zone between the corrugated flame zone and the distribution reaction zones. This mixture comprises $\text{CH}_4/\text{H}_2/\text{CO}_2$ (48/12/40%) diluted with 5% CO_2 and compressed at a temperature of 990 K and 11 bars.

Several injection experiments were performed on this mixture. Four of them will be presented in the following study; the first injection occurs before the top dead center (-5,5 msec BTDC), and injection 2, 3, and 4 at the top dead center.

The evolution of the pressure curve for combustion with and without particles is presented in Figure 158.

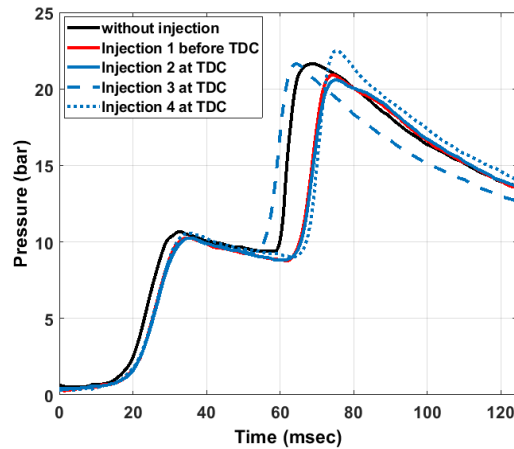
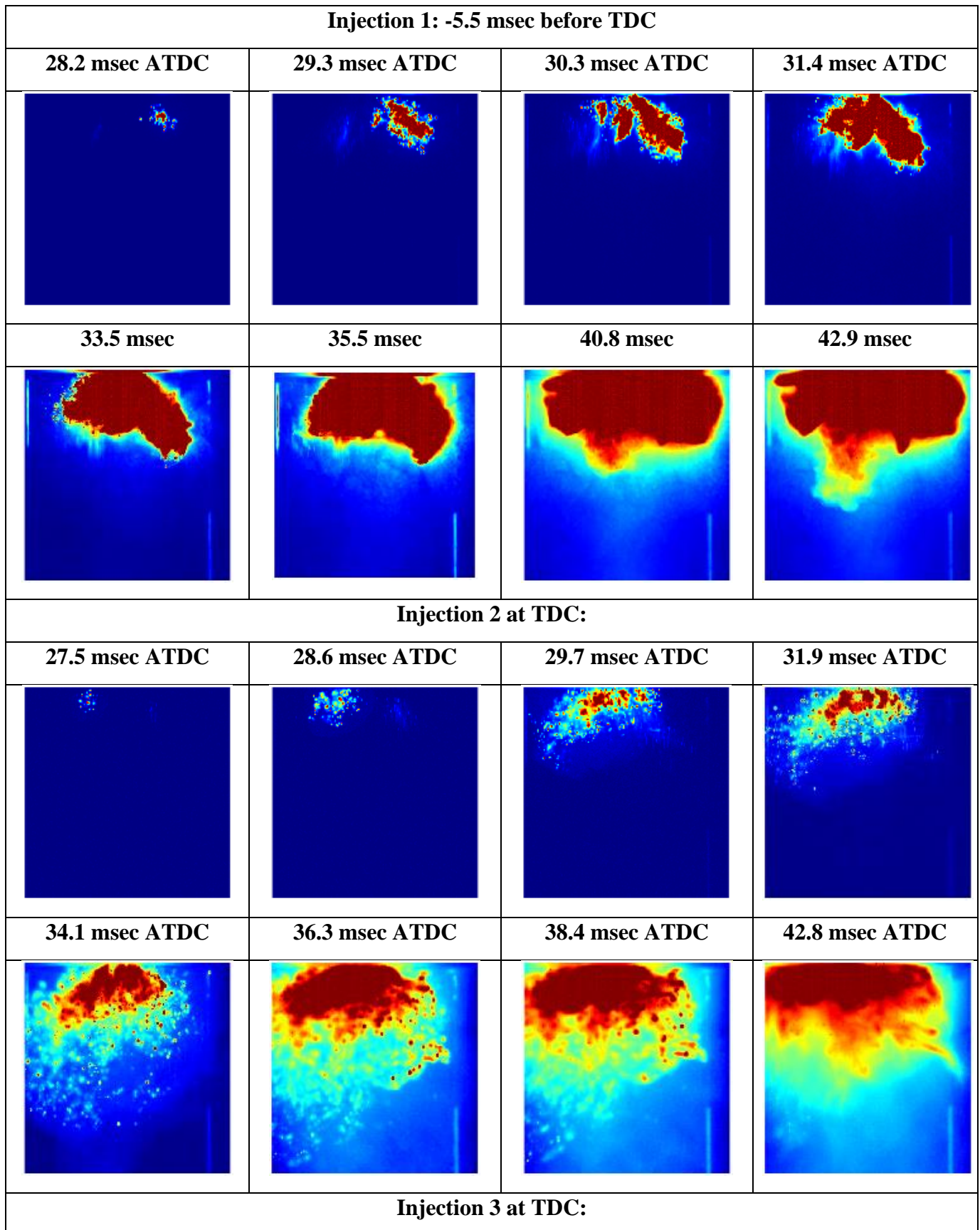


Figure 158: Pressure curve of mixture 15 with and without injection

Similar to previous mixtures, the pressure curve of injection 3 indicates that the particles promote the combustion of the gas mixture. The ignition delay time is reduced from 26 msec in gas combustion to 24.93msec in gas/solid combustion.

Injection tests 1, 2 and 4 exhibit similar combustion duration (16-18 msec) as well as the ignition delay time (34-37 msec) as shown in Table 46. However, the ignition delay times are shown to be longer than that of the gas mixture without injection. The images of the combustion process of the four injection tests are presented in Figure 159.



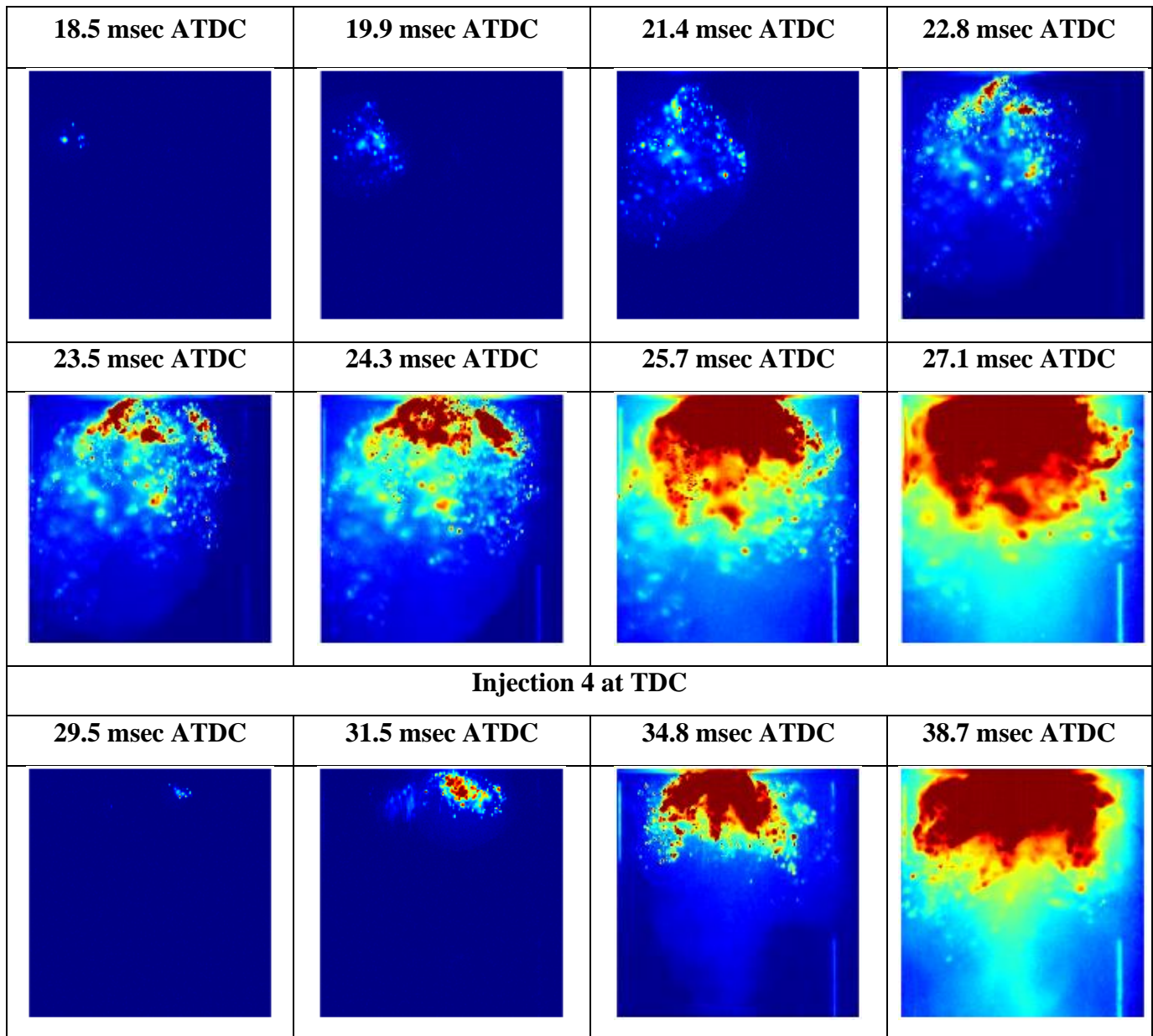


Figure 159: Combustion of mixture 15 with four particle injection tests

Table 46: Combustion characteristics of the mixture 15 with four injection tests

| Test | Auto-ignition delay times (msec) | Combustion duration (msec) | The velocity of pressure rises (MPa/msec) |
|-------------------|----------------------------------|----------------------------|---|
| Without injection | 26 | 18.2 | 0.0616 |
| Injection 1 | 35.14 | 16.2 | 0.00742 |
| Injection 2 | 34.93 | 18.2 | 0.006383 |
| Injection 3 | 24.93 | 16 | 0.0076 |
| Injection 4 | 36.81 | 16.3 | 0.00813 |

For tests 1, 2, and 4, the combustion is initiated by the injected particles at the exit of the nozzle. The heat release at the exit of the nozzle triggers the combustion of the injected jet, and the gas combustion is initiated from the upper top of the chamber.

Actually, mixtures 14 and 15 have the same end of compression temperature (990 K). However, for the same injection timing, the particles ignite in mixture 14, about 15 msec earlier than in mixture 15. This can be explained by the difference in fuel composition; Mixture 15 is richer in carbon dioxide with higher heat capacity. This will cause a decrease in the thermal diffusivity of the mixture; the ignition delay of solid particles decreases. This effect of the heat capacity of the ignition of the solid particle was validated by several authors in the literature. Molina and Shaddix[184] verified an increase in the ignition delay time of solid coal in O₂/CO₂ mixtures, claiming that such differences were due to the change in the volumetric heat capacity of the mixture gas, which leads to an increase the heat losses from the particle and delays ignition. Moreover, Zou et al. [199] studied the ignition of a single particle in a drop tube reactor and stated that the higher thermal capacity could reduce the rate of temperature increase of the particle, resulting in a delay of the ignition.

This result is highly important as it highlights the dependency of the solid ignition on the thermodynamic and transport properties of the reactive gas mixture.

The same results discussed previously on the effect of injection timing on the distribution of particles can be observed in Figure 160.

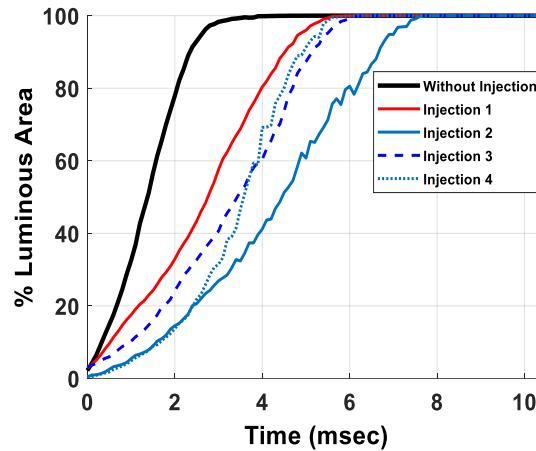


Figure 160: Percentage of the luminous surface of mixture 15 with four particle injection tests

Essential points to be highlighted:

- The ignition of solid particles depends on the transport properties of the gas mixture
- Good optimization of the characteristics of gas/particles leads to a better combustion process

Fundamental ideas of this section

Mixture 13:

- Mixture 13 is non-reactive in the conditions of experimentation; the injection of particles before or at the top dead boosted its reactivity and initiated the combustion
- The combustion process was shown to be similar for both injection times;
- It is the particles that initiate the combustion and not the injection pressure

Mixture 14

- The injection of particles on mixture 14 reduces the ignition delay times
- The injection before and at the top dead center leads to similar ignition delay time and similar combustion behavior

Mixture 15

- Even though the temperature in this mixture is similar to that in mixture 14, the particles are shown to ignite later
- The high heat capacity can explain this in mixture 15 due to the presence of carbon dioxide; it results in a decrease in the ignition delay times of particles

For all tests

- The particles have a positive effect in promoting and controlling combustion.
- The ignition delay times of gas/particles were reproducible, which highlights the effects of particles in controlling the ignition of gas mixtures under lean homogeneous conditions.
- For the three mixtures, the combustion chamber area was shown to be illuminated faster when the injection occurs before the top dead center. This can be an indicator that the particles injected before the top dead center are better distributed in the chamber.

VII. Conclusions of this chapter

The importance of the study in this chapter is that it sheds light on the positive effects of direct injection of solid particles into a reactive gas mixture.

This chapter was divided into two parts. Rapid cinematography was used in the first part to visualize the combustion phenomenon of twelve biogas/syngas mixtures selected to validate the approaches of chapter 3 and to provide further evidence on the different behavior that can exhibit each mixture. Two intensified cameras recorded the combustion process; the registered images' treatment allowed the qualitative analysis of the combustion behavior.

The effects of the equivalence ratio, end of compression temperature and fuel composition on the combustion process were validated experimentally by direct visualization. However, it was difficult to validate the combustion regimes qualitatively; further quantitative methodology should be considered.

In the second part of this chapter, the effects of direct injection of biomass powder into the reactive mixture on the lean homogeneous combustion were studied. This study highlights the benefits of injected biomass in the control and stability of the ignition timing of the HCCI engine.

For the different studied mixtures, the injected particles exhibit a positive effect on the combustion process in two different ways:

- Promoting the reactivity of a mixture that could not burn without particle injection;
- Reducing the ignition delay time of a biogas/syngas mixture with a long delay;

The most important thing to highlight is that several tests were conducted for each mixture. The results were satisfyingly reproducible, which shed light on the capability of particles in controlling the ignition timing.

For all the studied cases, the gas combustion is initiated by one or more particle ignition, then propagates and provokes the rest of the particles' combustion. The ignition delay time of solid biomass was shown to depend on the thermodynamic and transport properties of the reactive gas mixture. Hence, the characteristics of the biomass powder and the biogas/syngas mixtures should be optimized for improving the combustion process.

Conclusions and perspectives

This study focuses on the advantages of lean homogeneous combustion (HCCI) using biomass renewable energy as an alternative technology. The injection timing control was assured by direct injection of biomass powder into the combustion chamber's reactive gas mixture, which shows to have a positive effect both in controlling and stabilizing the lean combustion phenomenon. It is by far the first study on the direct injection of solid biomass in an engine application.

The work in this manuscript was divided into two parts. The first part focused on characterizing the lean homogeneous combustion of gaseous biomass (biogas/syngas), while the second part focused on studying the diphasic combustion gas/solid biomass.

Experimental and numerical studies were conducted for this purpose.

The experimental study was achieved on the SU rapid compression machine (SU RCM) with complete optical access. This device makes it possible to obtain and maintain thermodynamic conditions (pressure, temperature) necessary for a reactive mixture's auto-ignition. The SU rapid compression machine (SU RCM) was described briefly, and the performance and reproducibility of the experimental setup were highlighted. The comparisons of self-ignition times measured by different authors have shown that the trends we observed followed the literature. Nevertheless, the existing disparities can be due to the difference in each rapid compression machine's designs and conception, including turbulence levels and heat transfers.

Due to the complexity of lean homogeneous combustion behaviors, and the coexistence of different possible combustion regime, the numerical study was carried on Chemkin-Pro through a simplified approach. This approach consists of characterizing the combustion first on a closed homogeneous reactor and then on a premixed flame configuration. The effects of the initial conditions and fuel composition on the physical and chemical aspects were studied. Their effects on pollutant emissions were also investigated. This study highlighted the advantages of lean combustions in reducing pollutant emissions, in particular NO_x and carbon monoxide. It also highlights the importance of a fuel type biogas/syngas in minimizing carbon emissions while maintaining a specific mixture's reactivity. Thus, a database characterizing the biofuel combustion was built; it allows the optimization of the most suitable biogas/syngas mixtures in terms of pollutant emissions, ignition delays, and flame speeds in both studied configurations. It was found that from a closed reactor perspective, the biogas/syngas mixtures can be optimized by adjusting the percentages of hydrogen and carbon dioxide according to the emission chart (proposed in this manuscript) while fixing a minimum value of hydrogen to 10%. On the other hand, from a premixed laminar flame perspective, carbon monoxide should also be considered as it has an essential effect on stabilizing the biofuel combustion.

Because of the complexity of the combustion behavior, an approach to turbulent combustion was also considered, and the effects of the conditions of the mixture on the combustion behavior were highlighted. This approach's validity was validated by rapid cinematography that allowed the direct visualization of the combustion behavior by chemiluminescence. The combustion was shown to occur by propagating a flame front after being initiated locally by self-ignition or combustion occurring entirely by self-ignition but with the possibility of a start and a progression of the combustion on several sites of self-ignition.

However, this study is qualitative and simplified; a quantitative approach could be applied to an engine cycle to obtain more realistic results.

In the second part of this work, the innovative solution proposed to control the ignition timing of lean homogeneous combustion was studied.

In order to inject particles into the combustion chamber, an injector system was conceived on IJLRA to allow the direct injection of solid biomass.

It is a complex system that allows the direct injection of particles in a reproducible way and at a wide-angle, which assures their suspension and distribution in the chamber. The particle injector was implemented in the center of the RCM chamber. The combustion of solid biomass was studied to characterize the crucial factors that impact its combustion.

Finally, the study of the first effects of particle injection on the lean homogeneous combustion of gaseous biofuels was examined.

This study's results shed light on the positive effect of biomass particles in promoting and controlling the ignition timing in lean homogeneous conditions.

This study proves that the direct injection of solid particles into reactive gas mixtures is a promising technology that can control the ignition timing of lean homogeneous combustion. Hence, an optimization of the characteristics of the biomass powder and the biogas/syngas mixtures is essential for improving the combustion process.

In future studies, it would be interesting to study the different behavior related to different types of biomass, particle shapes, and size on the diphasic combustion gas/solid.

Furthermore, a parametrical study on the effects of the injection pressure, particle diameter, and fuel composition can be performed. Also, performing PIV measurements on the particle injection in the RCM chamber can be crucial to see if the injected particles induce a significant change in the chamber's internal aerodynamics.

Developing a multi-zones model that characterizes biomass powder's combustion can be used to detect the ignition delay time of particles for different initial conditions. It would also be interesting to enhance further the theoretical model by including gas-phase reaction effects on the particle boundary layer. The application of other visualization techniques, such as Schlieren or Shadowgraphy, to observe the volatile release near the particle surface and its influence on the surrounding flow of hot gases would be a very interesting study, particularly for high volatile biomass.

Figure List

| | |
|---|----|
| Figure 1: CO ₂ emissions: Share of key source categories and all remaining categories in 2018 for EU-KP [1] This image shows that road transportation along with public electricity and heat production have the higher share in CO ₂ emission in Europe for the year 2018. | 16 |
| Figure 2: Distribution by the source of GHG emissions in France between 1990-2017 [2] | 17 |
| Figure 3: Simplified diagram of the reaction mechanism of biomass gasification (adapted from [7]). | 19 |
| Figure 4: Different types of gasifiers [12] | 22 |
| Figure 5 : Comparison of SI, DI and HCCI combustion modes [27] | 27 |
| Figure 6: Comparative parameters of spark ignition (SI), compression ignition (CI) and homogeneous charge compression ignition (HCCI) engines [28] | 27 |
| Figure 7: (a) Effects of pressure and temperature on spontaneous ignition of cool flames and hot flames. (b) Temperature versus time history of LTI and HTI in two-stage ignition [31]. | 28 |
| Figure 8: The temperature fields and their distributions along the combustion chamber of an inert mixture of n-C ₇ H ₁₆ (load 180 mol/m ³ and equivalence ratio 0.8) measured at TDC, then after 10 msec and 40 msec of this instant [33]. | 29 |
| Figure 9 : Major HCCI benefits (solid circles) and drawbacks (dashed circles) pertinent to HCCI ignition timing[27] Controlling the HCCI combustion timing is very crucial in homogeneous combustion; it has numerous challenges but also benefits. | 31 |
| Figure 10 : Strategies for controlling the ignition timing and combustion phase of the HCCI engine [45] | 33 |
| Figure 11: Schematic diagram of the SU rapid compression machine (Horizontal view) | 37 |
| Figure 12: Comparison of different compression profiles; A. piston velocity versus time; B. Pressure curve in compression phase versus time | 39 |
| Figure 13: Diagram representing the filling and vacuum circuits of SU RCM | 41 |
| Figure 14: The chronogram of the complete firing procedure | 42 |
| Figure 15: Several ignition delay times definitions (the curve of dQ (heat release rate) is scaled by [2* Pmax/(3*dQmax)]). The pressure curve is used to estimate the ignition delay time, calculated by four methods IDT1, IDT2, IDT3 and IDT4 | 44 |
| Figure 16: Representation of the other RCMs A. schematic diagram of the MIT RCM and B. photo of the NUIG RCM | 50 |
| Figure 17: Comparison of the corrected self-ignition times of mixture 1 performed on SU RCM and Netherland RCM obtained from the literature [64] | 51 |
| Figure 18: Comparison of the corrected self-ignition times of mixture 2 performed on SU RCM and Netherland RCM obtained from the literature [64] | 51 |
| Figure 19 : Comparison of the corrected self-ignition times of mixture 3 performed on SU RCM and NUIG RCM [2] | 52 |
| Figure 20 : Pressure as a function of time for the different percentages of H ₂ A. compression phase B. heat exchange phase and C. end of combustion phase | 59 |
| Figure 21: Heat release profile as a function of time for different percentages of H ₂ | 60 |
| Figure 22 : Pressure and heat release profile as a function of time for different temperature values for H ₂ -CH ₄ mixture 20-80 % | 61 |
| Figure 23 : Standard deviation of auto-ignition delay time for CH ₄ /H ₂ /CO ₂ /CO mixtures | 62 |

| | |
|--|-----|
| Figure 24 : Ignition delay times of CH ₄ /H ₂ mixture as a function A. of temperature for different percentages of H ₂ B. of H ₂ percentages at different temperatures | 63 |
| Figure 25 : Self-ignition time of the CH ₄ /H ₂ / CO ₂ mixture A. for different percentages of CO ₂ B. at different temperatures | 65 |
| Figure 26: Auto-ignition delay times of CH ₄ /H ₂ /CO ₂ /CO mixtures A. for different percentages of CO; B. at different temperatures | 66 |
| Figure 27 : Schema of the ideal and actual lean homogeneous combustion | 73 |
| Figure 28: Simulation conditions of auto-ignition and propagating flame processes conducted on Chemkin-Pro | 75 |
| Figure 29: Hierarchical structure and overall interrelationships between oxidation mechanisms for simple hydrocarbon fuels [96] | 78 |
| Figure 30 : Pressure curves of models 1, 2, and 3 | 81 |
| Figure 31: Auto-ignition delay times comparison for different biomass-derived fuel mixtures simulated by model 1, model 2, and model 3 | 82 |
| Figure 32: Comparison of measured and calculated auto-ignition delay times using different chemical mechanism and for different biomass derived -fuel mixtures | 84 |
| Figure 33: Standard deviation of auto-ignition delay times | 85 |
| Figure 34: Closed homogeneous reactor | 88 |
| Figure 35: The molar fraction of created and consumed species due to the combustion of CH ₄ /H ₂ /CO ₂ /CO mixtures | 90 |
| Figure 36:Auto-ignition delay time as a function of the end-of-compression pressure for different biomass-derived fuel mixtures | 91 |
| Figure 37: Critical pressure versus temperature. Ignition is possible in the region above the curve for combustion chemistry when the global order is greater than 1 [106] | 92 |
| Figure 38: Auto-ignition delay time as a function of the end of compression temperature for different biomass-derived fuel mixtures | 92 |
| Figure 39: OH sensitivity as a function of time and temperature | 93 |
| Figure 40: Auto-ignition delay time as a function of the equivalence ratio of different biomass-derived fuel mixtures | 95 |
| Figure 41: normalized brute force sensitivity of auto-ignition delay times for methane/air mixtures for different equivalence ratio | 96 |
| Figure 42: Brute force sensitivity analysis of auto-ignition delay time | 97 |
| Figure 43: Auto-ignition temperature of different fuel composition P _c =15 bar, φ=0.6 | 98 |
| Figure 44: The effect of hydrogen addition on the ignition delay time of biomass-derived fuel mixtures | 98 |
| Figure 45: auto-ignition delay times of methane/hydrogen mixtures | 99 |
| Figure 46: The effect of carbon dioxide addition on the ignition delay time of biomass-derived fuel mixtures | 100 |
| Figure 47: The effect CO ₂ dilution rate on the ignition delay time of biomass-derived fuel mixtures | 100 |
| Figure 48: The emission indexes of pollutant species calculated by three methods | 105 |
| Figure 49: Influence of the pressure on pollutant emissions indexes | 107 |
| Figure 50: Influence of temperature on pollutant emissions indexes | 108 |
| Figure 51: Emission index of total greenhouse gases in the function of the equivalent ratio | 109 |

| | |
|--|-----|
| Figure 52: Influence of equivalence ratio on pollutant emission index for four biofuels without dilution | 109 |
| Figure 53: Influence of equivalence ratio on pollutant emission index for four biofuels diluted with 50 % CO ₂ | 110 |
| Figure 54: Influence of hydrogen on pollutant emissions index | 111 |
| Figure 55: Influence of carbon dioxide on pollutant emissions index | 112 |
| Figure 56: Influence of carbon monoxide on pollutant emissions index | 112 |
| Figure 57: Influence of CO ₂ dilution on pollutant emissions index of biomass-derived fuel mixtures | 113 |
| Figure 58: effect of hydrogen on biogas/syngas combustion process for different dilution rate | 114 |
| Figure 59: Auto-ignition delay times and pollutant emissions diagram (dilution 0% CO ₂), T _c between 920 and 1040K | 117 |
| Figure 60: Model used in Chemkin for the calculation of laminar premixed flame speed | 119 |
| Figure 61: Flame Speed as described by Borghi and Destriau[123] | 120 |
| Figure 62: Flame thickness calculation | 121 |
| Figure 63: Deviation of flow lines leading to the Darrieus-Landau instability[127]. | 123 |
| Figure 64: Schematic illustration of the mechanism of diffusive-thermal instability [128]. | 124 |
| Figure 65 : Influence of pressure on the flame speed | 125 |
| Figure 66: Influence of temperature on the flame speed | 126 |
| Figure 67: Influence of the equivalence ration on the flame speed | 126 |
| Figure 68: Influence of hydrogen percentages on the flame speed | 127 |
| Figure 69: Specific heat capacity of biofuel components and air for different temperature | 128 |
| Figure 70: Influence of the carbon monoxide percentages on the flame speed | 128 |
| Figure 71: Laminar flame speed (cm/s) as a function of fuel composition at fixed 1500 K (a) and 1900 K (b) adiabatic flame temperature at 4.4 atm with 460 K reactant temperature[134] | 129 |
| Figure 72: Influence of carbon dioxide percentages on the flame speed | 129 |
| Figure 73: Influence of the pressure on the pollutant emissions index | 131 |
| Figure 74: Influence of the temperature on the pollutant emissions index | 131 |
| Figure 75: Influence of the equivalence ratio on the pollutant emissions index | 132 |
| Figure 76: Influence of the hydrogen percentages on the pollutant emissions index | 133 |
| Figure 77: Influence of the carbon dioxide percentages on the pollutant emissions index | 133 |
| Figure 78: Influence of the carbon monoxide percentages on the pollutant emissions index | 134 |
| Figure 79: Evolutions of Lewis number diffusive based with the pressure, temperature and equivalence ratio of different types of biofuel | 137 |
| Figure 80: Evolutions of Lewis number with the fuel percentages at P _c =15 bar, T _c =960 K, and ϕ =0.6 | 138 |
| Figure 81: Evolutions of Lewis number with the dilution rate | 139 |
| Figure 82: effect of hydrogen and carbon monoxide addition on biofuel mixtures stability for different dilution rate | 139 |
| Figure 83: Flame speed and pollutant emissions diagram (dilution 0%), T _c between 920 and 1040 K | 142 |
| Figure 84: Range of optimized conditions in an homogeneous reactor approach and premixed flame configuration | 143 |
| Figure 85 : Schematic of turbulent field within a combustion chamber[145] | 144 |

| | |
|---|-----|
| Figure 86: The combustion diagram of Borghi | 147 |
| Figure 87 : Da and Ka as a function of temperature for different types of biofuel | 150 |
| Figure 88: Da and Ka as a function of the equivalence ratio for different types of biofuel | 150 |
| Figure 89 : Da and Ka as a function of the hydrogen percentage | 150 |
| Figure 90: Da and Ka as a function of the carbon monoxide percentage | 151 |
| Figure 91: Da and Ka as a function of pressure for different types of biofuel | 152 |
| Figure 92 : Da and Ka as a function of the carbon dioxide percentage | 152 |
| Figure 93 : First possible result of the diphasic combustion gas/particle | 158 |
| Figure 94 : Second possible result of the diphasic combustion gas/particle | 159 |
| Figure 95 : Scheme describing the experimental setup of the particle injection system | 160 |
| Figure 96: Chronogram of the injection valve command, opening, and start of injection | 161 |
| Figure 97: Definition of the jet penetration length L and the jet cone angle (θ) at L/2[150]. | 164 |
| Figure 98 : Jet depth determination | 165 |
| Figure 99: The evolution of the average jet cone angle θ with the injection time | 166 |
| Figure 100 : Scheme representing the multi-hole injection nozzles | 166 |
| Figure 101: The evolution of the field depth proportion with the injection time | 167 |
| Figure 102: The evolution of the jet area with the injection time | 167 |
| Figure 103: PIV measurement of the particle jet at different injection time | 170 |
| Figure 104: Turbulent jet flow from nozzle exit [155] | 171 |
| Figure 105: Horizontal and vertical components of average velocity at t_2 for different acquired tests | 172 |
| Figure 106 : Particle dispersion in the chamber using : a single nozzle and multi-hole nozzles | 173 |
| Figure 107: Structure of a single cellulose molecule | 176 |
| Figure 108: Demonstration of the hydrogen bonding that allows the parallel arrangement of the cellulose polymer chains [160] | 177 |
| Figure 109: Chemical structure of Xylan (Hemicellulose) | 177 |
| Figure 110: Chemical structures of the dominant building blocks of the three-dimensional polymer lignin P-Coumaryl-, Coniferyl-, and Sinapl alcohol | 178 |
| Figure 111: A model of the chemical structure of softwood lignin | 179 |
| Figure 112: A model of the chemical structure of hardwood lignin | 179 |
| Figure 113: Combustion steps of a biomass particle in the 10e100 micron size range[167]. | 181 |
| Figure 114: Different stages of biomass combustion versus temperature and time [169] | 182 |
| Figure 115: Time to reach 90% conversion and yields of tar, gas, and char at an imposed surface temperature of 823 K [177] | 184 |
| Figure 116: Pyrolysis gas release and char yields as a function of temperature [156] | 184 |
| Figure 117: Char yield and conversion time as a function of the initial porosity for T=900K[178] | 185 |
| Figure 118: Biomass particle combustion process | 187 |
| Figure 119 : Experimental setup for the study of particle combustion | 188 |
| Figure 120 : The experimental tests of solid biomass combustion | 189 |
| Figure 121: Load variations as a function of the injected volume for different possible N ₂ /particles proportions | 192 |
| Figure 122: Pressure variations as a function of the injected particles volume | 193 |

| | |
|--|-----|
| Figure 123: Pressure curves of Test 1a, b, and c of particle injection, with the end of compression temperature of 1155 K and an injection timing of 24,5 msec ATDC (the blue squares represent the start of injection) | 194 |
| Figure 124: Acquired images (binarized) of the particle's combustion for Test 1a, b, and c | 195 |
| Figure 125: Pressure curves of Test 3a and 3b before and at the TDC for a mixture compressed at 955 K. the blue square represents the theoretical injection timing, the red and pink squares represents the registered images of test 3a and 3b, respectively | 196 |
| Figure 126: Combustion images of particles at 955K for test 3a and 3b | 197 |
| Figure 127: Pressure curves for A. Tests 4, injection -5,5 msec BTDC, $T_c = 1050$ K and B. Test 5 injection at the TDC, $T_c = 955$ K. the blue square represents the injection timing, the pink squares represent the registered images of tests 4 and 5 | 198 |
| Figure 128: Combustion images of particles at 955K for tests 4 and 5 | 199 |
| Figure 129: Experimental setup of the cinematography process on the rapid compression machine. It shows how both cameras are located to allow a wider vision of the combustion process. | 206 |
| Figure 130: Chronogram of image acquisition for direct combustion viewing | 207 |
| Figure 131: Luminous intensities of camera 1 and 2 with A. heat production rate B. pressure curve | 210 |
| Figure 132 :The registered planes viewed by camera 1 and camera 2 in 3D | 211 |
| Figure 133: The locations of auto-ignition initiation sites in the combustion chamber (x, y and z) | 211 |
| Figure 134: The locations of auto-ignition initiation sites in the combustion chamber (x, z) and (y, z) | 212 |
| Figure 135: % Apparent area with time for various mixtures a. the effect of lean equivalence ratio, b. the global effect of equivalence ratio, c. Fuel composition effect | 213 |
| Figure 136: Mixtures 1-12 on the diagram of Borghi | 215 |
| Figure 137: Ratio of combustion regimes represented by the fluid elements[198] | 219 |
| Figure 138: Images acquired for the combustion process of mixture 1 ($\phi = 0.4$) | 221 |
| Figure 139: Images acquired for the combustion process of mixture 2 ($\phi = 0.6$) | 222 |
| Figure 140: Images acquired for the combustion process of mixture 3 ($\phi = 0.8$) | 223 |
| Figure 141: Images acquired for the combustion process of mixture 4 ($\phi = 0.6$) | 224 |
| Figure 142: Images acquired for the combustion process of mixture 5 ($\phi = 1$) | 225 |
| Figure 143: Images acquired for the combustion process of mixture 6 ($\phi = 1,2$) | 226 |
| Figure 144: Images acquired for the combustion process of mixture 7 | 227 |
| Figure 145: Images acquired for the combustion process of mixture 8 | 228 |
| Figure 146: Images acquired for the combustion process of mixture 9 | 229 |
| Figure 147: Images acquired for the combustion process of mixture 10 | 230 |
| Figure 148: Images acquired for the combustion process of mixture 11 | 231 |
| Figure 149: Images acquired for the combustion process of mixture 12 | 232 |
| Figure 150: Borghi diagram for mixture 13, 14 and 15 | 235 |
| Figure 151: Pressure curve of mixture 13 with and without injection | 236 |
| Figure 152 : Combustion of mixture 13 with three particle injection tests | 238 |
| Figure 153: Percentage of the luminous surface of combustion versus time after the start of combustion for the three injection tests | 239 |
| Figure 154: Images acquired for the combustion process of mixture 14 without injection | 240 |

| | |
|---|-----|
| Figure 155: Pressure curve of mixture 14 with and without injection | 241 |
| Figure 156: Combustion of mixture 14 with two particle injection tests | 242 |
| Figure 157: Percentage of the luminous surface of mixture 14 with two particle injection tests | 243 |
| Figure 158: Pressure curve of mixture 15 with and without injection | 244 |
| Figure 159: Combustion of mixture 15 with four particle injection tests | 246 |
| Figure 160: Percentage of the luminous surface of mixture 15 with four particle injection tests | 248 |

Table List

| | |
|---|-----|
| Table 1: The Euro V and Euro VI heavy-duty vehicle emission standards for diesel engines[6] | 18 |
| Table 2 : Selected sources for anaerobic digestion and the relative biogas composition | 21 |
| Table 3: Selected Biomass Gasification Technologies | 24 |
| Table 4: Percentages of components in biogas/syngas mixtures | 26 |
| Table 5: Technical characteristics of SU RCM | 42 |
| Table 6: Hydrogen and methane/hydrogen mixtures from the literature | 48 |
| Table 7: Comparison of three different RCMs | 49 |
| Table 8: percentages of components in biogas/syngas mixtures | 55 |
| Table 9: different configurations of H ₂ /CH ₄ mixtures | 56 |
| Table 10: different configurations of CH ₄ /H ₂ /CO ₂ | 56 |
| Table 11: different configurations of CH ₄ /H ₂ /CO ₂ /CO | 57 |
| Table 12: Experimental conditions corresponding to mixtures CH ₄ /H ₂ | 62 |
| Table 13: Experimental conditions corresponding to mixtures CH ₄ /H ₂ /CO ₂ | 64 |
| Table 14: Experimental conditions corresponding to mixtures CH ₄ /H ₂ /CO ₂ /CO | 66 |
| Table 15: Validation of Grimech3.0 mechanism by some authors in the literature | 77 |
| Table 16 : Validation of AramcoMech mechanism by some authors in the literature | 79 |
| Table 17: The simulation conditions of model 1 and 2 on different biogas/syngas mixtures | 81 |
| Table 18: Biogas/syngas mixtures and their initial conditions used in the comparison of the three reaction mechanisms | 83 |
| Table 19: Absolute deviation of each chemical mechanism | 86 |
| Table 20: Auto-ignition temperatures of CO with different percentage of hydrogen | 101 |
| Table 21: Global warming potential of three greenhouse gases | 103 |
| Table 22: Low heating value of biofuel components [121] | 105 |
| Table 23: the general effect of each parameter on auto-ignition properties | 115 |
| Table 24: optimized fuel mixture in auto-ignition point of view | 116 |
| Table 25: optimized fuel mixture in auto-ignition point of view | 141 |
| Table 26: Effect of parameters on the non-dimensional numbers Da and Ka | 153 |
| Table 27: Mixtures to study by direct visualization | 155 |
| Table 28: Summary of the injection system proprieties | 163 |
| Table 29: The number of acquired images for each delay time | 164 |
| Table 30 : Registered images for each delay by the two laser heads | 169 |
| Table 31: Composition of lignocellulose in several sources on a dry basis[158] | 175 |
| Table 32: Argon and Oxygen proportions for different end of compression temperatures | 189 |
| Table 33 : Experimental test conditions of the combustion of solid biomass | 190 |
| Table 34: Temperature decomposition of cornstarch in literature | 191 |

| | |
|--|-----|
| Table 35: Characteristic parameters of particle combustion for Test 1 (a, b, and c) and Test 2.. | 196 |
| <i>Table 36</i> : Characteristic parameters of particle combustion for Test 3 (a and b)..... | 198 |
| <i>Table 37</i> : Characteristic parameters of particle combustion for Test 4 and Test 5..... | 199 |
| Table 38: Studied mixtures with direct visualization..... | 209 |
| Table 39: Average and standard deviations of u' and lt | 214 |
| Table 40: Operational conditions of Mixtures 1,2, and 3..... | 216 |
| Table 41:Operational conditions of Mixtures 4,5, and 6..... | 216 |
| Table 42: Operational conditions of Mixtures 7-11 | 218 |
| Table 43: Biogas/syngas mixtures studied with solid biomass particles..... | 235 |
| Table 44: Combustion characteristics of the three injection tests..... | 237 |
| Table 45: Combustion characteristics of the mixture 14 with two injection tests | 241 |
| Table 46: Combustion characteristics of the mixture 15 with four injection tests..... | 247 |

Appendix Chapter 3

I. Sensitivity analysis

1. Mathematical approach

From a mathematical point of view, if the output of the model studied is Y , its sensitivity to an input factor X_i is simply [200]:

$$Y(X_i) = \frac{\partial Y}{\partial X_i} \quad (0.1)$$

Sensitivity analysis of a parameter solution Y of a certain model makes it possible to understand quantitatively the link between this solution and the different parameters contained in this model. [201]

In other words, it is the study of how the different input variations of a mathematical model influence the variability of its output.

Sensitivity analysis methods have several applications in the world of science. Their main applications are to simplify the physical models being studied and to explore the impact of various input assumptions.

Sensitivity measures can be efficiently computed by a range of techniques, from automated differentiation (where sensitivities are calculated with minimal run-time) to direct methods. (These methods are detailed in [200])

To this end, two approaches to sensitivities can be encountered: The local and the global sensibility.

These two principles of sensitivities, as well as the methods used in the literature to calculate them, are presented in the following section.

2. Local sensitivity

The majority of sensitivity analyses encountered in chemistry and physics are local and based on derivatives. Local sensitivities are useful for various applications, such as understanding the reaction path, the mechanism or the steps that determine the speed of reactions. They are also used in order to comprehend the complex phenomenology of combustion.

If we consider a system modeled by the continuous scalar function ϕ , which is an application of a variable X from a p -dimensional plane to an output variable Y in the real plane, we can see that the system is of a continuous scalar function. [202]

$$\varphi: \mathbb{R}^p \rightarrow \mathbb{R} \quad (0.2)$$

$$X = (X^{(1)}, X^{(2)}, \dots, X^{(p)}) \rightarrow Y = \varphi(X) \quad (0.3)$$

By definition, local sensitivity analyzes how a small disturbance close to an input space value:

$$x^0 = (x_1^0, \dots, x_p^0) \quad (0.4)$$

Influences the value of:

$$y = \varphi(x^0). \quad (0.5)$$

It consists of estimating:

$$A_i = \frac{\partial y}{\partial x_i}(x_1^0, \dots, x_p^0) \quad (0.6)$$

Which characterizes the effect of a disturbance on the input close to a nominal value on the random output value Y .

A classical approach to derive this quantity is to consider the OAT method [203] (detailed in the work of Saltelli et al. [200]).

3. Global sensitivity

The overall sensitivity analysis focuses on the variance of the output of the Y model and more specifically on how the input variability affects the output variance. This allows us to determine which parts of the output variance are due to the different inputs using Sobol index estimation.

These indices are a central tool in sensitivity analysis because they provide a quantitative and rigorous overview of how different inputs affect the output.

To apply the methods of global sensitivity analysis, the scalar function φ is considered to be defined on the integral

$$Y = \varphi(X) = \varphi_0 + \sum_{i=1}^p \varphi_i(X^{(i)}) + \sum_{i \leq 1 < j \leq p} \varphi_{i,j}(X^{(i)}, X^{(j)}) + \dots + \varphi_{1 \dots p}(X^{(1)}, \dots, X^{(p)}) \quad (0.7)$$

Applying the variance on this equation gives:

$$\text{Var}(Y) = V = \sum_{i=1}^p V_i + \sum_{i \leq 1 < j \leq p} V_{i,j} + \dots + V_{1 \dots p} \quad (0.8)$$

First-order sensitivity indices calculated for the variables $X(i)$

$$S_i = \frac{V_i}{V} = \frac{\text{Var}(E(Y|X^{(i)}))}{\text{Var}(Y)} \quad (0.9)$$

With E

Also, the sensitivity indices calculated in the second-order by the derivation of the variables $X^{(i)}$ and $X^{(j)}$ are:

$$S_{ij} = \frac{V_{ij}}{V} \quad (0.10)$$

In the same way, higher-order sensitivity indices will be interpreted.

According to these relationships, the closer the value of S_i is to unity, the greater the influence of variable $X^{(i)}$ on Y . As the input dimension increases, the number of Sobol indices increases exponentially and, therefore, the estimation of all these indices is impossible.

Thus, total sensitivity indices are then entered for each variable $X^{(i)}$:

$$S_{Ti} = \sum_k S_k \quad (0.11)$$

$$S_{Ti} = S_1 + S_{12} + S_{13} + S_{123} \quad (0.12)$$

These indices are normally estimated by the Monte Carlos correlation [202].

4. Sensitivity analysis on Chemkin-Pro

The first-order sensitivity coefficients used on Chemkin-Pro are those of gas temperature, species fractions and, where applicable, raw phase growth rates. They are calculated with the reaction rate coefficients.

The sensitivity analysis methods thus performed exploit the fact that the differential equations describing the sensitivity coefficients are linear, regardless of the non-linearity of the model problem itself [204].

These methods will be presented in the following for steady-state and transient regimes.

4.1. Sensitivity analysis for stationary solutions

Sensitivity coefficients are easily calculated in steady-state from the Jacobian calculation necessary to solve non-linear equations.

Moreover, the basic steady-state equations depend on both the solution vector and a set of model parameters:

$$F(\varphi(\alpha); \alpha) = 0 \quad (0.13)$$

With α the pre-exponential factors in Arrhenius' reaction speed expressions, and φ the solution vector.

The derivative of this basic equation with respect to α gives the following matrix equation for the sensitivity coefficients:

$$\frac{\partial F}{\partial \varphi} \frac{\partial \varphi}{\partial \alpha} + \frac{\partial F}{\partial \alpha} = 0 \quad (0.14)$$

$\frac{\partial F}{\partial \varphi}$ is the Jacobian matrix of the original system and $\frac{\partial F}{\partial \alpha}$ is that of partial derivatives of F with the parameters. The sensitivity coefficient matrix defined as $\frac{\partial \varphi}{\partial \alpha}$ contains quantitative information on how each reaction rate coefficient affects temperature and species fractions.

Each column of this matrix contains the dependence of the solution vector on a particular chemical reaction.

The resolution of the linear system of equations is easily performed knowing that the Jacobian and its LU factorization are already available from the solution of the original system (by Newton's method). The parameter derivatives are calculated similarly to the Jacobian calculation.

Sensitivity analysis for unsteady solutions

Just like the steady-state calculation, the sensitivity coefficients for the transient regime are calculated from the Jacobian of the model.

The sensitivity equations, in this case, are solved simultaneously with the dependent variables of the solution itself; so that the system of ordinary differential equations describing the physical problem is of the general form

$$F(\varphi, t, \alpha) = \frac{d\varphi}{dt} \quad (0.15)$$

With α the pre-exponential factors in Arrhenius reaction rate expressions and φ the vector of temperatures, mass fractions, surface site fractions, and bulk activities.

The first-order sensitivity coefficient matrix is defined as follows:

$$w_{j,i} = \frac{\partial \varphi_j}{\partial \alpha_i} \quad (0.16)$$

Where the subscripts i and j refer to the variables and dependent responses, respectively.

The derivative of this matrix with respect to the parameters gives the equation

$$\frac{dw_{j,i}}{dt} = \frac{\partial F}{\partial \varphi} w_{i,j} + \frac{\partial F_j}{\partial \alpha_i} \quad (0.17)$$

Similar to the steady-state case, this differential equation of the sensitivity coefficients is first considered linear even if it is not linear; the non-linearity will be easily corrected later in the computation as Newton's iteration for the correction step converges into a single iteration.

It is important to note that for a given moment, the sensitivity calculated in the transient state is calculated in the same way as the local sensitivity described in the steady-state.

In other words, the sensitivities are not integrated over time but are based solely on the local conditions at each time step.

To make the sensitivity coefficients more meaningful, they will be normalized and presented in logarithmic form.

$$\frac{\partial \ln Y_k}{\partial \ln \alpha_i} = \frac{\alpha_i \partial Y_k}{Y_k \partial \alpha_i} \quad (0.18)$$

For example, if the sensitivity studied is that of the gas temperature, the normalized sensitivity coefficients will be:

$$\frac{\partial \ln T}{\partial \ln \alpha_i} = \frac{\alpha_i \partial T}{T \partial \alpha_i} \quad (0.19)$$

For molar fractions of k species:

$$\frac{\partial \ln X_b^k}{\partial \ln \alpha_i} = \frac{\alpha_i \partial Y_k}{X_b^k \partial \alpha_i} \quad (0.20)$$

5. Combustion applications

Combustion is a very complex phenomenon characterized by the interaction and competition of various physical and chemical processes. The chemistry of combustion processes is described by a large number of parameters and therefore, sensitivity analysis is very useful for its understanding.

There are many applications of sensitivity analysis in the literature; the local sensitivity approach is used for all of these applications, yet the method with which the analysis has been performed may be different.

The local sensitivity matrix calculated on the Chemkin-Pro takes into account the change in a single variable (concentration of a species) as a result of the change in individual parameters (reaction rates).

Some authors study sensitivity analysis with one or more species; they generally choose the OH reactive radical, and sometimes the CH₃, H, HCO, etc. radicals [79], [205].

However, in many cases, it is interesting to investigate the effect of a parameter change on the concentrations of several species. This effect can be interpreted as the sensitivity of an objective function value. It is defined as the sum of the squares of the differences in the normalized sensitivity coefficients of the different concentrations. This sensitivity value, referred to as the total sensitivity [206] can easily be calculated from the normalized local sensitivities:

$$B_j = \sum_i \left(\frac{\partial \ln c_i}{\partial \ln k_j} \right)^2 \quad (0.21)$$

Where the summation *i* is done on all the species present in the group studied.

This sensitivity calculation shows the effect of individual parameter changes (the speed of a reaction in our case) on the calculated concentrations. Which makes it possible to find the main reactions taking place at the chosen time. This calculation was used by Turanyi [207] in his study on the combustion of the hydrogen mixture on the Chemkin software (with the Kinalc extension).

6. the case of our study

In our study, different input parameters are considered: temperature, pressure, richness, time or moment of the sensitivity analysis study, concentrations of the parameters, and reaction rates of the different reactions).

These components influence the results of the simulation, thus the output parameters the concentrations of the species in our case.

The sensitivity analysis is the study that will be able to find the input parameters that have the most influence on the self-ignition time of the reaction, while classifying them according to their influence on the output parameters.

However, the sensitivity analysis on Chemkin-Pro allows the calculation of the local sensitivity of species concentrations to reaction rates.

The question that arises is: which species should be used to study the sensitivity analysis?

Indeed, the main concentrations that govern self-ignition in HCCI mode are normally: H, OH, H₂O₂ and HO₂ (hydrogen, hydroxyl, hydrogen peroxide, and hydro-peroxide respectively): During the compression phase, H₂O₂ and HO₂ concentrations increase progressively with increasing pressure

and temperature. These two radicals also control the reactions at low temperatures (cold flame reactions).

The decomposition of H_2O_2 into OH radicals will take place at temperatures between 1050 and 1100 K. The OH radicals thus produced reacts rapidly with the fuel molecules and produce water and heat; at this stage, self-ignition is triggered and high-temperature reactions take place.

Finally, the concentrations of H and OH radicals increase very rapidly during self-ignition, while the H_2O_2 concentration decreases [104].

Thus, the study of the sensitivity of the concentrations of these radicals could be a good indicator of the sensitivity coefficients of the self-ignition times: a negative sensitivity of these concentrations means that they tend to disappear when the reaction speed i increases. This implies a positive self-ignition sensitivity coefficient with this reaction i .

Application example:

The general sensitivity calculation method is applied for the main radicals of methane combustion in HCCI mode: H, OH, HCO and H_2O_2 .

This analysis is done for the CH_4 mixture diluted with 70% nitrogen and argon, with a richness of 0.6, a pressure of 15 bars, and a temperature of 985 K, a few moments before self-ignition.

The sum of the squares of the normalized sensitivity coefficients of the concentrations of these radicals makes it possible to find the ten main reactions that most influence the concentration of these radicals for these conditions. (Total sensitivity detailed in the main part);

Chemical mechanism of Grimech3.0

| Reaction number | Reaction equation | | | |
|-----------------|---|----------|------|---------|
| 1 | $2\text{O} + (\text{M}) \rightleftharpoons \text{O}_2 + (\text{M})$ | 1.20E+17 | -1.0 | 0.0 |
| 2 | $\text{O} + \text{H} + (\text{M}) \rightleftharpoons \text{OH} + (\text{M})$ | 5.00E+17 | -1.0 | 0.0 |
| 3 | $\text{O} + \text{H}_2 \rightleftharpoons \text{H} + \text{OH}$ | 3.87E+04 | 2.7 | 6260.0 |
| 4 | $\text{O} + \text{HO}_2 \rightleftharpoons \text{OH} + \text{O}_2$ | 2.00E+13 | 0.0 | 0.0 |
| 5 | $\text{O} + \text{H}_2\text{O}_2 \rightleftharpoons \text{OH} + \text{HO}_2$ | 9.63E+06 | 2.0 | 4000.0 |
| 6 | $\text{O} + \text{CH} \rightleftharpoons \text{H} + \text{CO}$ | 5.70E+13 | 0.0 | 0.0 |
| 7 | $\text{O} + \text{CH}_2 \rightleftharpoons \text{H} + \text{HCO}$ | 8.00E+13 | 0.0 | 0.0 |
| 8 | $\text{O} + \text{CH}_2(\text{s}) \rightleftharpoons \text{H}_2 + \text{CO}$ | 1.50E+13 | 0.0 | 0.0 |
| 9 | $\text{O} + \text{CH}_2(\text{s}) \rightleftharpoons \text{H} + \text{HCO}$ | 1.50E+13 | 0.0 | 0.0 |
| 10 | $\text{O} + \text{CH}_3 \rightleftharpoons \text{H} + \text{CH}_2\text{O}$ | 5.06E+13 | 0.0 | 0.0 |
| 11 | $\text{O} + \text{CH}_4 \rightleftharpoons \text{OH} + \text{CH}_3$ | 1.02E+09 | 1.5 | 8600.0 |
| 12 | $\text{O} + \text{CO} + (\text{M}) \rightleftharpoons \text{CO}_2 + (\text{M})$ | 1.80E+10 | 0.0 | 2385.0 |
| 13 | $\text{O} + \text{HCO} \rightleftharpoons \text{OH} + \text{CO}$ | 3.00E+13 | 0.0 | 0.0 |
| 14 | $\text{O} + \text{HCO} \rightleftharpoons \text{H} + \text{CO}_2$ | 3.00E+13 | 0.0 | 0.0 |
| 15 | $\text{O} + \text{CH}_2\text{O} \rightleftharpoons \text{OH} + \text{HCO}$ | 3.90E+13 | 0.0 | 3540.0 |
| 16 | $\text{O} + \text{CH}_2\text{OH} \rightleftharpoons \text{OH} + \text{CH}_2\text{O}$ | 1.00E+13 | 0.0 | 0.0 |
| 17 | $\text{O} + \text{CH}_3\text{O} \rightleftharpoons \text{OH} + \text{CH}_2\text{O}$ | 1.00E+13 | 0.0 | 0.0 |
| 18 | $\text{O} + \text{CH}_3\text{OH} \rightleftharpoons \text{OH} + \text{CH}_2\text{OH}$ | 3.88E+05 | 2.5 | 3100.0 |
| 19 | $\text{O} + \text{CH}_3\text{OH} \rightleftharpoons \text{OH} + \text{CH}_3\text{O}$ | 1.30E+05 | 2.5 | 5000.0 |
| 20 | $\text{O} + \text{C}_2\text{H} \rightleftharpoons \text{CH} + \text{CO}$ | 5.00E+13 | 0.0 | 0.0 |
| 21 | $\text{O} + \text{C}_2\text{H}_2 \rightleftharpoons \text{H} + \text{HCCO}$ | 1.35E+07 | 2.0 | 1900.0 |
| 22 | $\text{O} + \text{C}_2\text{H}_2 \rightleftharpoons \text{OH} + \text{C}_2\text{H}$ | 4.60E+19 | -1.4 | 28950.0 |
| 23 | $\text{O} + \text{C}_2\text{H}_2 \rightleftharpoons \text{CO} + \text{CH}_2$ | 6.94E+06 | 2.0 | 1900.0 |
| 24 | $\text{O} + \text{C}_2\text{H}_3 \rightleftharpoons \text{H} + \text{CH}_2\text{CO}$ | 3.00E+13 | 0.0 | 0.0 |

| | | | | |
|----|---|----------|------|---------|
| 25 | $O + C_2H_4 \rightleftharpoons CH_3 + HCO$ | 1.25E+07 | 1.8 | 220.0 |
| 26 | $O + C_2H_5 \rightleftharpoons CH_3 + CH_2O$ | 2.24E+13 | 0.0 | 0.0 |
| 27 | $O + C_2H_6 \rightleftharpoons OH + C_2H_5$ | 8.98E+07 | 1.9 | 5690.0 |
| 28 | $O + HCCO \rightleftharpoons H + 2CO$ | 1.00E+14 | 0.0 | 0.0 |
| 29 | $O + CH_2CO \rightleftharpoons OH + HCCO$ | 1.00E+13 | 0.0 | 8000.0 |
| 30 | $O + CH_2CO \rightleftharpoons CH_2 + CO_2$ | 1.75E+12 | 0.0 | 1350.0 |
| 31 | $O_2 + CO \rightleftharpoons O + CO_2$ | 2.50E+12 | 0.0 | 47800.0 |
| 32 | $O_2 + CH_2O \rightleftharpoons HO_2 + HCO$ | 1.00E+14 | 0.0 | 40000.0 |
| 33 | $H + O_2 + (M) \rightleftharpoons HO_2 + (M)$ | 2.80E+18 | -0.9 | 0.0 |
| 34 | $H + 2O_2 \rightleftharpoons HO_2 + O_2$ | 2.08E+19 | -1.2 | 0.0 |
| 35 | $H + O_2 + H_2O \rightleftharpoons HO_2 + H_2O$ | 1.13E+19 | -0.8 | 0.0 |
| 36 | $H + O_2 + N_2 \rightleftharpoons HO_2 + N_2$ | 2.60E+19 | -1.2 | 0.0 |
| 37 | $H + O_2 + Ar \rightleftharpoons HO_2 + Ar$ | 7.00E+17 | -0.8 | 0.0 |
| 38 | $H + O_2 \rightleftharpoons O + OH$ | 2.65E+16 | -0.7 | 17041.0 |
| 39 | $2H + (M) \rightleftharpoons H_2 + (M)$ | 1.00E+18 | -1.0 | 0.0 |
| 40 | $2H + H_2 \rightleftharpoons 2H_2$ | 9.00E+16 | -0.6 | 0.0 |
| 41 | $2H + H_2O \rightleftharpoons H_2 + H_2O$ | 6.00E+19 | -1.2 | 0.0 |
| 42 | $2H + CO_2 \rightleftharpoons H_2 + CO_2$ | 5.50E+20 | -2.0 | 0.0 |
| 43 | $H + OH + (M) \rightleftharpoons H_2O + (M)$ | 2.20E+22 | -2.0 | 0.0 |
| 44 | $H + HO_2 \rightleftharpoons O + H_2O$ | 3.97E+12 | 0.0 | 671.0 |
| 45 | $H + HO_2 \rightleftharpoons O_2 + H_2$ | 4.48E+13 | 0.0 | 1068.0 |
| 46 | $H + HO_2 \rightleftharpoons 2OH$ | 8.40E+13 | 0.0 | 635.0 |
| 47 | $H + H_2O_2 \rightleftharpoons HO_2 + H_2$ | 1.21E+07 | 2.0 | 5200.0 |
| 48 | $H + H_2O_2 \rightleftharpoons OH + H_2O$ | 1.00E+13 | 0.0 | 3600.0 |
| 49 | $H + CH \rightleftharpoons C + H_2$ | 1.65E+14 | 0.0 | 0.0 |
| 50 | $H + CH_2 + (M) \rightleftharpoons CH_3 + (M)$ | 6.00E+14 | 0.0 | 0.0 |
| 51 | $H + CH_2(s) \rightleftharpoons CH + H_2$ | 3.00E+13 | 0.0 | 0.0 |
| 52 | $H + CH_3 + (M) \rightleftharpoons CH_4 + (M)$ | 1.39E+16 | -0.5 | 536.0 |

| | | | | |
|----|---|----------|------|---------|
| 53 | $\text{H} + \text{CH}_4 \rightleftharpoons \text{CH}_3 + \text{H}_2$ | 6.60E+08 | 1.6 | 10840.0 |
| 54 | $\text{H} + \text{HCO} + (\text{M}) \rightleftharpoons \text{CH}_2\text{O} + (\text{M})$ | 1.09E+12 | 0.5 | -260.0 |
| 55 | $\text{H} + \text{HCO} \rightleftharpoons \text{H}_2 + \text{CO}$ | 7.34E+13 | 0.0 | 0.0 |
| 56 | $\text{H} + \text{CH}_2\text{O} + (\text{M}) \rightleftharpoons \text{CH}_2\text{OH} + (\text{M})$ | 5.40E+11 | 0.5 | 3600.0 |
| 57 | $\text{H} + \text{CH}_2\text{O} + (\text{M}) \rightleftharpoons \text{CH}_3\text{O} + (\text{M})$ | 5.40E+11 | 0.5 | 2600.0 |
| 58 | $\text{H} + \text{CH}_2\text{O} \rightleftharpoons \text{HCO} + \text{H}_2$ | 5.74E+07 | 1.9 | 2742.0 |
| 59 | $\text{H} + \text{CH}_2\text{OH} + (\text{M}) \rightleftharpoons \text{CH}_3\text{OH} + (\text{M})$ | 1.06E+12 | 0.5 | 86.0 |
| 60 | $\text{H} + \text{CH}_2\text{OH} \rightleftharpoons \text{H}_2 + \text{CH}_2\text{O}$ | 2.00E+13 | 0.0 | 0.0 |
| 61 | $\text{H} + \text{CH}_2\text{OH} \rightleftharpoons \text{OH} + \text{CH}_3$ | 1.65E+11 | 0.7 | -284.0 |
| 62 | $\text{H} + \text{CH}_2\text{OH} \rightleftharpoons \text{CH}_2(\text{s}) + \text{H}_2\text{O}$ | 3.28E+13 | -0.1 | 610.0 |
| 63 | $\text{H} + \text{CH}_3\text{O} + (\text{M}) \rightleftharpoons \text{CH}_3\text{OH} + (\text{M})$ | 2.43E+12 | 0.5 | 50.0 |
| 64 | $\text{H} + \text{CH}_3\text{O} \rightleftharpoons \text{H} + \text{CH}_2\text{OH}$ | 4.15E+07 | 1.6 | 1924.0 |
| 65 | $\text{H} + \text{CH}_3\text{O} \rightleftharpoons \text{H}_2 + \text{CH}_2\text{O}$ | 2.00E+13 | 0.0 | 0.0 |
| 66 | $\text{H} + \text{CH}_3\text{O} \rightleftharpoons \text{OH} + \text{CH}_3$ | 1.50E+12 | 0.5 | -110.0 |
| 67 | $\text{H} + \text{CH}_3\text{O} \rightleftharpoons \text{CH}_2(\text{s}) + \text{H}_2\text{O}$ | 2.62E+14 | -0.2 | 1070.0 |
| 68 | $\text{H} + \text{CH}_3\text{OH} \rightleftharpoons \text{CH}_2\text{OH} + \text{H}_2$ | 1.70E+07 | 2.1 | 4870.0 |
| 69 | $\text{H} + \text{CH}_3\text{OH} \rightleftharpoons \text{CH}_3\text{O} + \text{H}_2$ | 4.20E+06 | 2.1 | 4870.0 |
| 70 | $\text{H} + \text{C}_2\text{H} + (\text{M}) \rightleftharpoons \text{C}_2\text{H}_2 + (\text{M})$ | 1.00E+17 | -1.0 | 0.0 |
| 71 | $\text{H} + \text{C}_2\text{H}_2 + (\text{M}) \rightleftharpoons \text{C}_2\text{H}_3 + (\text{M})$ | 5.60E+12 | 0.0 | 2400.0 |
| 72 | $\text{H} + \text{C}_2\text{H}_3 + (\text{M}) \rightleftharpoons \text{C}_2\text{H}_4 + (\text{M})$ | 6.08E+12 | 0.3 | 280.0 |
| 73 | $\text{H} + \text{C}_2\text{H}_3 \rightleftharpoons \text{H}_2 + \text{C}_2\text{H}_2$ | 3.00E+13 | 0.0 | 0.0 |
| 74 | $\text{H} + \text{C}_2\text{H}_4 + (\text{M}) \rightleftharpoons \text{C}_2\text{H}_5 + (\text{M})$ | 5.40E+11 | 0.5 | 1820.0 |
| 75 | $\text{H} + \text{C}_2\text{H}_4 \rightleftharpoons \text{C}_2\text{H}_3 + \text{H}_2$ | 1.32E+06 | 2.5 | 12240.0 |
| 76 | $\text{H} + \text{C}_2\text{H}_5 + (\text{M}) \rightleftharpoons \text{C}_2\text{H}_6 + (\text{M})$ | 5.21E+17 | -1.0 | 1580.0 |
| 77 | $\text{H} + \text{C}_2\text{H}_5 \rightleftharpoons \text{H}_2 + \text{C}_2\text{H}_4$ | 2.00E+12 | 0.0 | 0.0 |
| 78 | $\text{H} + \text{C}_2\text{H}_6 \rightleftharpoons \text{C}_2\text{H}_5 + \text{H}_2$ | 1.15E+08 | 1.9 | 7530.0 |
| 79 | $\text{H} + \text{HCCO} \rightleftharpoons \text{CH}_2(\text{s}) + \text{CO}$ | 1.00E+14 | 0.0 | 0.0 |
| 80 | $\text{H} + \text{CH}_2\text{CO} \rightleftharpoons \text{HCCO} + \text{H}_2$ | 5.00E+13 | 0.0 | 8000.0 |

| | | | | |
|-----|---|----------|------|---------|
| 81 | $\text{H} + \text{CH}_2\text{CO} \rightleftharpoons \text{CH}_3 + \text{CO}$ | 1.13E+13 | 0.0 | 3428.0 |
| 82 | $\text{H} + \text{HCCOH} \rightleftharpoons \text{H} + \text{CH}_2\text{CO}$ | 1.00E+13 | 0.0 | 0.0 |
| 83 | $\text{H}_2 + \text{CO} + (\text{M}) \rightleftharpoons \text{CH}_2\text{O} + (\text{M})$ | 4.30E+07 | 1.5 | 79600.0 |
| 84 | $\text{OH} + \text{H}_2 \rightleftharpoons \text{H} + \text{H}_2\text{O}$ | 2.16E+08 | 1.5 | 3430.0 |
| 85 | $2\text{OH} + (\text{M}) \rightleftharpoons \text{H}_2\text{O}_2 + (\text{M})$ | 7.40E+13 | -0.4 | 0.0 |
| 86 | $2\text{OH} \rightleftharpoons \text{O} + \text{H}_2\text{O}$ | 3.57E+04 | 2.4 | -2110.0 |
| 87 | $\text{OH} + \text{HO}_2 \rightleftharpoons \text{O}_2 + \text{H}_2\text{O}$ | 1.45E+13 | 0.0 | -500.0 |
| 88 | $\text{OH} + \text{H}_2\text{O}_2 \rightleftharpoons \text{HO}_2 + \text{H}_2\text{O}$ | 2.00E+12 | 0.0 | 427.0 |
| 89 | $\text{OH} + \text{H}_2\text{O}_2 \rightleftharpoons \text{HO}_2 + \text{H}_2\text{O}$ | 1.70E+18 | 0.0 | 29410.0 |
| 90 | $\text{OH} + \text{C} \rightleftharpoons \text{H} + \text{CO}$ | 5.00E+13 | 0.0 | 0.0 |
| 91 | $\text{OH} + \text{CH} \rightleftharpoons \text{H} + \text{HCO}$ | 3.00E+13 | 0.0 | 0.0 |
| 92 | $\text{OH} + \text{CH}_2 \rightleftharpoons \text{H} + \text{CH}_2\text{O}$ | 2.00E+13 | 0.0 | 0.0 |
| 93 | $\text{OH} + \text{CH}_2 \rightleftharpoons \text{CH} + \text{H}_2\text{O}$ | 1.13E+07 | 2.0 | 3000.0 |
| 94 | $\text{OH} + \text{CH}_2(\text{s}) \rightleftharpoons \text{H} + \text{CH}_2\text{O}$ | 3.00E+13 | 0.0 | 0.0 |
| 95 | $\text{OH} + \text{CH}_3 + (\text{M}) \rightleftharpoons \text{CH}_3\text{OH} + (\text{M})$ | 2.79E+18 | -1.4 | 1330.0 |
| 96 | $\text{OH} + \text{CH}_3 \rightleftharpoons \text{CH}_2 + \text{H}_2\text{O}$ | 5.60E+07 | 1.6 | 5420.0 |
| 97 | $\text{OH} + \text{CH}_3 \rightleftharpoons \text{CH}_2(\text{s}) + \text{H}_2\text{O}$ | 6.44E+17 | -1.3 | 1417.0 |
| 98 | $\text{OH} + \text{CH}_4 \rightleftharpoons \text{CH}_3 + \text{H}_2\text{O}$ | 1.00E+08 | 1.6 | 3120.0 |
| 99 | $\text{OH} + \text{CO} \rightleftharpoons \text{H} + \text{CO}_2$ | 4.76E+07 | 1.2 | 70.0 |
| 100 | $\text{OH} + \text{HCO} \rightleftharpoons \text{H}_2\text{O} + \text{CO}$ | 5.00E+13 | 0.0 | 0.0 |
| 101 | $\text{OH} + \text{CH}_2\text{O} \rightleftharpoons \text{HCO} + \text{H}_2\text{O}$ | 3.43E+09 | 1.2 | -447.0 |
| 102 | $\text{OH} + \text{CH}_2\text{OH} \rightleftharpoons \text{H}_2\text{O} + \text{CH}_2\text{O}$ | 5.00E+12 | 0.0 | 0.0 |
| 103 | $\text{OH} + \text{CH}_3\text{O} \rightleftharpoons \text{H}_2\text{O} + \text{CH}_2\text{O}$ | 5.00E+12 | 0.0 | 0.0 |
| 104 | $\text{OH} + \text{CH}_3\text{OH} \rightleftharpoons \text{CH}_2\text{OH} + \text{H}_2\text{O}$ | 1.44E+06 | 2.0 | -840.0 |
| 105 | $\text{OH} + \text{CH}_3\text{OH} \rightleftharpoons \text{CH}_3\text{O} + \text{H}_2\text{O}$ | 6.30E+06 | 2.0 | 1500.0 |
| 106 | $\text{OH} + \text{C}_2\text{H} \rightleftharpoons \text{H} + \text{HCCO}$ | 2.00E+13 | 0.0 | 0.0 |
| 107 | $\text{OH} + \text{C}_2\text{H}_2 \rightleftharpoons \text{H} + \text{CH}_2\text{CO}$ | 2.18E-04 | 4.5 | -1000.0 |
| 108 | $\text{OH} + \text{C}_2\text{H}_2 \rightleftharpoons \text{H} + \text{HCCOH}$ | 5.04E+05 | 2.3 | 13500.0 |

| | | | | |
|-----|---|----------|-----|---------|
| 109 | $\text{OH} + \text{C}_2\text{H}_2 \rightleftharpoons \text{C}_2\text{H} + \text{H}_2\text{O}$ | 3.37E+07 | 2.0 | 14000.0 |
| 110 | $\text{OH} + \text{C}_2\text{H}_2 \rightleftharpoons \text{CH}_3 + \text{CO}$ | 4.83E-04 | 4.0 | -2000.0 |
| 111 | $\text{OH} + \text{C}_2\text{H}_3 \rightleftharpoons \text{H}_2\text{O} + \text{C}_2\text{H}_2$ | 5.00E+12 | 0.0 | 0.0 |
| 112 | $\text{OH} + \text{C}_2\text{H}_4 \rightleftharpoons \text{C}_2\text{H}_3 + \text{H}_2\text{O}$ | 3.60E+06 | 2.0 | 2500.0 |
| 113 | $\text{OH} + \text{C}_2\text{H}_6 \rightleftharpoons \text{C}_2\text{H}_5 + \text{H}_2\text{O}$ | 3.54E+06 | 2.1 | 870.0 |
| 114 | $\text{OH} + \text{CH}_2\text{CO} \rightleftharpoons \text{HCCO} + \text{H}_2\text{O}$ | 7.50E+12 | 0.0 | 2000.0 |
| 115 | $2\text{HO}_2 \rightleftharpoons \text{O}_2 + \text{H}_2\text{O}_2$ | 1.30E+11 | 0.0 | -1630.0 |
| 116 | $2\text{HO}_2 \rightleftharpoons \text{O}_2 + \text{H}_2\text{O}_2$ | 4.20E+14 | 0.0 | 12000.0 |
| 117 | $\text{HO}_2 + \text{CH}_2 \rightleftharpoons \text{OH} + \text{CH}_2\text{O}$ | 2.00E+13 | 0.0 | 0.0 |
| 118 | $\text{HO}_2 + \text{CH}_3 \rightleftharpoons \text{O}_2 + \text{CH}_4$ | 1.00E+12 | 0.0 | 0.0 |
| 119 | $\text{HO}_2 + \text{CH}_3 \rightleftharpoons \text{OH} + \text{CH}_3\text{O}$ | 3.78E+13 | 0.0 | 0.0 |
| 120 | $\text{HO}_2 + \text{CO} \rightleftharpoons \text{OH} + \text{CO}_2$ | 1.50E+14 | 0.0 | 23600.0 |
| 121 | $\text{HO}_2 + \text{CH}_2\text{O} \rightleftharpoons \text{HCO} + \text{H}_2\text{O}_2$ | 5.60E+06 | 2.0 | 12000.0 |
| 122 | $\text{C} + \text{O}_2 \rightleftharpoons \text{O} + \text{CO}$ | 5.80E+13 | 0.0 | 576.0 |
| 123 | $\text{C} + \text{CH}_2 \rightleftharpoons \text{H} + \text{C}_2\text{H}$ | 5.00E+13 | 0.0 | 0.0 |
| 124 | $\text{C} + \text{CH}_3 \rightleftharpoons \text{H} + \text{C}_2\text{H}_2$ | 5.00E+13 | 0.0 | 0.0 |
| 125 | $\text{CH} + \text{O}_2 \rightleftharpoons \text{O} + \text{HCO}$ | 6.71E+13 | 0.0 | 0.0 |
| 126 | $\text{CH} + \text{H}_2 \rightleftharpoons \text{H} + \text{CH}_2$ | 1.08E+14 | 0.0 | 3110.0 |
| 127 | $\text{CH} + \text{H}_2\text{O} \rightleftharpoons \text{H} + \text{CH}_2\text{O}$ | 5.71E+12 | 0.0 | -755.0 |
| 128 | $\text{CH} + \text{CH}_2 \rightleftharpoons \text{H} + \text{C}_2\text{H}_2$ | 4.00E+13 | 0.0 | 0.0 |
| 129 | $\text{CH} + \text{CH}_3 \rightleftharpoons \text{H} + \text{C}_2\text{H}_3$ | 3.00E+13 | 0.0 | 0.0 |
| 130 | $\text{CH} + \text{CH}_4 \rightleftharpoons \text{H} + \text{C}_2\text{H}_4$ | 6.00E+13 | 0.0 | 0.0 |
| 131 | $\text{CH} + \text{CO} + (\text{M}) \rightleftharpoons \text{HCCO} + (\text{M})$ | 5.00E+13 | 0.0 | 0.0 |
| 132 | $\text{CH} + \text{CO}_2 \rightleftharpoons \text{HCO} + \text{CO}$ | 1.90E+14 | 0.0 | 15792.0 |
| 133 | $\text{CH} + \text{CH}_2\text{O} \rightleftharpoons \text{H} + \text{CH}_2\text{CO}$ | 9.46E+13 | 0.0 | -515.0 |
| 134 | $\text{CH} + \text{HCCO} \rightleftharpoons \text{CO} + \text{C}_2\text{H}_2$ | 5.00E+13 | 0.0 | 0.0 |
| 135 | $\text{CH}_2 + \text{O}_2 \rightleftharpoons \text{OH} + \text{H} + \text{CO}$ | 5.00E+12 | 0.0 | 1500.0 |
| 136 | $\text{CH}_2 + \text{H}_2 \rightleftharpoons \text{H} + \text{CH}_3$ | 5.00E+05 | 2.0 | 7230.0 |

| | | | | |
|-----|--|----------|------|---------|
| 137 | $2\text{CH}_2 \rightleftharpoons \text{H}_2 + \text{C}_2\text{H}_2$ | 1.60E+15 | 0.0 | 11944.0 |
| 138 | $\text{CH}_2 + \text{CH}_3 \rightleftharpoons \text{H} + \text{C}_2\text{H}_4$ | 4.00E+13 | 0.0 | 0.0 |
| 139 | $\text{CH}_2 + \text{CH}_4 \rightleftharpoons 2\text{CH}_3$ | 2.46E+06 | 2.0 | 8270.0 |
| 140 | $\text{CH}_2 + \text{CO} + (\text{M}) \rightleftharpoons \text{CH}_2\text{CO} + (\text{M})$ | 8.10E+11 | 0.5 | 4510.0 |
| 141 | $\text{CH}_2 + \text{HCCO} \rightleftharpoons \text{C}_2\text{H}_3 + \text{CO}$ | 3.00E+13 | 0.0 | 0.0 |
| 142 | $\text{CH}_2(\text{s}) + \text{N}_2 \rightleftharpoons \text{CH}_2 + \text{N}_2$ | 1.50E+13 | 0.0 | 600.0 |
| 143 | $\text{CH}_2(\text{s}) + \text{AR} \rightleftharpoons \text{CH}_2 + \text{AR}$ | 9.00E+12 | 0.0 | 600.0 |
| 144 | $\text{CH}_2(\text{s}) + \text{O}_2 \rightleftharpoons \text{H} + \text{OH} + \text{CO}$ | 2.80E+13 | 0.0 | 0.0 |
| 145 | $\text{CH}_2(\text{s}) + \text{O}_2 \rightleftharpoons \text{CO} + \text{H}_2\text{O}$ | 1.20E+13 | 0.0 | 0.0 |
| 146 | $\text{CH}_2(\text{s}) + \text{H}_2 \rightleftharpoons \text{CH}_3 + \text{H}$ | 7.00E+13 | 0.0 | 0.0 |
| 147 | $\text{CH}_2(\text{s}) + \text{H}_2\text{O} + (\text{M}) \rightleftharpoons \text{CH}_3\text{OH} + (\text{M})$ | 4.82E+17 | -1.2 | 1145.0 |
| 148 | $\text{CH}_2(\text{s}) + \text{H}_2\text{O} \rightleftharpoons \text{CH}_2 + \text{H}_2\text{O}$ | 3.00E+13 | 0.0 | 0.0 |
| 149 | $\text{CH}_2(\text{s}) + \text{CH}_3 \rightleftharpoons \text{H} + \text{C}_2\text{H}_4$ | 1.20E+13 | 0.0 | -570.0 |
| 150 | $\text{CH}_2(\text{s}) + \text{CH}_4 \rightleftharpoons 2\text{CH}_3$ | 1.60E+13 | 0.0 | -570.0 |
| 151 | $\text{CH}_2(\text{s}) + \text{CO} \rightleftharpoons \text{CH}_2 + \text{CO}$ | 9.00E+12 | 0.0 | 0.0 |
| 152 | $\text{CH}_2(\text{s}) + \text{CO}_2 \rightleftharpoons \text{CH}_2 + \text{CO}_2$ | 7.00E+12 | 0.0 | 0.0 |
| 153 | $\text{CH}_2(\text{s}) + \text{CO}_2 \rightleftharpoons \text{CO} + \text{CH}_2\text{O}$ | 1.40E+13 | 0.0 | 0.0 |
| 154 | $\text{CH}_2(\text{s}) + \text{C}_2\text{H}_6 \rightleftharpoons \text{CH}_3 + \text{C}_2\text{H}_5$ | 4.00E+13 | 0.0 | -550.0 |
| 155 | $\text{CH}_3 + \text{O}_2 \rightleftharpoons \text{O} + \text{CH}_3\text{O}$ | 3.56E+13 | 0.0 | 30480.0 |
| 156 | $\text{CH}_3 + \text{O}_2 \rightleftharpoons \text{OH} + \text{CH}_2\text{O}$ | 2.31E+12 | 0.0 | 20315.0 |
| 157 | $\text{CH}_3 + \text{H}_2\text{O}_2 \rightleftharpoons \text{HO}_2 + \text{CH}_4$ | 2.45E+04 | 2.5 | 5180.0 |
| 158 | $2\text{CH}_3 + (\text{M}) \rightleftharpoons \text{C}_2\text{H}_6 + (\text{M})$ | 6.77E+16 | -1.2 | 654.0 |
| 159 | $2\text{CH}_3 \rightleftharpoons \text{H} + \text{C}_2\text{H}_5$ | 6.84E+12 | 0.1 | 10600.0 |
| 160 | $\text{CH}_3 + \text{HCO} \rightleftharpoons \text{CH}_4 + \text{CO}$ | 2.65E+13 | 0.0 | 0.0 |
| 161 | $\text{CH}_3 + \text{CH}_2\text{O} \rightleftharpoons \text{HCO} + \text{CH}_4$ | 3.32E+03 | 2.8 | 5860.0 |
| 162 | $\text{CH}_3 + \text{CH}_3\text{OH} \rightleftharpoons \text{CH}_2\text{OH} + \text{CH}_4$ | 3.00E+07 | 1.5 | 9940.0 |
| 163 | $\text{CH}_3 + \text{CH}_3\text{OH} \rightleftharpoons \text{CH}_3\text{O} + \text{CH}_4$ | 1.00E+07 | 1.5 | 9940.0 |
| 164 | $\text{CH}_3 + \text{C}_2\text{H}_4 \rightleftharpoons \text{C}_2\text{H}_3 + \text{CH}_4$ | 2.27E+05 | 2.0 | 9200.0 |

| | | | | |
|-----|---|----------|------|---------|
| 165 | $\text{CH}_3 + \text{C}_2\text{H}_6 \rightleftharpoons \text{C}_2\text{H}_5 + \text{CH}_4$ | 6.14E+06 | 1.7 | 10450.0 |
| 166 | $\text{HCO} + \text{H}_2\text{O} \rightleftharpoons \text{H} + \text{CO} + \text{H}_2\text{O}$ | 1.50E+18 | -1.0 | 17000.0 |
| 167 | $\text{HCO} + (\text{M}) \rightleftharpoons \text{H} + \text{CO} + (\text{M})$ | 1.87E+17 | -1.0 | 17000.0 |
| 168 | $\text{HCO} + \text{O}_2 \rightleftharpoons \text{HO}_2 + \text{CO}$ | 1.34E+13 | 0.0 | 400.0 |
| 169 | $\text{CH}_2\text{OH} + \text{O}_2 \rightleftharpoons \text{HO}_2 + \text{CH}_2\text{O}$ | 1.80E+13 | 0.0 | 900.0 |
| 170 | $\text{CH}_3\text{O} + \text{O}_2 \rightleftharpoons \text{HO}_2 + \text{CH}_2\text{O}$ | 4.28E-13 | 7.6 | -3530.0 |
| 171 | $\text{C}_2\text{H} + \text{O}_2 \rightleftharpoons \text{HCO} + \text{CO}$ | 1.00E+13 | 0.0 | -755.0 |
| 172 | $\text{C}_2\text{H} + \text{H}_2 \rightleftharpoons \text{H} + \text{C}_2\text{H}_2$ | 5.68E+10 | 0.9 | 1993.0 |
| 173 | $\text{C}_2\text{H}_3 + \text{O}_2 \rightleftharpoons \text{HCO} + \text{CH}_2\text{O}$ | 4.58E+16 | -1.4 | 1015.0 |
| 174 | $\text{C}_2\text{H}_4 + (\text{M}) \rightleftharpoons \text{H}_2 + \text{C}_2\text{H}_2 + (\text{M})$ | 8.00E+12 | 0.4 | 86770.0 |
| 175 | $\text{C}_2\text{H}_5 + \text{O}_2 \rightleftharpoons \text{HO}_2 + \text{C}_2\text{H}_4$ | 8.40E+11 | 0.0 | 3875.0 |
| 176 | $\text{HCCO} + \text{O}_2 \rightleftharpoons \text{OH} + 2\text{CO}$ | 3.20E+12 | 0.0 | 854.0 |
| 177 | $2\text{HCCO} \rightleftharpoons 2\text{CO} + \text{C}_2\text{H}_2$ | 1.00E+13 | 0.0 | 0.0 |
| 178 | $\text{N} + \text{NO} \rightleftharpoons \text{N}_2 + \text{O}$ | 2.70E+13 | 0.0 | 355.0 |
| 179 | $\text{N} + \text{O}_2 \rightleftharpoons \text{NO} + \text{O}$ | 9.00E+09 | 1.0 | 6500.0 |
| 180 | $\text{N} + \text{OH} \rightleftharpoons \text{NO} + \text{H}$ | 3.36E+13 | 0.0 | 385.0 |
| 181 | $\text{N}_2\text{O} + \text{O} \rightleftharpoons \text{N}_2 + \text{O}_2$ | 1.40E+12 | 0.0 | 10810.0 |
| 182 | $\text{N}_2\text{O} + \text{O} \rightleftharpoons 2\text{NO}$ | 2.90E+13 | 0.0 | 23150.0 |
| 183 | $\text{N}_2\text{O} + \text{H} \rightleftharpoons \text{N}_2 + \text{OH}$ | 3.87E+14 | 0.0 | 18880.0 |
| 184 | $\text{N}_2\text{O} + \text{OH} \rightleftharpoons \text{N}_2 + \text{HO}_2$ | 2.00E+12 | 0.0 | 21060.0 |
| 185 | $\text{N}_2\text{O} + (\text{M}) \rightleftharpoons \text{N}_2 + \text{O} + (\text{M})$ | 7.91E+10 | 0.0 | 56020.0 |
| 186 | $\text{HO}_2 + \text{NO} \rightleftharpoons \text{NO}_2 + \text{OH}$ | 2.11E+12 | 0.0 | -480.0 |
| 187 | $\text{NO} + \text{O} + (\text{M}) \rightleftharpoons \text{NO}_2 + (\text{M})$ | 1.06E+20 | -1.4 | 0.0 |
| 188 | $\text{NO}_2 + \text{O} \rightleftharpoons \text{NO} + \text{O}_2$ | 3.90E+12 | 0.0 | -240.0 |
| 189 | $\text{NO}_2 + \text{H} \rightleftharpoons \text{NO} + \text{OH}$ | 1.32E+14 | 0.0 | 360.0 |
| 190 | $\text{NH} + \text{O} \rightleftharpoons \text{NO} + \text{H}$ | 4.00E+13 | 0.0 | 0.0 |
| 191 | $\text{NH} + \text{H} \rightleftharpoons \text{N} + \text{H}_2$ | 3.20E+13 | 0.0 | 330.0 |
| 192 | $\text{NH} + \text{OH} \rightleftharpoons \text{HNO} + \text{H}$ | 2.00E+13 | 0.0 | 0.0 |

| | | | | |
|-----|---|----------|------|---------|
| 193 | $\text{NH} + \text{OH} \rightleftharpoons \text{N} + \text{H}_2\text{O}$ | 2.00E+09 | 1.2 | 0.0 |
| 194 | $\text{NH} + \text{O}_2 \rightleftharpoons \text{HNO} + \text{O}$ | 4.61E+05 | 2.0 | 6500.0 |
| 195 | $\text{NH} + \text{O}_2 \rightleftharpoons \text{NO} + \text{OH}$ | 1.28E+06 | 1.5 | 100.0 |
| 196 | $\text{NH} + \text{N} \rightleftharpoons \text{N}_2 + \text{H}$ | 1.50E+13 | 0.0 | 0.0 |
| 197 | $\text{NH} + \text{H}_2\text{O} \rightleftharpoons \text{HNO} + \text{H}_2$ | 2.00E+13 | 0.0 | 13850.0 |
| 198 | $\text{NH} + \text{NO} \rightleftharpoons \text{N}_2 + \text{OH}$ | 2.16E+13 | -0.2 | 0.0 |
| 199 | $\text{NH} + \text{NO} \rightleftharpoons \text{N}_2\text{O} + \text{H}$ | 3.65E+14 | -0.5 | 0.0 |
| 200 | $\text{NH}_2 + \text{O} \rightleftharpoons \text{OH} + \text{NH}$ | 3.00E+12 | 0.0 | 0.0 |
| 201 | $\text{NH}_2 + \text{O} \rightleftharpoons \text{H} + \text{HNO}$ | 3.90E+13 | 0.0 | 0.0 |
| 202 | $\text{NH}_2 + \text{H} \rightleftharpoons \text{NH} + \text{H}_2$ | 4.00E+13 | 0.0 | 3650.0 |
| 203 | $\text{NH}_2 + \text{OH} \rightleftharpoons \text{NH} + \text{H}_2\text{O}$ | 9.00E+07 | 1.5 | -460.0 |
| 204 | $\text{NNH} \rightleftharpoons \text{N}_2 + \text{H}$ | 3.30E+08 | 0.0 | 0.0 |
| 205 | $\text{NNH} + (\text{M}) \rightleftharpoons \text{N}_2 + \text{H} + (\text{M})$ | 1.30E+14 | -0.1 | 4980.0 |
| 206 | $\text{NNH} + \text{O}_2 \rightleftharpoons \text{HO}_2 + \text{N}_2$ | 5.00E+12 | 0.0 | 0.0 |
| 207 | $\text{NNH} + \text{O} \rightleftharpoons \text{OH} + \text{N}_2$ | 2.50E+13 | 0.0 | 0.0 |
| 208 | $\text{NNH} + \text{O} \rightleftharpoons \text{NH} + \text{NO}$ | 7.00E+13 | 0.0 | 0.0 |
| 209 | $\text{NNH} + \text{H} \rightleftharpoons \text{H}_2 + \text{N}_2$ | 5.00E+13 | 0.0 | 0.0 |
| 210 | $\text{NNH} + \text{OH} \rightleftharpoons \text{H}_2\text{O} + \text{N}_2$ | 2.00E+13 | 0.0 | 0.0 |
| 211 | $\text{NNH} + \text{CH}_3 \rightleftharpoons \text{CH}_4 + \text{N}_2$ | 2.50E+13 | 0.0 | 0.0 |
| 212 | $\text{H} + \text{NO} + (\text{M}) \rightleftharpoons \text{HNO} + (\text{M})$ | 4.48E+19 | -1.3 | 740.0 |
| 213 | $\text{HNO} + \text{O} \rightleftharpoons \text{NO} + \text{OH}$ | 2.50E+13 | 0.0 | 0.0 |
| 214 | $\text{HNO} + \text{H} \rightleftharpoons \text{H}_2 + \text{NO}$ | 9.00E+11 | 0.7 | 660.0 |
| 215 | $\text{HNO} + \text{OH} \rightleftharpoons \text{NO} + \text{H}_2\text{O}$ | 1.30E+07 | 1.9 | -950.0 |
| 216 | $\text{HNO} + \text{O}_2 \rightleftharpoons \text{HO}_2 + \text{NO}$ | 1.00E+13 | 0.0 | 13000.0 |
| 217 | $\text{CN} + \text{O} \rightleftharpoons \text{CO} + \text{N}$ | 7.70E+13 | 0.0 | 0.0 |
| 218 | $\text{CN} + \text{OH} \rightleftharpoons \text{NCO} + \text{H}$ | 4.00E+13 | 0.0 | 0.0 |
| 219 | $\text{CN} + \text{H}_2\text{O} \rightleftharpoons \text{HCN} + \text{OH}$ | 8.00E+12 | 0.0 | 7460.0 |
| 220 | $\text{CN} + \text{O}_2 \rightleftharpoons \text{NCO} + \text{O}$ | 6.14E+12 | 0.0 | -440.0 |

| | | | | |
|-----|--|----------|------|----------|
| 221 | $\text{CN} + \text{H}_2 \rightleftharpoons \text{HCN} + \text{H}$ | 2.95E+05 | 2.5 | 2240.0 |
| 222 | $\text{NCO} + \text{O} \rightleftharpoons \text{NO} + \text{CO}$ | 2.35E+13 | 0.0 | 0.0 |
| 223 | $\text{NCO} + \text{H} \rightleftharpoons \text{NH} + \text{CO}$ | 5.40E+13 | 0.0 | 0.0 |
| 224 | $\text{NCO} + \text{OH} \rightleftharpoons \text{NO} + \text{H} + \text{CO}$ | 2.50E+12 | 0.0 | 0.0 |
| 225 | $\text{NCO} + \text{N} \rightleftharpoons \text{N}_2 + \text{CO}$ | 2.00E+13 | 0.0 | 0.0 |
| 226 | $\text{NCO} + \text{O}_2 \rightleftharpoons \text{NO} + \text{CO}_2$ | 2.00E+12 | 0.0 | 20000.0 |
| 227 | $\text{NCO} + (\text{M}) \rightleftharpoons \text{N} + \text{CO} + (\text{M})$ | 3.10E+14 | 0.0 | 54050.0 |
| 228 | $\text{NCO} + \text{NO} \rightleftharpoons \text{N}_2\text{O} + \text{CO}$ | 1.90E+17 | -1.5 | 740.0 |
| 229 | $\text{NCO} + \text{NO} \rightleftharpoons \text{N}_2 + \text{CO}_2$ | 3.80E+18 | -2.0 | 800.0 |
| 230 | $\text{HCN} + (\text{M}) \rightleftharpoons \text{H} + \text{CN} + (\text{M})$ | 1.04E+29 | -3.3 | 126600.0 |
| 231 | $\text{HCN} + \text{O} \rightleftharpoons \text{NCO} + \text{H}$ | 2.03E+04 | 2.6 | 4980.0 |
| 232 | $\text{HCN} + \text{O} \rightleftharpoons \text{NH} + \text{CO}$ | 5.07E+03 | 2.6 | 4980.0 |
| 233 | $\text{HCN} + \text{O} \rightleftharpoons \text{CN} + \text{OH}$ | 3.91E+09 | 1.6 | 26600.0 |
| 234 | $\text{HCN} + \text{OH} \rightleftharpoons \text{HOCN} + \text{H}$ | 1.10E+06 | 2.0 | 13370.0 |
| 235 | $\text{HCN} + \text{OH} \rightleftharpoons \text{HNCO} + \text{H}$ | 4.40E+03 | 2.3 | 6400.0 |
| 236 | $\text{HCN} + \text{OH} \rightleftharpoons \text{NH}_2 + \text{CO}$ | 1.60E+02 | 2.6 | 9000.0 |
| 237 | $\text{H} + \text{HCN} + (\text{M}) \rightleftharpoons \text{H}_2\text{CN} + (\text{M})$ | 3.30E+13 | 0.0 | 0.0 |
| 238 | $\text{H}_2\text{CN} + \text{N} \rightleftharpoons \text{N}_2 + \text{CH}_2$ | 6.00E+13 | 0.0 | 400.0 |
| 239 | $\text{C} + \text{N}_2 \rightleftharpoons \text{CN} + \text{N}$ | 6.30E+13 | 0.0 | 46020.0 |
| 240 | $\text{CH} + \text{N}_2 \rightleftharpoons \text{HCN} + \text{N}$ | 3.12E+09 | 0.9 | 20130.0 |
| 241 | $\text{CH} + \text{N}_2 + (\text{M}) \rightleftharpoons \text{HCNN} + (\text{M})$ | 3.10E+12 | 0.1 | 0.0 |
| 242 | $\text{CH}_2 + \text{N}_2 \rightleftharpoons \text{HCN} + \text{NH}$ | 1.00E+13 | 0.0 | 74000.0 |
| 243 | $\text{CH}_2(\text{S}) + \text{N}_2 \rightleftharpoons \text{NH} + \text{HCN}$ | 1.00E+11 | 0.0 | 65000.0 |
| 244 | $\text{C} + \text{NO} \rightleftharpoons \text{CN} + \text{O}$ | 1.90E+13 | 0.0 | 0.0 |
| 245 | $\text{C} + \text{NO} \rightleftharpoons \text{CO} + \text{N}$ | 2.90E+13 | 0.0 | 0.0 |
| 246 | $\text{CH} + \text{NO} \rightleftharpoons \text{HCN} + \text{O}$ | 4.10E+13 | 0.0 | 0.0 |
| 247 | $\text{CH} + \text{NO} \rightleftharpoons \text{H} + \text{NCO}$ | 1.62E+13 | 0.0 | 0.0 |
| 248 | $\text{CH} + \text{NO} \rightleftharpoons \text{N} + \text{HCO}$ | 2.46E+13 | 0.0 | 0.0 |

| | | | | |
|-----|--|----------|------|---------|
| 249 | $\text{CH}_2 + \text{NO} \rightleftharpoons \text{H} + \text{HNCO}$ | 3.10E+17 | -1.4 | 1270.0 |
| 250 | $\text{CH}_2 + \text{NO} \rightleftharpoons \text{OH} + \text{HCN}$ | 2.90E+14 | -0.7 | 760.0 |
| 251 | $\text{CH}_2 + \text{NO} \rightleftharpoons \text{H} + \text{HCNO}$ | 3.80E+13 | -0.4 | 580.0 |
| 252 | $\text{CH}_2(\text{S}) + \text{NO} \rightleftharpoons \text{H} + \text{HNCO}$ | 3.10E+17 | -1.4 | 1270.0 |
| 253 | $\text{CH}_2(\text{S}) + \text{NO} \rightleftharpoons \text{OH} + \text{HCN}$ | 2.90E+14 | -0.7 | 760.0 |
| 254 | $\text{CH}_2(\text{S}) + \text{NO} \rightleftharpoons \text{H} + \text{HCNO}$ | 3.80E+13 | -0.4 | 580.0 |
| 255 | $\text{CH}_3 + \text{NO} \rightleftharpoons \text{HCN} + \text{H}_2\text{O}$ | 9.60E+13 | 0.0 | 28800.0 |
| 256 | $\text{CH}_3 + \text{NO} \rightleftharpoons \text{H}_2\text{CN} + \text{OH}$ | 1.00E+12 | 0.0 | 21750.0 |
| 257 | $\text{HCNN} + \text{O} \rightleftharpoons \text{CO} + \text{H} + \text{N}_2$ | 2.20E+13 | 0.0 | 0.0 |
| 258 | $\text{HCNN} + \text{O} \rightleftharpoons \text{HCN} + \text{NO}$ | 2.00E+12 | 0.0 | 0.0 |
| 259 | $\text{HCNN} + \text{O}_2 \rightleftharpoons \text{O} + \text{HCO} + \text{N}_2$ | 1.20E+13 | 0.0 | 0.0 |
| 260 | $\text{HCNN} + \text{OH} \rightleftharpoons \text{H} + \text{HCO} + \text{N}_2$ | 1.20E+13 | 0.0 | 0.0 |
| 261 | $\text{HCNN} + \text{H} \rightleftharpoons \text{CH}_2 + \text{N}_2$ | 1.00E+14 | 0.0 | 0.0 |
| 262 | $\text{HNCO} + \text{O} \rightleftharpoons \text{NH} + \text{CO}_2$ | 9.80E+07 | 1.4 | 8500.0 |
| 263 | $\text{HNCO} + \text{O} \rightleftharpoons \text{HNO} + \text{CO}$ | 1.50E+08 | 1.6 | 44000.0 |
| 264 | $\text{HNCO} + \text{O} \rightleftharpoons \text{NCO} + \text{OH}$ | 2.20E+06 | 2.1 | 11400.0 |
| 265 | $\text{HNCO} + \text{H} \rightleftharpoons \text{NH}_2 + \text{CO}$ | 2.25E+07 | 1.7 | 3800.0 |
| 266 | $\text{HNCO} + \text{H} \rightleftharpoons \text{H}_2 + \text{NCO}$ | 1.05E+05 | 2.5 | 13300.0 |
| 267 | $\text{HNCO} + \text{OH} \rightleftharpoons \text{NCO} + \text{H}_2\text{O}$ | 3.30E+07 | 1.5 | 3600.0 |
| 268 | $\text{HNCO} + \text{OH} \rightleftharpoons \text{NH}_2 + \text{CO}_2$ | 3.30E+06 | 1.5 | 3600.0 |
| 269 | $\text{HNCO} + (\text{M}) \rightleftharpoons \text{NH} + \text{CO} + (\text{M})$ | 1.18E+16 | 0.0 | 84720.0 |
| 270 | $\text{HCNO} + \text{H} \rightleftharpoons \text{H} + \text{HNCO}$ | 2.10E+15 | -0.7 | 2850.0 |
| 271 | $\text{HCNO} + \text{H} \rightleftharpoons \text{OH} + \text{HCN}$ | 2.70E+11 | 0.2 | 2120.0 |
| 272 | $\text{HCNO} + \text{H} \rightleftharpoons \text{NH}_2 + \text{CO}$ | 1.70E+14 | -0.8 | 2890.0 |
| 273 | $\text{HOCN} + \text{H} \rightleftharpoons \text{H} + \text{HNCO}$ | 2.00E+07 | 2.0 | 2000.0 |
| 274 | $\text{HCCO} + \text{NO} \rightleftharpoons \text{HCNO} + \text{CO}$ | 9.00E+12 | 0.0 | 0.0 |
| 275 | $\text{CH}_3 + \text{N} \rightleftharpoons \text{H}_2\text{CN} + \text{H}$ | 6.10E+14 | -0.3 | 290.0 |
| 276 | $\text{CH}_3 + \text{N} \rightleftharpoons \text{HCN} + \text{H}_2$ | 3.70E+12 | 0.1 | -90.0 |

| | | | | |
|-----|---|----------|------|---------|
| 277 | $\text{NH}_3 + \text{H} \rightleftharpoons \text{NH}_2 + \text{H}_2$ | 5.40E+05 | 2.4 | 9915.0 |
| 278 | $\text{NH}_3 + \text{OH} \rightleftharpoons \text{NH}_2 + \text{H}_2\text{O}$ | 5.00E+07 | 1.6 | 955.0 |
| 279 | $\text{NH}_3 + \text{O} \rightleftharpoons \text{NH}_2 + \text{OH}$ | 9.40E+06 | 1.9 | 6460.0 |
| 280 | $\text{NH} + \text{CO}_2 \rightleftharpoons \text{HNO} + \text{CO}$ | 1.00E+13 | 0.0 | 14350.0 |
| 281 | $\text{CN} + \text{NO}_2 \rightleftharpoons \text{NCO} + \text{NO}$ | 6.16E+15 | -0.8 | 345.0 |
| 282 | $\text{NCO} + \text{NO}_2 \rightleftharpoons \text{N}_2\text{O} + \text{CO}_2$ | 3.25E+12 | 0.0 | -705.0 |
| 283 | $\text{N} + \text{CO}_2 \rightleftharpoons \text{NO} + \text{CO}$ | 3.00E+12 | 0.0 | 11300.0 |
| 284 | $\text{O} + \text{CH}_3 \rightleftharpoons \text{H} + \text{H}_2 + \text{CO}$ | 3.37E+13 | 0.0 | 0.0 |
| 285 | $\text{O} + \text{C}_2\text{H}_4 \rightleftharpoons \text{H} + \text{CH}_2\text{CHO}$ | 6.70E+06 | 1.8 | 220.0 |
| 286 | $\text{O} + \text{C}_2\text{H}_5 \rightleftharpoons \text{H} + \text{CH}_3\text{CHO}$ | 1.10E+14 | 0.0 | 0.0 |
| 287 | $\text{OH} + \text{HO}_2 \rightleftharpoons \text{O}_2 + \text{H}_2\text{O}$ | 5.00E+15 | 0.0 | 17330.0 |
| 288 | $\text{OH} + \text{CH}_3 \rightleftharpoons \text{H}_2 + \text{CH}_2\text{O}$ | 8.00E+09 | 0.5 | -1755.0 |
| 289 | $\text{CH} + \text{H}_2 + (\text{M}) \rightleftharpoons \text{CH}_3 + (\text{M})$ | 1.97E+12 | 0.4 | -370.0 |
| 290 | $\text{CH}_2 + \text{O}_2 \rightleftharpoons 2\text{H} + \text{CO}_2$ | 5.80E+12 | 0.0 | 1500.0 |
| 291 | $\text{CH}_2 + \text{O}_2 \rightleftharpoons \text{O} + \text{CH}_2\text{O}$ | 2.40E+12 | 0.0 | 1500.0 |
| 292 | $\text{CH}_2 + \text{CH}_2 \rightleftharpoons 2\text{H} + \text{C}_2\text{H}_2$ | 2.00E+14 | 0.0 | 10989.0 |
| 293 | $\text{CH}_2(\text{S}) + \text{H}_2\text{O} \rightleftharpoons \text{H}_2 + \text{CH}_2\text{O}$ | 6.82E+10 | 0.2 | -935.0 |
| 294 | $\text{C}_2\text{H}_3 + \text{O}_2 \rightleftharpoons \text{O} + \text{CH}_2\text{CHO}$ | 3.03E+11 | 0.3 | 11.0 |
| 295 | $\text{C}_2\text{H}_3 + \text{O}_2 \rightleftharpoons \text{HO}_2 + \text{C}_2\text{H}_2$ | 1.34E+06 | 1.6 | -384.0 |
| 296 | $\text{O} + \text{CH}_3\text{CHO} \rightleftharpoons \text{OH} + \text{CH}_2\text{CHO}$ | 2.92E+12 | 0.0 | 1808.0 |
| 297 | $\text{O} + \text{CH}_3\text{CHO} \rightleftharpoons \text{OH} + \text{CH}_3 + \text{CO}$ | 2.92E+12 | 0.0 | 1808.0 |
| 298 | $\text{O}_2 + \text{CH}_3\text{CHO} \rightleftharpoons \text{HO}_2 + \text{CH}_3 + \text{CO}$ | 3.01E+13 | 0.0 | 39150.0 |
| 299 | $\text{H} + \text{CH}_3\text{CHO} \rightleftharpoons \text{CH}_2\text{CHO} + \text{H}_2$ | 2.05E+09 | 1.2 | 2405.0 |
| 300 | $\text{H} + \text{CH}_3\text{CHO} \rightleftharpoons \text{CH}_3 + \text{H}_2 + \text{CO}$ | 2.05E+09 | 1.2 | 2405.0 |
| 301 | $\text{OH} + \text{CH}_3\text{CHO} \rightleftharpoons \text{CH}_3 + \text{H}_2\text{O} + \text{CO}$ | 2.34E+10 | 0.7 | -1113.0 |
| 302 | $\text{HO}_2 + \text{CH}_3\text{CHO} \rightleftharpoons \text{CH}_3 + \text{H}_2\text{O}_2 + \text{CO}$ | 3.01E+12 | 0.0 | 11923.0 |
| 303 | $\text{CH}_3 + \text{CH}_3\text{CHO} \rightleftharpoons \text{CH}_3 + \text{CH}_4 + \text{CO}$ | 2.72E+06 | 1.8 | 5920.0 |
| 304 | $\text{H} + \text{CH}_2\text{CO} + (\text{M}) \rightleftharpoons \text{CH}_2\text{CHO} + (\text{M})$ | 4.86E+11 | 0.4 | -1755.0 |

| | | | | |
|-----|--|----------|------|--------|
| 305 | $O + CH_2CHO \rightleftharpoons H + CH_2 + CO_2$ | 1.50E+14 | 0.0 | 0.0 |
| 306 | $O_2 + CH_2CHO \rightleftharpoons OH + CO + CH_2O$ | 1.81E+10 | 0.0 | 0.0 |
| 307 | $O_2 + CH_2CHO \rightleftharpoons OH + 2HCO$ | 2.35E+10 | 0.0 | 0.0 |
| 308 | $H + CH_2CHO \rightleftharpoons CH_3 + HCO$ | 2.20E+13 | 0.0 | 0.0 |
| 309 | $H + CH_2CHO \rightleftharpoons CH_2CO + H_2$ | 1.10E+13 | 0.0 | 0.0 |
| 310 | $OH + CH_2CHO \rightleftharpoons H_2O + CH_2CO$ | 1.20E+13 | 0.0 | 0.0 |
| 311 | $OH + CH_2CHO \rightleftharpoons HCO + CH_2OH$ | 3.01E+13 | 0.0 | 0.0 |
| 312 | $CH_3 + C_2H_5 + (M) \rightleftharpoons C_3H_8 + (M)$ | 9.43E+12 | 0.0 | 0.0 |
| 313 | $O + C_3H_8 \rightleftharpoons OH + C_3H_7$ | 1.93E+05 | 2.7 | 3716.0 |
| 314 | $H + C_3H_8 \rightleftharpoons C_3H_7 + H_2$ | 1.32E+06 | 2.5 | 6756.0 |
| 315 | $OH + C_3H_8 \rightleftharpoons C_3H_7 + H_2O$ | 3.16E+07 | 1.8 | 934.0 |
| 316 | $C_3H_7 + H_2O_2 \rightleftharpoons HO_2 + C_3H_8$ | 3.78E+02 | 2.7 | 1500.0 |
| 317 | $CH_3 + C_3H_8 \rightleftharpoons C_3H_7 + CH_4$ | 9.03E-01 | 3.6 | 7154.0 |
| 318 | $CH_3 + C_2H_4 + (M) \rightleftharpoons C_3H_7 + (M)$ | 2.55E+06 | 1.6 | 5700.0 |
| 319 | $O + C_3H_7 \rightleftharpoons C_2H_5 + CH_2O$ | 9.64E+13 | 0.0 | 0.0 |
| 320 | $H + C_3H_7 + (M) \rightleftharpoons C_3H_8 + (M)$ | 3.61E+13 | 0.0 | 0.0 |
| 321 | $H + C_3H_7 \rightleftharpoons CH_3 + C_2H_5$ | 4.06E+06 | 2.2 | 890.0 |
| 322 | $OH + C_3H_7 \rightleftharpoons C_2H_5 + CH_2OH$ | 2.41E+13 | 0.0 | 0.0 |
| 323 | $HO_2 + C_3H_7 \rightleftharpoons O_2 + C_3H_8$ | 2.55E+10 | 0.3 | -943.0 |
| 324 | $HO_2 + C_3H_7 \rightleftharpoons OH + C_2H_5 + CH_2O$ | 2.41E+13 | 0.0 | 0.0 |
| 325 | $CH_3 + C_3H_7 \rightleftharpoons 2C_2H_5$ | 1.93E+13 | -0.3 | 0.0 |

References

- [1] « Annual European Union greenhouse gas inventory 1990–2014 and inventory report 2016 ». Koninklijke Brill NV, doi: 10.1163/9789004322714_cclc_2016-0201-011.
- [2] « Key figures on climate - France, Europe and Worldwide - 2020 EDITION », p. 88.
- [3] « Chiffres clés », *ADEME*. <http://www.ademe.fr/expertises/mobilite-transport/chiffres-cles-observations/chiffres-cles> (consulté le mai 21, 2018).
- [4] « Greenhouse Gas Studies 2014 ». <http://www.imo.org/en/OurWork/Environment/PollutionPrevention/AirPollution/Pages/Greenhouse-Gas-Studies-2014.aspx> (consulté le oct. 08, 2020).
- [5] « Pollution : une hausse des émissions de CO₂ pour la première fois depuis 23 ans », *Europe 1*. <http://www.europe1.fr/societe/pollution-une-hausse-des-emissions-de-co2-pour-la-premiere-fois-depuis-23-ans-3571781> (consulté le mai 21, 2018).
- [6] M. Williams et R. Minjares, « A technical summary of Euro 6/VI vehicle emission standards », p. 12.
- [7] M. P. Morin, « Gazéification de la biomasse en double lit fluidisé circulant : étude des réactions élémentaires de gazéification et de combustion du char et de reformage des goudrons », p. 103.
- [8] D. Occitanie, « Présentation de la production de biogaz (méthanisation) », avr. 27, 2018. <http://draaf.occitanie.agriculture.gouv.fr/Presentation-de-la-production-de> (consulté le avr. 30, 2018).
- [9] V. Langenhove, « Renewables-Based Technology », p. 449.
- [10] C. R. Devia, « Biogaz en vue de son utilisation en production d'énergie: séparation des siloxanes et du sulfure d'hydrogène », p. 203.
- [11] H. Gruber *et al.*, « Fischer-Tropsch products from biomass-derived syngas and renewable hydrogen », *Biomass Convers. Biorefinery*, juin 2019, doi: 10.1007/s13399-019-00459-5.
- [12] R. Rauch, J. Hrbek, et H. Hofbauer, « Biomass gasification for synthesis gas production and applications of the syngas: Biomass gasification for synthesis gas production », *Wiley Interdiscip. Rev. Energy Environ.*, vol. 3, n° 4, p. 343-362, juill. 2014, doi: 10.1002/wene.97.
- [13] « Pyrolyse et gazéification de la biomasse », p. 155.
- [14] M. Fiore, V. Magi, et A. Viggiano, « Internal combustion engines powered by syngas: A review », *Appl. Energy*, vol. 276, p. 115415, oct. 2020, doi: 10.1016/j.apenergy.2020.115415.
- [15] E. Lebas, « Cogénération biomasse par turbine à air chaud », p. 28, 2011.
- [16] « NOTAR Gasifier », *Xylo watt*. <http://www.xylo watt.com/notar-gasifier/> (consulté le oct. 12, 2018).
- [17] « 2016-11-1-Sierra-Energy.pdf ». Consulté le: oct. 11, 2018. [En ligne]. Disponible sur: <https://www.globalsyngas.org/uploads/downloads/2016-11-1-Sierra-Energy.pdf>.
- [18] S. Jain, D. Li, et S. K. Aggarwal, « Effect of hydrogen and syngas addition on the ignition of iso-octane/air mixtures », *Int. J. Hydrog. Energy*, vol. 38, n° 10, p. 4163-4176, avr. 2013, doi: 10.1016/j.ijhydene.2013.01.027.
- [19] J. A. Smith et G. J. J. Bartley, « Stoichiometric Operation of a Gas Engine Utilizing Synthesis Gas and EGR for NO_x Control », *J. Eng. Gas Turbines Power*, vol. 122, n° 4, p. 617-623, oct. 2000, doi: 10.1115/1.1289386.
- [20] K. Vien, « Experiments on the effect of exhaust gas recirculation diluent on the laminar burning speed and stability of syngas/air flames », p. 43.

- [21] S. Bhaduri, H. Jeanmart, et F. Contino, « Tar Tolerant HCCI Engine Fuelled with Biomass Syngas: Combustion Control Through EGR », *Energy Procedia*, vol. 105, p. 1764-1770, mai 2017, doi: 10.1016/j.egypro.2017.03.507.
- [22] D. K. Marsh et A. K. Voice, « Quantification of knock benefits from reformat and cooled exhaust gas recirculation using a Livengood–Wu approach with detailed chemical kinetics », *Int. J. Engine Res.*, vol. 18, n° 7, p. 717-731, sept. 2017, doi: 10.1177/1468087416666728.
- [23] S. Onishi, S. H. Jo, K. Shoda, P. D. Jo, et S. Kato, « Active Thermo-Atmosphere Combustion (ATAC) - A New Combustion Process for Internal Combustion Engines », févr. 1979, p. 790501, doi: 10.4271/790501.
- [24] M. Noguchi, Y. Tanaka, T. Tanaka, et Y. Takeuchi, « A Study on Gasoline Engine Combustion by Observation of Intermediate Reactive Products during Combustion », févr. 1979, p. 790840, doi: 10.4271/790840.
- [25] T. Aoyama, Y. Hattori, J. Mizuta, et Y. Sato, « An Experimental Study on Premixed-Charge Compression Ignition Gasoline Engine », p. 9.
- [26] H. Bendu et S. Murugan, « Homogeneous charge compression ignition (HCCI) combustion: Mixture preparation and control strategies in diesel engines », *Renew. Sustain. Energy Rev.*, vol. 38, p. 732-746, oct. 2014, doi: 10.1016/j.rser.2014.07.019.
- [27] M. Shahbakhti, « Modeling and Experimental Study of an HCCI Engine for Combustion Timing Control », University of Alberta, 2009.
- [28] M. Mofijur, M. M. Hasan, T. M. I. Mahlia, S. M. A. Rahman, A. S. Silitonga, et H. C. Ong, « Performance and Emission Parameters of Homogeneous Charge Compression Ignition (HCCI) Engine: A Review », *Energies*, vol. 12, n° 18, p. 3557, sept. 2019, doi: 10.3390/en12183557.
- [29] Research scholar, Dept. of Mechanical Engineering., Maulana Azad National Inst. of Tech., Bhopal, India, P. Kumar, et A. Rehman, « Homogeneous Charge Compression Ignition (HCCI) Combustion Engine- A Review », *IOSR J. Mech. Civ. Eng.*, vol. 11, n° 6, p. 47-67, 2014, doi: 10.9790/1684-11624767.
- [30] G. Mittal, « A rapid compression machine—design, characterization, and autoignition investigations », PhD Thesis, Case Western Reserve University, 2006.
- [31] Y. Ju, C. B. Reuter, O. R. Yehia, T. I. Farouk, et S. H. Won, « Dynamics of cool flames », *Prog. Energy Combust. Sci.*, vol. 75, p. 100787, nov. 2019, doi: 10.1016/j.peccs.2019.100787.
- [32] J. Clarkson, J. F. Griffiths, J. P. MacNamara, et B. J. Whitaker, « Temperature fields during the development of combustion in a rapid compression machine », *Combust. Flame*, vol. 125, n° 3, p. 1162-1175, mai 2001, doi: 10.1016/S0010-2180(01)00236-X.
- [33] K. H. Tran, P. Guibert, C. Morin, J. Bonnet, S. Pounkin, et G. Legros, « TEMPERATURE MEASUREMENTS IN A RAPID COMPRESSION MACHINE USING ANISOLE PLANAR LASER-INDUCED FLUORESCENCE ». .
- [34] M. Ihme, « On the role of turbulence and compositional fluctuations in rapid compression machines: Autoignition of syngas mixtures », *Combust. Flame*, vol. 159, n° 4, p. 1592-1604, avr. 2012, doi: 10.1016/j.combustflame.2011.11.022.
- [35] M. Izadi Najafabadi et N. Abdul Aziz, « Homogeneous Charge Compression Ignition Combustion: Challenges and Proposed Solutions », *J. Combust.*, vol. 2013, p. 1-14, 2013, doi: 10.1155/2013/783789.
- [36] M. M. Hasan et M. M. Rahman, « Homogeneous charge compression ignition combustion: Advantages over compression ignition combustion, challenges and solutions », *Renew. Sustain. Energy Rev.*, vol. 57, p. 282-291, mai 2016, doi: 10.1016/j.rser.2015.12.157.

- [37] M. Shahbakhti, R. Lupul, et C. R. Koch, « Cyclic Variations of Ignition Timing in an HCCI Engine », in *ASME/IEEE 2007 Joint Rail Conference and Internal Combustion Engine Division Spring Technical Conference*, Pueblo, Colorado, USA, janv. 2007, p. 405-415, doi: 10.1115/JRC/ICE2007-40032.
- [38] G. T. Kalghatgi et R. A. Head, « Combustion Limits and Efficiency in a Homogeneous Charge Compression Ignition Engine », *Int. J. Engine Res.*, vol. 7, n° 3, p. 215-236, juin 2006, doi: 10.1243/14680874JER04605.
- [39] D. Kim et C. Lee, « Improved emission characteristics of HCCI engine by various premixed fuels and cooled EGR », *Fuel*, vol. 85, n° 5-6, p. 695-704, mars 2006, doi: 10.1016/j.fuel.2005.08.041.
- [40] A. Dubreuil, F. Foucher, C. Mounai'm-Rousselle, G. Dayma, et P. Dagaut, « HCCI combustion: Effect of NO in EGR », *Proc. Combust. Inst.*, vol. 31, n° 2, p. 2879-2886, janv. 2007, doi: 10.1016/j.proci.2006.07.168.
- [41] J.-O. Olsson *et al.*, « Compression Ratio Influence on Maximum Load of a Natural Gas Fueled HCCI Engine », mars 2002, p. 2002-01-0111, doi: 10.4271/2002-01-0111.
- [42] M. Shahbakhti et C. R. Koch, « Characterizing the cyclic variability of ignition timing in a homogeneous charge compression ignition engine fuelled with *n*-heptane/iso-octane blend fuels », *Int. J. Engine Res.*, vol. 9, n° 5, p. 361-397, oct. 2008, doi: 10.1243/14680874JER01408.
- [43] M. N. Schleppe, « SI - HCCI mode switching optimization using a physics based model », 2011, doi: 10.7939/R38K9M.
- [44] L. Manofsky, J. Vavra, D. N. Assanis, et A. Babajimopoulos, « Bridging the Gap between HCCI and SI: Spark-Assisted Compression Ignition », avr. 2011, p. 2011-01-1179, doi: 10.4271/2011-01-1179.
- [45] X. Duan, M.-C. Lai, M. Jansons, G. Guo, et J. Liu, « A review of controlling strategies of the ignition timing and combustion phase in homogeneous charge compression ignition (HCCI) engine », *Fuel*, vol. 285, p. 119142, févr. 2021, doi: 10.1016/j.fuel.2020.119142.
- [46] « 413_430_ing.pdf » .
- [47] « theses.fr – Alan Keromnes , Etude expérimentale et modélisation de la combustion par auto-inflammation sur machine à compression rapide ». <http://www.theses.fr/2008PA066609#> (consulté le avr. 01, 2020).
- [48] G. Mittal, M. P. Raju, et C.-J. Sung, « Vortex formation in a rapid compression machine: Influence of physical and operating parameters », *Fuel*, vol. 94, p. 409-417, avr. 2012, doi: 10.1016/j.fuel.2011.08.034.
- [49] J. Würmel, E. J. Silke, H. J. Curran, M. S. Ó Conaire, et J. M. Simmie, « The effect of diluent gases on ignition delay times in the shock tube and in the rapid compression machine », *Combust. Flame*, vol. 151, n° 1-2, p. 289-302, oct. 2007, doi: 10.1016/j.combustflame.2007.06.010.
- [50] D. Bradley, C. Morley, et H. L. Walmsley, « Relevance of Research and Motor Octane Numbers to the Prediction of Engine Autoignition », juin 2004, p. 2004-01-1970, doi: 10.4271/2004-01-1970.
- [51] S. Gersen, N. B. Anikin, A. V. Mokhov, et H. B. Levinsky, « Ignition properties of methane/hydrogen mixtures in a rapid compression machine », *Int. J. Hydrog. Energy*, vol. 33, n° 7, p. 1957-1964, avr. 2008.
- [52] S. Tanaka, F. Ayala, J. C. Keck, et J. B. Heywood, « Two-stage ignition in HCCI combustion and HCCI control by fuels and additives », *Combust. Flame*, p. 21, 2003.

- [53] S. Pounkin, « Etude des régimes de combustion initiés par auto-inflammation et des interactions de la turbulence avec la cinétique réactionnelle chimique », PhD Thesis, Paris 6, 2012.
- [54] P. Desgroux, L. Gasnot, et L. R. Sochet, « Instantaneous temperature measurement in a rapid-compression machine using laser Rayleigh scattering », *Appl. Phys. B Laser Opt.*, vol. 61, n° 1, p. 69-72, juill. 1995, doi: 10.1007/BF01090974.
- [55] J. F. Griffiths, P. A. Halford-Maw, et D. J. Rose, « Fundamental features of hydrocarbon autoignition in a rapid compression machine », *Combust. Flame*, vol. 95, n° 3, p. 291-306, nov. 1993, doi: 10.1016/0010-2180(93)90133-N.
- [56] G. Mittal et C.-J. Sung, « Aerodynamics inside a rapid compression machine », *Combust. Flame*, vol. 145, n° 1-2, p. 160-180, avr. 2006, doi: 10.1016/j.combustflame.2005.10.019.
- [57] H. Di *et al.*, « Effects of buffer gas composition on low temperature ignition of iso-octane and n-heptane », *Combust. Flame*, vol. 161, n° 10, p. 2531-2538, oct. 2014, doi: 10.1016/j.combustflame.2014.04.014.
- [58] T. Kamimoto, H. Kobayashi, et S. Matsuoka, « A Big Size Rapid Compression Machine for Fundamental Studies of Diesel Combustion », sept. 1981, p. 811004, doi: 10.4271/811004.
- [59] M. Gholamisheeri, B. C. Thelen, G. R. Gentz, I. S. Wichman, et E. Toulson, « Rapid compression machine study of a premixed, variable inlet density and flow rate, confined turbulent jet », *Combust. Flame*, vol. 169, p. 321-332, juill. 2016, doi: 10.1016/j.combustflame.2016.05.001.
- [60] Y. Qi, Z. Wang, J. Wang, et X. He, « Effects of thermodynamic conditions on the end gas combustion mode associated with engine knock », *Combust. Flame*, vol. 162, n° 11, p. 4119-4128, nov. 2015, doi: 10.1016/j.combustflame.2015.08.016.
- [61] B. C. Thelen, G. Gentz, et E. Toulson, « Computational Study of a Turbulent Jet Ignition System for Lean Burn Operation in a Rapid Compression Machine », avr. 2015, p. 2015-01-0396, doi: 10.4271/2015-01-0396.
- [62] M. Gholamisheeri, B. Thelen, et E. Toulson, « CFD Modeling and Experimental Analysis of a Homogeneously Charged Turbulent Jet Ignition System in a Rapid Compression Machine », mars 2017, p. 2017-01-0557, doi: 10.4271/2017-01-0557.
- [63] M. Uddi, A. K. Das, et C.-J. Sung, « Temperature measurements in a rapid compression machine using mid-infrared H₂O absorption spectroscopy near 76 μm », *Appl. Opt.*, vol. 51, n° 22, p. 5464, août 2012, doi: 10.1364/AO.51.005464.
- [64] S. Gersen, H. Darmeveil, et H. Levinsky, « The effects of CO addition on the autoignition of H₂, CH₄ and CH₄/H₂ fuels at high pressure in an RCM », *Combust. Flame*, vol. 159, n° 12, p. 3472-3475, déc. 2012, doi: 10.1016/j.combustflame.2012.06.021.
- [65] D. Lee et S. Hochgreb, « Hydrogen autoignition at pressures above the second explosion limit (0.6–4.0 MPa) », *Int. J. Chem. Kinet.*, vol. 30, n° 6, p. 385-406, janv. 1998.
- [66] S. Gersen, A. V. Mokhov, J. H. Darmeveil, et H. B. Levinsky, « Ignition properties of n-butane and iso-butane in a rapid compression machine », *Combust. Flame*, vol. 157, n° 2, p. 240-245, févr. 2010, doi: 10.1016/j.combustflame.2009.10.012.
- [67] D. Lee et S. Hochgreb, « Rapid Compression Machines: Heat Transfer and Suppression of Corner Vortex », *Combust. Flame*, vol. 114, n° 3-4, p. 531-545, août 1998, doi: 10.1016/S0010-2180(97)00327-1.
- [68] N. Donohoe *et al.*, « Ignition delay times, laminar flame speeds, and mechanism validation for natural gas/hydrogen blends at elevated pressures », *Combust. Flame*, vol. 161, n° 6, p. 1432-1443, 2014.

- [69] Y. Yamasaki et S. Kaneko, « Prediction of Ignition and Combustion Development in an HCCI Engine Fueled by Syngas », nov. 2014, p. 2014-32-0002, doi: 10.4271/2014-32-0002.
- [70] G. Przybyla, A. Szlek, D. Haggith, et A. Sobiesiak, « Fuelling of spark ignition and homogenous charge compression ignition engines with low calorific value producer gas », *Energy*, vol. 116, p. 1464-1478, déc. 2016, doi: 10.1016/j.energy.2016.06.036.
- [71] R. K. Cheng et A. K. Oppenheim, « Autoignition in methane-hydrogen mixtures », *Combust. Flame*, vol. 58, n° 2, p. 125-139, nov. 1984, doi: 10.1016/0010-2180(84)90088-9.
- [72] E. Porpatham, A. Ramesh, et B. Nagalingam, « Effect of hydrogen addition on the performance of a biogas fuelled spark ignition engine », *Int. J. Hydrog. Energy*, vol. 32, n° 12, p. 2057-2065, août 2007, doi: 10.1016/j.ijhydene.2006.09.001.
- [73] « moteur_combustion-Hydrogene.pdf » . .
- [74] Q. Ma, Q. Zhang, J. Chen, Y. Huang, et Y. Shi, « Effects of hydrogen on combustion characteristics of methane in air », *Int. J. Hydrog. Energy*, vol. 39, n° 21, p. 11291-11298, juill. 2014, doi: 10.1016/j.ijhydene.2014.05.030.
- [75] J. Huang, W. K. Bushe, P. G. Hill, et S. R. Munshi, « Experimental and kinetic study of shock initiated ignition in homogeneous methane-hydrogen-air mixtures at engine-relevant conditions », *Int. J. Chem. Kinet.*, vol. 38, n° 4, p. 221-233, avr. 2006, doi: 10.1002/kin.20157.
- [76] C. Liu *et al.*, « A rapid compression machine study of autoignition, spark-ignition and flame propagation characteristics of H₂/CH₄/CO/air mixtures », *Combust. Flame*, vol. 188, p. 150-161, févr. 2018, doi: 10.1016/j.combustflame.2017.09.031.
- [77] S. Bari, « Effect of carbon dioxide on the performance of biogas/diesel duel-fuel engine », *Renew. Energy*, vol. 9, n° 1-4, p. 1007-1010, sept. 1996, doi: 10.1016/0960-1481(96)88450-3.
- [78] M. Mohamed Ibrahim et A. Ramesh, « Investigations on the effects of intake temperature and charge dilution in a hydrogen fueled HCCI engine », *Int. J. Hydrog. Energy*, vol. 39, n° 26, p. 14097-14108, sept. 2014, doi: 10.1016/j.ijhydene.2014.07.019.
- [79] J. Shao, R. Choudhary, D. F. Davidson, R. K. Hanson, S. Barak, et S. Vasu, « Ignition delay times of methane and hydrogen highly diluted in carbon dioxide at high pressures up to 300 atm », *Proc. Combust. Inst.*, vol. 37, n° 4, p. 4555-4562, 2019, doi: 10.1016/j.proci.2018.08.002.
- [80] P. Sabia, M. Lubrano Lavadera, P. Giudicianni, G. Sorrentino, R. Ragucci, et M. de Joannon, « CO₂ and H₂O effect on propane auto-ignition delay times under mild combustion operative conditions », *Combust. Flame*, vol. 162, n° 3, p. 533-543, mars 2015, doi: 10.1016/j.combustflame.2014.08.009.
- [81] A. Schneider, J. Mantzaras*, et S. Eriksson, « Ignition and Extinction in Catalytic Partial Oxidation of Methane-Oxygen Mixtures with Large H₂O and CO₂ Dilution », *Combust. Sci. Technol.*, vol. 180, n° 1, p. 89-126, nov. 2007, doi: 10.1080/00102200701487087.
- [82] B. Koroglu, O. M. Pryor, J. Lopez, L. Nash, et S. S. Vasu, « Shock tube ignition delay times and methane time-histories measurements during excess CO₂ diluted oxy-methane combustion », *Combust. Flame*, vol. 164, p. 152-163, févr. 2016, doi: 10.1016/j.combustflame.2015.11.011.
- [83] O. Pryor, S. Barak, B. Koroglu, E. Ninnemann, et S. S. Vasu, « Measurements and interpretation of shock tube ignition delay times in highly CO₂ diluted mixtures using multiple diagnostics », *Combust. Flame*, vol. 180, p. 63-76, juin 2017, doi: 10.1016/j.combustflame.2017.02.020.

- [84] Th. Just, « B. Lewis, G. von Elbe: Combustion, Flames and Explosions of Gases, 3. Aufl., Academic Press, Orlando, San Diego, New York, Austin, Boston, London, Sydney, Tokyo, Toronto 1987. 739 Seiten, Preis: \$ 69.–. », *Berichte Bunsenges. Für Phys. Chem.*, vol. 93, n° 1, p. 101-102, janv. 1989, doi: 10.1002/bbpc.19890930123.
- [85] O. for E. C.-O. and Development, « Carbon monoxide - hydrogen combustion characteristics in severe accident containment conditions. Final report », Organisation for Economic Co-Operation and Development, NEA-CSNI-R--2000-10, 2000. Consulté le: mars 06, 2020. [En ligne]. Disponible sur: http://inis.iaea.org/Search/search.aspx?orig_q=RN:39039106.
- [86] Y. Yu, G. Vanhove, J. F. Griffiths, S. De Ferrières, et J.-F. Pauwels, « Influence of EGR and Syngas Components on the Autoignition of Natural Gas in a Rapid Compression Machine: A Detailed Experimental Study », *Energy Fuels*, vol. 27, n° 7, p. 3988-3996, juill. 2013, doi: 10.1021/ef400336x.
- [87] J. H. Chen, E. R. Hawkes, R. Sankaran, S. D. Mason, et H. G. Im, « Direct numerical simulation of ignition front propagation in a constant volume with temperature inhomogeneities », *Combust. Flame*, vol. 145, n° 1-2, p. 128-144, avr. 2006, doi: 10.1016/j.combustflame.2005.09.017.
- [88] P. Guibert, A. Keromnes, et G. Legros, « Development of a Turbulence Controlled Rapid Compression Machine for HCCI Combustion », juill. 2007, p. 2007-01-1869, doi: 10.4271/2007-01-1869.
- [89] R. J. Kee, M. E. Coltrin, et P. Glarborg, *Chemically reacting flow: theory and practice*. Hoboken, N.J: Wiley-Interscience, 2003.
- [90] « Page not found | UC Berkeley Mechanical Engineering ». https://me.berkeley.edu/gri_mech/ (consulté le sept. 09, 2019).
- [91] « Overview ». <http://combustion.berkeley.edu/gri-mech/overview.html#whatisgrimech> (consulté le mars 01, 2018).
- [92] M. Fischer et X. Jiang, « An assessment of chemical kinetics for bio-syngas combustion », *Fuel*, vol. 137, p. 293-305, décembre 2014, doi: 10.1016/j.fuel.2014.07.081.
- [93] W. Zeng, H. Ma, Y. Liang, et E. Hu, « Experimental and modeling study on effects of N₂ and CO₂ on ignition characteristics of methane/air mixture », *J. Adv. Res.*, vol. 6, n° 2, p. 189-201, mars 2015, doi: 10.1016/j.jare.2014.01.003.
- [94] N. Stylianidis, U. Azimov, et M. Birkett, « Investigation of the Effect of Hydrogen and Methane on Combustion of Multicomponent Syngas Mixtures using a Constructed Reduced Chemical Kinetics Mechanism », *Energies*, vol. 12, n° 12, p. 2442, juin 2019, doi: 10.3390/en12122442.
- [95] D. Lapalme et P. Seers, « Influence of CO₂, CH₄, and initial temperature on H₂/CO laminar flame speed », *Int. J. Hydrog. Energy*, vol. 39, n° 7, p. 3477-3486, févr. 2014, doi: 10.1016/j.ijhydene.2013.12.109.
- [96] « Combustion Chemistry Centre ». http://www.nuigalway.ie/c3/Mechanism_release/frontmatter.html (consulté le avr. 08, 2018).
- [97] W. K. Metcalfe, S. M. Burke, S. S. Ahmed, et H. J. Curran, « A Hierarchical and Comparative Kinetic Modeling Study of C₁ – C₂ Hydrocarbon and Oxygenated Fuels: KINETIC STUDY OF C₁ – C₂ HYDROCARBON AND OXYGENATED FUELS », *Int. J. Chem. Kinet.*, vol. 45, n° 10, p. 638-675, oct. 2013, doi: 10.1002/kin.20802.

- [98] C.-W. Zhou *et al.*, « An experimental and chemical kinetic modeling study of 1,3-butadiene combustion: Ignition delay time and laminar flame speed measurements », *Combust. Flame*, vol. 197, p. 423-438, nov. 2018, doi: 10.1016/j.combustflame.2018.08.006.
- [99] H. C. Lee, « A Detailed Chemical Kinetics Mechanism for Biogas and Syngas Combustion », p. 290.
- [100] « ChemKin_Theory_PaSR.pdf ». .
- [101] R. Minetti, M. Carlier, M. Ribaucour, E. Therssen, et L. R. Sochet, « A Rapid Compression Machine Investigation of Oxidation and Auto-Ignition of n-Heptane: Measurements and Modeling », p. 12.
- [102] H. J. Curran, P. Gaffuri, W. J. Pitz, et C. K. Westbrook, « A Comprehensive Modeling Study of n-Heptane Oxidation », *Combust. Flame*, vol. 114, n° 1-2, p. 149-177, juill. 1998, doi: 10.1016/S0010-2180(97)00282-4.
- [103] X. He *et al.*, « An experimental and modeling study of iso-octane ignition delay times under homogeneous charge compression ignition conditions », *Combust. Flame*, vol. 142, n° 3, p. 266-275, août 2005, doi: 10.1016/j.combustflame.2005.02.014.
- [104] V. Manente, « Characterization of Glow Plug and HCCI Combustion Processes in a Small Volume at High Engine Speed », p. 132.
- [105] W. D. Manha, « Propellant Systems Safety », in *Safety Design for Space Systems*, Elsevier, 2009, p. 661-694.
- [106] S. McAllister, J.-Y. Chen, et A. C. Fernandez-Pello, *Fundamentals of Combustion Processes*. New York, NY: Springer New York, 2011.
- [107] L. J. Spadaccini et M. B. Colket, « Ignition delay characteristics of methane fuels », *Prog. Energy Combust. Sci.*, vol. 20, n° 5, p. 431-460, janv. 1994, doi: 10.1016/0360-1285(94)90011-6.
- [108] D. Healy *et al.*, « Methane/ethane/propane mixture oxidation at high pressures and at high, intermediate and low temperatures », *Combust. Flame*, vol. 155, n° 3, p. 441-448, nov. 2008, doi: 10.1016/j.combustflame.2008.07.003.
- [109] U. Burke *et al.*, « An ignition delay and kinetic modeling study of methane, dimethyl ether, and their mixtures at high pressures », *Combust. Flame*, vol. 162, n° 2, p. 315-330, févr. 2015, doi: 10.1016/j.combustflame.2014.08.014.
- [110] D. He et W. Yan, « Influences of different diluents on ignition delay of syngas at gas turbine conditions: A numerical study », *Chin. J. Chem. Eng.*, vol. 25, n° 1, p. 79-88, janv. 2017, doi: 10.1016/j.cjche.2016.06.003.
- [111] « 1-s2.0-030438949400082R-main.pdf ». .
- [112] D. Jung, « Autoignition and Chemical-Kinetic Mechanisms of Homogeneous Charge Compression Ignition Combustion for the Fuels with Various Autoignition Reactivity », *Adv. Chem. Kinet.*, déc. 2017, doi: 10.5772/intechopen.70541.
- [113] P. Kongsereparp et M. D. Checkel, « Investigating the Effects of Reformed Fuel Blending in a Methane- or n-Heptane-HCCI Engine Using a Multi-Zone Model », avr. 2007, p. 2007-01-0205, doi: 10.4271/2007-01-0205.
- [114] V. Hosseini et M. D. Checkel, « Effect of Reformer Gas on HCCI Combustion - Part I: High Octane Fuels », avr. 2007, p. 2007-01-0208, doi: 10.4271/2007-01-0208.
- [115] A. B. Mansfield et M. S. Wooldridge, « High-pressure low-temperature ignition behavior of syngas mixtures », *Combust. Flame*, vol. 161, n° 9, p. 2242-2251, sept. 2014, doi: 10.1016/j.combustflame.2014.03.001.
- [116] K. Olchewsky, C. Fuller, M. Holton, et P. Gokulakrishnan, « Autoignition Temperature Measurements of Hydrogen Mixtures », 2017.

- [117] N. Dronniou, « Etude théorique et expérimentale des stratégies de combustion homogène - Application aux moteurs Diesel pour véhicules industriels », p. 678.
- [118] A. B. Sahu et R. V. Ravikrishna, « A detailed numerical study of NO_x kinetics in low calorific value H₂/CO syngas flames », *Int. J. Hydrog. Energy*, vol. 39, n° 30, p. 17358-17370, oct. 2014, doi: 10.1016/j.ijhydene.2014.08.031.
- [119] J. B. Heywood, *Internal combustion engine fundamentals*. New York: McGraw-Hill, 1988.
- [120] M. Brander, « Greenhouse Gases, CO₂, CO₂e, and Carbon: What Do All These Terms Mean? », p. 3.
- [121] L. Waldheim et T. Nilsson, « HEATING VALUE OF GASES FROM BIOMASS GASIFICATION », p. 61.
- [122] G. A. Lavoie, J. B. Heywood, et J. C. Keck, « Experimental and Theoretical Study of Nitric Oxide Formation in Internal Combustion Engines », *Combust. Sci. Technol.*, vol. 1, n° 4, p. 313-326, févr. 1970, doi: 10.1080/00102206908952211.
- [123] R. Borghi et M. Destriau, *Combustion et les flamme...* Editions OPHRYS.
- [124] E. Mallard et H.-L. LE CHATELIER, « Recherches expérimentales et théoriques sur la combustion des mélanges gazeux explosifs », *Librairie Alain Brieux*. <http://www.alainbrieux.com/recherches-experimentales-et-theoriques-sur-la-combustion-des-melanges-gazeux-explosifs-ako69798.html> (consulté le févr. 23, 2020).
- [125] L. Landry, « Etude expérimentale des modes de combustion essence sous forte pression et forte dilution », p. 177, 2009.
- [126] B. Galmiche, « Caractérisation expérimentale des flammes laminaires et turbulentes en expansion », p. 261.
- [127] C. Clanet et G. Searby, « First Experimental Study of the Darrieus-Landau Instability », *Phys. Rev. Lett.*, vol. 80, n° 17, p. 3867-3870, avr. 1998, doi: 10.1103/PhysRevLett.80.3867.
- [128] F. A. Williams, *Combustion theory: the fundamental theory of chemically reacting flow systems*, 2nd ed. Menlo Park, Calif: Benjamin/Cummings Pub. Co, 1985.
- [129] S. McAllister, J.-Y. Chen, et A. C. Fernandez-Pello, « Chemical Kinetics », in *Fundamentals of Combustion Processes*, New York, NY: Springer New York, 2011, p. 49-73.
- [130] T. Boushaki, Y. Dhué, L. Selle, B. Ferret, et T. Poinsot, « Effects of hydrogen and steam addition on laminar burning velocity of methane-air premixed flame: Experimental and numerical analysis », *Int. J. Hydrog. Energy*, vol. 37, n° 11, p. 9412-9422, juin 2012, doi: 10.1016/j.ijhydene.2012.03.037.
- [131] M. Ilbas, A. Crayford, I. Yilmaz, P. Bowen, et N. Syred, « Laminar-burning velocities of hydrogen-air and hydrogen-methane-air mixtures: An experimental study », *Int. J. Hydrog. Energy*, vol. 31, n° 12, p. 1768-1779, sept. 2006, doi: 10.1016/j.ijhydene.2005.12.007.
- [132] R. Ennetta et A. Yahya, « Etude de la combustion du méthane enrichi à l'hydrogène », p. 13, 2012.
- [133] T. Lieuwen, V. McDonnell, E. Petersen, et D. Santavicca, « Fuel Flexibility Influences on Premixed Combustor Blowout, Flashback, Autoignition, and Stability », *J. Eng. Gas Turbines Power*, vol. 130, n° 1, p. 011506, janv. 2008, doi: 10.1115/1.2771243.
- [134] « Properties of Hydrogen-Containing Fuels », p. 6.
- [135] F. Liu, H. Guo, et G. J. Smallwood, « The chemical effect of CO₂ replacement of N₂ in air on the burning velocity of CH₄ and H₂ premixed flames », *Combust. Flame*, vol. 133, n° 4, p. 495-497, juin 2003, doi: 10.1016/S0010-2180(03)00019-1.
- [136] C. Cohé, C. Chauveau, I. Gökalp, et D. F. Kurtuluş, « CO₂ addition and pressure effects on laminar and turbulent lean premixed CH₄ air flames », *Proc. Combust. Inst.*, vol. 32, n° 2, p. 1803-1810, 2009, doi: 10.1016/j.proci.2008.06.181.

- [137] C. D'Ippolito, « A Numerical Study of Syngas Laminar Premixed Flames: Effects of Lewis Number and Flame Stretch », p. 161.
- [138] C. K. Westbrook et F. L. Dryer, « Simplified Reaction Mechanisms for the Oxidation of Hydrocarbon Fuels in Flames », *Combust. Sci. Technol.*, vol. 27, n° 1-2, p. 31-43, déc. 1981, doi: 10.1080/00102208108946970.
- [139] A. Clarke, « Calculation and Consideration of the Lewis Number for Explosion Studies », *Process Saf. Environ. Prot.*, vol. 80, n° 3, p. 135-140, mai 2002, doi: 10.1205/095758202317576238.
- [140] H. J. Burbano, J. Pareja, et A. A. Amell, « Laminar burning velocities and flame stability analysis of H₂/CO/air mixtures with dilution of N₂ and CO₂ », *Int. J. Hydrog. Energy*, vol. 36, n° 4, p. 3232-3242, févr. 2011, doi: 10.1016/j.ijhydene.2010.11.089.
- [141] C. M. Vagelopoulos et F. N. Egolfopoulos, « Laminar flame speeds and extinction strain rates of mixtures of carbon monoxide with hydrogen, methane, and air », *Symp. Int. Combust.*, vol. 25, n° 1, p. 1317-1323, janv. 1994, doi: 10.1016/S0082-0784(06)80773-3.
- [142] H. S. Zhen, C. W. Leung, C. S. Cheung, et Z. H. Huang, « Combustion characteristic and heating performance of stoichiometric biogas–hydrogen–air flame », *Int. J. Heat Mass Transf.*, vol. 92, p. 807-814, janv. 2016, doi: 10.1016/j.ijheatmasstransfer.2015.09.040.
- [143] H. S. Zhen, C. W. Leung, C. S. Cheung, et Z. H. Huang, « Characterization of biogas-hydrogen premixed flames using Bunsen burner », *Int. J. Hydrog. Energy*, vol. 39, n° 25, p. 13292-13299, août 2014, doi: 10.1016/j.ijhydene.2014.06.126.
- [144] P. Guibert, A. Keromnes, et G. Legros, « An Experimental Investigation of the Turbulence Effect on the Combustion Propagation in a Rapid Compression Machine », *Flow Turbul. Combust.*, vol. 84, n° 1, p. 79, janv. 2010, doi: 10.1007/s10494-009-9225-z.
- [145] K. P. Grogan, S. Scott Goldsborough, et M. Ihme, « Ignition regimes in rapid compression machines », *Combust. Flame*, vol. 162, n° 8, p. 3071-3080, août 2015, doi: 10.1016/j.combustflame.2015.03.020.
- [146] H. G. Im, P. Pal, M. S. Wooldridge, et A. B. Mansfield, « A Regime Diagram for Autoignition of Homogeneous Reactant Mixtures with Turbulent Velocity and Temperature Fluctuations », *Combust. Sci. Technol.*, vol. 187, n° 8, p. 1263-1275, août 2015, doi: 10.1080/00102202.2015.1034355.
- [147] T. Poinsot et D. Veynante, *Theoretical and Numerical Combustion*. R.T. Edwards, Inc., 2005.
- [148] J. Klingmann et B. Johansson, « Measurements of Turbulent Flame Speed and Integral Length Scales in a Lean Stationary Premixed Flame », févr. 1998, p. 981050, doi: 10.4271/981050.
- [149] C. Du, M. Andersson, et S. Andersson, « The Influence of Ethanol Blending in Diesel fuel on the Spray and Spray Combustion Characteristics », *SAE Int. J. Fuels Lubr.*, vol. 7, n° 3, p. 823-832, oct. 2014, doi: 10.4271/2014-01-2755.
- [150] S. Thongchai et O. Lim, « Macroscopic Spray Behavior of a Single-Hole Common Rail Diesel Injector Using Gasoline-Blended 5% Biodiesel », *Energies*, vol. 13, n° 9, p. 2276, mai 2020, doi: 10.3390/en13092276.
- [151] « SPRAY ENGINEERING HANDBOOK ». www.pnr-nozzles.com.
- [152] M. Weclas et J. Cypris, « “Distribution-nozzle” concept: a method for Diesel spray distribution in space for charge homogenization by late injection strategy », p. 2.
- [153] M. Weclas et J. Cypris, « Characterization of the distribution-nozzle operation for mixture homogenization by a late-diesel-injection strategy », *Proc. Inst. Mech. Eng. Part J. Automob. Eng.*, vol. 226, n° 4, p. 529-546, avr. 2012, doi: 10.1177/0954407011420499.

- [154] W. Thielicke et E. J. Stamhuis, « PIVlab – Towards User-friendly, Affordable and Accurate Digital Particle Image Velocimetry in MATLAB », *J. Open Res. Softw.*, vol. 2, oct. 2014, doi: 10.5334/jors.bl.
- [155] Y. Aiba, K. Murai, M. Omiya, et J. Komotori, « Observation of Particle Behavior in Fine Particle Peening process », p. 5.
- [156] P. Basu, *Biomass gasification and pyrolysis: practical design and theory*. Burlington, MA: Academic Press, 2010.
- [157] S. V. Vassilev, D. Baxter, L. K. Andersen, et C. G. Vassileva, « An overview of the chemical composition of biomass », *Fuel*, vol. 89, n° 5, p. 913-933, mai 2010, doi: 10.1016/j.fuel.2009.10.022.
- [158] Y. Sun et J. Cheng, « Hydrolysis of lignocellulosic materials for ethanol production: a review q », *Bioresour. Technol.*, p. 11, 2002.
- [159] J.-Lo. FAULONI', G. A. Carlson, et P. Hatcher, « A three-dimensional model for lignocellulose from gymnospermous wood », p. 11.
- [160] P. Harmsen, W. Huijgen, L. Bermudez, et R. Bakker, « Literature review of physical and chemical pretreatment processes for lignocellulosic biomass », p. 54.
- [161] F. Shafizadeh, « Introduction to pyrolysis of biomass », *J. Anal. Appl. Pyrolysis*, vol. 3, n° 4, p. 283-305, avr. 1982, doi: 10.1016/0165-2370(82)80017-X.
- [162] S. Wang, B. Ru, H. Lin, et Z. Luo, « Degradation mechanism of monosaccharides and xylan under pyrolytic conditions with theoretic modeling on the energy profiles », *Bioresour. Technol.*, vol. 143, p. 378-383, sept. 2013, doi: 10.1016/j.biortech.2013.06.026.
- [163] H. Lu, « EXPERIMENTAL AND MODELING INVESTIGATIONS OF BIOMASS PARTICLE COMBUSTION », p. 220.
- [164] S. Willför, J. Hemming, M. Reunanen, C. Eckerman, et B. Holmbom, « Lignans and Lipophilic Extractives in Norway Spruce Knots and Stemwood », *Holzforschung*, vol. 57, n° 1, p. 27-36, janv. 2003, doi: 10.1515/HF.2003.005.
- [165] A. Anca-Couce, « Reaction mechanisms and multi-scale modelling of lignocellulosic biomass pyrolysis », *Prog. Energy Combust. Sci.*, vol. 53, p. 41-79, mars 2016, doi: 10.1016/j.peccs.2015.10.002.
- [166] M. G. Groenli, « A theoretical and experimental study of the thermal degradation of biomass », p. 339.
- [167] B. Piriou, G. Vaitilingom, B. Veyssière, B. Cuq, et X. Rouau, « Potential direct use of solid biomass in internal combustion engines », *Prog. Energy Combust. Sci.*, vol. 39, n° 1, p. 169-188, févr. 2013, doi: 10.1016/j.peccs.2012.08.001.
- [168] S. Sadaka et D. M. Johnson, « Biomass Combustion », p. 6.
- [169] N. Razmjoo, « Characterization of conversion zones in a reciprocating grate furnace firing wet woody biomass ». 2018.
- [170] H. Fatehi, « Numerical simulation of ignition mode and ignition delay time of pulverized biomass particles », *Combust. Flame*, p. 11, 2019.
- [171] H. Lu, E. Ip, J. Scott, P. Foster, M. Vickers, et L. L. Baxter, « Effects of particle shape and size on devolatilization of biomass particle », *Fuel*, vol. 89, n° 5, p. 1156-1168, mai 2010, doi: 10.1016/j.fuel.2008.10.023.
- [172] Y. Wang *et al.*, « Experimental study on mercury transformation and removal in coal-fired boiler flue gases », *Fuel Process. Technol.*, vol. 90, n° 5, p. 643-651, mai 2009, doi: 10.1016/j.fuproc.2008.10.013.

- [173] D. V. Suriapparao et R. Vinu, « Effects of Biomass Particle Size on Slow Pyrolysis Kinetics and Fast Pyrolysis Product Distribution », *Waste Biomass Valorization*, vol. 9, n° 3, p. 465-477, mars 2018, doi: 10.1007/s12649-016-9815-7.
- [174] A.-C. Johansson, H. Wiinikka, L. Sandström, M. Marklund, O. G. W. Öhrman, et J. Narvesjö, « Characterization of pyrolysis products produced from different Nordic biomass types in a cyclone pilot plant », *Fuel Process. Technol.*, vol. 146, p. 9-19, juin 2016, doi: 10.1016/j.fuproc.2016.02.006.
- [175] S. A. EL-Sayed et M. E. Mostafa, « Analysis of Grain Size Statistic and Particle Size Distribution of Biomass Powders », *Waste Biomass Valorization*, vol. 5, n° 6, p. 1005-1018, déc. 2014, doi: 10.1007/s12649-014-9308-5.
- [176] R. K. Jalan et V. K. Srivastava, « Studies on pyrolysis of a single biomass cylindrical pellet kinetic and heat transfer effects », *Energy Convers.*, p. 28, 1999.
- [177] A. M. C. Janse, R. W. J. Westerhout, et W. Prins, « Modelling of flash pyrolysis of a single wood particle », *Chem. Eng. Process. Process Intensif.*, vol. 39, n° 3, p. 239-252, mai 2000, doi: 10.1016/S0255-2701(99)00092-6.
- [178] R. S. Miller et J. Bellan, « Analysis of Reaction Products and Conversion Time in the Pyrolysis of Cellulose and Wood Particles », *Combust. Sci. Technol.*, vol. 119, n° 1-6, p. 331-373, oct. 1996, doi: 10.1080/00102209608952004.
- [179] P. Debiagi, G. Gentile, A. Cuoci, A. Frassoldati, E. Ranzi, et T. Faravelli, « A predictive model of biochar formation and characterization », *J. Anal. Appl. Pyrolysis*, vol. 134, p. 326-335, sept. 2018, doi: 10.1016/j.jaap.2018.06.022.
- [180] E. Ranzi, P. E. A. Debiagi, et A. Frassoldati, « Mathematical Modeling of Fast Biomass Pyrolysis and Bio-Oil Formation. Note I: Kinetic Mechanism of Biomass Pyrolysis », *ACS Sustain. Chem. Eng.*, vol. 5, n° 4, p. 2867-2881, avr. 2017, doi: 10.1021/acssuschemeng.6b03096.
- [181] A. V. Bridgwater, « Review of fast pyrolysis of biomass and product upgrading », *Biomass Bioenergy*, vol. 38, p. 68-94, mars 2012, doi: 10.1016/j.biombioe.2011.01.048.
- [182] A. Demirbas, « Effects of temperature and particle size on bio-char yield from pyrolysis of agricultural residues », *J. Anal. Appl. Pyrolysis*, vol. 72, n° 2, p. 243-248, nov. 2004, doi: 10.1016/j.jaap.2004.07.003.
- [183] E. Ranzi, P. E. A. Debiagi, et A. Frassoldati, « Mathematical Modeling of Fast Biomass Pyrolysis and Bio-Oil Formation. Note II: Secondary Gas-Phase Reactions and Bio-Oil Formation », *ACS Sustain. Chem. Eng.*, vol. 5, n° 4, p. 2882-2896, avr. 2017, doi: 10.1021/acssuschemeng.6b03098.
- [184] A. Molina et C. R. Shaddix, « Ignition and devolatilization of pulverized bituminous coal particles during oxygen/carbon dioxide coal combustion », *Proc. Combust. Inst.*, vol. 31, n° 2, p. 1905-1912, janv. 2007, doi: 10.1016/j.proci.2006.08.102.
- [185] Y. Yuan, S. Li, G. Li, N. Wu, et Q. Yao, « The transition of heterogeneous–homogeneous ignitions of dispersed coal particle streams », *Combust. Flame*, vol. 161, n° 9, p. 2458-2468, sept. 2014, doi: 10.1016/j.combustflame.2014.03.008.
- [186] R. Khatami, C. Stivers, et Y. A. Levendis, « Ignition characteristics of single coal particles from three different ranks in O₂/N₂ and O₂/CO₂ atmospheres », *Combust. Flame*, vol. 159, n° 12, p. 3554-3568, déc. 2012, doi: 10.1016/j.combustflame.2012.06.019.
- [187] J. Riaza, M. Ajmi, J. Gibbins, et H. Chalmers, « Ignition and Combustion of Single Particles of Coal and Biomass under O₂/CO₂ Atmospheres », *Energy Procedia*, vol. 114, p. 6067-6073, juill. 2017, doi: 10.1016/j.egypro.2017.03.1743.

- [188] X. Liu *et al.*, « Thermal degradation and stability of starch under different processing conditions », *Starch - Stärke*, vol. 65, n° 1-2, p. 48-60, janv. 2013, doi: 10.1002/star.201200198.
- [189] P. Aggarwal et D. Dollimore, « A thermal analysis investigation of partially hydrolyzed starch », *Thermochim. Acta*, vol. 319, n° 1-2, p. 17-25, oct. 1998, doi: 10.1016/S0040-6031(98)00355-4.
- [190] X. Liu, L. Yu, H. Liu, L. Chen, et L. Li, « Thermal Decomposition of Corn Starch with Different Amylose/Amylopectin Ratios in Open and Sealed Systems », *Cereal Chem. J.*, vol. 86, n° 4, p. 383-385, juill. 2009, doi: 10.1094/CCHEM-86-4-0383.
- [191] C. Beninca, I. M. Demiate, L. G. Lacerda, M. A. S. Carvalho Filho, M. Ionashiro, et E. Schnitzler, « Thermal behavior of corn starch granules modified by acid treatment at 30 and 50°C », *Eclética Quím.*, vol. 33, n° 3, p. 13-18, 2008, doi: 10.1590/S0100-46702008000300002.
- [192] P. Aggarwal et D. Dollimore, « The combustion of starch, cellulose and cationically modified products of these compounds investigated using thermal analysis », *Thermochim. Acta*, vol. 291, n° 1-2, p. 65-72, avr. 1997, doi: 10.1016/S0040-6031(96)03103-6.
- [193] S. Walton, X. He, B. Zigler, M. Wooldridge, et A. Atreya, « An experimental investigation of iso-octane ignition phenomena », *Combust. Flame*, vol. 150, n° 3, p. 246-262, août 2007, doi: 10.1016/j.combustflame.2006.07.016.
- [194] « Chapter 2 Chemiluminescence: the phenomenon », in *Comprehensive Analytical Chemistry*, vol. 29, Elsevier, 1992, p. 7-52.
- [195] L. Zheng et Y. Zhang, « High Speed Digital Imaging for Flame Studies: Potentials and Limitations », *Energy Procedia*, vol. 66, p. 237-240, 2015, doi: 10.1016/j.egypro.2015.02.039.
- [196] J. Neuman, « Development of a Rapid Compression Controlled-Expansion Machine for Chemical Ignition Studies », p. 117.
- [197] R. X. Yu *et al.*, « Effect of Turbulence on HCCI Combustion », p. 15.
- [198] N. Fukushima *et al.*, « Combustion regime classification of HCCI/PCCI combustion using Lagrangian fluid particle tracking », *Proc. Combust. Inst.*, vol. 35, n° 3, p. 3009-3017, 2015, doi: 10.1016/j.proci.2014.07.059.
- [199] C. Zou, L. Cai, D. Wu, Y. Liu, S. Liu, et C. Zheng, « Ignition behaviors of pulverized coal particles in O₂/N₂ and O₂/H₂O mixtures in a drop tube furnace using flame monitoring techniques », *Proc. Combust. Inst.*, vol. 35, n° 3, p. 3629-3636, 2015, doi: 10.1016/j.proci.2014.06.067.
- [200] A. Saltelli, M. Ratto, S. Tarantola, et F. Campolongo, « Sensitivity Analysis for Chemical Models », *Chem. Rev.*, vol. 105, n° 7, p. 2811-2828, juill. 2005, doi: 10.1021/cr040659d.
- [201] A. Saltelli, Éd., *Global sensitivity analysis: the primer*. Chichester: Wiley, 2008.
- [202] J. Morio, « Global and local sensitivity analysis methods for a physical system », *Eur. J. Phys.*, vol. 32, n° 6, p. 1577-1583, nov. 2011, doi: 10.1088/0143-0807/32/6/011.
- [203] K. J. Hughes, J. F. Griffiths, M. Fairweather, et A. S. Tomlin, « Evaluation of models for the low temperature combustion of alkanes through interpretation of pressure-temperature ignition diagrams », *Phys Chem Chem Phys*, vol. 8, n° 27, p. 3197-3210, 2006, doi: 10.1039/B605379C.
- [204] « ChemKin_Theory_PaSR.pdf ». .
- [205] B. Abareishi, H. Mohagheghi, et K. Kalalabadi, « Investigate auto-ignition of stoichiometric methane-air mixture », p. 17.

- [206] S. Vajda, P. Valko, et T. Turányi, « Principal component analysis of kinetic models », *Int. J. Chem. Kinet.*, vol. 17, n° 1, p. 55-81, 1985, doi: 10.1002/kin.550170107.
- [207] T. Turányi, « Applications of sensitivity analysis to combustion chemistry », *Reliab. Eng. Syst. Saf.*, vol. 57, n° 1, p. 41-48, juill. 1997, doi: 10.1016/S0951-8320(97)00016-1.